Universidad Autónoma de Madrid

Facultad de Ciencias

Departamento de Física Teórica

THE DEVELOPMENT OF TRITIUM TRANSPORT MODELS FOR THE DUAL COOLANT LITHIUM LEAD BREEDING BLANKET CONCEPT: THE EFFECT OF MAGNETOHYDRODYNAMICS ON TRITIUM BEHAVIOR

Author:
Fernando Roca Urgorri

Directed by: Ángel Ibarra Sánchez

Tutored by: Luís Miguel Robledo Martín

A dissertation for the degree of Doctor of Philosophy

Madrid 2018

Agradecimientos

Este trabajo ha sido posible gracias al apoyo y tutela de todo el equipo de *Breeding Blankets* del CIEMAT. Sus profesionales han permitido que el trabajo técnico de esta tesis saliera adelante aportando su gran experiencia en cada una de sus especialidades. Me gustaría destacar de entre todos ellos la figura de Carlos Moreno Tejera, sin cuya gran aportación este trabajo no habra sido posible. Además, quiero agradecer a todos aquellos trabajadores y trabajadoras del CIEMAT que, sin importar su ámbito de trabajo, han creado un ambiente laboral único en el que me he sentido verdaderamente acogido.

Por supuesto, quiero agradecer a todos mis amigos y amigas que me han ayudado cuando lo necesitaba. Ya he perdido la cuenta de los problemas que he solucionado gracias a ellos. Gracias porque sé que puedo contar con vosotros. La vida da muchas vueltas pero espero que nuestas vueltas se sigan cruzando.

No quiero perder esta oportunidad para agradecer a mi familia. Cualquiera de mis logros se deberá siempre a ellos, nadie pudo nunca soñar con un punto de partida mejor que el mío. Gracias a mi madre, por escucharme siempre, por sus consejos, si en verdad me parezco a ella seré afortunado. Gracias a mi padre por mostrar siempre entusiasmo, por animarme a seguir adelante, nadie tuvo nunca mejor fan. Gracias a mi hermana, que siempre cuidó de mi, a quien admiro más de lo que se imagina y que siempre será uno de mis mayores referentes. Gracias a mis abuelas y a mis abuelos, por todo lo que me han enseñado y por todo lo que me quieren. Gracias también a todo el matriarcado gallego, es maravilloso saber que tengo un lugar al que llamar hogar a 600 kilómetros. Gracias por último a Carmen, mi nueva familia, la luz de mis días y mis noches, sin ti no sería como soy ahora, sin ti esta tesis sería otra. Gracias a todos.

Contents

Agradecimientos **iii**

Acronyms **xi**

List of Figures **xv**

List of Tables **xxiii**

Introducción **xxvii**

Introduction **1**

Objectives 1

Structure of the dissertation 3

1 Research context **5**

1.1 Motivation for fusion energy research 5

1.2 Thermonuclear fusion by magnetic confinement 9

1.2.1 Fundamentals of nuclear fusion reactions 9

1.2.2 Magnetic confinement devices 13

1.3 Tritium 16

1.3.1 Breeding blanket concepts 17
1.3.2 Tritium modeling for breeding blankets 22
1.4 The DCLL breeding blanket concept 26
1.4.1 The European DCLL design 32

2 Theoretical framework for MHD in liquid metal flows 39
2.1 MHD phenomena in liquid metals 39
2.1.1 Fluid dynamics differential description 40
2.1.2 MHD differential description 44
2.1.3 Fully developed MHD flows 49
2.1.4 MHD quasi-2-dimensional approach 51
2.1.5 Analytic solutions of MHD flows 52
2.2 Heat transfer in liquid metal flows 56
2.2.1 Differential description of heat transfer 56
2.2.2 Magneto-convection phenomena 59

3 Theoretical framework for tritium transport 61
3.1 Tritium permeation 61
3.1.1 Diffusion/advection phenomena 62
3.1.2 Surface phenomena 64
3.1.3 Isotopic effects 68
3.1.4 Boundary layer approximation 70
3.2 Analytic solutions 72

3.2.1 Interface between two solid materials 72
3.2.2 Recombination boundary conditions 74

4 Initial system level model of the DCLL blanket 77

4.1 Previous codes and algorithms 77
4.2 The EcosimPro simulation tool 79
4.2.1 Fluid materials 81
4.2.2 Solid materials 82
4.2.3 Interfaces 83
4.2.4 Ancillary systems 84
4.3 Tritium transport system level model for DCLL blanket 84
4.3.1 Process flow diagrams 84
4.3.2 Model inputs 89
4.3.3 Reference case results 92
4.3.4 Parametric studies 96
4.3.5 Discussion 100

5 Computational MHD analyses for the DCLL blanket 103

5.1 Computational tools used for MHD 103
5.1.1 OpenFOAM libraries 105
5.1.2 ANSYS-Fluent simulation platform 106
5.2 MHD issues in the European DCLL 109
5.2.1 MHD constants 110

5.2.2 Pressure drop in the breeding zone 111
5.2.3 Pressure drop in the BSS 112
5.2.4 Other sources of pressure drop 114
5.3 MHD analyses of the DCLL BSS 116
5.3.1 Input conditions 117
5.3.2 Simulation results 119
5.3.3 Discussion 121
5.4 Pressure drop in fringing magnetic fields 122
5.4.1 Input conditions 123
5.4.2 Simulation results 124
5.4.3 Discussion 127
5.5 MHD evaluation of different FCI designs 127
5.5.1 Input conditions 128
5.5.2 Pressure drop and flow distribution results 133
5.5.3 Heat transfer results 137
5.5.4 Discussion 141
5.6 Effect of the helium cooling channels on the PbLi gap flow . . . 142
5.6.1 Input conditions 142
5.6.2 Simulation results 144
5.6.3 Discussion 147
5.7 Magneto-convective analyses of the DCLL OB equatorial module 148
5.7.1 Inputs conditions 149

5.7.2 Simulation results 152

5.7.3 Discussion 156

6 Deep level tritium transport model for DCLL blanket 159

6.1 Numerical formulation 159

6.1.1 Customization capabilities of ANSYS-Fluent 163

6.1.2 Fluent tritium transport validation test 163

6.2 Tritium transport in laminar flows 165

6.2.1 Deep level model results 165

6.2.2 Upgrade of component level models 168

6.3 Tritium transport in laminar flows with volumetric generation . 172

6.3.1 Deep level model results 173

6.3.2 Upgrade of component level models 175

6.4 Tritium transport models in MHD fully developed flows 180

6.4.1 MHD profiles in the the PbLi channel 180

6.4.2 Tritium transport in MHD flows without volumetric generation 182

6.4.3 Tritium transport in MHD flows with volumetric generation 185

6.5 Tritium transport model of the DCLL gap flow 190

6.5.1 Deep level model results 191

6.5.2 Upgrading of system level models 194

6.6 Discussion 200

7 Advanced system level model of the DCLL blanket 203

7.1 Model description 203
7.1.1 Process flow diagrams 205
7.1.2 Input parameters 208
7.2 Reference case results 212
7.3 Parametric studies 216
7.3.1 T solubility in PbLi 216
7.3.2 PbLi mass flow rate 217
7.3.3 TES extraction efficiency 219
7.4 Discussion 219

Conclusions **223**

Conclusiones **227**

Bibliography **231**

Publications and conference contributions **247**

Acronyms

BB Breeding Blanket

BCS Bardeen Cooper Schrieffer theory

BL Boundary Layer

BSS Back Supporting Structure

BW Back Wall

CANDU Canadian Deuterium Uranium

CEA *Commissariat l'Énergie Atomique et aux Énergies Alternatives*

CFD Computational Fluid Dynamics

CIEMAT Centro de Investigaciones Energéticas Medioambientales y Tecnológicas

CPS Coolant Purification System

DCLL Dual Coolant Lithium Lead

DDD Design Description Document

DEMO DEMOnstration Power Station

DR Design Report

DT Deuterium-Tritium

ENEA *Agenzia nazionale per le nuove tecnologie, l'energia e lo sviluppo economico sostenibile*

EU European Union

FCI Flow Channel Insert

FNSF Fusion Nuclear Science Facility

FUS-TPC Fusion Tritium Permeation Code

FW First Wall

HCCB Helium Cooled Ceramic Breeder

HCCR Helium Cooled Ceramic Reflector

HCLL Helium Cooled Lithium Lead

HCPB Helium Cooled Ceramic Pebble

HX Heat Exchanger

IFMIF International Fusion Material Irradiation Facility

IB Inboard

INL Idaho National Laboratory

ITER International Thermonuclear Experimental Reactor

JET Joint European Torus

KIT Karlsruhe Institute of Technology

MHD MagnetoHydroDynamics

MMS Multi-Module Segment

MPI Message Passing Interface

Mtoe Million tonnes of oil equivalent

LLCB Lithium Lead Ceramic Breeder

LOCA Loss Of Coolant Accident

OB Outboard

PFD Process Flow Diagram

PISO Pressure-Implicit with Splitting of Operators

Q2D Quasi 2 Dimensional

QCD Quantum ChromoDynamics

QFT Quantum Field Theory

RW Radial Wall

SCLL Self Cooled Lithium Lead

SG Steam Generator

TBM Test Blanket Module

TBS Test Blanket System

TBR Tritium Breeding Ratio

TES Tritium Extraction System

TLK Tritium Laboratory Karlsruhe

UDF User Defined Functions

UDS User Defined Scalars

UN United Nations

WCCB Water Cooled Ceramic Breeder

WCLL Water Cooled Lithium Lead

List of Figures

1.1 Global energy consumption in different regions. 6

1.2 World fuel consumption classified by energy carrier. 6

1.3 World electricity generation classified by power station type. . . 7

1.4 Binding energy per nucleon as function of the nucleon number. . 10

1.5 Cross sections for D - T, D - D and D - ^{3}He reactions. 13

1.6 Scheme of a tokamak device. 14

1.7 Model of the TJ-II stellarator. 15

1.8 Cross section of tritium production reactions from lithium. . . . 18

1.9 Cross section of neutron multiplication reactions. 20

1.10 Scheme of the tritium fuel cycle with a HCPB blanket. 22

1.11 Feedback loop for tritium modeling optimization. 26

1.12 Scheme of a generic blanket. 28

1.13 Scheme of the MHD interactions. 30

1.14 2014 DEMO geometry. 32

1.15 Geometrical configuration of one DCLL sector. 33

1.16 Geometry of the OB equatorial module for different versions of the DCLL design. 34

1.17 FW cooling scheme for DCLL version 1. 35

1.18 Helium channels of the radial stiffening plates for version 1 and 2. 36

1.19 DCLL channel representation with a sandwich-like FCI. 37

2.1 Notation for surface stresses in a fluid. 41

2.2 Hartmann flow solution. 48

2.3 Shercliff flow computed with Fluent. 54

2.4 Electrical currents induced in the Hunt flow next to a corner. . . 54

2.5 Hunt flow computed with Fluent. 55

2.6 Pressure drop as a function of the wall conductance ratio in a square section channel. 56

3.1 Scheme of the basic processes that affects tritium transport in the DCLL. 68

3.2 Sketch of the tritium concentration next to the BL. 71

3.3 Configuration of the first tritium transport analytic example . . 73

3.4 Analytic solution of the first tritium transport analytic example. 74

3.5 Configuration of the second tritium transport analytic example. 75

3.6 Analytic solution of the second tritium transport analytic example. 76

4.1 Flowchart of the HCPB system level model. 78

4.2 Flowchart of the FNSF system modeled with TMAP. 79

4.3 Example of an EcosimPro schematic file. 80

4.4 Discretization scheme followed by the EcosimPro tritium transport components. 81

4.5 Minimal geometrical representative unit of the DCLL. 85

4.6 PFD of one of the 16 lead-lithium loops in the DCLL blanket. . 86

4.7 Flowchart of one of the 4 parallel circuits of the breeder module. 87

4.8 Flowchart of one lead-lithium channel. 88

4.9 Permeation surface approximation for the cooled walls. 88

4.10 Flowcharts of a cooled wall and the heat exchanger. 89

4.11 Compendium of tritium solubility measures in PbLi. 90

4.12 Generation pulses considered for the DCLL system level model. 91

4.13 Geometrical input data of the initial tritium transport model at system level for the DCLL. 92

4.14 Permeation rate in a single PbLi channel. 93

4.15 Tritium inventory obtained with the preliminary model. 94

4.16 Tritium permeation rate in the reference case. 95

4.17 Parametric study of the PbLi mass flow rate. 97

4.18 Parametric study of the TES extraction efficiency. 98

4.19 Parametric study of the T solubility in PbLi 1. 99

4.20 Parametric study around the T solubility in PbLi 2. 100

5.1 Comparison between Fluent result and analytic solution. 108

5.2 Detailed view of the connection between the module and the BSS channels. 112

5.3 Back view of the BSS cold channel. 113

5.4 Schematic view of the bottom part of the BB. 115

5.5 Scheme of the mesh used for solving the BSS flow. 119

5.6 Velocity profile of the BSS. 119

5.7 MHD BLs next in the BSS channels. 120

5.8 Induced currents in the BSS cross section. 120

5.9 Induced magnetic field in the BSS cross section. 121

5.10 Pressure along the BSS channels. 121

5.11 Non-uniform magnetic field distribution in a PbLi channel. . . . 123

5.12 Contours of the electric potential and pressure field in a central plane perpendicular to the magnetic field. 124

5.13 Induced currents and velocity vectors next to the fringing regions. 125

5.14 Velocity profile in the middle of the fringing region. 126

5.15 Pressure drop along different axis of the channel. 126

5.16 FCI design options under consideration for the European DCLL. 128

5.17 Sketch of the cross section of one DCLL central front channel. . 129

5.18 Detailed part of the computational mesh used for the thin sandwich FCI design. 130

5.19 Helium flow path and temperatures in the DCLL. 132

5.20 Velocity profiles for the central front channel with 3 different FCI designs and without FCI. 134

5.21 Current distribution for the DCLL central poloidal channel with a thin sandwich FCI. 135

5.22 Axial velocity next to the Side wall along a radial line that crosses the center of the channel (y = 0). 135

5.23 Temperature contours in the central radial-poloidal plane. . . . 138

5.24 Temperature contours in the middle section (z=L/2). 139

5.25 Distribution of He channels among the EUROFER walls. 143

5.26 Detailed view of the computational mesh used for the He channels study. 144

5.27 Gap flow velocity profile. 145

5.28 Induced currents next to the corner of the DCLL front channel. 145

5.29 Induced magnetic field along different radial and toroidal lines. . 146

5.30 Velocity profile in the center of the Hartmann gap. 147

5.31 Radial-poloidal section of the DCLL OB equatorial module. . . 150

5.32 Volumetric heat generation in the DCLL OB equatorial breeder zone. 151

5.33 Detailed view of the mesh used for the magneto-convective computation. 151

5.34 Temperature contours in the radial-poloidal section of the DCLL. 152

5.35 Velocity streamlines in the radial-poloidal section of the DCLL. 153

5.36 Vector field in the middle part of the DCLL OB equatorial module.154

5.37 Vector field in the top part of the DCLL OB equatorial module. 155

5.38 Velocity and temperature profile in the front channel of the DCLL module. 155

6.1 Comparison between analytic solutions and numerical results close to an interface. 164

6.2 Comparison between analytic solutions and numerical results when considering recombination boundary conditions. 164

6.3 Geometrical inputs for the tritium transport analysis in laminar regime. 166

6.4 Velocity profile and concentration profile in the mid sectional plane. 167

6.5 PFD of a PbLi channel. 168

6.6 Upgraded PFDs of a PbLi channel. 170

6.7 Comparison between component level and deep level models (laminar regime). 170

6.8 Concentration profile in a channel with volumetric generation. . 173

6.9 Concentration BL next to the channel walls. 174

6.10 Concentration profile in next to the FW with a generating BL. . 177

6.11 Optimization study around the generation in the FW BL. . . . 178

6.12 Concentration profile in the BL after the optimization process. . 179

6.13 Fully developed velocity profiles with and without magnetic field. 181

6.14 Fully developed flows for different Hartmann numbers. 182

6.15 Concentration BL in MHD flows. 183

6.16 Correlation between the Hartmann number and the Sherwood number in a rectangular section PbLi channel. 185

6.17 Concentration contours in a PbLi channel with Ha = 7500 and exponential-shaped volumetric generation. 186

6.18 Concentration profile along a line perpendicular to the magnetic field in a PbLi channel with volumetric generation. 187

6.19 Concentration and velocity profiles next to a BL for high Hartmann number in a PbLi channel with volumetric generation. 188

6.20 Concentration profile along a line parallel to the magnetic field. 189

6.21 Concentration contours in the mid sectional plane of the PbLi gap flow. 192

6.22 Tritium diffusion flux inside the wall of one DCLL channel. . . . 193

6.23 Concentration at the interface PbLi gap/wall (PbLi side). 194

6.24 PFD used for upgrading the gap flow system level model. 196

6.25 Tritium inventory in the wall. Deviation of system level model results with respect to deep level model results. 197

6.26 Parametric sweep of K_t and ψ_{RW} with $\psi_{FW} = 20$ for the DCLL gap flow. 198

6.27 Parametric sweep of ψ_{FW} for the DCLL gap flow ($K_t = 2 \cdot 10^{-5}$ and $\psi_{RW} = 0.4$). 198

6.28 Parametric sweep of K_t and ψ_{RW} with $\psi_{FW} = 25$ for the DCLL gap flow. 199

7.1 Minimal geometrical unit and its corresponding flowchart of the advanced DCLL tritium transport model at system level. 205

7.2 PFD used for modelling the BSS manifolds of the DCLL blanket. 206

7.3 PFD for the advanced tritium transport model of the DCLL blanket and its main auxiliary systems. 207

7.4 Dimensions of one OB DCLL segment. 208

7.5 PbLi temperature map in the DCLL breeder zone. 209

7.6 Schematic view of one tube of the PbLi HX. 211

7.7 Global outcomes of the DCLL advanced tritium transport model at system level. 213

7.8 Concentration in PbLi and extraction rate zoomed in on the peak values. 214

7.9 Sensitivity analysis of tritium solubility in Pbli. 217

7.10 Sensitivity analysis of the PbLi mass flow rate. 218

7.11 Sensitivity analysis of the PbLi mass flow rate. 219

List of Tables

1.1 Breeding blanket concepts. 20

1.2 PbLi-based BB classification 1. 29

1.3 PbLi/helium-based BB classification 2. 31

4.1 Macroscopic constants of tritium in the materials of interest. . . 90

4.2 Results of the DCLL initial tritium transport model at system level. 96

5.1 Characteristic dimensionless constants of the DCLL outboard channels. 110

5.2 Characteristic dimensionless constants of the DCLL inboard channels. 111

5.3 Summary of the MHD pressure drop sources in the European DCLL. 116

5.4 Input parameters for the MHD calculations of the DCLL BSS. . 118

5.5 Dimensionless parameters for the fringing magnetic field study. . 123

5.6 Input parameters for the FCI comparison study. 133

5.7 Materials properties used in the FCI comparison study. 133

5.8 Pressure drop associated to 3 different FCI designs. 136

5.9 Characteristic velocities of the fully developed flow computations. 137

5.10 Flow distribution for 3 different FCI designs. 137

5.11 Net heat fluxes through the channel walls (from PbLi to He) for 3 different FCI designs. 140

5.12 Outcomes of the magneto-convective and forced convective computations. 156

6.1 Input data for the tritium transport simulation in laminar regime. 167

6.2 Results of tritium transport in laminar regime. 171

6.3 Integrated generation rate in the different regions of the PbLi channel. 176

6.4 Permeation rate and inventories in a PbLi channel with generation. 180

6.5 Inputs for the MHD fully developed computations. 181

6.6 Deep level tritium transport results for different Hartmann numbers in an PbLi channel immersed in a magnetic field. . . . 184

6.7 Deep level tritium transport results for different Hartmann numbers in a PbLi channel with volumetric generation. 190

6.8 Results of the deep level tritium transport study of the DCLL gap flow. 194

6.9 Results comparison between deep level model and system level models for the gap flow of the DCLL. 200

7.1 PbLi loops input parameters. 210

7.2 He loops input parameters. 210

7.3 Input data for the HX tritium transport model. 212

7.4 Hydrogen transport properties of 316L steel. 212

7.5 Main global outcomes of the DCLL system level advanced model. 215

The development of tritium transport models for the Dual Coolant Lithium Lead breeding blanket concept: The effect of magnetohydrodynamics on tritium behavior

Desarrollo de modelos de transporte de tritio para el concepto de envoltura regeneradora de doble refrigerante DCLL: el efecto de la magnetohidrodinámica en el comportamiento del tritio

Fernando Roca Urgorri

Abstract

El tritio es uno de los combustibles necesarios para los futuros reactores de fusión por confinamiento magnético. Se trata de un elemento inestable y muy escaso en la naturaleza, lo que lo convierte en un recurso valioso y estratégico para la sociedad. Es por ello que, desde hace varias décadas, se están desarrollando distintos diseños de envolturas regeneradoras (*breeding blankets*), cuya función es regenerar el tritio quemado en el reactor. De esta manera, se pretende desarrollar una tecnología de fusión autosuficiente respecto al tritio, es decir, que no dependa de la inyección constante de tritio proveniente de fuentes externas.

Al igual que los demás isótopos de hidrógeno, el tritio no puede confinarse fácilmente debido a su capacidad de permear a través de las estructuras sólidas conforme a las leyes de la difusión. Por ello, la creación de herramientas computacionales predictivas rápidas y de suficiente precisión resulta fundamental para el diseño de la envoltura. En concreto, el objetivo principal de este proyecto de investigación es desarrollar modelos de transporte de tritio optimizados para el concepto de envoltura regeneradora de doble refrigerante DCLL (*Dual Coolant Lithium Lead*).

Para cumplir este objetivo, se ha empleado una metodología nueva basada en el uso recursivo de modelos a nivel de sistema y de modelos tridimensionales de elementos finitos. Los primeros son rápidos y consumen pocos recursos, sin embargo, su precisión está sumamente limitada por su baja dimensionalidad. Por el contrario, los modelos de elementos finitos ofrecen una gran precisión pero requieren una cantidad muy considerable de tiempo y recursos. El uso combinado de ambos tipos de modelos ha permitido realizar una optimización de los modelos a nivel de sistema y, así, incrementar enormemente su precisión en comparación con otros modelos desarrollados en el pasado.

El desarrollo de modelos de transporte de tritio tridimensionales requiere de un estudio fluidodinámico previo de la envoltura. En efecto, la envoltura DCLL está basada en una aleación líquida de litio-plomo que fluye en torno al plasma del reactor. La dinámica del metal líquido está dominada por los efectos magnetohidrodinámicos: potentes fuerzas de Lorentz causadas por el campo magnético del reactor. Estas fuerzas modifican el perfil de velocidades del metal líquido, lo que repercute muy significativamente en el transporte de tritio. En el presente trabajo se han realizado los primeros estudios en los que se analiza el efecto de las fuerzas MHD en la evolución del tritio. Gracias a los resultados obtenidos, se ha logrado reducir notablemente la incertidumbre asociada a los modelos de transporte del DCLL a nivel de sistema.

Introducción

Objetivos

A lo largo de las últimas décadas la comunidad científica ha dedicado importantes recursos a la obtención de energía civil de fusión termonuclear. De todas las posibilidades exploradas, la reacción de fusión del deuterio y el tritio es una de las más prometedoras. Uno de los componentes clave para el desarrollo de futuros reactores deuterio-tritio es la conocida como envoltura regeneradora. La función principal de este componente es regenerar el tritio quemado en la reacción nuclear de fusión para su futuro procesamiento y reinyección en el reactor. Por tanto, la envoltura regeneradora es fundamental para que el desarrollo del ciclo de combustible del tritio sea sostenible y eficiente.

Las condiciones a las que está sometida la envoltura dentro del reactor son muy exigentes. Ninguna de las tecnologías conceptuales propuestas es capaz por el momento de dar una solución completa a todas las necesidades de este componente. Dentro de las actividades llevadas a cabo por el consorcio EUROfusion, el Centro de Investigaciones Energéticas Medioambientales y Tecnológicas (CIEMAT) lidera las tareas de diseño de uno de los conceptos propuestos como envoltura regeneradora: el *Dual Coolant Lithium Lead (DCLL)*. Este concepto ofrece una serie de ventajas que lo hacen muy prometedor en comparación con sus competidores. Sin embargo, también conlleva una serie de retos que deben ser solventados por la comunidad investigadora. Por este motivo, una cantidad muy importante de recursos materiales y humanos está siendo invertida en Europa para desarrollar un diseño viable de envoltura DCLL.

Dentro de los retos asociados al DCLL y a cualquier otro concepto de envoltura regeneradora, mantener los inventarios y las pérdidas de tritio en niveles mínimos es una prioridad. Esto se debe principalmente al riesgo radiológico asociado al tritio pero también a la escasez de este preciado combustible. En este contexto, el desarrollo de herramientas predictivas capaces de monitorizar las concentraciones y flujos de tritio en toda la envoltura cobra especial relevancia.

El presente proyecto doctoral se enmarca dentro de las tareas de diseño del DCLL europeo. El principal objetivo de este trabajo es desarrollar e implementar un modelo de transporte de tritio fiable y de gran precisión que incluya la envoltura regeneradora y la mayor parte de sus subsistemas auxiliares. El modelado de un sistema tan vasto como éste no puede abordarse de manera directa. Por un lado, los modelos a nivel de sistema basados en diagramas de flujo arrastran importantes errores e incertidumbres de origen tanto teórico como experimental. Por otro lado, simular el sistema completo utilizando modelos tridimensionales de volúmenes finitos conllevaría una cantidad desproporcionada e inabarcable de tiempo y recursos computacionales.

Ninguna de las estrategias de modelado previas puede por sí misma proporcionar un modelo como el que se persigue. Por ello, en este trabajo se ha empleado una nueva metodología basada en el uso recursivo de ambos tipos de modelos. Por un lado, se han desarrollado modelos tridimensionales detallados de geometrías concretas que se han identificado como fundamentales para el transporte de tritio en la envoltura DCLL europea. Por otro lado, los resultados de estos modelos se han utilizado para la optimización de modelos a nivel de sistema lo que ha permitido aumentar significativamente su precisión manteniendo tiempos de computación relativamente cortos.

Dadas las características de la envoltura DCLL, el desarrollo de modelos tridimensionales de transporte de tritio conlleva forzosamente el estudio de los efectos magnetohydrodinámicos (MHD) en metales líquidos. Los fenómenos MHD son procesos multifísicos que involucran el estudio y acoplamiento de los campos electromagnéticos y el campo de velocidad del fluído.

Con independencia del desarrollo de modelos de transporte de tritio, las simulaciones de fenómenos MHD son de gran importancia para el diseño del DCLL. Por este motivo, el estudio de los efectos MHD asociados a la

geometría del DCLL se ha incluido como un objetivo independiente de este trabajo. Profundizar en el estudio de los fenómenos MHD aumenta significativamente la contribución del presente trabajo al diseño del DCLL.

Por último, la influencia que los fenómenos MHD tienen en el transporte de tritio dentro del blanket es un fenómeno que apenas ha sido estudiado y nunca para unas condiciones relevantes para el DCLL. Estos efectos son fundamentales en el comportamiento del tritio dentro de la envoltura regeneradora. Por ello, el estudio de los procesos físicos involucrados en la interacción entre la MHD y el transporte de tritio es el último de los objetivos principales de este trabajo.

Estructura de la memoria

La presente memoria está estructurada en siete capítulos. De la manera habitual, el trabajo tiene una estructura piramidal, de modo que la información expuesta en cada capítulo está fundamentada en resultados, desarrollos teóricos y conceptos que son explicados en apartados previos.

En el capítulo 1 se expone de manera introductoria el contexto en el cual se ubica este trabajo. Se introducen los conceptos básicos de la energía civil de fusión prestando una especial atención al concepto de envoltura regeneradora y al papel crucial que juega el tritio en el desarrollo de futuros reactores de fusión. En este capítulo se explican en detalle las estrategias de modelado de transporte de tritio que se han empleado. Por último, se proporciona una descripción del actual estado de diseño del DCLL europeo, el cual ha servido de base a toda la investigación desarrollada durante este proyecto.

En el capítulo 2 se introducen todos los conceptos teóricos necesarios para el estudio de procesos MHD en metales líquidos. Se desarrollan las ecuaciones fundamentales que describen estas interacciones estudiando su aplicabilidad así como ciertas simplificaciones relevantes para las condiciones de trabajo del DCLL.

En el capítulo 3 se realiza una descripción teórica de los procesos de transporte de masa. Se estudia la permeación de isótopos de hidrógeno a través de sistemas sólidos y líquidos. También se describen los procesos de superficie en las interfases entre materiales incluyendo la formación de capas

límite de concentración. La formulación teórica expuesta servirá de base para la elaboración de modelos de transporte de tritio en las envolturas regeneradoras y en todos sus sistemas auxiliares.

En el capítulo 4 se presenta el primer modelo de transporte de tritio realizado para el DCLL europeo. Se analizan los resultados proporcionados por este modelo en contexto con modelos anteriores desarrollados para diferentes conceptos de envolturas regeneradoras. Se presentan los resultados de diversos estudios paramétricos para estudiar el impacto de dichos parámetros sobre el sistema.

En el capítulo 5 se exponen los cálculos MHD llevados a cabo para el análisis del DCLL. Se estudian diferentes geometrías, todas relevantes para el concepto de envoltura DCLL, utilizando diferentes herramientas computacionales. Parte de los resultados de estos cálculos son utilizados para la implementación de modelos tridimensionales de transporte de tritio en el siguiente capítulo.

En el capítulo 6 se realiza la conexión entre los fenómenos de transporte de tritio y los procesos MHD. Se presentan los resultados de modelos tridimensionales multifísca de transporte de tritio en las geometrías más relevantes del DCLL. Las simulaciones permiten el análisis de la interacción de las fuerzas MHD, la generación volumétrica de tritio y los fenómenos de transporte. Además, los resultados de algunas de estas simulaciones sirven como base para la optimización de los componentes de los modelos de transporte de tritio a nivel de sistema.

En el capítulo 7 se presenta el desarrollo y los resultados de un modelo avanzado de transporte de tritio a nivel de sistema para toda la envoltura DCLL con sus sistemas auxiliares. A diferencia del modelo inicial del capítulo 4, el modelo avanzado hace uso de la información obtenida en los capítulos 5 y 6 para integrar los efectos 3D y MHD en el transporte de tritio.

En un último apartado, se presentan las conclusiones a las que se ha llegado durante el desarrollo de la tesis. Se analizan los resultados finales y se examinan tanto los éxitos obtenidos en la investigación como los problemas abiertos que se deberán abordar en futuras etapas.

La bibliografía así como la lista de contribuciones científicas generadas a lo largo del periodo doctoral se encuentran al final del documento.

Introduction

Objectives

In the last few decades, the scientific community has spent great efforts in the development of the civil thermonuclear fusion energy technology. The fusion reaction of tritium and deuterium is one of the most promising options of the one explored for this purpose. One of the main components for the development of future Deuterium-Tritium (DT) reactors is the so called Breeding Blanket (BB). The main function of this component is regenerating the tritium burnt in the fusion reaction for its future processing and re-injection in the plasma. Therefore, the BB is essential for the developing of an efficient and sustainable tritium fuel cycle.

The operational conditions of the blanket inside the reactor are very demanding. None of the conceptual technologies proposed so far is able yet of accomplishing all the needs of this component. In the framework of the EUROfusion consortium activities, Centro de Investigaciones Energéticas Medioambientales y Tecnológicas (CIEMAT) leads the design activities of one of the blanket concepts under consideration: the Dual Coolant Lithium Lead (DCLL). This offers some conceptual advantages that make it very promising. However, it also entails challenges that have to be addressed by the scientific community. For this reason, an important amount of economic and human resources are being invested in Europe for developing a viable design of DCLL blanket.

One of the priority challenges associated to any BB, including the DCLL, is keeping the tritium inventories and tritium permeation losses in minimal levels. This is mainly due to the tritium radiological hazard but also due to the scarcity

of this valuable fuel. In this context, the development of predictive tools able to monitor tritium fluxes and concentrations along the blanket and its auxiliary systems is of special relevance.

The present research project falls within the scope of the design activities of the European DCLL. The main objective of this work is developing a reliable and accurate tritium transport model of the complete DCLL blanket and its ancillary systems. The modeling of such a vast system cannot be addressed directly. On the one hand, system level models based on Process Flow Diagram (PFD) entails important errors and uncertainties both theoretical and experimental. On the other hand, simulating the complete system using 3-dimensional models of finite volumes would require an immeasurable amount of computational time and resources.

None of the mentioned modeling strategies can provide the goal model by itself. For this reason, in this work a new methodology based on the recursive use of both kind of models is employed. Indeed, detailed 3D models of particular geometries which are identified as fundamental for tritium transport in the DCLL are developed. Thereafter, results of such models are used for the optimization of system level models. This allows increasing significantly the system level model accuracy while maintaining relatively short computational times.

Due to the characteristic of the DCLL blanket, the development of 3-dimensional tritium transport models necessarily implies the study of MagnetoHydroDynamics (MHD) effects in liquid metal flows. MHD phenomena are multiphysics processes that involves the coupling of the electromagnetic field and the fluid velocity field.

Beyond the development of 3D tritium transport models, MHD simulations are of great importance for the DCLL design. For this reason, the study of the MHD effects associated to the European DCLL geometry is considered an independent objective of this work. A deeper analysis of the MHD phenomena increases significantly the contribution of this work to the DCLL design.

Finally, the influence of the MHD effects on tritium transport inside a liquid metal blanket is a phenomenon that has not been deeply studied and never under DCLL relevant conditions. These effects are crucial for computing tritium behavior inside the BB. For this reason, studying the interaction between the

MHD and tritium transport is the final main objective of this work.

Structure of the dissertation

The present document is structured in seven chapters. As it is common, the work has a pyramidal structure. This way, the information exposed in every chapter is based on the results, theoretical developments and concepts that are explained in previous chapters.

In chapter 1 the context in which this work is developed is presented. The basic concepts of civil fusion energy are introduced paying special attention to the concept of BB and the role of tritium in the development of future fusion reactors. In this chapter, the different tritium transport modeling strategies are explained in detail. Lastly, a complete description of the actual European DCLL design is given. This design is one of the most important objects of study in this dissertation.

In chapter 2 the theoretical concepts needed for the study of the MHD phenomena in liquid metal flows are exposed. The fundamental differential equations that describe these interactions are developed. The applicability of the formulation and of certain simplifications to the work conditions of the DCLL is discussed.

In chapter 3 a theoretical description of the mass transport phenomena is presented. The permeation of hydrogen isotopes through solid and liquid materials is studied. The surface processes through the interfaces of the materials including the concentration Boundary Layer (BL) formation is analyzed as well. The development of tritium transport models presented in the subsequent chapters is based on this theoretical description.

In chapter 4 the first tritium transport model developed for the European DCLL is presented. Results provided by the model are analyzed in context with previous models developed for other BB concepts. The results of some parametric studies are discussed as well for analyzing their impact on the model results.

In chapter 5 the MHD computations carried out for the European DCLL

blanket are presented. Different geometries are analyzed, all of them relevant for the DCLL using different computational tools. Some of the results of the MHD analyses are used for the implementation of 3D tritium transport models in the next chapter.

In chapter 6 the connection between tritium transport and MHD phenomena is developed. Results from multiphysics 3D tritium transport models in the most relevant geometries of the DCLL are obtained. Simulations allow analyzing the interaction between the MHD forces, the tritium volumetric generation and mass transport phenomena. Moreover, some of the results are used for the optimization of the components used in the tritium transport models at system level.

In chapter 7 the development and results of an advanced tritium transport model at system level of the DCLL blanket and their auxiliary systems are presented. In contrast with the model of chapter 4, the advanced model make use of the information obtained in chapters 5 and 6 for the integrating MHD and 3D effects in tritium transport.

In the last section, the final conclusions derived from the research work are presented. The final results are analyzed and both the achievements of the research and the open issues are discussed.

The bibliography and the list of scientific contributions (journal publications, participation in scientific congress and technical reports) generated along the doctoral period are found at the end of the document.

Chapter 1

Research context

In this chapter an overview of the world energy production system is discussed together with the potential role that fusion energy can play on it. The fundamental concepts of thermonuclear fusion energy are introduced. Special attention is paid to the role of tritium as primary fuel of fusion reactors. The concept of BB is presented as the main component of the tritium fuel cycle. The tritium modeling strategies for BB developed during the doctoral period are explained as well. Finally, the European design of the DCLL concept is described in detail as this is the main subject of the present dissertation.

1.1 Motivation for fusion energy research

World energy consumption has experienced an important growth over the last few decades. The economic growth, the population rise and the improvement of social conditions of certain parts of the planet are the main factors that explain the increase of the demand. Analyzing the statistics of world primary energy consumption [1–3], this accelerated trend can be clearly observed (fig:1.1).

Data of energy demand classified by energy carrier show that most of the energy demand is currently being satisfied by burning fossil fuels: coal, oil and natural gas (fig:1.2). The actual transport system of people and goods is almost completely based on oil-derivatives fuels, which turns this fuel in the

most consumed energy carrier of the world. Besides, there are vast regions of the planets that mostly burn coal and organic fuels for primary uses.

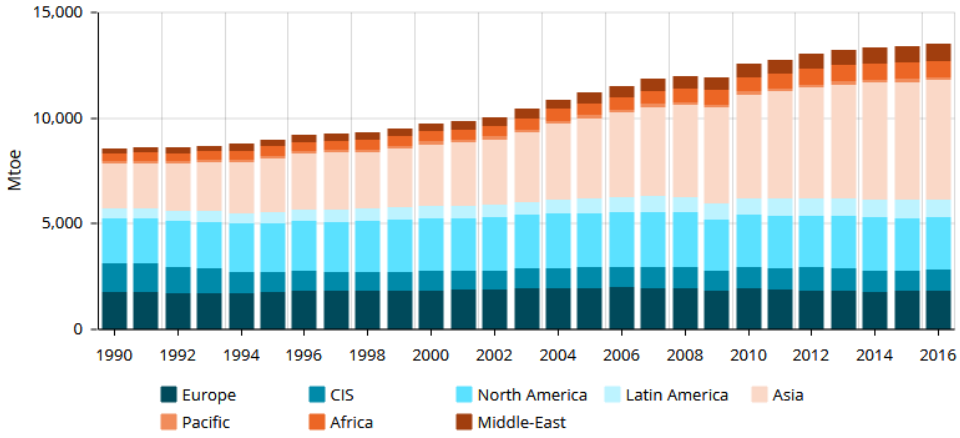

Figure 1.1: Global energy consumption in different regions measured in Million tonnes of oil equivalent (Mtoe) [3].

This global dependency on fossil fuels is not only unsustainable in time but it is also hazardous for the environment and public health. Indeed, the effect of CO_2 and other greenhouse gasses associated to fossil fuels combustion on global warming has been categorically confirmed (e.g. [4]). Besides, it is well known by the scientific community that these gases are associated with severe growths of mortality and respiratory diseases (see for example the *London Smog Episode* of 1952 [5]).

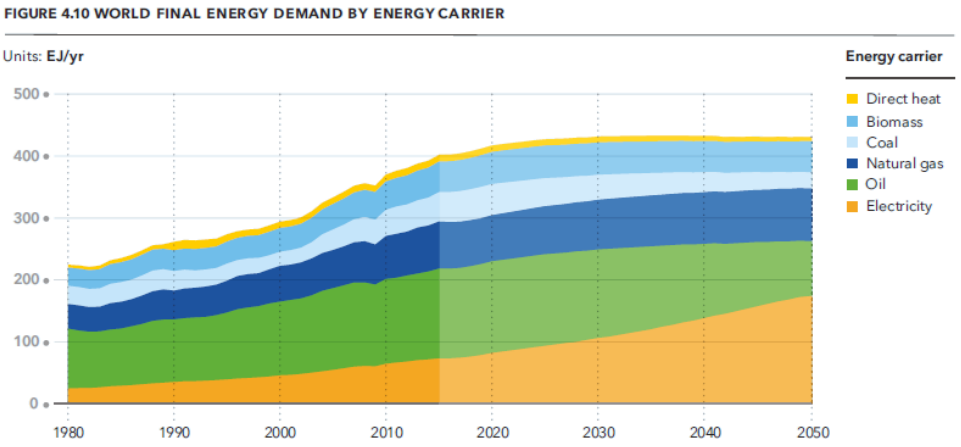

Figure 1.2: World fuel consumption classified by energy carrier [1].

It is the harmful nature of fossil fuels the reason why the international community is looking for alternatives. For this reason, predictions of future energy consumption (fig:1.2) include an important rise of the electricity demand which should become dominant in the next decades.

Unfortunately, the world electricity generation system is also dominated by fossil fuels, mostly by coal. Indeed, in 2016 more than 75% of the electricity production came from non-renewable sources [3]. This implies that the electricity generation system is forced to drastically and rapidly evolve if severe damage to the environment is to be avoided.

Important investments in renewable electric sources have been made in the last decade following this approach. According to the United Nations (UN), the global investment in renewable capacity totaled $241.6 billion in 2017 (excluding large hydroelectric) which was roughly double that in fossil fuel generation [6]. Predictive models of the electricity production system show the exponential growth that generation based on solar, wind and hydraulic sources must accomplish (fig: 1.3).

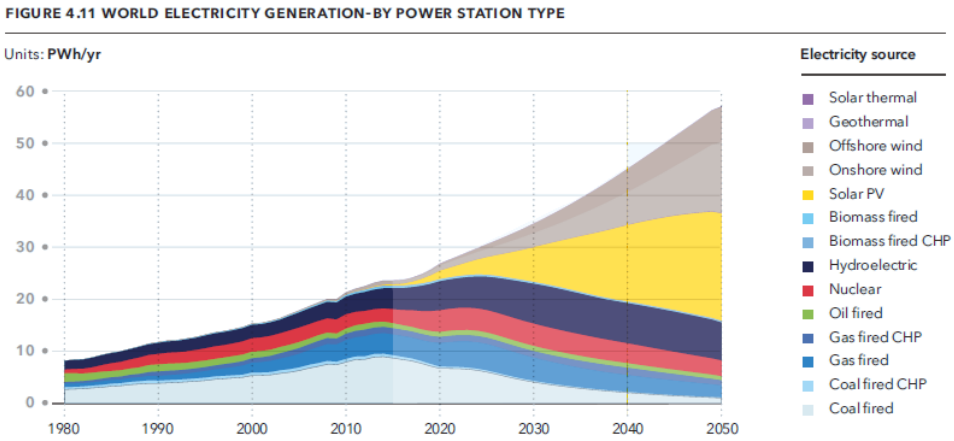

Figure 1.3: World electricity generation classified by power station type [1].

Even in relatively optimistic scenarios like the one shown in fig:1.3, fission nuclear power generation will still be necessary in the following decades. This is a technology with no contribution to global warming. Thus, it is believed that its presence will be unavoidable for reducing fossil fuels consumption. However, the well-known problems associated to this technology, mainly the ones related to nuclear waste and to power stations safety, have no complete solution. Therefore,

it is unsatisfactory for many sectors of public opinion assuming that nuclear fission energy will still play an important role in the power generation system if fossil fuel dependency is to be overcome.

In this environment, nuclear fusion technology stands as a long term alternative to the future electricity production system. Its actual state of development makes impossible that nuclear fusion energy can be efficiently converted to electricity before 2050. For this reason, fusion energy is not included in predictive models. Despite this delay, nuclear fusion is still a very attractive concept for the society as it has the potential to drastically change the complete energy production system.

Fusion technology shares with fission technology the absence of greenhouse gas emissions thus, it will not contribute to the global warming. Moreover, nuclear fusion does not suffer from the main problems associated to fission power stations. On the one hand, fusion reactors are intrinsically safe. The nuclear fusion reactions can be interrupted without external power sources making impossible runaway reactions such as the one of Fukushima [7]. On the other hand, the radioactive waste produced in fusion plants is expected to be mostly of short and medium life and classified as Low and Intermediate Level. Consequently, it could be recycled or disposed in standard facilities [8].

For the mentioned reasons, the fusion energy objective is at least providing an alternative to fission energy. Moreover, fusion reactions release such an enormous amount of energy per unit mass in comparison with their competitors that they have the potential of completely extinguish the social dependence on fossil fuels. Therefore, despite the technological challenges associated to the fusion research, it is a very rewarding field from the social and the environmental perspective that can provide the key of an economically and ecologically sustainable energy production system.

1.2 Thermonuclear fusion by magnetic confinement

1.2.1 Fundamentals of nuclear fusion reactions

In any nucleus, the positively charged protons are strongly repelled by themselves due to the Coulomb interaction. The nuclear forces compensate this repulsion and they are fundamentally responsible of the stability of complex matter in universe. The energy associated to these forces is called nuclear binding energy.

Nuclear fusion technology aims at using the binding energy of the nuclei for electricity generation. For this purpose, it is necessary to understand the nature of this energy and the principles of the nuclear interaction. The length scale inside a nucleus is of the order of Fermi (10^{-15} m). Thus, any nucleus is a quantum system. The nuclear forces that keep the nucleons together are the result of gluons exchanges between quarks as described by the Quantum ChromoDynamics (QCD) (e.g. [9]) theory, which is well integrated in the standard model of particle physics. Nevertheless, it is not necessary to go in such deep level to compute the nucleus binding energy. Other nuclear structure theories with different degrees of complexity, such as the Bardeen Cooper Schrieffer theory (BCS) theory (e.g. [10]), the shell model (e.g. [11]) or even the semi-empirical liquid drop model (e.g. [12]), have succeed in reproducing the binding energies of several elements.

Empirical evidences of the nuclear binding energy (E_b) manifest with the experimental measurements of the nuclei masses. Indeed, with the logic exception of the protium (^{1}H), the mass of any nucleus (M_{nuc}) is smaller than the sum of its nucleons masses (1.1). The relation of this mass defect and the binding energy was anticipated by the special relativity theory [13] which states (among many other things) that every particle has an intrinsic energy (energy at rest) directly proportional to its mass. The opposite equivalence is also true, the energy of a system of particles contributes to its total mass. With this equivalence between mass and energy, it is possible to identify the mass defect with the binding energy of a nucleus.

$$M_{nuc} \neq \Sigma_i^A m_i \quad \Rightarrow \quad M_{nuc} + E_b = \Sigma_i^A m_i \tag{1.1}$$

The binding energy per nucleon is not a simple function as it is the result of the quantum interactions between quarks. As a consequence, it depends on the number of nucleons in a non-trivial way (fig:1.4).

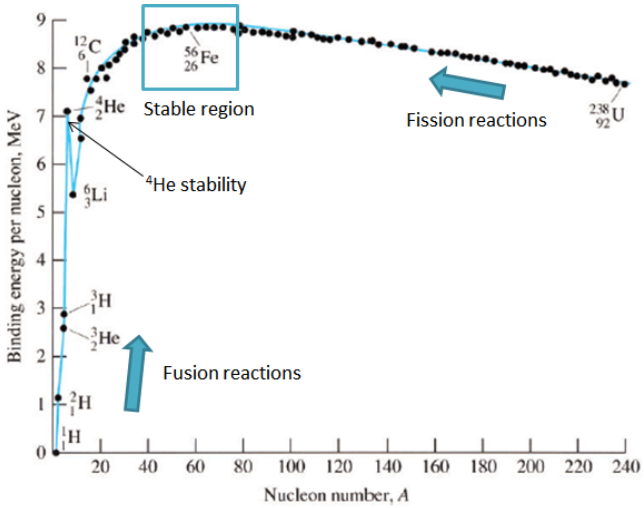

Figure 1.4: Binding energy per nucleon as function of the nucleon number.

Similar to an exothermic chemical reaction, if the products of a nuclear reaction (either fission of fusion) have more binding energy than the reactants, the difference of energy is released and it can be potentially used for different applications.

Observing fig:1.4, it is found that the binding energy of heavy nuclei decreases when the nucleon number increases. As a consequence, when a heavy nucleus splits into smaller ones (either naturally or inducingly), the final system is more stable and the energy difference is released. This is the physical phenomenon behind fission energy. The civil nuclear fission technology was implanted in several countries during the second half of the XX century. Indeed, the first self-sustained nuclear fission reactor was achieved by Enrico Fermi in 1942 (see for ex. [14]).

On the contrary, the binding energy of the light nuclei increases with the number of nucleons. As a consequence, if two light nuclei fuse into a heavy one, the new nucleus will be more stable (it will have more binding energy) than the previous two and the energy difference will be released.

The ^{56}Fe nucleus is the one with the highest binding energy per nucleon, which means that ^{56}Fe is the most stable nucleus in universe. The binding energy per nucleon decreases for nuclei lighter than it. For most of these nuclei, the lighter they are the more unstable (the less binding energy). There is an important exception to this rule, the ^{4}He nucleus. This is particularly stable taking into account its small size. The exceptional stability of ^{4}He is well explained by the nuclear shell-model as this nucleus is what is called a double magic isotope [11].

Of all fusion reactions that have been observed (e.g. [15]), it is crucial to identify the most suitable one for civil fusion energy applications. Finding a reaction with high energy release is logically one important criterion. From this perspective, the ^{4}He stability valley is identified as an opportunity for having reactions with high energy density. Due to its great stability, a reaction of ^{4}He formation will be very efficient in comparison with other reactions with similar reactants. This is one of the reasons why the following two reactions are attractive for commercial applications.

$$D(^2H) + T(^3H) \rightarrow {}^4He(3.52MeV) + n(14.06MeV) \quad (1.2)$$

$$D(^2H) + {}^3He \rightarrow {}^4He(3.67MeV) + p(14.67MeV) \quad (1.3)$$

The energy is released in form of kinetic energy which is mostly absorbed by the lighter particle, a neutron or a proton. Civil fusion technology objective is converting into electricity as much of this particle energy as possible. From this perspective, reaction (1.3) is more attractive as the proton could be decelerated using electric fields, directly generating electric energy. On the contrary, the energy of the neutron coming from (1.2) must be converted in a thermal cycle, which is expected to be less efficient. Besides, high fluxes of fast neutrons have associated important technological issues. They activate a wide variety of elements which increases the environmental impact and the radiological hazard. The intense neutron flux damages significantly the reactor material decreasing the quality of their properties and reducing their operational life.

There are more factors to take into account when selecting which fusion reaction is the most convenient for civil applications. The abundance of the reactants, in other words, the abundance of fuel for future fusion reactors, is a crucial aspect. Unfortunately, reactions (1.2) and (1.3) does not have common

reactants. Indeed, ^{3}He and tritium (^{3}H) are very rare isotope on earth. Moreover, tritium is an unstable isotope with a short life-time (around 12.32 years). On the contrary, deuterium (^{2}H) is a stable isotope which is present in relatively large proportions in regular water. The extraction techniques of deuterium from water are well developed and efficient. As a consequence, from the fuel availability perspective, fusion reactions based only on deuterium are very attractive:

$$\begin{aligned} D + D &\rightarrow {}^3He(0.82MeV) + n(2.45MeV) \\ D + D &\rightarrow T(1.01MeV) + p(3.03MeV) \end{aligned} \tag{1.4}$$

Reaction (1.4) produces particles (either neutron of proton with a 50% chance) whose energy is one order of magnitude less than the particles coming from the reactions of ^{4}He formation.

Besides the abundance of the reactants and the amount of energy released, there is a third element that has a capital influence on the commercial viability of a fusion reaction. This is the probability that the reaction will take place, in other words, how likely the reaction will happen in a fusion reactor.

In any scattering process between two particles (not necessarily a nuclear fusion reaction), the probability of an event to take place is represented by the cross section (σ). This is defined as the effective area that the target particle offers to the incident one. Thus, it has units of area (1 barn = 10^{-28} cm^2). It is worth noting that the interaction between the particles are ruled by the Quantum Field Theory (QFT) and they are in general far from the macroscopic intuition of a scattering process. As a consequence, the cross section does not necessary represent the physical geometrical section of the target.

The cross section depends on many factors depending of the kind of interaction (electromagnetic, weak, gravity, nuclear...) the particles may experiment. In fusion reactions the cross section will not only depend on the nuclear interactions as they are limited to a very short range. The nuclei are positively charged thus the Coulomb barrier must be overcome before a fusion reaction can take place. As a consequence, nuclei need to have a sufficiently large energy in order to have relevant probabilities of reacting. Experimental results of cross sections for the reactions (1.2), (1.3) and (1.4) are exposed in fig:1.5.

For commercial applications, it is of interest that fusion reactions can take place at the lowest energy possible. The cross section of reaction (1.2) is at least 2 orders of magnitude higher that the other two when the nuclei have energies lower than 100 KeV. This means that D-T reaction is by far the most accessible of the three.

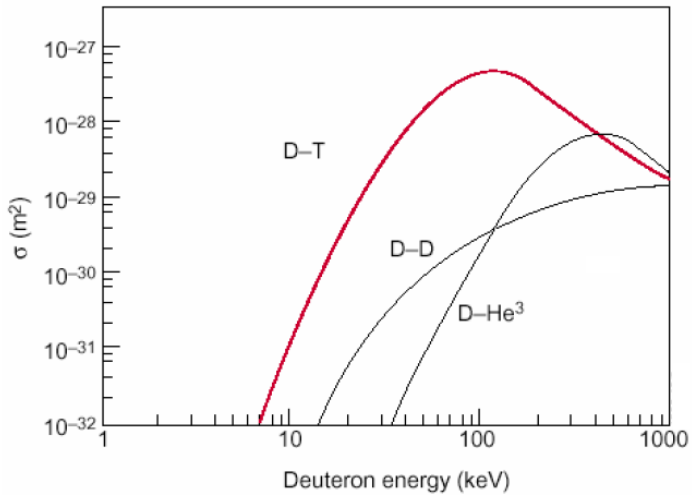

Figure 1.5: Cross sections for D - T, D - D and D - ^{3}He reactions [16].

The high cross section of the D-T reaction (1.2) is an advantage that cannot be ignored. This added to its high energy release have made that the D-T reaction has been chosen for the fusion energy research programs in Europe. However, this reaction has two important drawbacks which have been already stated. First, the light particle released in the reaction is a neutron and not a proton. Second, it uses tritium, an almost nonexistent radioactive element as fuel. Both problems should be addressed by the scientific community if a safe and cost-efficient fusion energy alternative is to be developed.

1.2.2 Magnetic confinement devices

In order to overcome Coulomb repulsion, the initial energy of the light nuclei (tritium and deuterium) has to be sufficiently large if reasonable probabilities of fusion reaction are wanted. From the engineering point of view, this means that the fuel of a fusion reactor needs to be heated up, compressed and confined during a sufficiently long time.

For civil fusion energy applications, the observation of the fusion phenomena is clearly not sufficient, the fuel has to be burnt at a sufficiently high rates for having a self-sustained system. In other words, the energy produced in the fusion reactor has to be larger than the energy wasted in generating and maintaining the reaction. If this condition is satisfied the plant can operate without external energy sources. At that moment, it is said that the reactor has reached the *ignition* conditions.

The requirements for reaching ignition conditions imply very high temperatures and either high particle density or long confinement times. Magnetic confinement reactors follow the second option: they have a moderate particle density but relatively large confinement times.

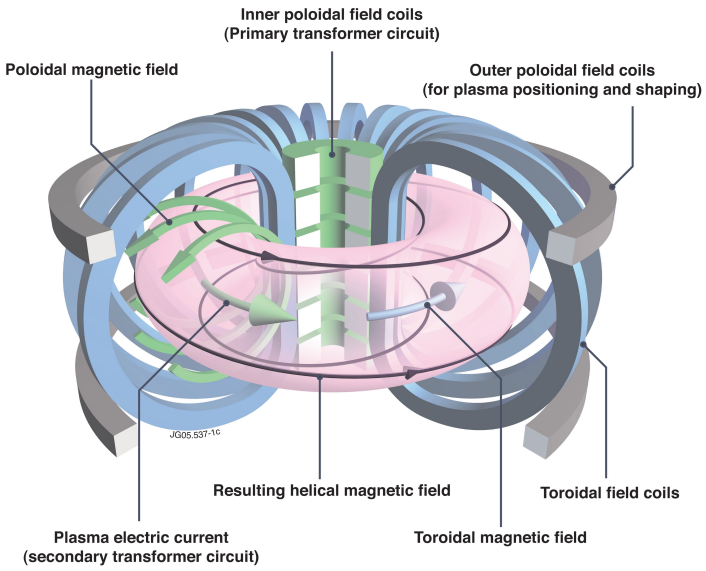

Figure 1.6: Scheme of a tokamak device (courtesy of EUROfusion).

Due to the high temperatures (10^8 K for DT reactors) the deuterium and tritium gas mixture will be fully ionized in plasma state. The confinement of this plasma cannot be achieved in a conventional vessel as any direct contact of the plasma with the wall of the vessel would intermediately cool down the fuel to unacceptable limits. Logically, it would also critically damage the structural wall. Magnetic confinement devices generates strong magnetic fields to confine the fusion fuel. As any other charged particle, the plasma ions follow the magnetic lines describing helical trajectories. Taking benefit of this phenomenon, toroidal devices generates close magnetic fields lines that confine

the charged ions to a limited region of the space. This way the confinement can be achieved without direct contact between the plasma and physical walls.

There are two main types of toroidal magnetic confinement systems: the *tokamak* and the *stellarator*. The tokamak was first proposed by Sajarov and Tamnn in 1951 [17]. This plasma confinement device has perfect toroidal symmetry. It generates the magnetic field using poloidal and toroidal coils (fig: 1.6). Part of the poloidal field is produced by a current induced in the plasma. On the contrary, the stellarator [18] has no toroidal symmetry. The magnetic field is generated only by external coils following a more complex geometry (fig: 1.7).

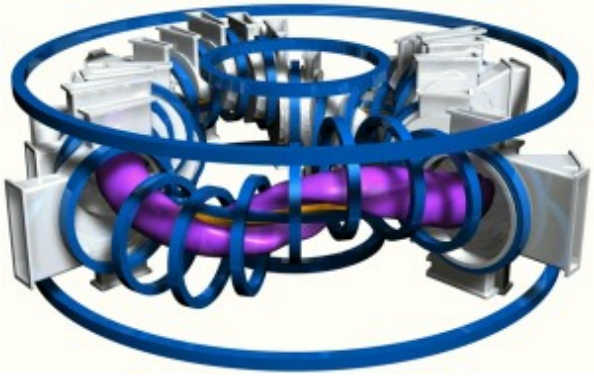

Figure 1.7: Model of the TJ-II stellarator (courtesy of LNF-CIEMAT).

In this dissertation, only tokamak fusion reactors have been considered as they are the base-line option for the European fusion research roadmap. Several tokamaks have been built for experimental purposes all over the world. The Joint European Torus (JET) in the UK is the biggest tokamak built and one of the few that has been able to operate with tritium and deuterium plasma producing a significant amount of fusion reactions. The International Thermonuclear Experimental Reactor (ITER) tokamak which is currently being built in France will be the biggest tokamak ever built and the first one able to reproduce ignition conditions for moderate periods of time.

The DEMOnstration Power Station (DEMO) project [19] is the next generation device projected by the European fusion community. This project is presently coordinated by the EUROfusion consortium, created in 2014 for this purpose. DEMO will be the first prototype of fusion reactor as it will be able to maintain the ignition conditions for long periods of time. The objective of

this European facility will be injecting electricity to the network coming a fusion source. It is planned that this prototype plant will be operating in the 2050s [20]. Most of the work developed for the present dissertation is based on the future DEMO reactor aiming at contributing to its development.

1.3 Tritium

As it was introduced in sec: 1.2, deuterium and tritium are the reactants (conventionally named fuels) selected for the European demonstration reactor. The current reserves of tritium come mainly from the Canadian Deuterium Uranium (CANDU) fission reactors which produce small amounts of tritium per year from heavy water [21].

Tritium is a radioactive element as it is a beta emitter (eq:1.5). It has a relatively short half life (12.3 years). The emitted radiation is not very energetic and it is not able to penetrate human skin. However, tritium is a hydrogen isotope. Therefore, it can bind to every organic and inorganic molecule that protium can. This means that tritium can be inhaled, ingested or absorbed through the skin. Once inside the human body in sufficiently large concentrations, there is a real risk of severe and irreversible health damage [22]. For these reasons, careful and responsible tritium control will be necessary in any future nuclear fusion facility. Avoiding leakages of tritiated water (HTO and T_2O molecules) and tritiated air (HT and T_2 molecules) to the environment in both operation and accidental conditions will be an strict safety requirement for the fusion plant.

$$T \quad \rightarrow \quad {}^3He + e^- + \bar{\nu}_e + 18.6KeV \tag{1.5}$$

Tritium has already some commercial applications that make this rare element very valuable. Indeed, tritium decay is the only cost-efficient source of ^{3}He (1.5). This helium isotope is extremely rare and it has many uses already. Examples are: neutron detectors, very low temperature (millikelvin) refrigerators and magnetic-resonance imaging. The technological applications of ^{3}He added to the tritium military uses make that tritium prices are in the range on $10,000-30,000 per gram [23]. Moreover, speculations about future cost set the tritium price in $100,000-200,000 per gram when ITER starts

burning the worldwide reserves.

As a consequence, due to the incredibly large tritium price, a fusion reactor based on the constant injection of tritium cannot be cost-efficient if tritium is coming from external sources. Beyond their cost, even if for some reason tritium prices collapse, a single fusion reactor would extinguish the current tritium reserves in few days.

1.3.1 Breeding blanket concepts

Due to the limited tritium availability, alternative sources of this element have been identified for fusion applications. The most promising is based on lithium. Indeed, it is known that two different lithium isotopes (^{6}Li and ^{7}Li) transmute into tritium via neutron capture (1.6) [15].

$$^6Li + n \rightarrow T + \alpha(^4He) + 4.8MeV \tag{1.6}$$

$$^7Li + n + 2.5MeV \rightarrow T + \alpha(^4He) + n' \tag{1.7}$$

Lithium is a fairly common element on earth. There are large natural reserves which are primarily located in South America. It has a relatively low price (around $9 per kg in 2017) although its value has experienced an exponential growth during the last decade caused by the lithium batteries development. As a consequence, would be very efficient using lithium and the fast neutrons produced in the D-T reaction for tritium regeneration. Besides, reaction (1.6) is exothermic and it could make a substantial contribution to the thermal power output of the fusion reactor.

The cross section of the tritium production reaction as a function of the neutron energy is exposed in fig: 1.8. The cross section of ^{6}Li is high for most of the neutron energy spectrum while the cross section of ^{7}Li is only relevant for fast neutrons. Consequently, with an appropriate location of lithium in the reactor, nearly all the neutrons that slow down to thermal energies from their initial 14.1 MeV could be absorbed by ^{6}Li and generate heat and tritium. Unfortunately, the natural proportions of the two isotopes are: 7.5% of ^{6}Li and 92.5% ^{7}Li. As a consequence, applying ^{6}Li enrichment techniques will be probably necessary.

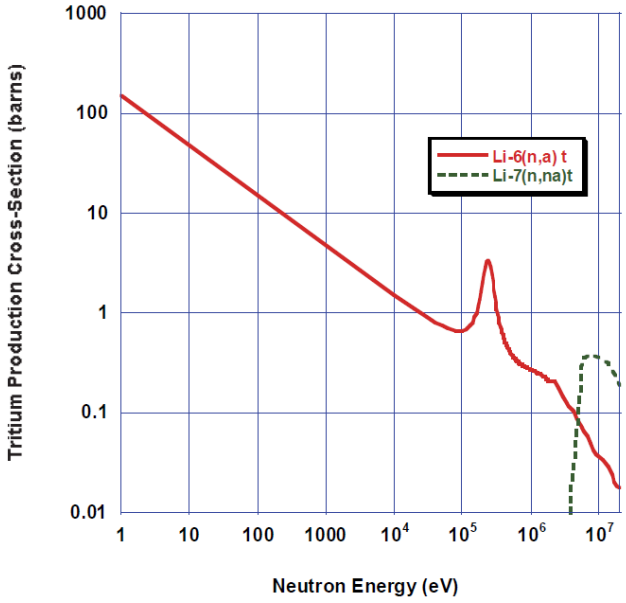

Figure 1.8: Cross section of tritium production reactions from lithium.

For the previous reasons, lithium, in any of its forms, has to be present in future DT reactors. Indeed, it can be seen as fuel itself as fusion reactions cannot be maintained for long periods without its presence. However, it is more common and also more precise calling lithium *breeder* instead of fuel as its function is breeding tritium. Neutrons are produced in the plasma in every direction. Thus, the breeder should be located surrounding the plasma covering the largest possible area. It is therefore necessary to develop a component fully integrated in the reactor which contains the breeder material. This component is known as Breeding Blanket (BB). A considerable amount of effort and resources have been spent during the last few decades on the development of BB technologies and on the conceptual design of specific BB concepts.

Any blanket concept has to be designed with the objective of accomplishing the following three functions:

1. It has to regenerate tritium and extract it out of the reactor for its processing and future injection in the plasma.
2. It has to be able to extract the thermal power of the incoming neutrons out of the reactor for the subsequent energy conversion.
3. It has to provide the main shielding against radiation.

The last 2 functions are a consequence of the location of the blanket next to the plasma. Both, the thermal power extraction and the shielding capabilities are of extreme importance for having an efficient and safe power plant.

The first function is needed to ensure the tritium self-sufficiency of the plant. This means that after the initial ignition, the plant should be able to operate without injection of external tritium, only tritium regenerated in the BB should be used for maintaining the fusion reaction. For fulfilling this function, condition (1.8) needs to be satisfied. This condition is based on the Tritium Breeding Ratio (TBR) which is one of the most important measures of the blanket performance.

$$TBR := \frac{tritium\ bred}{tritium\ burnt} > 1 \tag{1.8}$$

In practice, it is naive thinking that the complete amount of tritium bred in the blanket can be extracted, processed and injected in the plasma. Unavoidably, tritium losses will arise during these processes. For this reason, it is considered in the European blanket research teams that the minimal TBR needed for a functional blanket is 1.1. The neutron capture reaction of ^{6}Li (1.6) produces a single triton (tritium nucleus) per neutron while the fusion reactor produces a single neutron per burnt triton. Therefore, a BB of only ^{6}Li will never be able to have a TBR greater than 1. Alternatively, ^{7}Li produces a neutron which could be potentially be used for a subsequent capture reaction. However, as observed in fig: 1.8, ^{7}Li has a small cross section for most of neutron energy spectrum. As a consequence, pure lithium blankets concepts are not considered viable.

For increasing the TBR up to acceptable levels neutron multipliers will be added to the blankets. Lead (Pb) and Beryllium (Be) are the most promising ones. The neutron multiplication reactions of those elements are (1.9) and (1.10). Both reactions have cross sections adequate for fusion applications (fig: 1.9).

$$^9Be + n + 3MeV \rightarrow 2\alpha + n' + n'' \tag{1.9}$$

$$^{208}Pb + n + 10MeV \rightarrow {}^{207}Pb + n' + n'' \tag{1.10}$$

There are different classes of blankets concepts which consider different possibilities. They are usually classified following three criteria: the form of the breeder material (metallic, ceramic, salt...), the kind of neutron multiplier

and the coolant they use for extracting the thermal power. Tab: 1.1 shows some of the BB concepts that are being developed all over the world classified by their three distinctive characteristics.

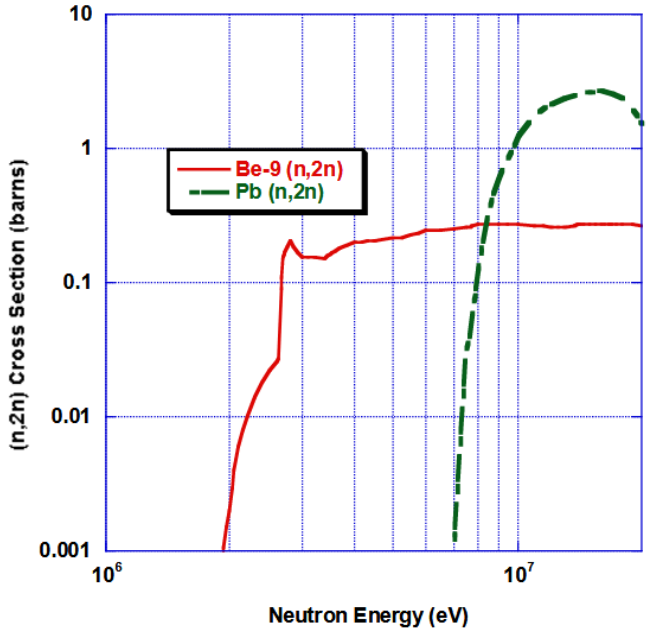

Figure 1.9: Cross section of neutron multiplication reactions.

BB	Breeder Material	Neutron Multiplier	Coolant
Helium Cooled Ceramic Pebble (HCPB)	Li_4SiO_4 or Li_2TiO_3 pebble beds	Be pebble beds	He
Helium Cooled Lithium Lead (HCLL)	PbLi liquid metal alloy	Pb	He
Water Cooled Lithium Lead (WCLL)	PbLi liquid metal alloy	Pb	H_2O
Dual Coolant Lithium Lead (DCLL)	PbLi liquid metal alloy	Pb	PbLi and He
Self Cooled Lithium Lead (SCLL)	PbLi liquid metal alloy	Pb	PbLi
Water Cooled Ceramic Breeder (WCCB)	Li_2TiO_3 pebble beds	Be pebble beds	H_2O
Helium Cooled Ceramic Reflector (HCCR)	Li_4SiO_4 pebble beds	Be pebble beds[1]	He
Helium Cooled Ceramic Breeder (HCCB)	Li_4SiO_4 pebble beds	Be pebble beds	He
Lithium Lead Ceramic Breeder (LLCB)	Li_2TiO_3 pebble beds and PbLi	Pb	PbLi and He

Table 1.1: Breeding blanket concepts.

As part of the ITER project, there is a specific program conceived for testing the functioning of some of the blanket concepts. The Test Blanket Module (TBM) program [24] consists of 6 different modules that will be introduced into 3 different equatorial ports of the machine. Each of these modules contains the basics components of the corresponding BB concept that is going to be tested. Due to their limited size, the TBM will not fully satisfy

[1]This blanket includes graphite as neutron reflector.

the blanket functions but its performance can be scaled to the real size of a blanket providing very valuable information for the complete blanket design. Besides the test modules, the TBM program includes several ancillary systems: tritium recovery, corrosion products purification, pumping... These systems need to be adapted to the requirements of each specific blanket concept. They will have a crucial influence on the TBM performance and they will be validated as well in ITER. TBM and ancillary systems are called Test Blanket System (TBS).

The TBS that are going to be tested in ITER are developed by different members of this international project. The European Union (EU) is responsible of the HCLL and HCPB. Japan is responsible of the WCCB whereas Korea is responsible of the HCCR. China and India, both with the support of the Russian Federation, are responsible of the HCCP and LLCB, respectively.

Beyond the TBM project, the EUROfusion consortium is developing designs for 4 different BB concepts adapted to the European DEMO reactor [25]. Unlike the TBS, DEMO blankets will cover most of the surface next to plasma. They have to fully satisfy every function associated to a functional blanket. The 4 concepts under consideration in the EU are: HCPB, HCLL, WCLL and DCLL. Different members of the EUROfusion consortium are leading the design of the 4 concepts:

- Karlsruhe Institute of Technology (KIT) in Germany is leading the design of the HCPB concept.
- *Commissariat l'Énergie Atomique et aux Énergies Alternatives* (CEA) in France is leading the design of the HCLL concept.
- *Agenzia nazionale per le nuove tecnologie, l'energia e lo sviluppo economico sostenibile* (ENEA) in Italy is leading the design of the WCLL concept.
- CIEMAT in Spain is leading the design of the DCLL concept.

Despite this management division, there is a strong and fluid collaboration between the mentioned institutions and the rest of the laboratories, universities and companies that conform the consortium. Moreover, transverse units perform analyses in support of the four blanket design teams. This is case of the CIEMAT tritium modeling unit in which the present dissertation has been developed.

1.3.2 Tritium modeling for breeding blankets

The tritium generated in BB needs to be removed from the blanket, extracted from the blanket loops, processed and finally reinjected in the plasma. Fig: 1.10 shows a very simplified scheme of the tritium fuel cycle of the HCPB blanket. Similar fuel cycles are needed for any other concept. Along this long cycle, tritium can be lost if no control of tritium concentration and fluxes is performed in the different parts of the blanket and associated systems.

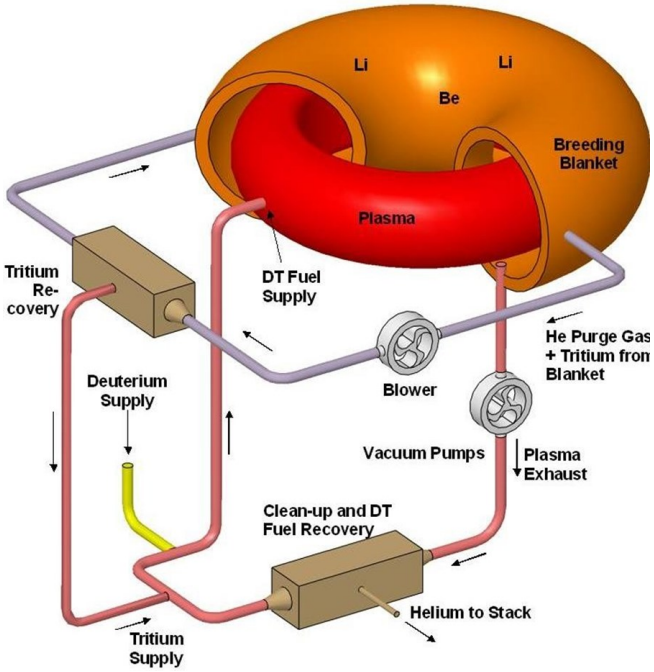

Figure 1.10: Scheme of the tritium fuel cycle with a HCPB blanket (courtesy of ITER foundation).

Tritium losses in the fuel cycle can be an important issue for most blanket concepts. The main reason is that tritium cannot be easily confined in a vessel or in a closed loop as it permeates through solid materials. Permeation of hydrogen through metallic solids is a physical phenomenon known since the nineteenth century [26]. Permeation is a physical and chemical process in which nuclear interactions plays no role. As a consequence, tritium and deuterium atoms, which have approximately the same radius than the hydrogen atom, permeate as well through solids. The physics of permeation processes and their mathematical formulation are described in detail in sec: 3.

The difficulties found in effectively confining tritium has important consequences for breeding blankets mainly for two important reasons:

1. The tritium self-sufficiency of the reactor can be compromised if the permeation losses are too large.
2. Inside the blankets, tritium can potentially permeate from the breeder material to the primary coolant circuits. From there, it can permeate again to the secondary coolant loop and consequently to the environment. This perspective seriously compromises the safety of the power plant.

Whether the previous two issues are going to affect the blanket performance depends on the specific design of each concept. In any case, tritium control is a crucial point for the blanket design perspective as both safety and tritium self-sufficiency must be guaranteed at any time. Therefore, it is necessary to know how tritium will behave inside the different subsystems and components. Because of this, predictive tools of tritium behavior are of great importance for fusion technology programs.

Tritium transport models are the tool used for predictive purposes in BB applications˙ A good amount of models developed with different codes and algorithms have been developed in past for both DEMO and ITER (e.g. [27]). A detailed review of previous models and modeling tools can be found in sec: 4.1

Tritium transport models can have different degrees of complexity depending on how deep they go in describing the geometrical design details of the blanket and the physical phenomena involved in tritium transport. The following classification of tritium models in terms of their complexity is used in this dissertation:

1. Deep level models: 3-dimensional models of high accuracy, they can include a wide variety of multiphysics effects. They usually require Computational Fluid Dynamics (CFD) algorithms (finite volume methods) and high computational resources for simulating limited regions of the space.
2. Component level models: low dimensional models (usually 1D) of specific physical systems. They can include a variable amount of effects. However,

their 1D nature implies that they will be always limited in accuracy. They are used as elementary units for developing system level models.

3. System level models: models developed by combining several component level models (simply called components) following a PFD (sometimes called flowchart). They describe complex systems using relatively small computational times and resources. By including several 1D components in flowcharts, system level models can emulate 3D effects. Nevertheless, their accuracy will be always limited by the dimensionality of their components.

The vast majority of tritium transport models developed in the past for BB technologies lay in the system level category (see sec: 4.1). However, there is an important lack of knowledge and experience in the development of deep level models. They have important limitations that explain this small progress. Their main drawback is that deep level models are not able to simulate sufficiently large systems without spending huge amount of computational time and resources. At the current stage of development of the different types of blanket (pre-conceptual/conceptual design phase), global information of tritium behavior in the whole system is generally considered more valuable than studying specific local effects.

Following the previous work philosophy, system level models based on approximate components are very attractive for the fusion community. However, it is important to quantify the accuracy of the system level models. Otherwise, models in which important amount of project resources have been invested can produce results significantly distant from the physical reality. This risk has important consequences over blanket design choices.

The best way of testing the accuracy of the component level models is the experimental work in tritium transport. Unfortunately, this work is limited by the available experimental resources. Indeed, there are not so many experimental facilities that can manage tritium safely (the main one in Europe is the Tritium Laboratory Karlsruhe (TLK)). Besides, a good amount of physical and chemical effects are hard to reproduce in laboratory in relevant fusion conditions. One good example of experimental limitations is the neutronic radiation that the blanket will support. There is not a single experimental or industrial facility in the world which is able to generate neutrons with the relevant energy spectrum

and enought intensity (solving this problem is the objective of the International Fusion Material Irradiation Facility (IFMIF) project [28]).

When no experiments are available, deep level models become very handy for testing specific components with high degree of accuracy (ideally after previous experimental validation of the code). For the present dissertation, deep level models of relevant DCLL geometries have been developed with this purpose (sec: 6).

The main objective of the present doctoral dissertation is improving the quality of the DCLL system level models. For accomplishing this objective, the work methodology is based on using the three kinds of tritium transport models following a feedback loop. This methodology follows the next steps:

1. Initial component level models based on well established physical principles are developed. Complex phenomena (e.g. multiphysics effects) are simplified or even ignored in this step.
2. The initial components are used for implementing an initial system level model. This model allows identifying the most relevant regions of the blanket geometry in terms of tritium permeation.
3. Deep level models of the relevant geometries are developed including as most relevant physical effects (e.g. MHD) as possible. Boundary conditions and inputs of this model are taken from the results of the system level model.
4. The accuracy of the initial components is evaluated compared with the deep level results.
5. Upgrades and modifications of component level models are developed trying to reproduce as good as possible the deep level results.
6. An advanced tritium transport model of the DCLL blanket is developed using the upgraded component level models.
7. Repeat steps 3 to 6 until the system level model results does not change with every iterations.

Fig: 1.11 shows schematically the feedback loop that has been employed for this work. In this flowchart, component level models (or components) are

indicated in light orange, system level models are indicated in red and deep level models are indicated in green.

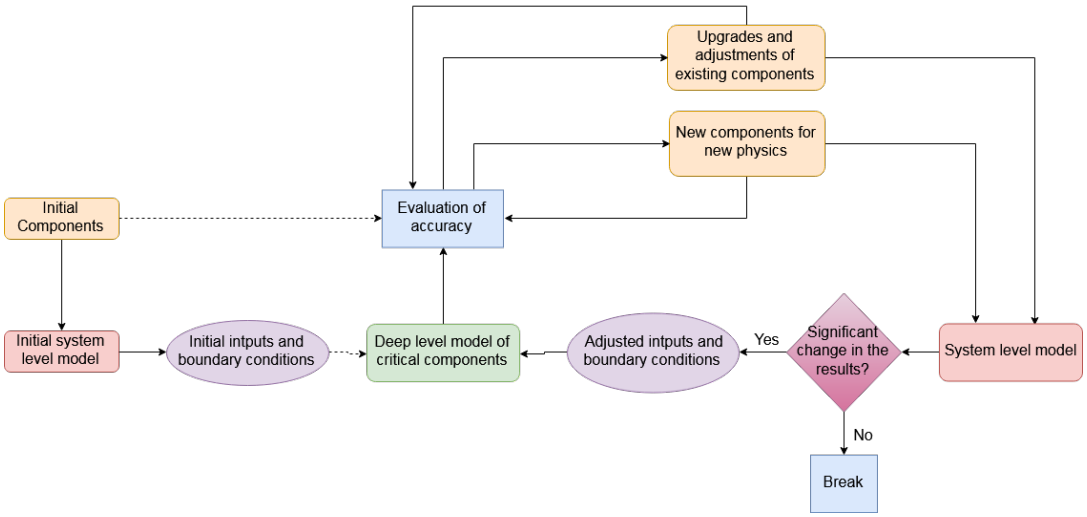

Figure 1.11: Feedback loop for tritium modeling optimization.

1.4 The DCLL breeding blanket concept

F The DCLL blanket is one of the 4 BB concepts that are currently being developed in Europe within the framework of the EUROfusion consortium. As shown in tab: 1.1, in this concept the tritium breeder (Li) and the neutron multiplier (Pb) are mixed forming a liquid metal alloy (PbLi). The use of liquid PbLi alloy is common to several BB concepts, not only DCLL. In contrast with solid concepts based on ceramic breeders (e.g. HCPB or HCCB), the fluid breeder can circulate within the blanket connected to an external circuit following a closed loop. Consequently, the liquid PbLi can be used not only as tritium breeder and neutron multiplier but also as tritium carrier. The function of the tritium carrier is dragging the bred tritium out of the blanket where it can be extracted and processed. Accomplishing three functions with only one material simplifies the design of the blanket which makes PbLi-based blankets very attractive.

The DCLL is probably a more ambitious concept than most of the PbLi-based concepts. The reason is that it uses the liquid PbLi not only for the three

previous functions but also as the primary coolant of the blanket. This means that the heat generated in the PbLi, which should be the majority of the heat generated in the blanket, is directly removed by the PbLi flow (self-cooling). Consequently, the PbLi alloy needs to follow a thermal cycle which includes a heat exchanger for the energy conversion. In contrast, other liquid metal based concepts, such as the HCLL and the WCLL, need an extra fluid (helium or water) for cooling the breeder and produce energy. Using compressible fluids, such as He, for cooling the complete system requires wasting an important amount of energy in recompressing and pumping the gas. Alternatively, cooling the system with water will limit considerably the maximum allowable coolant temperature (below water critical temperature). As a consequence, self-cooling the PbLi flow is expected to be beneficial from the plant efficiency perspective.

In practice, the PbLi cooling mechanism is translated into different PbLi velocity scales. On the one hand, the so called *low velocity concepts* use the PbLi movement only for removing the bred tritium out of the blanket. Therefore, the PbLi needs to be cooled externally using other fluid (e.g. water). On the other hand, the *high velocity concepts* uses the PbLi flow for removing part the thermal power. In these concepts the PbLi is called to be self-cooled.

As shown in sec: 1.3.1, the DCLL concept is the only high velocity concept under development within the European program. Two low velocity concepts, the HCLL and the WCLL are under consideration as well.

Despite PbLi fills most of the blanket volume, the structural components occupy a considerable amount as well. As any other blanket material, the structural materials are subjected to very large thermal loads, in particular the First Wall (FW) material, which is the closest to the plasma (fig: 1.12). As a consequence, the structure needs to be cooled in order to avoid unacceptable temperatures in the materials. In particular, the structural material that is being considered in Europe for both ITER and DEMO is a reduced activation ferritic-martensitic steel (EUROFER). The thermal operational window of this steel is 350 °C - 550 °C [29]. Out of this temperature range the mechanical properties of EUROFER are not considered good enough. A considerable amount of resources are being invested in R&D programs related to the improvement of the EUROFER properties (e.g. [30]).

Cooling the structure using only the liquid metal flow is an attractive idea from the conceptual point of view but it would require enormous flow rates

next to the FW. During the nineties, European teams studied this promising possibility, called the SCLL concept, for both the TBM program [31] and for DEMO blankets [32]. American and Russian teams also worked in SCLL concepts of pure liquid lithium [33]. The SCLL concept is most likely the most ambitious blanket concept ever conceived. However, the very high velocities needed for cooling the FW present important drawbacks that have been considered as critical problems by most members of the community. The first European study of the DCLL concept [34] was conceived as a more realistic alternative that follows a similar philosophy than the SCLL. It introduces a secondary coolant (helium) for cooling the FW and other sensible parts of the structure while the breeder alloy is still self-cooled. Later studies of the DCLL were made in Germany [35] which have served as base for the subsequent development under the EUROfusion program.

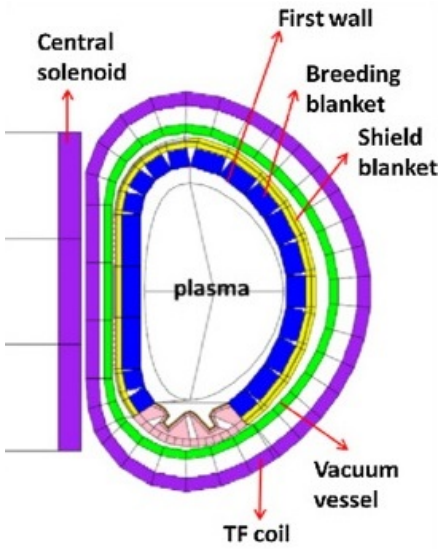

Figure 1.12: Scheme of a generic blanket [36].

Cooling the structure independently of the PbLi flow opens the possibility of increasing the PbLi temperature. Indeed, if the structural materials are kept at acceptable temperatures using a secondary coolant, the PbLi could potentially reach outlet temperatures higher than 550 °C. This could increase considerable the efficiency of the plant potentially allowing lower velocities. Complete balance of plant calculations should be conducted taking into account specific blankets design options and subsystems to confirm the potential increase of the efficiency. In any case, it is possible to distinguish between two DCLL possibilities: the

high temperature DCLL concept and the low temperature DCLL concept. A summary of the conceptual differences between the liquid metal-based blankets is exposed in tab: 1.2.

		Breeder Coolant	Structure Coolant	Velocity Scale
HCLL		He	He	Low
WCLL		H_2O	H_2O	Low
DCLL	Low T	PbLi	He	High
	High T	PbLi	He	Moderate
SCLL		PbLi	PbLi	Very High

Table 1.2: PbLi-based BB classification.

Each blanket concept shown in tab: 1.2 has different advantages and weaknesses. A discussion of all benefits and drawbacks is out of the scope of the present work. Nevertheless, there are three important issues that are introduced here since they importantly (or even critically) affect the blanket functionality. Those are: tritium permeation losses, MHD pressure drop and corrosion.

Tritium permeation losses are pressent in every blanket concept. Indeed, tritium tends to permeate from the Pbli circuits where it is generated to the helium (or water) circuits. As explained in sec: 1.3, this permeation is considered a fundamental issue as both the safety of the plant and the tritium self-sufficiency are compromised. A detailed description of the permeation phenomenon is given in sec: 3 but it is possible to advance two important factors that affect tritium permeation: the permeation surface and the extraction rate. The permeation surface is the contact surface between the PbLi and He (or H_2O) flows through the solid materials. Low velocity concepts needs more contact surface for cooling the PbLi bulk. This exposes them to large tritium losses. Moreover, high mass flow rates are believed to be beneficial for the extraction rate. In fact, if tritium is drag out from the blanlket at high rates it reaches the extraction systems faster having fewer time to permeate to the secondary coolant circuits. Nevertheless, it is worth noting that the extraction techniques are still under development. Therefore, it is unclear which will be their response with the fluid velocity.

Due to the previous factors, low velocity concepts can have serious issues concerning tritium permeation. Predictive models of the HCLL and WCLL

concepts(e.g. [37, 38]) show unacceptable permeation rates. However, the results are subjected to large uncertainties. Whether tritium permeation is a critical issue for low velocity concepts requires of further research. The R&D activities on anti-permeation barriers that are being investigated are of extreme importance for the viability of low velocity concepts.

Concerning the MHD pressure drop, all liquid metal-based concepts suffer from it. The reason is that PbLi is a good electrical conductor moving immersed into a very intense magnetic field (3-9 T) (the magnetic field is needed for the plasma confinement). Electrical currents are induced in the PbLi flow which generates Lorentz forces that are in general opposed to the flow. A scheme of the basic MHD interaction is shown in fig: 1.13, a detailed description of the MHD phenomena is exposed in chap: 2. Due to the intensity of the magnetic field, MHD effects will constitute an important pressure drop source that can be critical on PbLi pumping requirements. High velocity concepts pumping needs are logically more demanding. For addressing this issue, MHD pressure drop mitigation strategies are under development (e.g. [39]). These are necessary for high velocity concepts and probably necessary for some regions of low velocity concepts as well (manifolds).

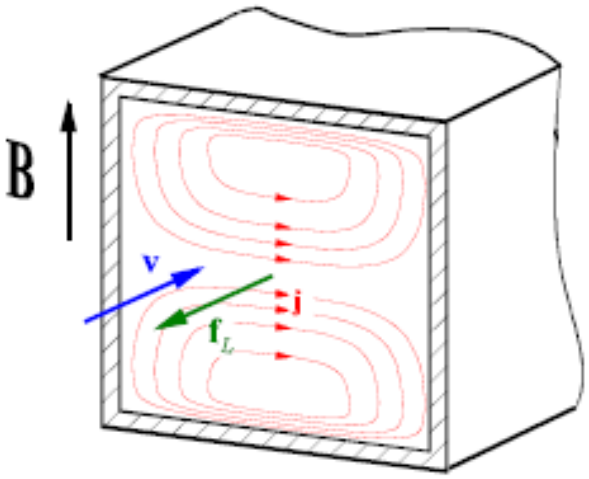

Figure 1.13: Scheme of the MHD interactions [40].

Unlike tritium permeation and MHD effects, corrosion studies are not part of the objectives of the present work. However, corrosion is very important for the viability of high velocity and high temperature concepts. In fact, PbLi is a corrosive agent for EUROFER. According to different experiments [41, 42], due

to the chemical and physical interaction between the steel components and the PbLi, several μm of steel are loss per year in each wall of the blanket in contact with PbLi. High corrosion rates will not only compromise the structural integrity of the blanket but the corrosion products dissolved in PbLi can alter also the correct functioning of the breeder and ancillary systems. According to the experimental results [43], corrosion is an issue that will affect every PbLi-based blanket but it will affect more severely the high velocity and high temperature concepts. Anti-corrosion barriers are being developed as part of European R&D programs for addressing this problem.

Tab: 1.3 shows a classification of PbLi-based blanket concepts in terms of the importance of the three mentioned issues on their functioning. A comparison of the plant efficiency based on conceptual differences is also depicted.

		Tritium Permeation Losses	MHD Pressure Drop	Corrosion	Efficiency of the Plant
HCLL		Very Important/Critical	Important	Important	Low/Moderate
WCLL		Very Important/Critical	Important	Important	Low/Moderate
DCLL	Low T	Not very important	Very important	Important	Moderate
	High T	Not very important	Very important	Very Important/Critical	High
SCLL		Not very important	Critical	Very important/Critical	High

Table 1.3: PbLi/helium-based BB classification in terms of their response to different issues.

The EUROfusion consortium decided in 2014 to focus on the development of 3 PbLi-based concepts: the HCLL, the WCLL and the low temperature DCLL. The risk associated to the MHD pressure drop and to the structure corrosion discarded the other two possibilities (tab: 1.2). The HCLL concept will be tested in the ITER TBS which will allow quantifying experimentally the tritium permeation losses.[1] The DCLL concept was chosen as a more challenging but rewarding concept which heavily relies on the development of viable MHD pressure drop mitigation mechanism.

[1]Recently, the European TBM project is considering testing the WCLL concept instead of the HCLL.

1.4.1 The European DCLL design

The present doctoral dissertation is based on the European work performed for the DCLL since the beginning of the EUROfusion activities. The EUROfusion blanket program is very active and it is in constant evolution. The designs of the blankets are constantly being adapted to project requirements and engineering and physical problems are continuously being detected, analyzed and corrected. During the doctoral period different versions of the DCLL concept were developed by the design team. The most important ones are presented in this chapter.

The EU-DCLL is a modular design. This has not changed with the evolution of the versions. This means that the PbLi and helium circuits are divided in several modules. The size of the modules depends on their exact position in the blanket but their geometries are analogous. The blanket is divided into 18 or 16 sectors (depending on the version) along the toroidal direction. Sectors are completely equal to each other respecting the toroidal symmetry of the reactor (not taking into account the penetrations of other systems like fuel injectors or heating devices). Each sector has their own independent PbLi and helium external piping as well as the ancillary systems associated to it. The number of blanket sectors is imposed by the geometry of reactor. They have to match with the number of toroidal field coils. Fig: 1.14 depicts the geometry of the DEMO 2014 reactor (16 sectors) [44].

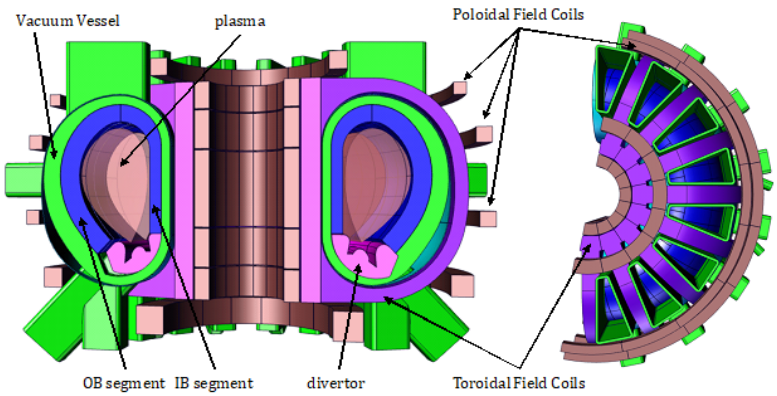

Figure 1.14: 2014 DEMO geometry provided by EUROfusion [44].

Each sector consists of 5 Multi-Module Segment (MMS); 3 of them located in the Outboard (OB) zone while the other 2 are located in the Inboard (IB)

zone. Fig: 1.15 shows the multi-module configuration of one sector. The PbLi enters and leaves the blanket through feeding and collecting pipes, respectively. The PbLi feeding pipes are connected to the bottom part of the segments. The collecting pipes are connected to the upper part in case of IB segments and to the middle part in case of OB segments. The arrangement of the pipes is strongly determined by the shape of the available ports of the vacuum vessel.

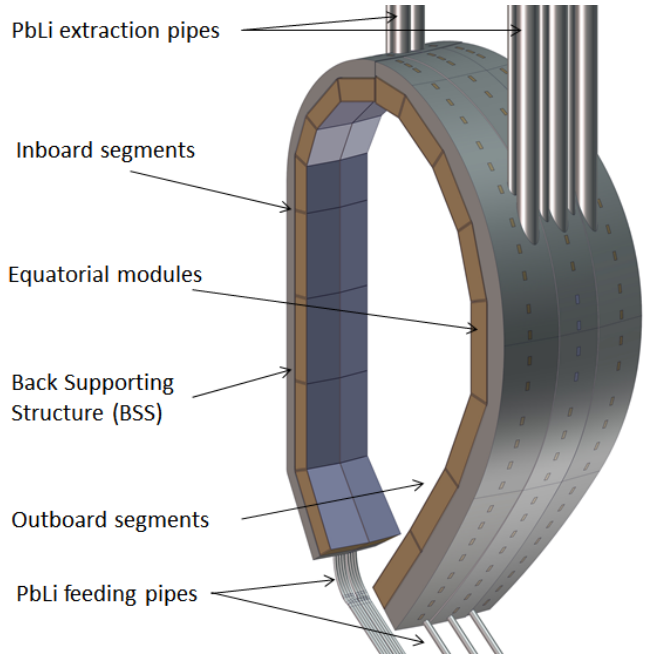

Figure 1.15: Geometrical configuration of one DCLL sector showing 3 OB segments and 2 IB segments, each one composed of a series of modules and a BSS.

Every segment, both IB and OB, is formed by a certain number of modules. The modules are attached to a common BSS. The BSS has not only a mechanical function but it also acts as manifold for the PbLi and He flows. For this reason, PbLi channels and He channels with rectangular cross section are placed in the BSS along the poloidal direction (fig: 1.16). These channels feed the modules with cold PbLi/He and collect both coolants once they have been warmed.

The design activities of the DCLL and the rest of the blankets developed within the framework of EUROfusion focus on the OB equatorial module (fig: 1.15). The module geometry determines the flow path of both coolants which has important implications in the blanket functionality and the results

of the engineering analyses performed for it (structural, thermal-hydraulics, MHD, tritium transport...).

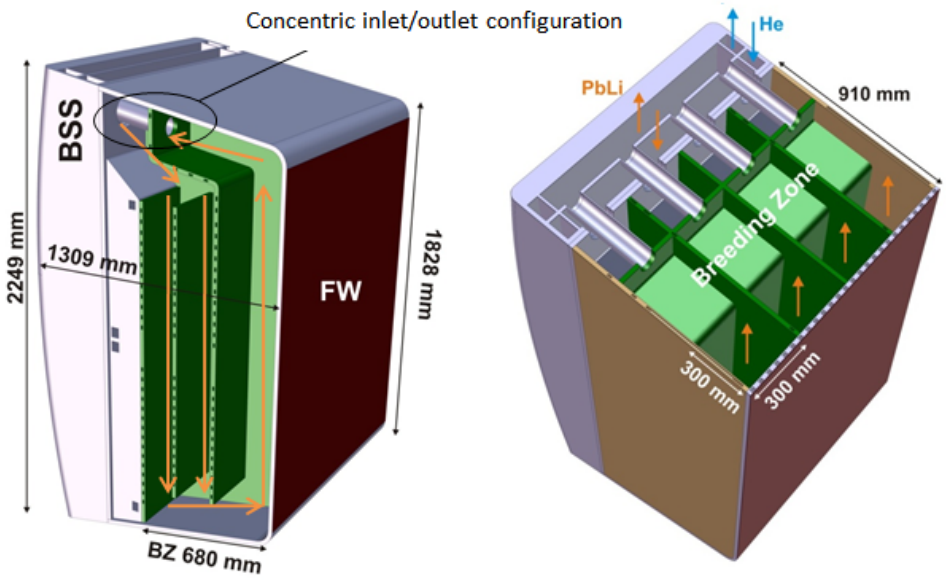

(a) Version 1.

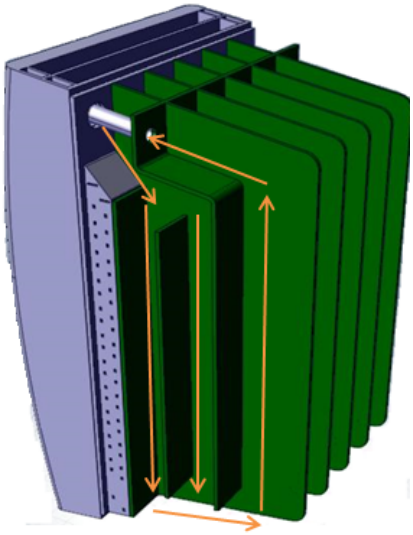

(b) Version 2.

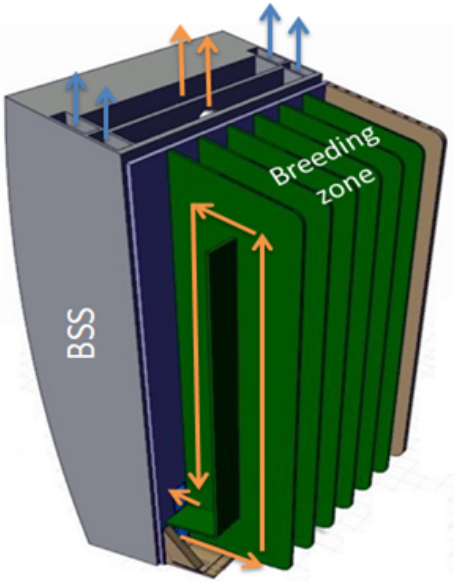

(c) Version 3.

Figure 1.16: Geometry of the OB equatorial module for different versions of the DCLL design. In orange the PbLi flow path, in blue the He flow.

Fig: 1.16 depicts the 3 main versions of the DCLL OB equatorial module. These versions and the rest of the detailed information about the DCLL design

and engineering analyses can be found in the corresponding Design Report (DR) documents [45, 46] and the Design Description Document (DDD) [47, 48] associated to the EUROfusion DCLL blanket.

The first consolidated version of the DCLL followed a similar flow path configuration than the previous European studies on the DCLL concept [35]. The breeder zone is formed by 4 equal parallel toroidal circuits. Each one consist on 3 parallel poloidal channels. The PbLi descends along 2 rear channels and then ascends along a front channel close to the FW.

Concerning the helium circuit, in the 3 versions shown in fig: 1.16 the cooling of the FW was based on poloidal circulation of helium (fig: 1.17). The rest of the helium channels present important differences between the versions. Note that the PbLi flow helps with the cooling of the structure too up to the point that there are walls which does not need of helium cooling.

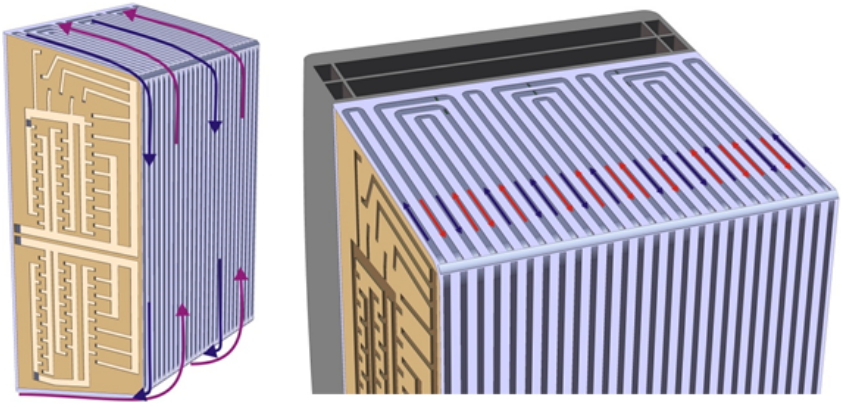

Figure 1.17: FW cooling scheme for DCLL version 1 [45].

Version 2 does not change the shape of PbLi flow path with respect to version 1. However, it introduces important modifications. Firstly, the number of toroidal parallel PbLi circuits is increased from 4 to 6. This change was motivated by the structural analyses of in-box Loss Of Coolant Accident (LOCA) conditions. The extra radial stiffeners give more stability to the structure in the accidental case in which the high pressurized helium (8 MPa) enters in the PbLi channels. Another important change is a significant reduction of the amount of helium channels. Thermohydraulic estimations of version 1 showed that the PbLi is able to cool some parts of the structure

efficiently. Therefore it was decided to reduce the density of He channels (fig: 1.18).

Important changes were adopted when transitioned to version 3. Those were mainly motivated by the new geometry of the DEMO 2015 machine, by the PbLi draining requirements of the segments and by MHD considerations.

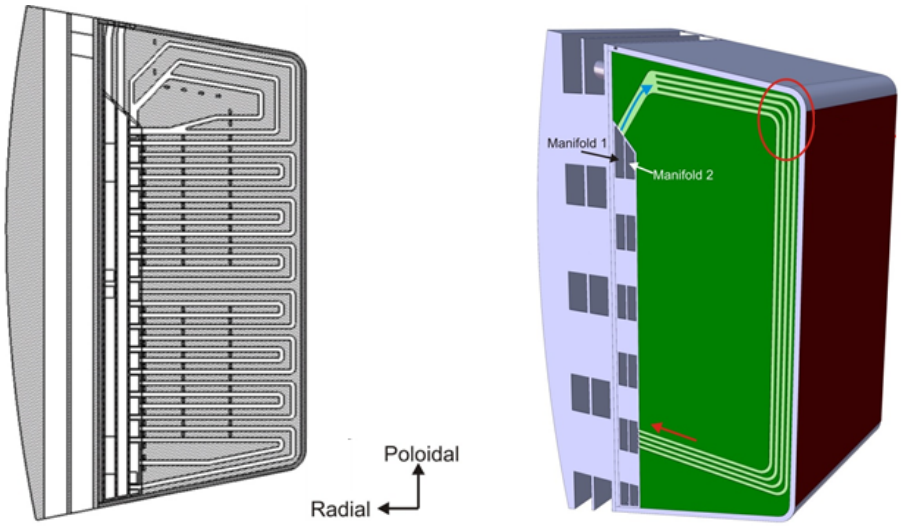

(a) Version 1. (b) Version 2.

Figure 1.18: Helium channels of the radial stiffening plates for version 1 and version 2 [45].

Furthermore, the new DEMO configuration allowed increasing the thickness of the BSS, improving the structural quality of the segment without loosing breeder volume (and consequently TBR). On the other hand, having the PbLi inlet and outlet at the top of the module made impossible the draining of the segment by gravity. Moreover, MHD estimations showed that the concentric inlet/outlet configuration of version 1 and 2 (fig 1.16) is an important source of pressure drop [49]. For these reasons the PbLi inlet and outlet were relocated in the inferior part of the module using two parallel (not concentric) channels. The change in the inlet and outlet positions changed the PbLi flow path. In this version, the PbLi flows first along the front channel and then descends along the rear channel. The new radial dimension provided by the DEMO 2015 configuration allowed reducing the number of channels from 3 to 2. This way, the amount of breeder volume was increased and the flow path was simplified.

As explained in sec: 1.4, the DCLL concept relays in the development of effective pressure drop mitigation mechanisms. The baseline solution adopted by the European DCLL is the Flow Channel Insert (FCI). FCI are ceramic structures that are embedded in the PbLi channels of the blanket. The FCI should be able to decouple the PbLi from the metallic structure as the ceramic is a good electric insulator. Isolating the PbLi from the walls reduce the pressure drop in orders of magnitude (see sec: 2.1.5). Figure 1.19 shows a diagram of the DCLL channel with an FCI. Different designs options are being considered but the baseline option consists on a thin sandwich-like structure with an alumina core in between of 2 EUROFER layers [39]. In between the FCI and the channel walls there is a 2 mm gap filled with PbLi.

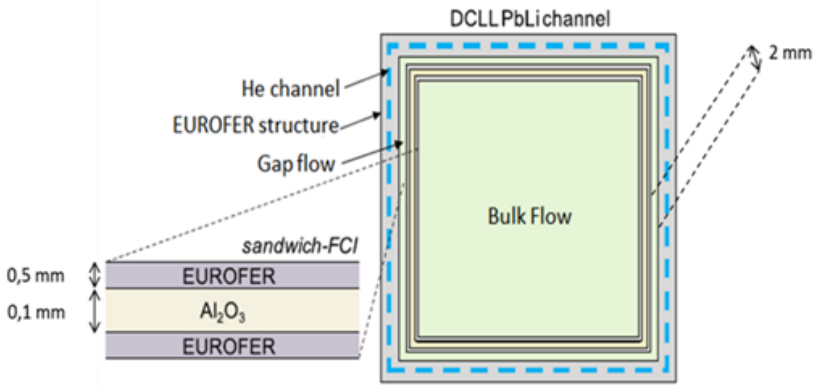

Figure 1.19: DCLL channel representation with a sandwich-like FCI.

The different analyses, either tritium transport or MHD, performed during the doctoral period were based on the latest available DCLL version. Those analyses helped in the designs activities and contribute to the evolution of the module. In each section of the present dissertation, the version of the DCLL that has been modeled or simulated is introduced with the extra relevant information needed for the corresponding calculations.

Chapter 2

Theoretical framework for MHD in liquid metal flows

In this chapter, the MHD phenomena are presented in detail. The derivation of the MHD differential equations is exposed focusing on the physical interpretation of each term. The dimensionless constants that determine the different MHD regimes of the system are defined. Two different approximate formulations, the fully developed formulation and the Quasi 2 Dimensional (Q2D) formulation are presented together with some analytic solutions relevant for code validation purposes. Finally, the heat transfer phenomena coupled with MHD (magneto-convection) are explained.

2.1 MHD phenomena in liquid metals

Magnetohydrodynamics is a multiphysics phenomenon that describes the crossed interaction between two vector fields: the fluid velocity field and the electromagnetic field. Therefore, the description of the MHD phenomena combine the fluid dynamics and the electromagnetic theories.

2.1.1 Fluid dynamics differential description

Fluid dynamics is the study of the motion of fluids. The dynamic description of a fluid is made in terms of the velocity vector field: $u_i(t, x_j)$. Obtaining the velocity field of a fluid in every point and at any instant is equivalent to solving the system of study.

In contrast to a discrete particle description, fluid dynamics is based in the continuum approximation of the fluids which state that fluid matter occupies the whole space in which is contained. The continuum approximation is valid for most macroscopic fluid applications including PbLi flow in fusion BB.

Assuming the previous approximation, fluid dynamics differential equations are derived from the conservation of mass and momentum (see for ex. [50]).

As any other conservation law, mass conservation (also known as continuity equation) implies that in any control volume of the domain, the variation of the mass density scalar field $\rho(t, x_i)$ is equal to the net mass flux $(u_i \cdot \rho)$ that enters or leaves the volume (assuming no source or sink inside the control volume). The continuity equation takes its differential form in the limit of an infinitesimally small control volume:

$$\partial_t \rho + \partial_i (u^i \rho) = 0 \tag{2.1}$$

Where ∂_t means the partial derivative with respect to time while ∂_i means the partial derivative with respect to the x_i spatial coordinate. It is worth noting that the Einstein summation convention is employed from now on.

It is said that the fluid is incompressible if the following conditions are satisfied:

$$\begin{aligned} \partial_t \rho &\approx 0 \\ |u^i \partial_i \rho| &<< |\rho \partial_i u^i| \end{aligned} \tag{2.2}$$

Therefore, incompressible flows are divergence free ($\partial_i u^i = 0$). Most liquids in nature, including PbLi, can be treated as incompressible fluids unless they are subjected to very intense and localized temperature gradients.

Analogous equation than (2.1) can be obtained for the momentum conservation. The momentum or more precisely, the momentum density ρu_i must be conserved in any control volume of the system. The momentum flux is defined as $(\rho u_j u_i)$ which implies that differential the momentum conservation equation is written as follows:

$$\partial_t(\rho u_i) + \partial_j(u^j u_i \rho) = \sum_k S_{ki} \tag{2.3}$$

Expanding the derivatives using the chain law and applying the mass conservation (2.1) the momentum conservation can be simplified:

$$\rho \partial_t u_i + \rho u^j \partial_j u_i = \sum_k S_{ki} \tag{2.4}$$

As in any other mechanical system, the source and sink terms $S_{ki}(t, x_j)$ of the momentum equation represents the extra forces that acts on the control volume. These forces can be external forces, like gravity (ρg_i), or internal forces that represent the interaction of the fluid with itself.

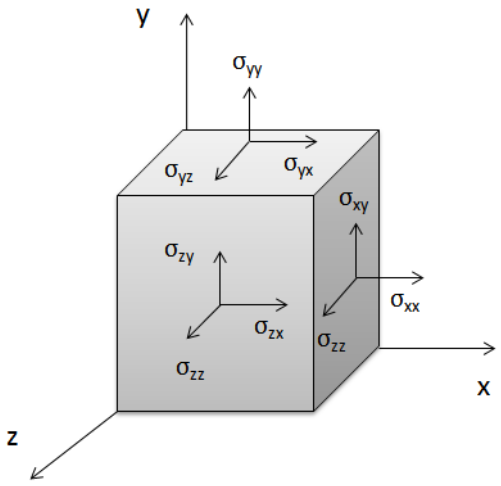

Figure 2.1: Notation for surface stresses in a fluid.

Concerning the internal forces, any differential volume is subjected to surface stresses. These stresses are generated by the adjacent fluid volumes that rub the first one. The surface stresses affects every side of the volume in every possible direction (fig: 2.1). Thus, they are represented by a second order tensor $\sigma_{ij}(x_k)$.

Surface stresses are typically split into two different components: the pressure and the viscous forces (2.5). On the one hand, the pressure always applies in the direction normal to side of the differential control volume. It represents the pushing effect of the adjacent volumes. On the other hand, the viscous forces apply in every direction and they represent the friction created by the adjacent volumes:

$$\sigma_{ij} = -p\delta_{ij} + \tau_{ij} \tag{2.5}$$

In (2.5), $p(x_i)$ is the pressure scalar field, δ_{ij} is the Kronecker Delta tensor and τ_{ij} is the viscous stress tensor. For isotropic fluids (like the PbLi), the viscous stress tensor is symmetric ($\tau_{ij} = \tau_{ji}$). The net contribution of the strees tensor to the momentum equations is obtained by applying the divergence along each corresponding direction:

$$\rho\partial_t u_i + \rho u^j \partial_j u_i = \partial_j \tau_i^j - \partial_i p + \sum_k S_{ki} \tag{2.6}$$

For solving (2.6) an expression for the stress tensor in terms of the velocity components must be derived. The simplest assumption is to assume that $\tau_{ij} = 0$ which leads to the Euler equation and to the Bernouilli equation when integrating along a streamline (e.g. [50]). These fluids are called inviscid and they are approximations of real fluids.

The so called Newtonian fluids accepts an empirical relation between the viscous stress tensor and the velocity field. A great many of fluids (including the liquid PbLi) can be described with the following Newtonian relation:

$$\tau_i^j = \eta(\partial_i u^j + \partial^j u_i) \tag{2.7}$$

Where η is the dynamic viscosity of the fluid. Using (2.7) the net viscous force that acts over the fluid can be expressed in terms of the derivatives of the velocity field:

$$\partial_j \tau_i^j = \eta(\partial_i \partial_j u^j + \partial_j \partial^j u_i) \tag{2.8}$$

The first term of (2.8) vanishes for incompressible fluids. Therefore the

differential equation of motion for a fluid can be written as follows:

$$\rho(\partial_t u_i + u^j \partial_j u_i) = \eta \partial_j \partial^j u_i - \partial_i p + \sum_k S_{ki} \tag{2.9}$$

Equation (2.9) is commonly known as Navier-Stokes equation. From the assumptions made during the derivation it can be state that the equation is valid for incompressible, Newtonian, isotropic fluids with no mass generation sources or sinks.

From left to right, the physical interpretation of (2.9) terms are: inertia forces, advection term, viscosity forces, fluid pressure, and external sink/sources.

It is sometimes convenient, especially for CFD applications, expressing the Navier-Stokes equation using dimensionless variables. For this purpose it is necessary to define the characteristic length (L) and velocity (u_0) of the system. With this 2 magnitudes we can define the following normalized variables: $\hat{u} := u/u_0$ and $\hat{p} := p/\rho {u_0}^2$. Assuming no external forces (they should be analyzed independently) the dimensionless Navier-Stokes equation is written as follows:

$$\partial_t \hat{u}_i + \hat{u}^j \partial_j \hat{u}_i = \frac{1}{Re} \partial_j \partial^j \hat{u}_i - \partial_i \hat{p} \tag{2.10}$$

Where Re is the Reynolds number which is defined as:

$$Re := \frac{\rho u_0 L}{\eta} \tag{2.11}$$

The Reynolds number represents the ratio between the inertia forces and the viscous forces. It is a very important dimensionless constant for any fluid system as it determines its regime:

- For Re $<$ 2000 the flow is in laminar regime. The viscous forces are dominant maintaining the structure of the flow.
- For Re $>$ 4000 the flow in turbulent regime. Inertial effects dominate the flow creating non-stationary and unstructured flows.
- For 2000 $>$ Re $>$ 4000 the flow is in intermediate or transitioned regime.

Inertial oscillations appear in the flow but they are still limited by viscous forces.

2.1.2 MHD differential description

As it was introduced in sec: 1.4, the MHD effects in fluid mechanics arise as the result of the currents induced in an electrically conducting fluid. Therefore, MHD is a multiphysics phenomenon that combines the fluid dynamics described in sec: 2.1.1 and the electromagnetic theory whose fundamental equations are the Maxwell equations (see for ex. [51]):

$$\partial_i E^i = \frac{\rho_e}{\epsilon} \tag{2.12}$$

$$\partial_i B^i = 0 \tag{2.13}$$

$$(\nabla \times \vec{E})_i = -\partial_t B_i \tag{2.14}$$

$$(\nabla \times \vec{B})_i = \mu j_i + \mu\epsilon\partial_t E_i \tag{2.15}$$

Where $E_i(t, x_j)$ is the electric field, $B_i(t, x_j)$ is the magnetic field, ρ_e is the density of electric charge, j_i is the density of electric currents, ϵ is the electric permittivity of the media and μ is the magnetic permeability of the media.

The first equation, also known as Gauss law, relates the electric field with their sources. The second equation states the solenoidal nature of the magnetic field (there are no magnetic monopoles). The third equation, known as Faraday law of induction, relate both kind of fields. The last equation is the Ampere law with the Maxwell addition which relates the magnetic field with their sources and introduce another relation between the electric and magnetic field. The Maxwell equations together with the Lorentz force expression describes every non-relativistic electromagnetic phenomena. The Lorentz force per unit volume is expressed as follows:

$$f_i = \rho_e E_i + (\vec{j} \times \vec{B})_i \tag{2.16}$$

Liquid metals are very good electrical electrical conductors. Therefore, charge accumulations are not expected and the fluid can be approximated as neutral ($\rho_e \sim 0$). Under this approximation Lorentz forces can be rewritten as

follows:

$$f_i \simeq (\vec{j} \times \vec{B})_i \tag{2.17}$$

Due to charge conservation, the neutral fluid approximation entails that the current density is divergence free ($\partial_i j^i = 0$). This implies that all currents form closed loops.

In the same way that the electromagnetic forces affects the evolution of the velocity field. The velocity field also affects the induced magnetic field. This effect is given by the generalized Ohm's law (2.18) including the extra magnetic term generated by the velocity of the moving conductor:

$$j_i = \sigma(E_i + (\vec{u} \times \vec{B})_i) \tag{2.18}$$

Where σ is the conductivity of the media.

In liquid metal BB applications there is an intense external magnetic field generated by the superconductor coils of the reactor. According to the Ohm's law, the induced currents are proportional to this field. As a consequence, the variation of the induced electric field with time is small in comparison with the intensity of the induced currents. Therefore, the Maxwell addition to the Ampere law can be neglected in BB applications:

$$(\nabla \times \vec{B})_i \simeq \mu j_i \tag{2.19}$$

Substituting (2.19) in (2.17) and using (2.13) together with the vector identity (2.20), the Lorentz force can be expressed in terms of the magnetic field:

$$(\nabla \times (\vec{A} \times \vec{B}))_i = B_j \partial^j A_i + A_i \partial_j B^j - A_j \partial^j B_i - B_i \partial_j A^j \tag{2.20}$$

$$f_i = (\vec{j} \times \vec{B})_i = \frac{1}{\mu}((\nabla \times \vec{B}) \times \vec{B})_i = \frac{1}{\mu}\left(-\frac{1}{2}\partial_i B_j B^j + B^j \partial_j B_i\right) \tag{2.21}$$

Therefore, (2.21) can be included in the Navier-Stokes equation (2.9) as the following external source term:

$$\rho(\partial_t u_i + u^j \partial_j u_i) = \eta \partial_j \partial^j u_i - \partial_i p + \frac{1}{\mu}\left(-\frac{1}{2}\partial_i B_j B^j + B^j \partial_j B_i\right) \tag{2.22}$$

The evolution of the magnetic field is obtained introducing the generalized Ohm's law in the Faraday induction equation. Indeed, substituting (2.18) in (2.14) and using (2.19) and (2.20) the effect of the fluid movement on the magnetic field is obtained.

$$\begin{aligned}
\partial_t B_i &= -(\nabla \times \vec{E})_i = \\
&= -(\nabla \times (\frac{1}{\sigma}\vec{j} - \vec{u} \times \vec{B})_i = \\
&= -\frac{1}{\sigma\mu}(\nabla \times (\nabla \times \vec{B}))_i + (\nabla \times (\vec{u} \times \vec{B}))_i = \\
&= \frac{1}{\sigma\mu}\partial_j \partial^j B_i + B_j \partial^j u_i - u_j \partial^j B_i
\end{aligned} \tag{2.23}$$

The first term of the right side in (2.23) is the magnetic diffusion term while the other two are advection terms which represents the cross effect between the u field and the B field.

Summarizing, a liquid metal flow immersed into a external magnetic field is well described by the following system of equations:

$$\rho(\partial_t u_i + u^j \partial_j u_i) = \eta \partial_j \partial^j u_i - \partial_i p + \frac{1}{\mu}\left(-\frac{1}{2}\partial_i B_j B^j + B^j \partial_j B_i\right) \tag{2.24}$$

$$\partial_t B_i = \frac{1}{\sigma\mu}\partial_j \partial^j B_i + B_j \partial^j u_i - u_j \partial^j B_i \tag{2.25}$$

$$\partial_i B^i = 0 \tag{2.26}$$

$$\partial_i u^i = 0 \tag{2.27}$$

The previous description of the MHD problem is written in what is called the B-formulation. As in the fluid-dynamic case, there are non-linear terms which limits the the analytic solutions to very specific geometries and conditions (see sec: 2.1.5).

As with the pure fluid dynamic problem, it is convenient to rewrite the equations in a dimensionless form. For this purpose the variables u, B and p are normalized in terms of u_0, B_0 and $B_0^2 \sigma u_0 L$ respectively. Where u_0 is the characteristic velocity of the system, B_0 is the external magnetic field and L

is the characteristic length of the system. The dimensionless description of the MHD problem written in the B-formulation is expressed as follows:

$$\frac{1}{N}(\partial_t \hat{u}_i + \hat{u}^j \partial_j \hat{u}_i) = \frac{\partial_j \partial^j \hat{u}_i}{Ha^2} - \partial_i \hat{p} + \frac{1}{Rm}\left(-\frac{1}{2}\partial_i \hat{B}_j \hat{B}^j + \hat{B}^j \partial_j \hat{B}_i\right) \tag{2.28}$$

$$\partial_t \hat{B}_i = \frac{1}{Rm}\partial_j \partial^j \hat{B}_i + \hat{B}_j \partial^j \hat{u}_i - \hat{u}_j \partial^j \hat{B}_i \tag{2.29}$$

$$\partial_i \hat{B}^i = 0 \tag{2.30}$$

$$\partial_i \hat{u}^i = 0 \tag{2.31}$$

Three new dimensionless numbers arises from this analysis. They determine the relation between the different forces involved in the MHD problems:

- Hartmann number: $Ha \equiv B_0 L\sqrt{\frac{\sigma}{\eta}}$. It (more precisely its square) represents the ratio between the Lorentz forces and the viscous forces.
- Reynolds magnetic number: $Rm \equiv u_0 L \sigma \mu$. It represents the ratio between the magnetic field own diffusion and the advection forces generated by the coupling with the flow.
- Interaction parameter: $N \equiv \frac{B_0^2 \sigma L}{\rho u_0}$. It represents the ratio between the Lorentz forces and the inertial terms.

The Reynolds number is still a relevant parameter for the system but it can be written in terms of the other: $Re = Ha^2/N$.

The Hartmann number is a very important parameter for MHD systems. For Hartmann numbers greater than 10, the MHD effects dominate over viscous effects except in the vicinity of the walls where viscous BLs are developed. The thickness of these layers depends on the Hartmann number on the following way:

- Hartmann BLs: for the walls perpendicular to the external magnetic field (*Hartmann walls*) the thickness of the viscous layer scales with: $\sim Ha^{-1}$.
- Side BLs: for the walls parallel to the external magnetic field (*Side walls*) the thickness of the viscous layer scales with: $\sim Ha^{-0.5}$.

An illustrative example of the BL formation can be found in the Hartmann flow [52]. This is the flow between 2 infinite parallel walls under a transverse magnetic field (Fig: 2.2). In this flow with analytic solution, the dependency of the Hartmann BL with the Hartmann number can be easily observed. Note that the viscous BL formation is a general phenomena and it is not limited to this simple solution.

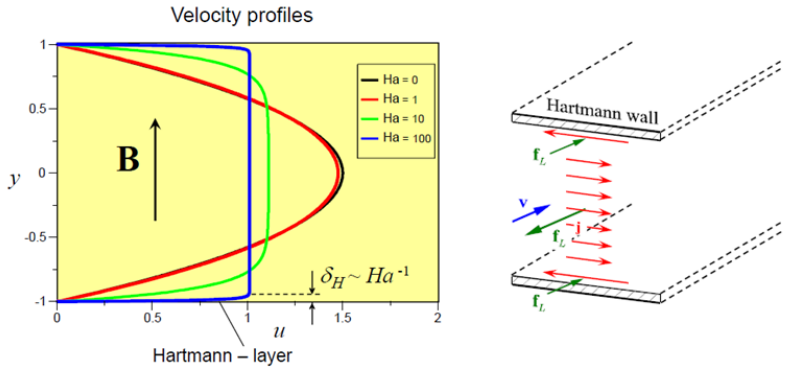

Figure 2.2: Hartmann flow solution [40].

The Hartmann number does not depend on the flow velocity. Thus, every liquid metal-based concept have similar Hartmann numbers. The order of magnitude of the Hartmann number varies from 10^3 to 10^4 depending on the blanket region. This means that MHD Lorentz forces will complete dominate the PbLi dynamics in any PbLi-based blanket concept.

The interaction parameter is also considerable large in fusion blankets, especially in a low velocity concept where it takes values up to 10^4 or 10^5. For the DCLL this parameter is around one order of magnitude lower than for the low velocity concepts but still significantly high. This large interaction parameter means that local inertial effects (inlets, bends, flow expansions...) are confined to small regions as the MHD interaction suppresses them very efficiently.

Concerning the Reynolds magnetic number, this parameter determines the degree of coupling between the magnetic field and the velocity field. When the Reynolds magnetic number is very small ($Rm << 1$), according with (2.29) the induced magnetic field is barely influenced by the flow. This means that the value of the induced field can be neglected since the flow barely produces it. In this situation, the magnetic field lines are almost frozen. As a consequence,

according with the third Maxwell law (2.14), the electric field is irrotational and the electric potential scalar field ϕ is well defined.

Under these circumstances, the MHD equations admit another formulation which is based on the electric potential as the only independent variable of the electromagnetic problem. Indeed, using the Ohm's law (2.18) the Lorentz force can be expressed in terms of the electric potential and the external magnetic field. Besides, taking the divergence of the Ohm's law it is possible to obtain a Poisson equation for the potential that closes the system of equations:

$$f_i = (\vec{j} \times \vec{B}_0)_i \tag{2.32}$$

$$\partial_j \partial^j \phi = \partial^j (\vec{u} \times \vec{B}_0)_j = B_0^j (\nabla \times \vec{u})_j \tag{2.33}$$

Normalizing the electric potential with $u_0 B_0 L$, the complete MHD problems expressed in the ϕ-formulation is written as follows:

$$\frac{1}{N}(\partial_t \hat{u}_i + \hat{u}^j \partial_j \hat{u}_i) = \frac{1}{Ha^2} \partial_j \partial^j \hat{u}_i - \partial_i \hat{p} + (\vec{j} \times \vec{B}_0)_i \tag{2.34}$$

$$\partial_j \partial^j \hat{\phi} = \partial^k (\vec{u} \times \vec{B}_0)_k \tag{2.35}$$

$$\partial_i \hat{u}^i = 0 \tag{2.36}$$

In the DCLL concept, the magnetic Reynolds number takes values from the order 10^{-3} to 10^{-1}. Therefore, the ϕ-formulation is only applicable in certain regions. For the low velocity concepts, the ϕ-formulation can be used in almost every zone.

2.1.3 Fully developed MHD flows

The complexity of the MHD problems makes that when applicable, adequate approximations can reduce importantly the computational times and resources needed for solving the MHD problems.

The fully developed approximation is a very useful approach for BB technologies. The reason is that the interaction parameter is very high in most of the blanket. This means that, the inertial effects generated by changes in the flow path geometry (flow expansion, bends,...) are mitigated rapidly by the magnetic field. For the same reason, transient periods should be relatively

short. As a consequence, the flow is expected to be fully developed in most of the PbLi flow path.

Fully developed models can be applied for computations of straight poloidal channels under a transverse (toroidal) magnetic field which is a common geometry of the DCLL design. Important and interesting phenomena such as the FCI pressure mitigation, the electrical coupling between parallel channels or the effect of the He channels in the EUROFER electrical conductivity can be studied using this approximation.

The fully developed formulation describes only the steady state of the system. Besides, it is based on 3 important assumptions:

1. All current are cross sectional, there are no axial currents in the flow. This implies that the induced magnetic field only has axial component.
2. The velocity has only axial component and there is no dependence on the axial coordinate.
3. The pressure depends linearly on the axial coordinate and there is no dependence with the cross sectional coordinates.

The fully developed assumptions can be expressed mathematically by identifying the axial coordinate with z and the external magnetic field coordinate with y:

$$\vec{B} = B_0\hat{y} + B_{ind}(x,y)\hat{z} \tag{2.37}$$

$$\nabla p = Q\hat{z} \tag{2.38}$$

$$\vec{u} = U(x,y)\hat{z} \tag{2.39}$$

Using these approximations, the general set of 6 MHD equations (momentum and induction equations) with 6 variables, $u_i(t,x_j)$ and $B_i(t,x_j)$, expressed in the B-formulation can be reduced to a set of only two equations: a 2D momentum (2.40) and a 2D induction equation (2.41). These equations are written in terms of only two variables: the axial velocity $U(x,y)$ and the induced magnetic field $B_{ind}(x,y)$.

$$\eta\left(\partial_{xx}U + \partial_{yy}U\right) - Q + \frac{B_0}{\mu}\partial_y B_{ind} = 0 \tag{2.40}$$

$$\frac{1}{\mu}\left(\partial_x\left(\frac{1}{\sigma}\partial_x B_{ind}\right) + \partial_y\left(\frac{1}{\sigma}\partial_y B_{ind}\right)\right) + B_0\partial_y U = 0 \tag{2.41}$$

Similarly, the fully developed problem can be expressed in the ϕ-formulation as well:

$$\eta(\partial_{xx}U + \partial_{yy}U) - Q - \sigma B_0(\partial_x\phi - UB_0) = 0 \tag{2.42}$$

$$\partial_{xx}\phi + \partial_{yy}\phi + B_0\partial_x U = 0 \tag{2.43}$$

2.1.4 MHD quasi-2-dimensional approach

The Q2D description of the MHD problems is another possible simplification that can be very useful for fusion applications. It was firstly employed and developed in [53]. It is based in the ϕ-formulation which means that it is valid only for moderate Reynolds magnetic fields.

Q2D models describe flows in rectangular section channels with insulated walls where the magnetic field is transverse to the flow. In such flows, there is almost no dependence on the dimension parallel to the magnetic field. The only dependence is constrained to the thin Hartmann layers (see sec: 2.1.5). Moreover, under this approximation any component of the velocity field parallel to the magnetic field is strongly suppressed by the field.

Under the previous assumption, the Q2D equations are obtained by integrating the original set of 3D equations along the direction of the external magnetic field B_0. From this integration, a set of 2D equations are obtained for the two components of the velocity field ($u_{\perp i}$) which are perpendicular to external field (e.g. [54]):

$$\rho(\partial_t u_{\perp i} + u_{\perp j}\partial^j u_{\perp i}) = \partial_i p + \eta\partial_j\partial^j u_{\perp i} - \frac{u_{\perp i}}{\tau} \tag{2.44}$$

$$\partial^j u_{\perp j} = 0 \tag{2.45}$$

The Lorentz force appears in (2.44) as a source term that depends linearly with the velocity. This way, the electromagnetic equations and the flow equations

are decoupled from each other. This implies that only the fluid motion is needed to be computed. The proportionality constant is known as Hartmann braking time whose expression for the case with electrically insulated walls is written as follows [53]:

$$\tau = \frac{a^2}{Ha \cdot \eta} \tag{2.46}$$

Q2D models have been employed for studying the turbulence in liquid metal flows under transverse magnetic fields in different blankets applications [55–57]. They have been used also for treating magneto-convection effects as first approximation [58] which is the application employed in the present dissertation (sec: 5.7).

2.1.5 Analytic solutions of MHD flows

MHD equations constitute a non-linear system of coupled differential equations. The mathematical complexity of the system makes the MHD problems computationally expensive in time and resources. However, there are some analytic solutions of MHD flows which have important applications, including blanket technologies.

These solutions are found only in very specific geometries. One of them in particular, known as the Hunt flow [59] is of special relevance for code validation purposes. It consists on a fully developed flow in a rectangular section channel under a transverse magnetic field. The Side walls of the channels (parallel to the magnetic field) are perfectly insulated while the Hartmann walls (perpendicular to the magnetic field) have a finite conductivity (σ_w).

The general solution of this system is written in terms of dimensionless variables. The geometrical dimensions of the channel are normalized by the semi-length of the dimension parallel to the external magnetic field. Therefore, a channel with dimensions $2a \times 2b$ can be represented by the dimensionless variables: $\xi = x/a \in [-1, 1]$ and $\zeta = y/a \in [-b/a, b/a]$. The solution is expressed as a Fourier series with hyperbolic terms. Hyperbolic terms cannot be computed with precision for high Hartmann numbers. Fortunately, the solution has been reformulated in terms of exponentials functions [60] which

are easier to handle in a computer:

$$U = \sum_{k=0}^{\infty} \frac{2(-1)^k \cos(\alpha_k \xi)}{\frac{b}{a}\alpha_k^3}(1 - V_2 - V_3) \tag{2.47}$$

The coefficients that appear in (2.47) are:

$$V_2 = \frac{\left(C_w \cdot r_{2k} + \frac{1-exp(-2r_{2k})}{1+exp(-2r_{2k})}\right) \frac{\exp(-r_{1k}(1-\zeta))+\exp(-r_{1k}(1+\zeta))}{2}}{\frac{1+\exp(-2r_{1k}}{2} C_w \cdot N + \frac{1+\exp(-2(r_{1k}+r_{2k})}{1+\exp(-2r_{2k}}} \tag{2.48}$$

$$V_3 = \frac{\left(C_w \cdot r_{1k} + \frac{1-exp(-2r_{1k})}{1+exp(-2r_{1k})}\right) \frac{\exp(-r_{2k}(1-\zeta))+\exp(-r_{2k}(1+\zeta))}{2}}{\frac{1+\exp(-2r_2}{2} C_w \cdot N + \frac{1+\exp(-2(r_{1k}+r_{2k})}{1+\exp(-2r_{21k}}} \tag{2.49}$$

$$N = \sqrt{Ha^2 + 4\alpha_k^2} \tag{2.50}$$

$$r_{1k}, r_{2k} = \frac{1}{2}(N \pm Ha) \tag{2.51}$$

$$\alpha_k = \left(k + \frac{1}{2}\right)\frac{b\pi}{a} \tag{2.52}$$

The coefficient C_w is the wall conductance ratio and it is defined as follows:

$$C_w = \frac{\sigma_w t_w}{\sigma_l a} \tag{2.53}$$

Where σ_w and σ_l are the electrical conductivities of the Hartmann wall and the liquid metal, respectively and t_w is the thickness of the Hartmann wall.

Considering first the particular case with $C_w = 0$. It corresponds to a channel with perfectly insulated walls. This flow was firstly studied by Shercliff in 1953 [61] who derived the following correlation for the pressure drop of such channels:

$$\partial_z p[\frac{Pa}{m}] = \frac{\eta \cdot Ha \cdot U_0}{a^2\left(1 - 0.852\frac{a}{b\sqrt{Ha}} - \frac{1}{Ha}\right)} \tag{2.54}$$

Shercliff flow is characterized by having flat profile in most of the domain, called core flow. The velocity goes to zero rapidly next to the walls forming BLs. Fig: 2.3 shows a Shercliff flow computed with the simulation platform ANSYS-Fluent (sec: 5.1.2) using a fully developed approximation. The shape of this kind

of flows can be observed.

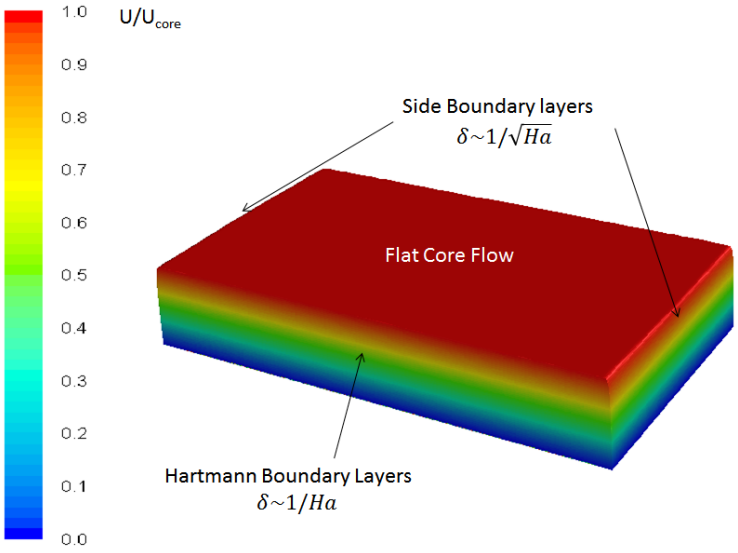

Figure 2.3: Shercliff flow computed with Fluent.

When Hartmann walls have no perfect insulation ($C_w \neq 0$), the solution (2.47) present a considerable different shape. In this case, the induced currents penetrate in the walls (fig: 2.4) which completely changes the intensity of the Lorentz force in the Side BLs. Moreover, the density of induced currents in the core are higher for conducting walls which produces stronger Lorentz forces in the core flow.

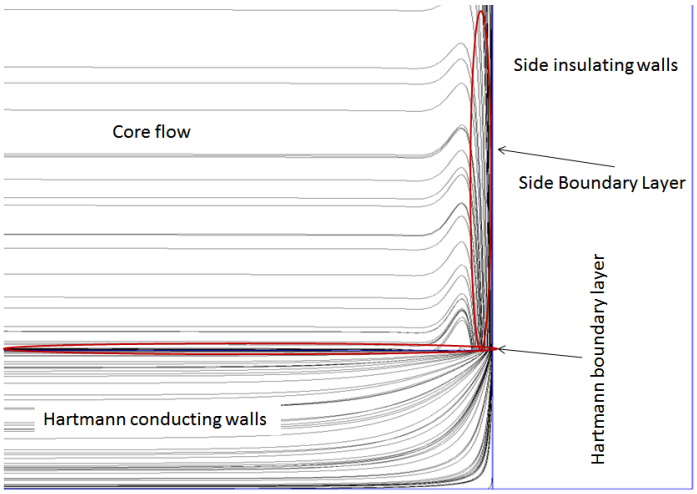

Figure 2.4: Electrical currents induced in the Hunt flow next to a corner.

The result of this flow is again a flat core in most of the channel section. The thin Hartmann layers are similar than in the Shercliff flow. On the contrary, the Side BLs develops two jets where the velocity takes values orders of magnitude higher than the core flow. Fig: 2.5 shows the computed flow of a channel with moderate conducting wall ($C_w = 0.05$) and high Hartmann number ($Ha \sim 7 \cdot 10^3$).

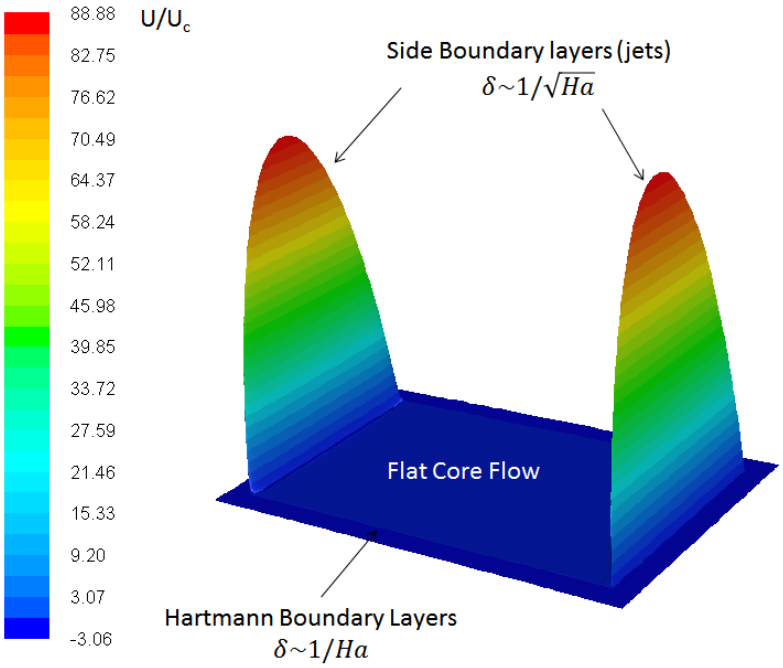

Figure 2.5: Hunt flow computed with Fluent.

The wall conductance ratio has a capital importance on the pressure drop, especially in the more realistic case of a channel with the same conductivity in all walls. Indeed, according with [62], the pressure drop of a rectangular duct with arbitrary conducting walls follows the next correlation:

$$\partial_z p[\frac{Pa}{m}] \sim B_0^2 U_0 \sigma \frac{C_w}{1 + \frac{a}{3b} + C_w} \tag{2.55}$$

Fig: 2.6 shows the dependence of the pressure drop with the C_w in a square section channel. Pressure drop mitigation techniques in breeding blankets are based in electrically decoupling the PbLi from the structure as efficiently as possible (left part of the graph). FCI or ceramic coatings are placed in between the liquid metal and the walls with this purpose.

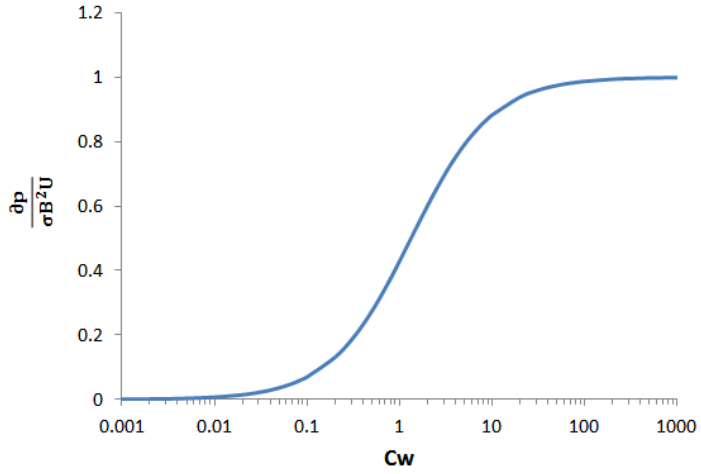

Figure 2.6: Pressure drop as a function of the wall conductance ratio in a square section channel.

2.2 Heat transfer in liquid metal flows

Heat transfer phenomena have a capital importance in the balance of plant of future fusion power stations. The BB is the system in charge of extracting the power out from the reactor. Consequently, accurate predictions of heat transfer in liquid metal are necessary for designing PbLi-based concepts. This is particularly important for the DCLL concept as the liquid metal is the primary coolant of the system.

2.2.1 Differential description of heat transfer

Heat transfer phenomena can be derived from the energy conservation equations (e.g. [63]). Indeed, the energy of any control volume of the system must be conserved. In the limit of an infinitely small volume, the differential description of the energy transfer phenomenon is obtained. Analogous to the mass conservation equation (continuity equation (2.1)) the energy conservation can be written as follows:

$$\partial_t(\epsilon) + \partial_j q^j = \sum_k S_{q_k} \tag{2.56}$$

Where ϵ is the internal energy, q is the heat flux density (W/m^2) and S_{q_k} are the energy sources and sinks that may be present in the system. Inside a fluid the heat flux has 2 different terms: The conduction term which is described by the Fourier law (2.57) [64] and the advection term (2.58) which is analogous to the mass flux in (2.1) and represents the dragging of the fluid:

$$q_{ci} = -\kappa \partial_i T \tag{2.57}$$

$$q_{ai} = u_i \epsilon \tag{2.58}$$

Where κ is the thermal conductivity. The mass equivalence to heat transfer by conduction is the diffusion process which is discussed in detail in sec: 3.1.

Introducing the concept of specific heat capacity ($d\epsilon = \rho c_p dT$), the energy conservation equation can be written in terms of only temperature. Assuming a constant heat specific capacity and using the mass conservation equation (2.1) the temperature equation takes the following form:

$$\rho \cdot C_p(\partial_t T + u_j \partial^j T) - \partial_j(\kappa \partial^j T) = \sum_k S_{q_k} \tag{2.59}$$

Equation (2.59) with $S_q = 0$ is valid for an incompressible fluid under the inviscid approximation and with no internal or external heat sources (chemical reactions, electric currents...).

When the fluid is viscous and admits the Newtonian relation of the stress tensor (2.7), there is some energy dissipation that comes from the friction of the fluid with itself. This work can be expressed as the divergence of the vector field times the stress tensor which is usually called viscous dissipation function Φ [50]:

$$\Phi := \partial_j(u_i \tau^{ij}) = \partial_j u_i \partial^i u^j = (\partial_j u_i)(\partial^i u^j) \tag{2.60}$$

When a magnetic field is applied to a conducting flow, there is some energy gain due to the Joule heating which is expressed in terms of j^2/σ. This term constitute a coupling between the electromagnetic equations and the heat transfer equations which can complicate considerable heat transfer computations. Nevertheless, in BB applications there is a huge heat generation source created by the interacting neutrons and photons. Both, the Ohmic gain

and the viscous dissipation can be neglected in comparison with this source.

The heat deposited by the photons and neutrons is calculated using *Monte Carlo* computations. Neutronics analyses of the DCLL [65, 66] show that the heat generation term can be approximated with an exponential function along the radial direction (r) of the tokamak:

$$S_n = p \exp(-b \cdot r + \omega) \tag{2.61}$$

The parameters p, b and ω are obtained as a best fitting of the neutronic computations.

Finally, the heat transfer differential equation is obtained (2.62). This equation is valid for incompressible, Newtonian fluids under strong magnetic field and strong neutron flux (PbLi-based BB concepts under fusion conditions).

$$\rho \cdot c_p(\partial_t T + u_j \partial^j T) - \partial_j(\kappa \partial^j T) - p \exp(-b \cdot r + \omega) = 0 \tag{2.62}$$

For constant thermal conductivity it is possible to rewrite (2.62) in terms of dimensionless variables:

$$Re \cdot Pr(\partial_t \hat{T} + \hat{u}_j \partial^j \hat{T}) - \partial_j \partial^j \hat{T} - \hat{p} \exp(-\hat{b} \cdot \hat{r} + \hat{\omega}) = 0 \tag{2.63}$$

Where $Pr := c_p \eta / \kappa$ is known as the Prandtl number and it represents the ratio between the diffusion of momentum and the thermal diffusion in the fluid. The product between the Reynolds number and the Prandtl number is known as Peclet number which represents the ratio between the advective heat transport rate and the diffusive heat transport rate. In most of liquid metals, the heat transport is much more effective than the momentum transport which implies low Prandtl numbers. The Peclet number depends on the velocity of Pbli. Therefore, it takes small values for low velocity concepts (10^1) and moderate values for high velocity concepts (10^2).

2.2.2 Magneto-convection phenomena

The previous section describes the coupling between the heat transfer and the fluid equations. Indirectly, this implies a relation between MHD forces and heat transport. According with the description performed so far, the coupling affects only in one direction as the temperature field does not affect the flow dynamics. However, this scenario changes when gravity forces are introduced in the MHD fluid equation:

$$\rho(\partial_t u_i + u^j \partial_j u_i) = \eta \partial_j \partial^j u_i - \partial_i p + \frac{1}{\mu}\left(-\frac{1}{2}\partial_i B_j B^j + B^j \partial_j B_i\right) - \rho g \delta_{iz} \quad (2.64)$$

Where g is the gravity acceleration that points in the z direction. The density of the fluid depends on the temperature, which means that gravity forces will have different intensity in cold regions and hot regions. This process is known as buoyancy.

It is common and valid for a wide variety of fluids (including PbLi) to approximate the density function to a first order Taylor polynomial around the average temperature of the system T_0:

$$\rho(T) \simeq \rho(T_0) + \frac{\partial \rho}{\partial T}|_{T=T_0}(T - T_0) := \rho_0 \left(1 - \beta(T - T_0)\right) \quad (2.65)$$

Where β is the thermal expansion coefficient of the PbLi.

Boussinesq approximation consists of expanding the density function up to zero order for the inertial terms and up to first order only in the gravity term. This approximation is valid in BB applications since the high interaction parameter implies little influence of inertial effects. Consequently, the momentum conservation equation including coupling with the induced magnetic field and with the thermal field is written as follows:

$$\rho_0(\partial_t u_i + u^j \partial_j u_i) = \\ \eta \partial_j \partial^j u_i - \partial_i p_d + \frac{1}{\mu}\left(-\frac{1}{2}\partial_i B_j B^j + B^j \partial_j B_i\right) + \rho_0 \beta (T - T_0)) g \delta_{iz} \quad (2.66)$$

Note that the pressure gradient absorbs the constant term $\rho_0 g$. This term does not change the behavior of the system as it only changes the origin of

pressures. The redefined pressure is known as dynamic pressure and it is defined as: $p_d := p - \rho_0 g z$.

Similarly to the rest of differential equations, it is convenient to rewrite (2.66) in terms of dimensionless numbers. The temperature increment can be normalized by the characteristic temperature difference of the system (ΔT_0).

$$\frac{1}{N}(\partial_t \hat{u}_i + \hat{u}^j \partial_j \hat{u}_i) = \frac{1}{Ha^2}\partial_j \partial^j \hat{u}_i - \partial_i \hat{p} + \frac{1}{Rm}\left(-\frac{1}{2}\partial_i \hat{B}_j \hat{B}^j + \hat{B}^j \partial_j \hat{B}_i\right) - \frac{Gr}{Ha^2 Re}\Delta\hat{T} \quad (2.67)$$

Where $Gr := \frac{g\beta\Delta T_0 L^3 \rho_0^2}{\eta^2}$ is the Grashof number which represents the ratio between the buoyancy forces and the viscous forces. The definition of Grashof number comes from regular convection problems. However, when describing magneto-convection as in (2.67) the gravity terms is also compared with the Lorentz forces. Consequently, the number that defines the scale relations between the magneto-convection forces and the other effects is a combination of three numbers:

$$\frac{Gr}{Ha^2 Re} = \frac{GrN}{Ha^4} = \frac{buoyancy \times viscous}{Lorentz \times inertia} \quad (2.68)$$

Chapter 3

Theoretical framework for tritium transport

In this chapter, the theoretical description of tritium transport phenomena is exposed. The differential equations that rule the tritium behavior in the bulk of the materials and in the interfaces between different domains are derived. Thereafter, a description of the BL approximation is given. Lastly, steady-state analytic solutions of 2 simple geometries are presented as they are used for the validation of tritium transport codes in chap: 6.

3.1 Tritium permeation

As mentioned in sec: 1.3, hydrogen isotopes are small atoms that can permeate through solids and liquid systems. From the microscopic perspective, hydrogenic atoms can travel through the voids of the solid crystalline structures or travel diluted in the fluid systems. From the macroscopic perspective, permeation is a process that affect the evolution of the concentration scalar field subjected to the laws of mass conservation (continuity). This picture is valid when the amount of solute is much smaller than the amount of solvent (stationary medium approximation [67]). The previous perspective is used for tritium transport models in blanket applications. The concentration scalar field is mainly affected by two different phenomena, the diffusion/advection processes in the bulk of the material

(either fluid or solid) and the surface processes in the material interfaces.

3.1.1 Diffusion/advection phenomena

In a similar way that the mass of fluid, the momentum and the energy are conserved in any control volume, the mass of tritium diluted in a material has to be conserved as well. The concentration scalar field $c(t, x_i)$, which represents the amount of moles of tritium atoms per unit volume, is subjected to analogous differential equations to (2.1) and (2.56). Therefore, using the same arguments employed in sec: 2.1.1 it is possible to write the following mass conservation equation:

$$\partial_t c + \partial^j (u_j c) + \partial_j J^j = S_c \tag{3.1}$$

Where $u_i(t, x_j)$ is the velocity of the fluid and $J_i(t, x_j)$ is defined as the diffusion flux of atoms measured in $mol/m^2 s$. The second term of (3.1) is recognizable as an advection term, in other words, the dragging effect that the flow applies on the scalar field. The diffusion flux J is the analogous to the heat conducting flux q defined in sec: 2.2.1. Indeed, mass diffusion is an analogous effect to conduction. In the same way that there is a net heat flux from the hot parts of the system to the cold ones, there is a net flux of mass from the regions of higher concentration to the regions of lower concentrations.

Both phenomena, conduction and diffusion, have their origin in the stochastic movement of particles inside the materials. The macroscopic consequences of this movement are represented by the Fourier law (2.57) and the so called Fick law [68], which is written as follows:

$$J_i = -D\partial_i c \tag{3.2}$$

Where D is the diffusivity constant of the material which is analogous to the thermal conductivity κ. An extensive theoretical discussion of the diffusion process in several geometries and conditions can be found in [69].

For BB applications, the lithium present in the breeder constitutes a volumetric source of tritium. The interaction of neutrons with lithium atoms produces tritium and energy (or heat). Consequently, the shape of the

volumetric heat generation function (2.63) is very similar to the tritium generation function:

$$S_c = p_c exp(-br + \omega) \tag{3.3}$$

The parameters p_c, b and ω are obtained from the neutronic computations (e.g. [65] for the DCLL). r is the radial coordinate of the torus. It is worth mentioning that the exponential factor b and ω are approximately equal than those in (2.57).

Finally, the differential equation that governs the evolution of the tritium concentration field can be written as follows:

$$\partial_t c + u_j \partial^j c - \partial_j (D \partial^j c) - p_c \exp(-br + \hat{\omega}) = 0 \tag{3.4}$$

$$Re \cdot Sc(\partial_t \hat{c} + \hat{u}_j \partial^j \hat{c}) - \partial_j \partial^j \hat{c} - \hat{p}_c \exp(-\hat{b}\hat{r} + \hat{\omega}) = 0 \tag{3.5}$$

The variables of equation (3.5) are normalized in terms of the characteristic velocity (u_0), length (L) and concentration (c_0). When the diffusivity constant does not depend on the spatial coordinates, a new dimensionless number appears in 3.5. The so called Schmidt number is defined as: $Sc := \eta/\rho D$. This number represents the ratio between the momentum flow and the mass diffusion. The Schmidt number is equivalent to the Prandtl number in heat transfer problems.

Equation (3.4) is also valid for computing the evolution of the concentration field along solid materials. Inside these materials there is not generation of tritium via transmutation ($S_c = 0$). Moreover, the velocity scalar field is also null ($u_j = 0$) as the solid is not flowing by definition. Consequently, the tritium mass conservation equation in solids is simply written as follows:

$$\partial_t c - \partial_j (D \partial^j c) = 0 \tag{3.6}$$

It is important to recall that there is not an analogous mass transfer effect to buoyancy. In other words, the velocity field and everything that may affect it (MHD, convection...) affects the evolution of the concentration scalar field but not the other way around. The concentration scalar field does not impact on the evolution of the flow. From a computational point of view this means that the tritium transport simulations can be treated with independence of the flow

dynamics computations.

Equation (3.4) gives a macroscopic description of complex and random interactions at atomic and molecular level. This description has limitations and it should not be considered complete in every scenario. There are some physical phenomena that can importantly affect to tritium evolution in certain conditions but are not included in (3.4). Examples of these effects are: the trapping of hydrogenic atoms in the solid lattice [70], the solvant saturation, the Soret effect (thermodiffusion) [71] or the tritium decay losses. Modifications and additions of the original equations can be performed for including these effects.

3.1.2 Surface phenomena

Besides the diffusion and advection processes which are present in the bulk of the materials, there are other phenomena that take place in the surfaces and interfaces between materials. These can affect significantly or even dominate tritium dynamics.

The chemical form of the dissolved gas at both sides of the interface determines the way it moves across the surfaces. Tritium is present in atomic form (T) when dissolved in metals both solid (EUROFER) and liquid (PbLi). On the contrary, it is present in molecular form (T_2 or HT) when is solved in a gas. When tritium is present in water (gas or liquid) it is dissolved in form of T_2 and HT but it also form tritiated water molecules (HTO and T_2O) that are part of the solvent.

When a molecule does not experiment chemical processes of recombination and dissociation at the surface, Henry's law applies (3.7) [72]. This law generally applies to gaseous/liquid interfaces. It relates the concentration of the gas in the surface of the liquid with the partial pressure of the species in the gaseous side.

$$c = K_h p \tag{3.7}$$

Where K_h is known as the Henry constant.

Interfaces gas/liquid in which no chemical processes takes place are not

present in blankets. Consequently, Henry's law is not usually applied to BB tritium transport modeling.

On the contrary, interfaces gas/metal are of great interest for BB applications. In fact, these interfaces are present in every blanket concepts which are cooled using helium flows. In these interfaces, chemical processes of dissociation and recombination take place catalyzed by the surface. For a molecule (Q_2)[1] enters the solid, it first has to dissociate into its atoms. The opposite process is also true, before an atom (Q) leaves the solid it has to recombine with other of its kind to form a molecule (either homonuclear or heteronuclear).

The molecular flux of homonuclear molecules Q_2 from the gas to the solid (via dissociation) is proportional to the partial pressure of the molecules (p_{Q_2}) in the gas. The molecular flux in the opposite direction is proportional to the probability of an atom to find a partner in the surface: $c_Q(c_Q - 1\frac{atom}{m^3}) \simeq c_Q^2$. Consequently, the net molecular flux of Q_2 molecules across the surface is defined as follows:

$$J_{Q_2} = \frac{1}{2} J_Q = \sigma K_d p_{Q_2} - \sigma K_r c_Q^2 \tag{3.8}$$

Due to mass conservation, the molecular flux J_{Q_2} is half the atomic flux J_Q. In (3.8), K_d is the dissociation coefficient and K_r is the recombination coefficient. Both constant are intrinsic properties of the solid material. A theoretical expression of the recombination coefficient in metals is given in [73] in terms of the microscopic properties of the solid. σ is the sticking coefficient that represents the effect of the surface geometry (roughness). Experimental measurements provide values for σK_d and σK_r which can be used directly in tritium transport models.

It is of interest considering the case in which recombination and dissociation process balance and the interface reaches the thermodynamic equilibrium. In these conditions, the net molecular flux is null. Thus, the partial pressure of the gas at one side of the interface is related with the concentration of the surface using the following expression:

[1] Q refers to any hydrogen isotope: H, D or T.

$$c_Q = \sqrt{\frac{K_d p_{Q_2}}{K_r}} = K_s \sqrt{p_{Q_2}} \tag{3.9}$$

Where the constant K_s is known as the solubility constant or Sievert constant. The equation (3.9) is known as Sieverts' law. The solubility of a metal measures the amount of gas that the solid absorbs for a given external pressure. Another property which is often found in literature is the permeability (Φ). This constant is defined as the product of the diffusivity and the solubility (3.10). Experimentally, the permeability of a solid can be measured directly with membrane experiments (e.g. [74]) while the solubility is an indirect measurement.

$$\Phi \equiv K_s D \tag{3.10}$$

Whether the surface of a gas/metal interface is in equilibrium depends on the material properties and the value of the concentration at the surface. A dimensionless number called permeation number (W) [75] can be defined as the ratio between surface processes and diffusion processes (3.11). This parameter is useful for identifying the permeation regime of a solid in contact with a gas.

$$W := L c_0 \frac{\sigma K_r}{D} = L \frac{\sigma K_d}{\Phi} \sqrt{p_0} \tag{3.11}$$

Where L is the characteristic permeation length of the system (the thickness of the solid along the diffusion direction), p_0 is the partial pressure in the gas phase and c_0 is the concentration at the solid surface. Three different permeation regimes can be classified according to the values of this number:

- For $W >> 1$, it is said that the system is in *diffusion limited regime*. The dynamic of the surface processes are much faster than the diffusion in the bulk. This way, the interface can be considered at thermodynamic equilibrium at any time. It reacts almost instantaneously in comparison with the reaction time of the bulk. In this conditions Sieverts' law (3.9) can be directly applied in the gas/metal interface.
- For $W << 1$, it is said that the system is in *surface limited regime*. The interface is not at equilibrium and Sieverts' law is not valid. The surface processes are much slower than the diffusion in the solid bulk. It can be

considered that the atomic species crosses through the solid instantaneously (flat concentration profile). Equation (3.8) has to applied at the interface and the diffusion in the bulk can be ignored.

- For $W \sim 1$, the system is in the *intermediate regime*. Diffusion processes and surface processes have comparable time scales. Therefore, the interface is not at equilibrium and (3.8) has to be applied together with the mass conservation in the bulk of the solid (3.1).

An example of the different permeation regimes and the influence of the permeation number is shown in sec: 3.2.

In metal/metal interfaces (PbLi/steel for example) where tritium is in atomic form at both sides, there are no recombination or dissociation processes. The partial pressure associated to the concentration can be defined using Sieverts' law (3.9). It is important noting that this pressure is not the partial pressure of tritium outside the material (there is no gas phase outside) but it is a measure of the tendency of the solved gas to go across the interface. This partial pressure balances at both sides of the interface. In this kind of interfaces it is assumed that the balance of pressure at both sides is a very fast process which means that the pressure can be considered equal at both sides of the interface at any time. This introduces the following discontinuity in the concentration field:

$$\frac{c_1}{K_{s1}} = \frac{c_2}{K_{s2}} \tag{3.12}$$

Where each sub-index represents each side of the interface.

On the contrary, the flow is a continuous function as it is required by mass conservation:

$$-D_1 \partial_i c_1 = -D_2 \partial_i c_2 \tag{3.13}$$

The discontinuity of the concentration scalar field is one of the most notorious differences between mass transfer and heat transfer (the temperature is a continuous function).

Fig: 3.1 shows a diagram that collects every basic effect that affects the tritium transport inside the DCLL blanket. Tritium is generated via

transmutation in the PbLi (right side), then some is dragged by the PbLi and the rest sticks to the surface and permeates across the structural materials (center) by diffusion. When reaching the interface steel/helium dissociation and recombination processes takes place. The net flux at the surface makes that some T_2 molecules enter in the helium flow where the gas (left side) drags it by advection.

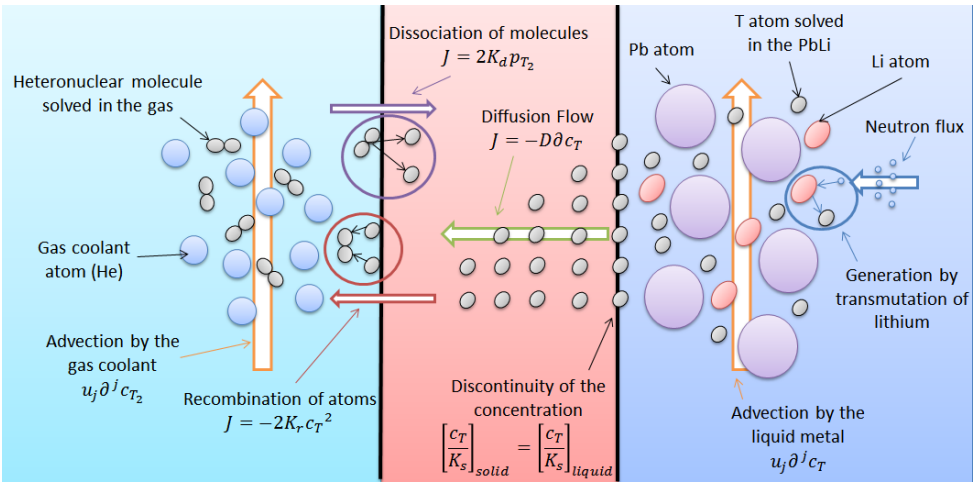

Figure 3.1: Scheme of the basic processes that affects tritium transport in the DCLL. The gas domain is colored in light blue, the solid domain is colored in red and the liquid metal domain is colored in dark blue.

3.1.3 Isotopic effects

In the last two sections, the basic phenomena that affect tritium evolution in the DCLL blanket are described. These are the effects that have been taken into account when developing the initial tritium transport models at system and component level for the DCLL blanket (chap: 4).

Despite the DCLL baseline design does not include the presence of any other hydrogen isotope rather than tritium in the systems, a discussion about the different isotopic effects that affects tritium transport is considered necessary. The reason is that adding hydrogen to the coolant (helium or water) is under consideration for every blanket concept.

The main isotopic effects affecting tritium transport in BB are the following:

1. Hydrogen isotopes have different masses which can affect the value of their transport properties. Indeed, these isotopes will have different diffusivity constants as the different masses offer different resistance to the diffusion random movement. There is a classical relation between the diffusivity and the inverse square root of the isotope mass ($D \sim m^{-0.5}$) [76]. Recombination and dissociation coefficients at the interface also exhibit this classical dependence [73] as well. It is worth mentioning that the isotopic difference in the diffusivity is not always confirmed by experiments (e.g. in PbLi [77]).

2. Hydrogen isotopes and other molecules chemically react spontaneously. The reactions can take place in the gas/solid interfaces or in the bulk of the coolant. In the case of the interface, the effect over the permeation rate is notorious. Indeed, permeation can be enhanced or mitigated via the formation of heteronuclear molecules (HT). These phenomena are known as co-permeation [78] and counter-permeation [79] depending on the diffusion direction of both kind of isotopes.

3.1.3.1 Isotopic reactions

When hydrogen is present in the coolant, recombination and dissociation processes of HT, T_2 and H_2 molecules take place at the interface (e.g. [80]). The molecular flux of each specie follows a very similar equation than (3.8). The only difference is the recombination term of the HT flux. In this case, the probability of a H atom to find a T atom has to be added to the probability of a T atom to find a H atom ($2c_T c_H$). Therefore, molecular fluxes in these interfaces can be written as follows:

$$J_{H_2} = \sigma K_d p_{H_2} - \sigma K_r c_H^2 \tag{3.14}$$

$$J_{HT} = \sigma K_d p_{HT} - 2\sigma K_r c_H c_T \tag{3.15}$$

$$J_{T_2} = \sigma K_d p_{T_2} - \sigma K_r c_T^2 \tag{3.16}$$

The atomic flows at the solid side of the interface are deduced from the conservation of matter:

$$J_H = 2J_{H_2} + J_{HT} \tag{3.17}$$

$$J_T = 2J_{T_2} + J_{HT} \tag{3.18}$$

Due to chemical reactions of HT recombination, the tritium permeation flux can be importantly increased when there is hydrogen in the coolant (e.g. [37]).

Isotopic exchange reactions in the bulk of the coolant can change the molecular form in which the tritium inventory is present in this medium. The most representative and illustrative example is the tritiated water formation:

$$H_2O + HT \longleftrightarrow HTO + H_2 \tag{3.19}$$

Reaction (3.19) could be very relevant if it were decided to add some water in the helium as it was proposed for the HCPB (e.g. [81]). In any case, it is of extreme importance for the WCLL blanket concept as it is deduced by the transport models dedicated to this blanket (e.g. [37, 82]).

Isotopic exchange reactions can be treated using chemical kinetics equations (e.g. [83]). Therefore, the reaction rate of HTO formation and HT destruction (ζ) is written in terms of the kinetic constants (k_1 and k_2) and the concentration of the different species:

$$\zeta_{HTO} = -k_1 c_{HTO} c_{H_2} + k_2 c_{H_2O} c_{HT} \tag{3.20}$$

$$\zeta_{HT} = k_1 c_{HTO} c_{H_2} - k_2 c_{H_2O} c_{HT} \tag{3.21}$$

3.1.4 Boundary layer approximation

In sec: 3.1.1 and 3.1.2, the complete differential formulation of mass transport in solid and liquid media is presented. However, it is very common in literature and convenient under several circumstances describing the mass transfer problem in terms of the mass transfer coefficient (e.g. [84, 85]).

This description is based on the BL approximation. BL refers to the fluid region close to a solid interface where the viscosity forces are dominant and the velocity is small ($u_i \to 0$). BL grows in thickness after the entrance of the fluid into a pipe or a channel until the flow is fully developed.

When no generation is considered, the steady state equation in the thin BL ($u_i \simeq 0$) is simple:

$$\partial_i J^i \simeq 0 \quad \Rightarrow \quad \partial_i \partial^i c \simeq 0 \tag{3.22}$$

The dependence of the concentration with coordinate normal to the wall follows a linear profile close to the interface as shown schematically in fig: 3.2.

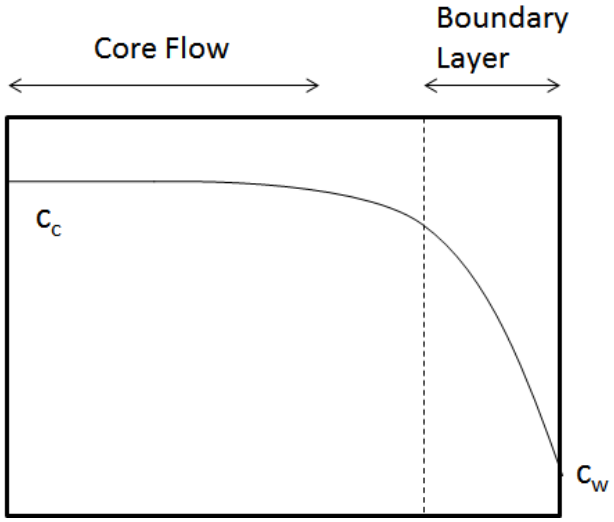

Figure 3.2: Sketch of the tritium concentration next to the BL.

The permeation flux normal to the surface (J_n) is proportional to the difference between the core concentration (c_c) and the wall concentration (c_w).

$$J_n = K_t(c_c - c_w) \tag{3.23}$$

The previous equation is sometimes classified as a convective boundary condition whose thermal analogy (based on heat transfer coefficient h_t) is extensively used in thermohydraulics computations. K_t is the mass transfer coefficient and has units of (m/s). This coefficient depends mainly on the velocity profile. Therefore, it is influenced by the viscosity, the flow regime and the magnetic field (if any).

If the flow were completely stagnant in the BL, the permeation would be only affected by diffusion. Thus, the mass transfer coefficient would be equal to D/δ, being δ the thickness of the BL. The more dominant is advection in comparison

with diffusion in the BL, the more K_t differs from this value. The ratio between advection and diffusion is represented by the Sherwood dimensionless number:

$$Sh := \frac{K_t L}{D} \tag{3.24}$$

Where L is the characteristic diffusion length in the system. When $Sh \to 1$ the transport is dominated by diffusion while when $Sh >> 1$ the transport is dominated by advection. The Sherwood number is analogous to the Nusselt number (Nu) in heat transfer problems.

3.2 Analytic solutions

In this section the steady state transport equation (3.1) is solved analytically for 2 simple 1D geometries in a solid domain. The purpose is showing simple examples of the surface processes presented in sec: 3.1.2 that help understanding the physics involved in the more complex tritium transport models of subsequent chapters. Moreover, these analytic solutions are used for validating the 3D tritium transport code used in sec: 6.1.

3.2.1 Interface between two solid materials

The first system is chosen in order to analyze the interface between two different domains without recombination or dissociation (3.12). For this purpose, a system formed by two solids with different properties is presented (fig: 3.3). Under these simple conditions, the system is essentially 1 dimensional. Arbitrarily, the properties of EUROFER at different temperatures have been taken [74].

Dirichlet conditions are imposed at both sides of the material. It is worth noting that imposing constant concentration at both sides is equivalent to impose diffusion limited regime.

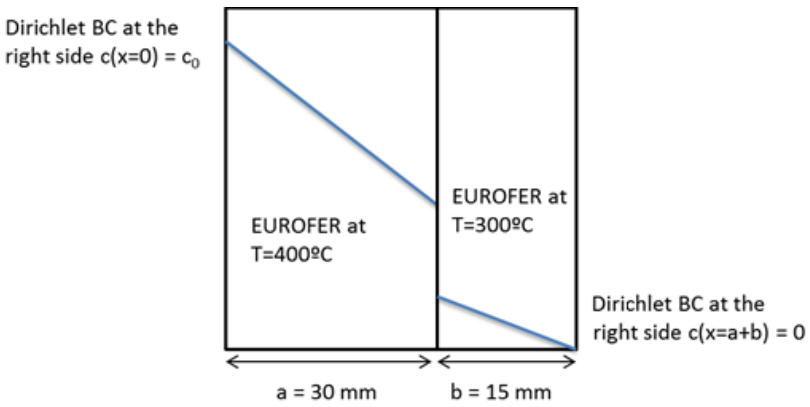

Figure 3.3: Configuration of the first tritium transport analytic example

The general steady state solution of the continuity equation at both sides of the interface is trivial:

$$c_i(x) = A_i x + B_i \quad i = 1, 2 \tag{3.25}$$

Where the sub-index represent the two solids of the system. A_i and B_i are integration constants. From the Dirichlet boundary conditions at the left and right side, 2 constrains on the integration constants are obtained:

$$B_1 = c_0 \tag{3.26}$$

$$B_2 = -A_2(a + b) \tag{3.27}$$

The other two constrains are obtained when imposing the concentration discontinuity (3.12) and the flux continuity (3.13) in the interface between both solids (x=a):

$$\frac{A_1 a + c_0}{K_{s_1}} = -\frac{A_2 b}{K_{s_2}} \tag{3.28}$$

$$D_1 A_1 = D_2 A_2 \tag{3.29}$$

The previous system of algebraic equations has the following solution:

$$\frac{c_1(x)}{c_0} = 1 - \frac{x}{a + b\frac{\Phi_1}{\Phi_2}} \tag{3.30}$$

$$\frac{c_2(x)}{c_0} = \frac{a + b - x}{a\frac{D_2}{D_1} + b\frac{K_{s_1}}{K_{s_2}}} \tag{3.31}$$

The solution is depicted in fig: 3.4. The discontinuity in the concentration can be clearly observed.

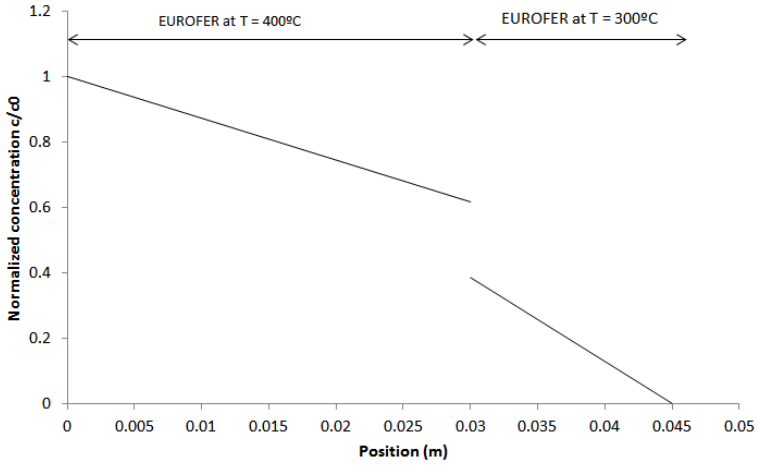

Figure 3.4: Analytic solution of the first tritium transport analytic example.

3.2.2 Recombination boundary conditions

The second system to be studied consists on a 1D material in which two different kind of boundary conditions are imposed in the two sides: Dirichlet condition in the left side and Neumann condition in the right side. The Neumann condition imposed is (3.8) with $p_{Q_2} = 0$ (vacuum). The system configuration is exposed in fig: 3.5

The general steady state solution of this system is also (3.25) (with i=1). The difference between both examples is only the expression of the integration constants. Indeed, every concentration profile in an isothermal solid is linear after reaching the steady state. The integration constants are obtained by imposing the boundary conditions:

$$B = c_0 \tag{3.32}$$

$$-D(\partial_x c)(x=a) = 2\sigma K_r c(x=a)^2 \quad \Rightarrow \tag{3.33}$$

$$-D \cdot A = 2\sigma K_r (A \cdot a + c_0)^2$$

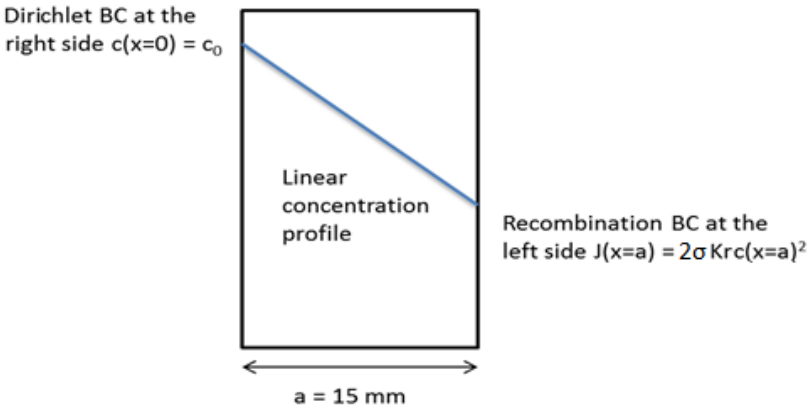

Figure 3.5: Configuration of the second tritium transport analytic example.

After some algebra (3.33) can be solved and the slope of the concentration profile (which is proportional to the diffusion flux) is obtained:

$$A = \frac{-D}{4a^2\sigma K_r}\left(1 + 4ac_0\frac{\sigma K_r}{D} - \sqrt{1 + 8ac_0\frac{\sigma K_r}{D}}\right) \tag{3.34}$$

It is wort noting that the permeation number (3.11) appears in the solution. When $W >> 1$, then $A \sim c_0/a$ which is equivalent to impose the boundary condition: $c(a) = 0$. The system is therefore in the diffusion limited regime. In the other limit case when $W << 1$ the system is in the surface limited regime, A tends to zero and the concentration profile tends to be flat ($c(x) \sim c_0$). The permeation flux of the surface limited regime can be obtained by expanding A around $c_0 = 0$ up to the first not zero term. In this case the permeation flux is given only by the boundary condition in the surface:

$$A(c_0) \approx A(0) + \partial_c A(0)c_0 + \frac{1}{2}\partial_{cc}A(0)c_0^2 = \frac{1}{2}\partial_{cc}A(0)c_0^2 = \frac{2\sigma K_r c_0^2}{D} \tag{3.35}$$

Three different concentrations in the right side of the solid have been considered. This way, diffusion limited, surface limited and intermediate

regime are presented in fig: 3.6. Arbitrarily, EURFOER properties at 400°C have been used in this example [74].

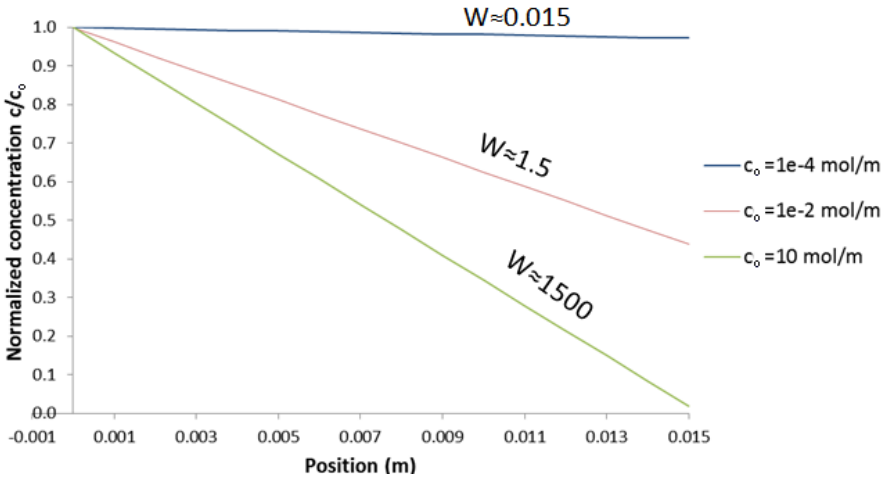

Figure 3.6: Analytic solution of the second tritium transport analytic example.

Chapter 4

Initial system level model of the DCLL blanket

In this chapter, the system modeling strategy employed for the DCLL tritium transport models is presented. In the first section, the main codes used in the past for tritium transport modeling in BB are discussed. Thereafter, the object oriented modeling platform EcosimPro, which has been used for the system level models presented in this dissertation, is introduced. The component level models developed for the EcosimPro tritium transport libraries are explained in detail. The initial tritium transport model of the DCLL blanket at system level is presented next. The input data used, the PFDs developed for the model and the results are exposed. Finally, the assumptions made and the identified uncertainties are discussed.

4.1 Previous codes and algorithms

Tritium transport models have being used for the development of BB concepts since the early stages of blanket projects. As explained in the introductory chapters (sec: 1.3), most of the past models follows the system level approach. This is the case of the KATRIM code [86] and the Fusion Tritium Permeation Code (FUS-TPC) (e.g. [87, 88]). Both codes were developed in Germany for the European fusion programs.

For computing the global behavior of tritium inside the blanket, codes like KATRIM and FUS-TPC considers only global design parameters of the blanket, such as the total mass of the breeder, the total mass of coolant, the contact surface, etc. These codes provide useful information for a first evaluation of a blanket concept but they are limited in accuracy due to their simplicity. For example, they cannot distinguish between different regions of the blanket which can have very different temperatures and consequently very different transport properties.

The mentioned codes use PFD for connecting the blankets and the main auxiliary systems: the Tritium Extraction System (TES), the Coolant Purification System (CPS) and the Steam Generator (SG) (fig: 4.1). Therefore, in these models the blanket and the rest of subsystems are treated with a single component level model (see sec: 1.3.2). This is often called black box approach. The components of this flowcharts have zero dimensionality as they did not describe the systems from the geometrical point of view.

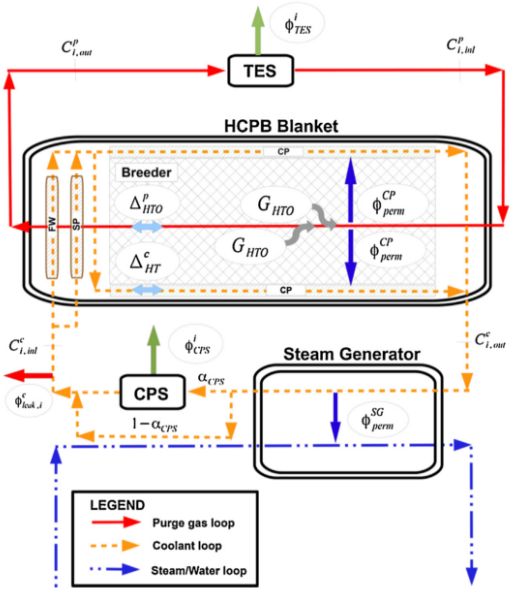

Figure 4.1: Flowchart of the HCPB system level model developed with FUS-TPC code [87].

Other codes model the blanket using a deeper description than the black box approach. This is the case of TMAP, one of the oldest component level tritium transport codes [89, 90]. This code was developed in the Idaho National Laboratory (INL) and it is written in FORTRAN77. It describes

tritium behavior in 1-dimension solid materials. The TMAP component level models are discretized only along the diffusion dierection. The code describes in detail both bulk diffusion and flux across surfaces. Recent models of the American Fusion Nuclear Science Facility (FNSF) have been developed using a newer version of TMAP. They combines the solid components of TMAP using a PFD for modeling the FNSF blanket (fig: 4.2) [91, 92].

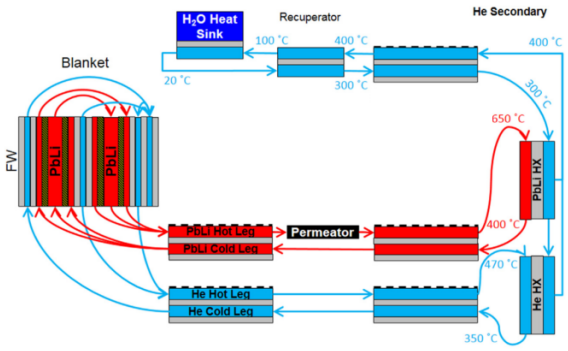

Figure 4.2: Flowchart of the FNSF system modeled with TMAP [91].

Concerning the deep level models (multiphysics 3-dimensional models), some work have been performed using commercial CFD platforms. This is the case of COMSOL [93, 94] and ANSYS-Fluent [95]. Unfortunately, these works are not very extensive. Therefore, more tritium transport analyses using these codes are still needed.

4.2 The EcosimPro simulation tool

In this work, a code based in the object oriented simulation tool EcosimPro has been employed for developing the system level models of the DCLL blanket. EcosimPro strength resides in the possibility of easily combining source code and PFDs. On the one hand, EcosimPro allows the user to program libraries of customized components. On the other hand, it also allows to connect different components in schematics. In practice, these schematics are PFDs in which the different components are in dynamic communication. That way the outputs of one component can be used as inputs for other component in the next integration time step.

This programming environment is very well suited for the development of tritium transport models. Indeed, the EcosimPro library components can be designed as component level models of specific parts of the blanket (for example a solid material or a PbLi flow). Moreover, EcosimPro schematics can be used for building the flowcharts of the system level models. Fig: 4.3 shows the schematic that models a PbLi pipe. In this schematic, the symbols of different components of the tritium transport libraries developed for this work can be observed.

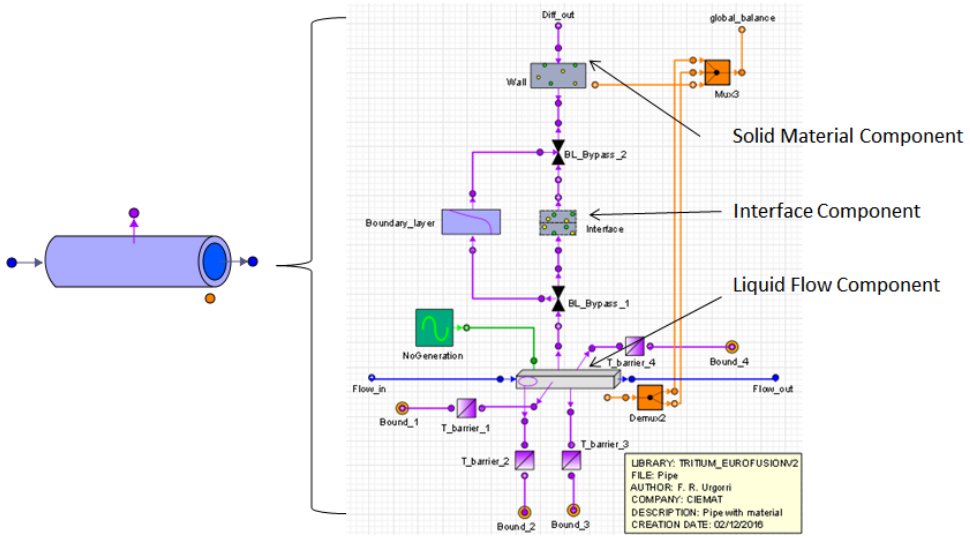

Figure 4.3: Example of an EcosimPro schematic file.

The components of the tritium transport libraries developed for this research are in general 1-dimensional. The spatial discretization of the components is introduced directly by the user in the code. Conversely, the temporal integration method is treated internally by the simulation platform. This is performed using the DASSL algorithm [96]. DASSL is designed for solving the systems of differential/algebraic equations. It uses the backward differentiation formula for integrating the derivatives and the Newton-Raphson method for solving the algebraic systems of equations.

EcosimPro capabilities for tritium transport calculations have been tested against results of the LIBRETTO experimental campaign [97].

Despite EcosimPro components are in general 1-dimensional, they are in some aspects much more flexible than the TMAP component level code. EcosimPro libraries discretizes the PbLi and He flows along the axial direction

(flow direction) while the solid components (EUROFER walls) are discretized also along the diffusion direction. That way, combining 1D components along different directions, a 2D situation can be emulated (fig: 4.4). Note that in the solid materials diffusion along the flow direction is not considered. Therefore, 2D effects are not fully described despite a 2D mesh is defined.

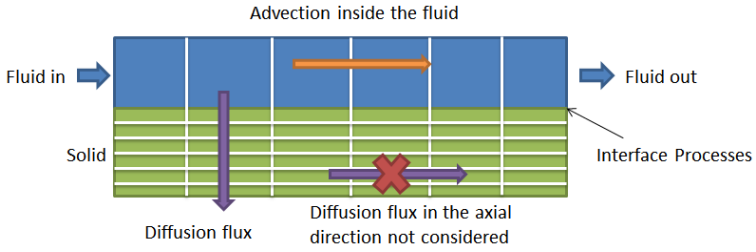

Figure 4.4: Discretization scheme followed by the EcosimPro tritium transport components.

When developing tritium transport models with EcosimPro, the boxes of the flowcharts (or EcosimPro components) can be elementary or compound. An elementary box contains certain amount of differential and algebraic equations that have to be solved. In other words, they are component level model.

Alternatively, a compound box contains a PFD inside it. The breeder blanket box, for example, is described by an internal flowchart formed by boxes which can be elementary or also compound (see sec: 4.3.1). Therefore, from the most external flowchart the model is programmed layer by layer until a PFD composed by only elementary boxes is found.

The PFDs designed for the DCLL preliminary system level model are found in sec: 4.3. A mathematical description of the main elementary components of the EcosimPro tritium transport libraries is given first. The equations presented are based in the tritium transport theory developed in sec: 3.1.

4.2.1 Fluid materials

When tritium is dissolved inside the PbLi, tritium concentration ($c_{PbLi}(t, x_i)$) is described by (4.1). This 1D equation contains the phenomena of advection, diffusion, generation and permeation.

$$\partial_t c_{PbLi}(t, x_i) = -\frac{u(x_{i+1})c_{PbLi}(t, x_{i+1})}{\Delta x} + \frac{u(x_i)c_{PbLi}(t, x_i)}{\Delta x} + G(t, x_i) - \frac{S_i}{V_i} J_n(t, x_i) \quad (4.1)$$

Where Δx is the discretization length, x_i is the position of the i-th cell, S_i is the permeation surface of the i-th cell, V_i is the volume of the i-th cell, $u(x_i)$ is the axial component of the velocity of the lead-lithium and $J_n(t, x_i)$ is the component of the tritium flux normal to the channel walls in the i-th node.

The function $G(t, x_i)$ represents the generation of tritium inside the liquid metal. It is composed by a temporal component and a spatial component. The temporal component is given by the DEMO reactor pulses [98] while the spatial component follows the exponential profile explained in sec: 3.1.1:

$$G(t, r) = G_t(t) p \exp(-b(r - \omega)) \quad (4.2)$$

Equations (4.1) and (4.2) describe the evolution of tritium concentration in PbLi flows. However, the description of the tritium concentration in helium or water flows is almost the same. The main difference is that instead of atomic tritium, helium and water flows considers T_2, H_2 and HT molecules. Indeed, EcosimPro employed the same component for modeling PbLi and He flows as different scalar field for the T atoms and T_2 molecules can be defined. Logically, the generation parameter p is set to zero when no PbLi is present.

4.2.2 Solid materials

Inside the structural walls and the FCI materials tritium concentration evolves affected only by diffusion. The diffusion flux points to the concentration gradient direction which is mainly the direction normal to the contact surface. The tritium flux and tritium concentration inside the materials follow (4.3) and (4.4) respectively.

$$J_y(t, x_i, y_j) = -D\frac{c_{mat}(t, x_i, y_{j+1}) - c_{mat}(t, x_i, y_j)}{\Delta y} \quad (4.3)$$

$$\partial_t c_{mat}(t, x_i, y_j) = \frac{J_y(t, x_i, y_{j-1}) \cdot S_{j-1} - J_y(t, x_i, y_j) \cdot S_j}{V_j} \quad (4.4)$$

$c_{mat}(t, x_i, y_j)$ is the concentration of tritium inside the material, y_j is the position of the j-th node along the direction normal to the surface of the material, Δy is the distance between nodes, S_j is the diffusion surface of the j-face, V_j is the volume of the j-cell, x_i is the position of the i-th node along the axial direction of the lead-lithium (or helium) flow, $J_y(t, x_i, y_j)$ is the normal component of the diffusion flux and D is the diffusivity constant of tritium in the material.

It is worth noticing that the diffusivity constant depends on the temperature. A simplified temperature field in the different regions of the blanket is imposed as an input parameter.

4.2.3 Interfaces

Inside the lead-lithium, the alumina and the EUROFER, tritium is present in its atomic form. As a consequence, there is neither recombination nor dissociation at the interfaces between any of those materials. As explained in sec: 3.1.2, the system tends to balance the partial pressures at both sides of this kind of interfaces which introduces the following discontinuity in the concentration:

$$\frac{c_{PbLi}}{K_{sPbLi}} = \frac{c_{mat}}{K_{smat}} \tag{4.5}$$

K_{smat} and K_{sPbLi} are the solubility constants of tritium in the material and in lead-lithium respectively. Equivalent equations are imposed in the interfaces alumina/steel.

The molecular flux that enters or leaves the helium flow (4.1) can be written in terms of the constants of recombination (σK_r) and dissociation (σK_d) at the interface between the EUROFER and the coolant as shown in sec: 3.1.2 and 3.1.3. In the case of the DCLL, no hydrogen is considered in the secondary coolant. Consequently, only T_2 molecules are present in the interfaces and in the He flow:

$$J_{m_{T_2}} = \sigma K_d p_{T_2} - \sigma K_r c_T^2 \tag{4.6}$$

p_{T_2} is the partial pressure of T_2 dissolved inside the coolant (He or water)

and c_T is the atomic concentration of tritium in the EUROFER. With this description it is not assumed neither a diffusion limited process nor a surface limited process, the regime depends on the specific values of the constants and the concentrations.

4.2.4 Ancillary systems

In order to fully describe the complete lead-lithium loop it is necessary to take into account the effect of the TES, the Heat Exchanger (HX) and the pump.

The TES is placed outside of the blanket and it has been described as a black box that extracts tritium with certain efficiency η following (4.7).

$$c(t)_{out} = (1 - \eta)c(t)_{in} \tag{4.7}$$

The pump is a simple component that imposes a constant mass flow rate (W) in the PbLi loop:

$$W[kg/s] = u_{PbLi} \cdot S \cdot \rho_{PbLi} = W_0 \tag{4.8}$$

Where S is the section of the PbLi pipes, u_PbLi is the velocity, ρ_{PbLi} is the average density and W_0 is a constant value.

The HX is not an elementary component as it described by a PFD formed by elementary components (see sec: 4.3.1).

4.3 Tritium transport system level model for DCLL blanket

4.3.1 Process flow diagrams

The system level models developed by the CIEMAT tritium modeling team are based on the description of what is called the minimal geometrical representative unit of the blanket. An important assumption made in these

models is that the tritium dynamics of the whole blanket can be obtained by scaling the results of this representative unit. This is the main approximation performed by this kind of models. The approximation is the result of the system level nature.

In some blanket concepts, such as the HCPB, the design allows the identification of small geometrical structures that are repeated along the complete blanket with little variations [81, 99]. This is not the situation in the DCLL whose design is not based in the repetition of small geometries. Nevertheless, the modular approach of the DCLL design provides the necessary periodicity for identifying big repeated structures. Indeed, a parallel toroidal circuit of one module is taken as the minimal representative unit (fig: 4.5).

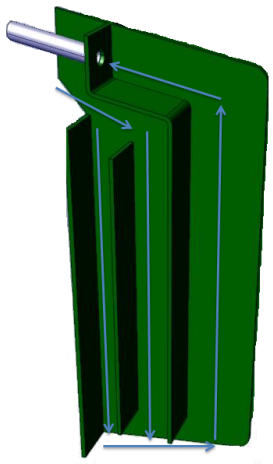

Figure 4.5: Minimal geometrical representative unit of the DCLL.

The preliminary system level model of the DCLL is based on version 1 of the design described in sec: 1.4.1. The tritium transport model of the DCLL blanket has been programmed under the assumption that all the blanket modules are equal (formed by 4 equal representative units). This simplification allows computing the evolution of tritium concentration and tritium fluxes in one outboard equatorial module and then multiply the results by the total number of modules fed by one lead-lithium loop. This assumption is conservative from the safety point of view because the equatorial modules are the biggest ones of the blanket. As a consequence, they will retain more tritium inventory than the others.

Fig: 4.6 depicts the flowchart used for modeling one of the 16 lead-lithium loops which feeds 38 modules of the blanket. The tritium is generated in the blanket and then dragged out of the system by the lead-lithium flow. Thereafter, it goes through the TES where most of it is extracted. The remaining tritium goes through the heat exchanger before re-entering the blanket closing the loop. Tritium can permeate from the PbLi loop to the He loop inside the blanket and from the PbLi loop to the water loop inside the HX.

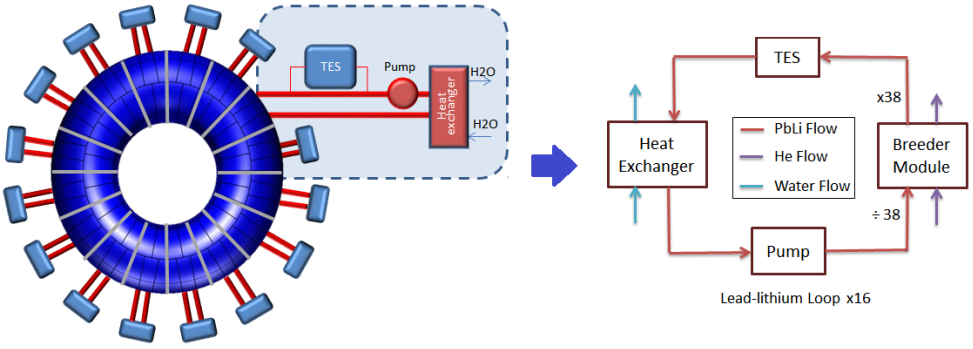

Figure 4.6: PFD of one of the 16 lead-lithium loops in the DCLL blanket.

As it can be observed in the description of the OB module (sec: 1.4.1, version 1) the module is formed by 4 parallel circuits which are very similar. Fig: 4.7 depicts the flowchart used for modeling each parallel circuit of the DCLL module. Each box of the diagram computes the tritium concentration and tritium fluxes evolutions using 1D equations. As mentioned, the PbLi, helium and the water flows are discretized along the axial direction of each duct. In contrast, the EUROFER walls and the alumina layers are also discretized along the direction normal to their surfaces which is the tritium permeation direction (fig: 4.4).

The PbLi channels that appear in the module PFD cannot be modeled using a simple 1D flow. Due to the MHD interactions, a liquid metal flow under a strong transverse magnetic field in a duct with electrical insulating walls develops an almost flat velocity profile with thin BLs next to the walls (see sec: 2.1.5, fig: 2.3). The thickness of these layers is different for the walls parallel to the magnetic field (Side layers) and for the walls perpendicular to the magnetic field (Hartmann layers). In both types of layers the lead-lithium is essentially stagnant. Besides, the channel has to include the two lead-lithium flows separated by the FCI. Fig 4.8 depicts the PFD of a lead-lithium squared

section channel which includes the bulk flow, the MHD BLs, the FCI materials and the gap flow.

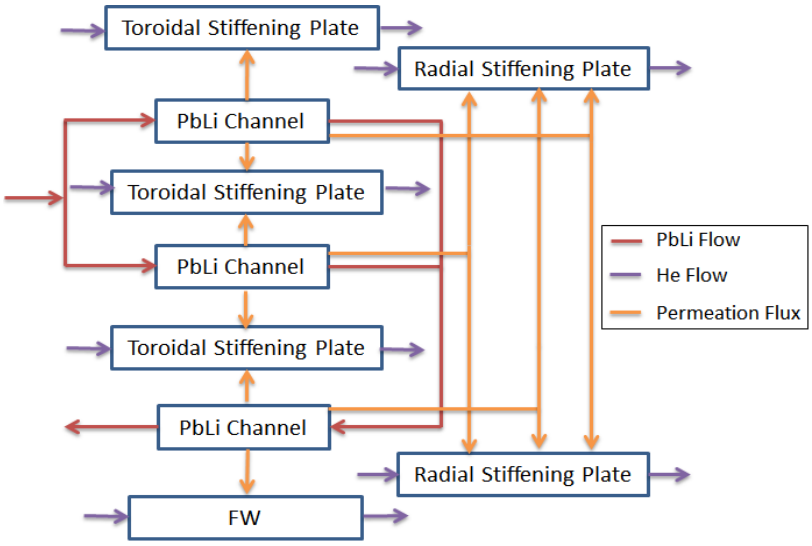

Figure 4.7: Flowchart of one of the 4 parallel circuits of the breeder module.

In the design of the DCLL there are multiple helium channels drilled in the EUROFER walls. Nevertheless, those channels have been approximated with a single helium flow sandwiched between two EUROFER layers. The contact area between the steel and the helium has been corrected in order to minimize the effect of this approximation (Fig: 4.9). The correction factor (Ψ) has been taken from previous 2D calculations of tritium permeation in this kind of geometries [100]. The PFD of one helium cooled wall and the HX is shown in fig: 4.10. The HX is described very similarly to a cooled wall. It consists on a flow of lead-lithium and a flow of water separated by a membrane of steel.

This initial model is focused on describing the tritium evolution inside the blanket. The description of the external PbLi and He circuits is not as detailed as the blanket channels. Indeed, the He circuit is not closed in this model. This implies that the tritium permeated to the helium loop is considered a tritium loss. This approach is conservative but needs to be updated in the advanced version of the system level model (chap: 7).

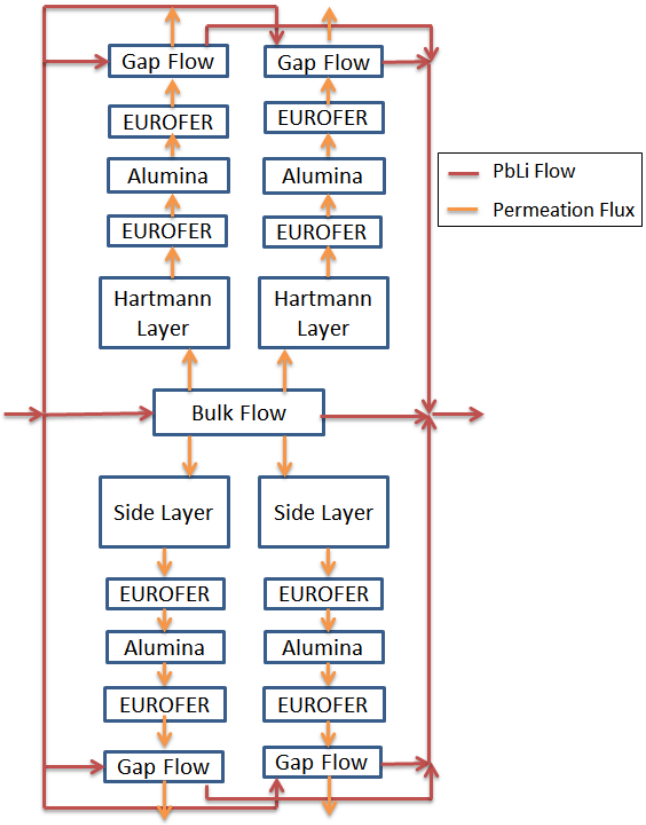

Figure 4.8: Flowchart of one lead-lithium channel.

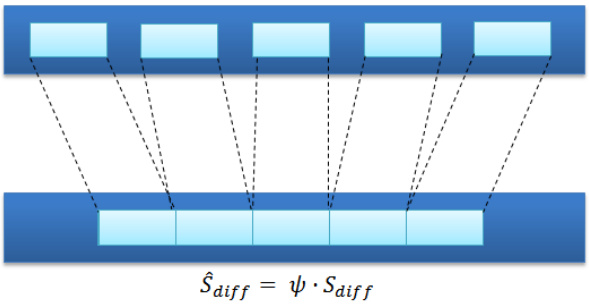

Figure 4.9: Permeation surface approximation for the cooled walls.

It is important to recall that the assumptions related the MHD interactions are based only in the physical intuition given by the observation of MHD velocity profiles. When this model was developed, the dedicated MHD analyses of the DCLL exposed in sec: 5 had not been performed. As a consequence, the MHD assumptions are one of the most important points for the optimization process

explained in sec: 1.3.2. The advanced system level model of the DCLL blanket developed for this work (chap: 7) includes corrections based on specific 3D deep level tritium transport analyses which takes into account the MHD effects in the PbLi flow.

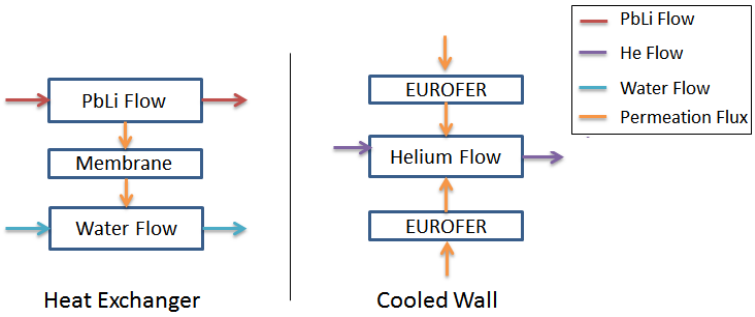

Figure 4.10: (left) flowchart of the HX; (right) flowchart of a cooled wall.

4.3.2 Model inputs

Different kind of inputs can be distinguished in this model. Firstly, the material properties that affect tritium transport. Secondly, the inputs affected by the reactor characteristics (mainly the tritium generation rate). Lastly, the parameters that depend on the specific design of the BB, for example the geometry of the PbLi channels.

The properties of the hydrogen isotopes in EUROFER [74], alumina [101, 102] and PbLi [77] have been obtained from experimental measures. The recombination and dissociation coefficients of EUROFER were not available when this model was developed. The properties of another steel with very similar solubility (OPTIFER-IVb) were taken instead [75]. The values of the macroscopic constants are summarized in tab: 4.1. They follow an Arrhenius-like dependence with the temperature.

$$K = K_0 \exp\left(\frac{E_a}{RT}\right) \tag{4.9}$$

Some of the previous properties present an important dispersion of the experimental measurements. The hydrogen (and tritium) solubility in PbLi

		EUROFER	PbLi	Alumina
D	$D_0(m^2/s)$	$2.64 \cdot 10^{-7}$	$4.03 \cdot 10^{-8}$	$2.90 \cdot 10^{-5}$
	E_a (kJ/mol)	-22.30	-19.50	-198.71
K_s	K_{s0} (mol/Pa$^{0.5}$m^3)	$2.25 \cdot 10^{-2}$	$1.29 \cdot 10^{-3}$	189.79
	E_a (kJ/mol)	-15.10	-1.35	-119.50
σK_r	σK_{r0}(m^4/mol s)	$2.84 \cdot 10^{-7}$	—	—
	E_a (kJ/mol)	28.68	—	—
σK_d	σK_{d0}(mol/Pa s m^2)	$2.99 \cdot 10^{-8}$	—	—
	E_a (kJ/mol)	-29.23	—	—

Table 4.1: Macroscopic constants of tritium in the materials of interest.

shows the most pronounced scatter. Indeed, experimental measurements that differs in two order of magnitudes can be found in literature (Fig: 4.11) [103].

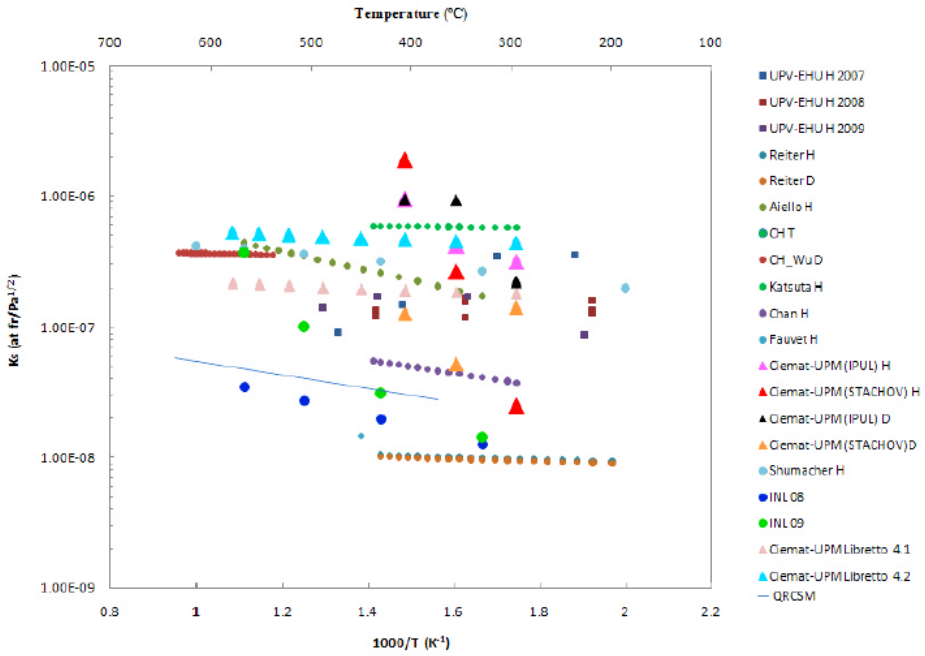

Figure 4.11: Compendium of tritium solubility measures in PbLi [103].

For this initial system level model it was decided using Reiter's measurements for the solubility of tritium in PbLi [77]. The choice is conservative from the safety point of view as this value is the lowest one available in literature. Indeed, the lowest the solubility in Pbli is, the highest the permeation rate from the PbLi to the helium is. Consequently, Reiter's solubility should provide the worst

scenario in terms of permeation rate. In any case, a sensitivity analysis of the tritium solubility in PbLi is performed in sec: 4.3.4.

Concerning the geometrical input data, they were taken from the version 1 details of the European DCLL design [45] (sec: 1.4.1). This design was developed for the DEMO 2014 machine [98] whose fusion power (1572 MW) together with the blanket TBR determine the tritium generation rate. This generation rate is usually referred to full generation conditions. This implies considering that the machine is operating uninterruptedly. However, DEMO will operate following pulses of 2 hours of full generation and 40 minutes of dwell time. The exact temporal shape of the pulses (function $G_t(t)$ in equation (4.2)) is still being investigated. A square shaped function has been taken for this work (fig: 4.12) as first approach.

The total full generation rate of this particular DCLL design for the DEMO 2014 machine is 251.3 g/day. However, the real generation rate (taking into account the reactor pulsed operation) is only 75% of this vale $\sim$ 188.5 g/day.

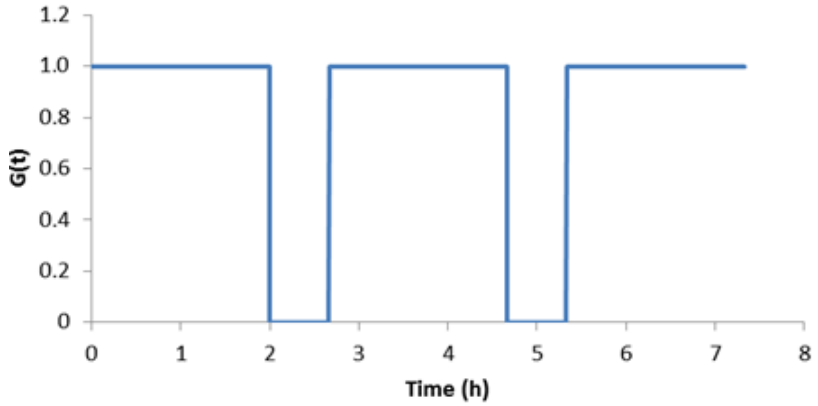

Figure 4.12: Generation pulses considered for the DCLL system level model.

Regarding the rest of DCLL design inputs, they are exposed in the diagram of fig: 4.13. The data concerning the HX have been taken from the numerical analyses of balance of plant performed for the DCLL [104]. This work analyzes the possibility of using a super-critic CO_2 cycle. However, no final choice about the DCLL HX has been made yet.

As shown in the previous figure, the efficiency of the TES has been set to 80%. The final design of this system is not yet decided since the possible

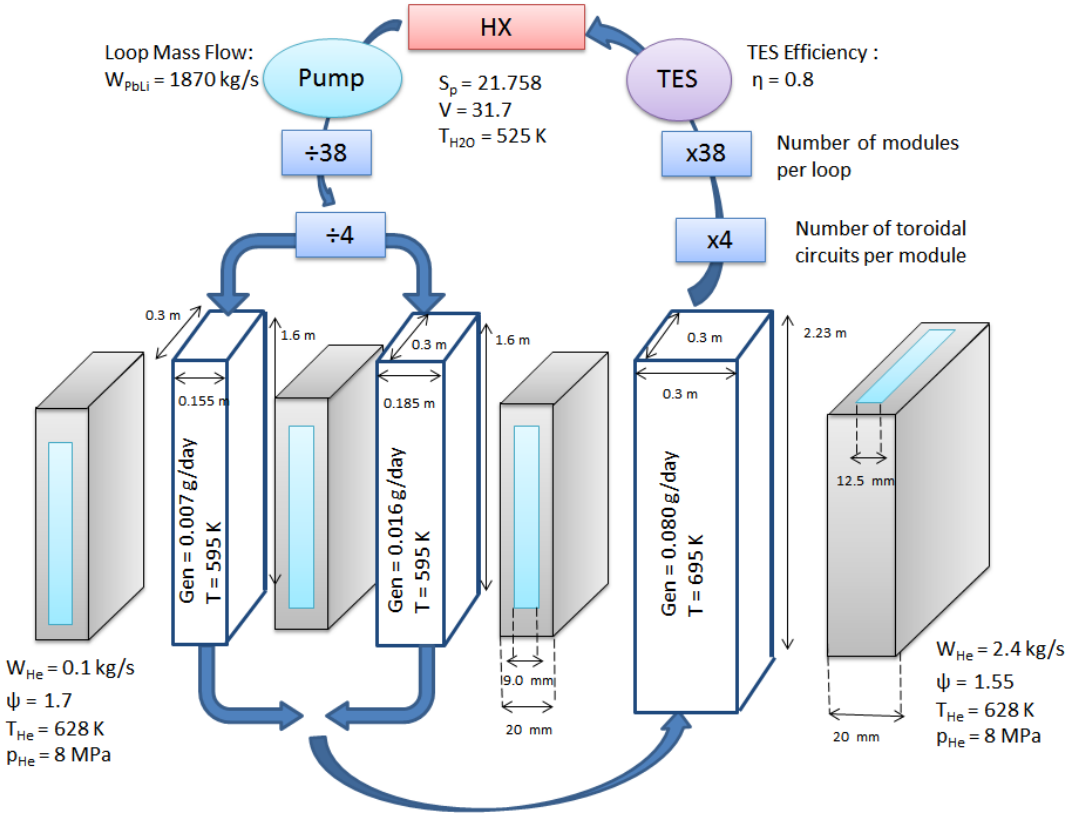

Figure 4.13: Geometrical input data of the initial tritium transport model at system level for the DCLL.

extraction techniques need of experimental validation. Conceptual analyses of a TES shows that an efficiency of 80% can be achieved using the permeation against vacuum technique [105]. This value has been taken for the reference case but a parametric study around the TES extraction efficiency is performed also in sec: 4.3.4.

4.3.3 Reference case results

4.3.3.1 Single Channel Results

Before simulating the reference case, a calculation of a single lead-lithium channel has been performed. The objective of this previous study is analyzing the impact of the FCI on tritium permeation. Fig: 4.14 depicts the permeation of tritium from the bulk flow of the PbLi channel to the FCI that surrounds it

during a few hours of full generation. Two different phenomena can be observed in this figure. Firstly, the permeation is faster through the Hartmanm layers than through the Side layers. This is a consequence of the difference between the layers thickness. Secondly, the permeation rate goes to zero after a few hours. This is because the alumina, which has a very low permeability [101], is acting as a very efficient permeation barrier. During the first hours, tritium permeates from the bulk flow to the internal EUROFER layer of the FCI. However, the layer saturates relatively quick because of the alumina barrier. At this point no more tritium is able to permeate.

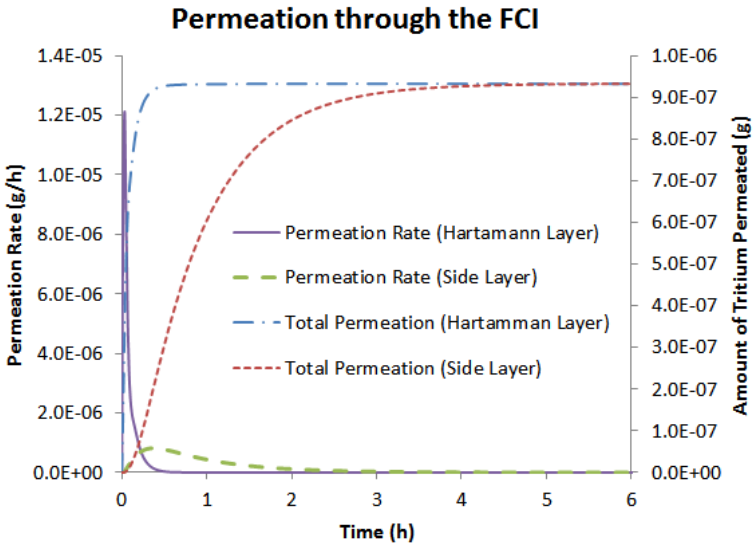

Figure 4.14: Permeation from the core of one PbLi channel to the FCI through the Hartmann and Side BL. Permeation rates are shown in the left axis while the total amounts of tritium permeated are shown in the right axis.

The consequence of these results is that, in terms of tritium transport, the bulk flow and the gap flow are isolated from each other. Therefore, only the tritium generated inside the gaps of the channels is susceptible to permeate to the helium circuit.

The decoupling between the core flow and the gap flow obtained in this analyses has important consequences in the development of the present research project. This analysis is one of the main reason why the later deep level model of sec: 6.5 is focused in the gap flow system. In terms of evaluating both tritium permeation and tritium inventory, the gap is probably the most important geometry of the whole DCLL blanket.

4.3.3.2 Complete model results

The results of complete model (fig: 4.6) are presented in this section. The set of inputs parameters already exposed are called the reference case. Several results are obtained for the this case. Besides the reference, one secondary model has been considered. In this second case, the same input parameters and flowcharts have been used but none of the lead-lithium channels contain FCI. This way, it is possible to observe the influence of the FCI on the complete model results. Fig: 4.15 shows the inventory of tritium in the DCLL blanket for the reference case compared with the case without FCI.

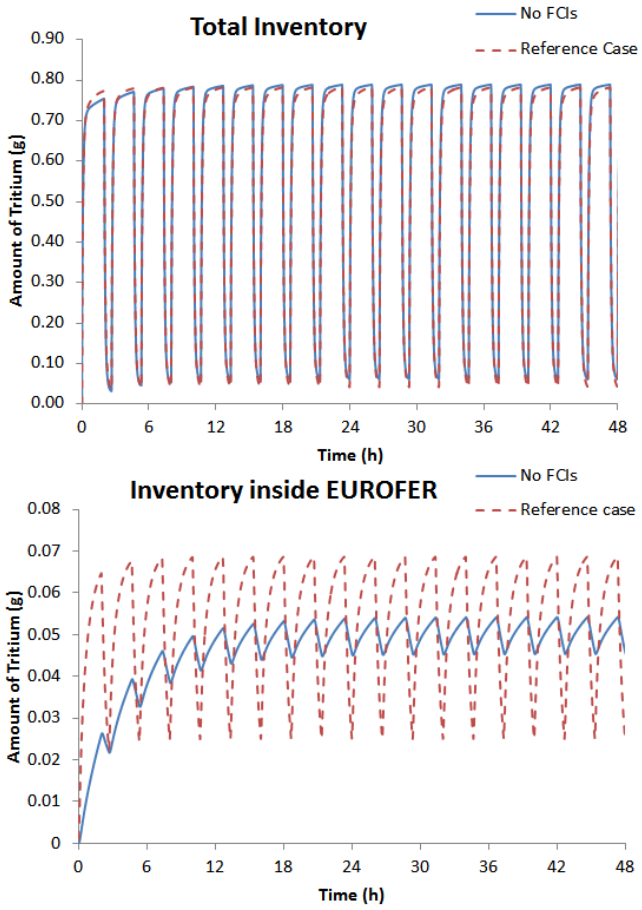

Figure 4.15: Total inventory of tritium in the whole system (up). Part of the inventory located in the EUROFER (walls and EUROFER FCIs layers) (down).

Due to the pulsed generation, the total inventory oscillates between the 768 mg and 66 mg. Those values correspond to the end of the burn time and the

end of the dwell time, respectively. The inventory is considerably smaller than those obtained for other liquid metal based blankets concepts [37, 106]. The reason is the high PbLi mass flow rate of the DCLL concept. This high number increases the number of circulations of lead-lithium through the TES per unit time. Consequently, the extraction rate of tritium is boosted and the inventory remains in low values.

Regarding permeation, small inventories imply a relatively low permeation from the lead-lithium gaps to the helium channels. Results for tritium permeation from the lead-lithium to the helium for the whole DCLL blanket are shown in fig: 4.16. Moreover, the model calculates a negligible permeation in the HX due to the high PbLi mass flow rates in this ancillary system (> 1 ton/s).

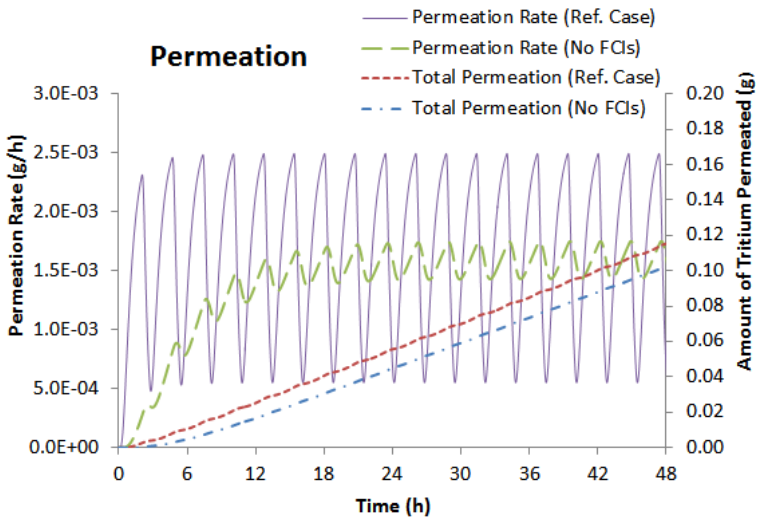

Figure 4.16: Total permeation (right axis) and permeation rates(left axis) from the lead-lithium gaps to the helium circuits inside the DCLL blanket.

Contrary to what it was expected at first, fig: 4.16 shows that the FCI has a little but detrimental effect over tritium permeation. The gap between the FCI and the wall constitutes a small volume of lead-lithium close to a considerable large permeation surface. In addition, the flow rates of the liquid metal at the gaps are much smaller than in the core of the channel. As a consequence, when the FCI is considered the tritium concentration close to the walls is slightly bigger than the case without FCI.

Quantitatively, the difference between both cases is small; the permeation rate oscillates around 1.66 mg/h in the reference case and around 1.58 mg/h in the case without FCIs. The tritium permeated to the coolant constitutes 0.031% and 0.028% of the tritium generated in the reference case and in the case without FCIs, respectively. Almost the rest of the tritium generated (more than 99.9%) is extracted by the TES with the exception of the tritium inventory located in the structural materials, the FCIs and the PbLi. The inventory in the secondary coolant is not estimated by this model since the He coolant loop is not closed.

A summary of the results provided by the model in the reference case is shown in tab: 4.2.

	Maximum	Minimum
Inventory PbLi (mg)	699.80	41.60
Inventory EUROFER (mg)	68.20	24.40
Extraction rate (g/day)	250.56	0.96
Permeation rate (mg/day)	39.84	20.16

Table 4.2: Results of the DCLL initial tritium transport model at system level.

4.3.4 Parametric studies

System level models present important uncertainties. The sources are various. They can be caused by the experimental uncertainty of certain key parameters, the already discussed T solubility in PbLi is a good example. They can also be caused by the uncertainties in the blanket design. Indeed, the DCLL blanket project was in a pre-conceptual design phase when the model was developed. Therefore, there are many aspects that were still under evaluation or even had not been studied yet. These can have an important impact in the tritium real behavior that the model cannot possibly take into account. Finally, it cannot not be undervalued the uncertainties introduced by the model itself. Any system level model introduces uncertainties in the assumptions they made when modeling the different phenomena. For example, the MHD assumptions in the PbLi flow already discussed at the end of sec: 4.3.1.

For the reasons mentioned above, the results of the reference case shall not be taken as definitive. The real value of the system level models lies in the possibility of performing sensitivity analyses of certain parameters. This allows to analyze their influence in the global tritium behavior. The reference case is just a base scenario for these comparisons. Indeed, parametric studies are helpful for evolving the design to its final version as they can identify and solve potential problems.

For this initial model, 3 parametric studies have been performed by varying 3 different parameters: the mass flow rate of lead lithium (W_{PbLi}), the extraction efficiency (η) of the TES, and the T solubility in lead-lithium (Ks_{PbLi}). In every case, the rest of the inputs are fixed to the reference values. Instead of comparing absolute values, the ratios of the results with respect to the total tritium generated in the blanket (∼188.5 g/day) are presented. Therefore, the extraction ratio, the inventory ratio and the permeation ratio are defined as the relative amount of tritium extracted by the TES, retained in the materials and permeated to the helium, respectively.

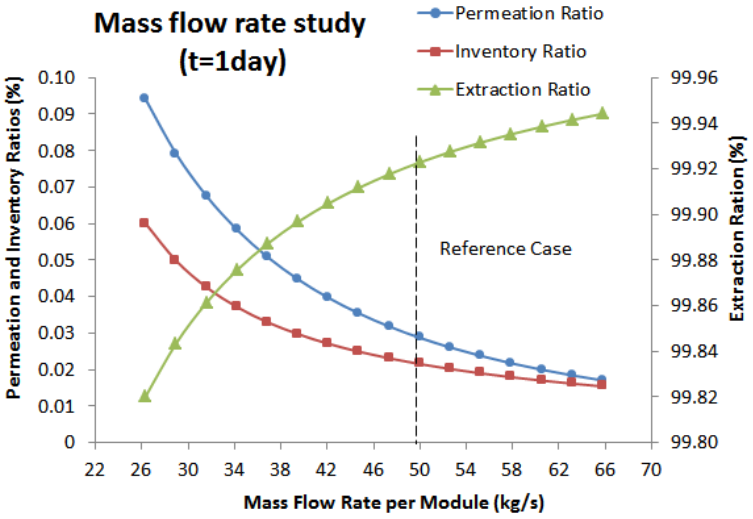

Figure 4.17: Extraction ratio, permeation ratio and inventory ratio after one day of operation as a function of the mass flow rate of lead-lithium per module.

Fig: 4.17 presents the influence of the lead-lithium mass flow rate over the tritium behavior. Increasing the mass flow rate makes tritium extraction more effective due to the raise of the number of circulations through the TES per unit time. A higher extraction rate translates into a smaller inventory. Naturally,

a smaller inventory implies smaller concentrations of tritium inside the liquid metal which generates smaller concentration gradients. As a consequence, a lower permeation of tritium is obtained for higher mass flow rates.

In fig: 4.17 the uncertainty that the lead-lithium flow rate introduces in the model results can be analyzed. If for any reason the mass flow is not equally distributed between the modules and the channels or the pumping power fails in maintaining the pressure, the permeation of tritium will grow at the expense of the extraction. For small flow rate deviations around the reference case value the uncertainty in the permeation is relatively small. In more dramatic scenarios, for flow deviations of dozens of kg/s the permeation of tritium doubles or triples its value with respect to the reference case value.

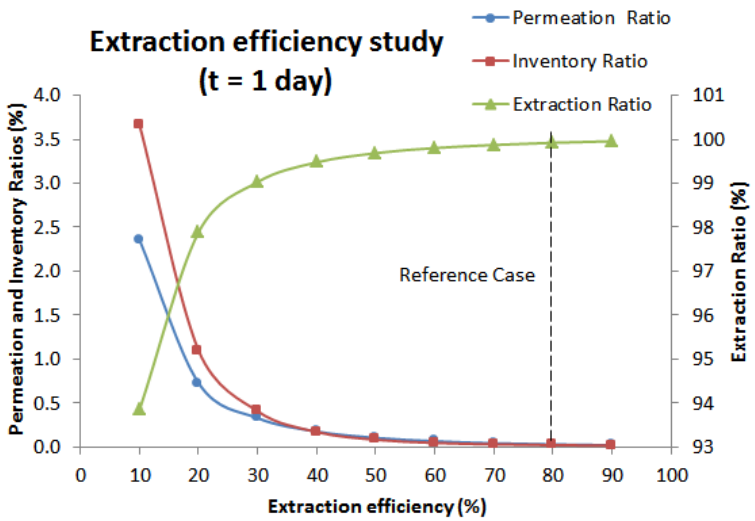

Figure 4.18: Extraction ratio, permeation ratio and inventory ratio after one day of operation as a function of the extraction efficiency η.

Regarding the extraction efficiency study, the results shown in fig: 4.18 are qualitatively similar to those of fig: 4.17. This is because an increase of any of the two parameters boosts the extraction rate. In this model 100% of the lead-lithium is processed by the TES. In addition, the TES is modeled as a "black box system" ruled by (4.7). Under these conditions, the extraction of tritium is very effective due to the huge mass flow rate of lead-lithium that circulates through the TES per unit time. Fig: 4.18 shows that it is not necessary to have a high extraction efficiency η to have a good extraction rate as long as the TES can process the majority of the PbLi flow. Results show that with an

extraction efficiency of a 30% it is possible to extract around the 99% of the tritium generated.

The extraction efficiency introduces a very unlike uncertainty in the model results. For values of the extraction efficiency higher than 40%, there is relatively little uncertainty. However, for lower values of this parameter the extraction rate falls rapidly. The permeation rate and inventory grows significantly fast. As a consequence, for $\eta < 40\%$, the extraction efficiency introduces an important uncertainty in the permeation rate.

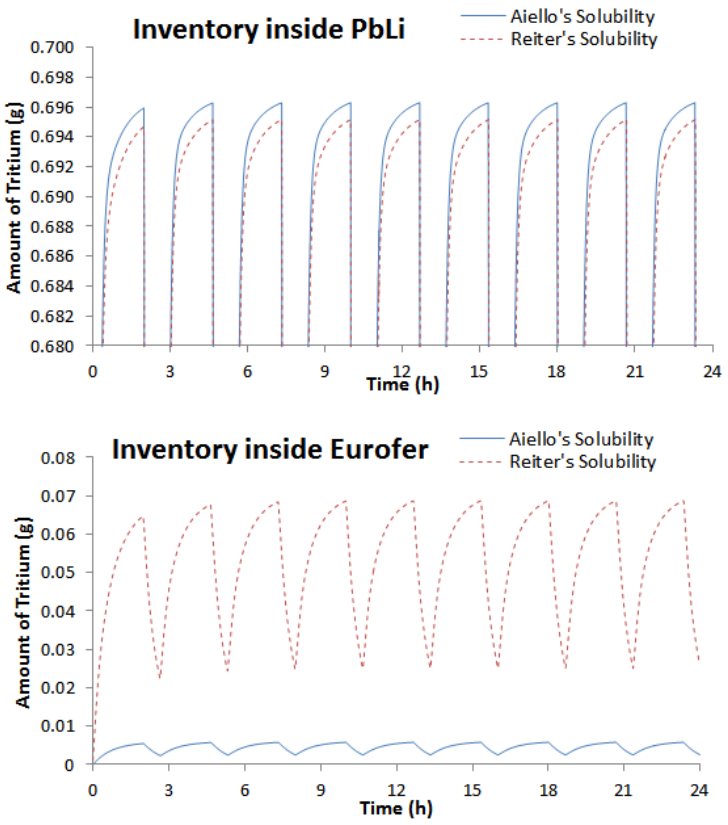

Figure 4.19: Tritium inventory inside PbLi for two extreme values of T solubility in PbLi (up). Tritium inventory inside EUROFER materials for two extreme values of T solubility in PbLi (down).

The last sensitivity study is related to tritium solubility in PbLi. This parameter plays a very important role on tritium permeation but there is a considerable dispersion in the experimental measuremetns avaliable in literature. As mentioned, the reference scenario considers the lowest value avaliable for this constant: Reiter's solubility [77]. In the works of Aiello et

al. [107] a value one order of magnitude higher than Reiter's was measured. This means that Aiello's solubility is one of the highest measurements available in literature (4.11). The sensitivity analysis compares the model results obtained when using both solubility values.

Fig: 4.19 and fig: 4.20 show the heavy impact that the tritium solubility in lead-lithium has over the permeation rate. Both measurements of the solubility constant differ in one order of magnitude which is translated into one order of magnitude difference in the tritium inventory inside EUROFER. Besides, the small tritium concentration in the steel causes a three order of magnitude difference for the permeation rate to the helium circuit. Of the three studied parameters, the PbLi solubility is clearly the one that introduces more uncertainty in the model results.

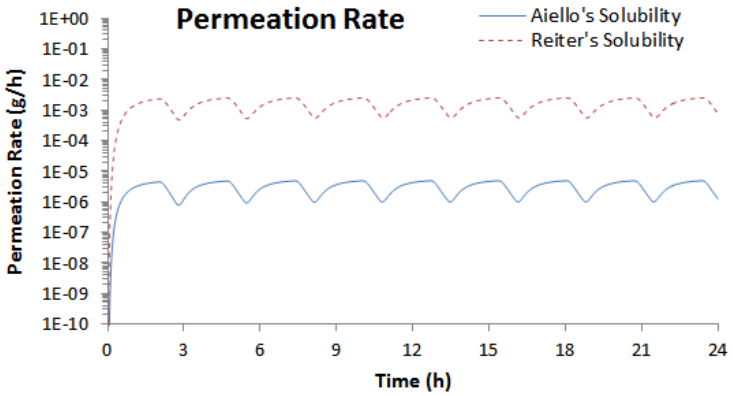

Figure 4.20: (up)Permeation rate from PbLi flow to the helium circuit for two extreme values of T solubility in PbLi.

4.3.5 Discussion

Despite the preliminary approach of this model and its limitations, important conclusions can be derived from their results. Simulations show that the enormous mass flow rate that characterizes the DCLL concept added to an extraction system able to process 100% of the flow produces of a very high extraction rate. These also cause comparatively low inventories and permeation rates. Indeed, for the reference case, after 2 days more than 99.9% of the tritium generated is extracted by the TES. Just 0.031% of the tritium

ends up in the helium coolant circuit. Therefore, the model confirms one of the predicted strengths of the DCLL concept: very low tritium permeation losses.

The effect of the FCI on tritium permeation has been analyzed. It has been found that even though the alumina is an effective permeation barrier, the presence of the PbLi gap has a detrimental effect on tritium permeation to the helium circuit. This result was not expected beforehand since it was believed that the alumina would act as an effective permeation barrier. In the light of these results it was decided to focus 3D tritium transport analyses on the gap flow (sec: 6.5).

The sensitivity analyses performed shows the important effect that experimental and design uncertainties have over the model results. In particular, the tritium solubility in PbLi manifests the most important experimental dispersion. This constant changes the outcomes of the model in orders of magnitude.

Chapter 5

Computational MHD analyses for the DCLL blanket

In this chapter, the MHD computations related the European DCLL are presented. These calculations fulfill a double objective. On the one hand, they are developed for assisting the DCLL design activities with dedicated MHD and thermal analysis of its geometry. On the other hand, they are a necessary step for the implementation of deep level tritium transport models presented in the next chapter. This way, the effect of MHD on tritium behavior can be studied. Before presenting results, a review of the computational tools employed is given. Moreover, a classification of the main MHD issues of the DCLL design in terms of their importance is discussed. Thereafter, computational results regarding several of the identified issues are presented.

5.1 Computational tools used for MHD

As it is explained in chap: 2, MHD effects arise in every PbLi-based blanket due to the intense magnetic field in which the blanket is immersed. In sec: 5.2 the representative dimensionless numbers of the DCLL are presented. Typically, the Hartmann number of any PbLi-based blanket is of the order of magnitude 10^3 and 10^4. This high number implies that, as a result of the intense field, the MHD effects are expected to dominate the PbLi dynamics. Therefore, it is completely necessary performing MHD computations if realistic

deep level tritium transport models are to be developed. MHD problems have been formulated using conservation laws. Thus, finite volume methods are well suited for this problems as they typically are in fluid dynamics. Unfortunately, solving MHD liquid metal problems at high Hartmann numbers is computationally very expensive. There are various reasons for this high cost:

1. The number of differential equations that have to be solved is increased in comparison with regular fluid dynamic problems. Indeed, there are 3 new first order equations when using the B-formulation or 1 new second order differential equation when using the Φ-formulation.

2. The thickness of the Hartmann BL scales with Ha^{-1}. This means that very fine meshes are needed in these regions with nodal distances that are normally of the order of μm. This means that even when using an exponential or hyperbolic mesh grading towards the BL, the computational meshes are very large. It is indeed common that simple MHD systems requires meshes with a few millions of cells.

3. When the Hartmann number is high, very large velocity and field (or potential) gradients are developed between adjacent cells in the MHD BLs. Consequently, it is usually needed to include a pseudo-time term (transient approach) in order to obtain convergence. Moreover, the time step required is typically small; 10^{-4} or 10^{-5} seconds.

Considering the previous difficulties, it is of great interest to use an MHD code with highly parallelization capabilities. Acceleration techniques based on GPUs have also great potential. The previous possibility is an open field of research that can be very fruitful and should be explored in future.

Historically, homemade codes were the first attempt of solving numerically the MHD problems at high Hartmann numbers for blanket applications. Indeed, MHD solvers were created in both Europe [108] and the US [109]. Homemade codes are very specialized but they are also quite limited to the cases for which they were created. Consequently, they were partly substituted by more general computational tools.

In the past few years, commercial codes are starting to be used for MHD computations. This is the case of HIMAG, a code that have been extensively

used by the US research teams (e.g. [110]). Both CFD codes of ANSYS: CFX [111, 112] and Fluent [113, 114] have been tested recently. COMSOL multiphysics platform has been also validated for MHD applications [115, 116]. In Europe the open source libraries of OpenFOAM written in C++ have been by far the most used tool for blanket MHD applications (e.g. [117]).

All of the previous tools are based in pure CPU calculations. They present decent parallelization properties that allow their use in computer clusters (normally using Message Passing Interface (MPI) message-passing standard). This is probably one of the reasons behind their success. It is worth mentioned that despite their advantages, commercial codes (including OpenFOAM) are not designed for solving specific problem. They are thought to be robust and adaptable to as many calculations as possible. Thus, they may not compete in computational speed with highly specialized codes. As mentioned, the development of highly parallelizable codes specialized in MHD, possibly based in GPU architecture are an interesting open field of computational research.

In the present dissertation only 2 of the previous codes are used for achieving MHD calculations: OpenFOAM and ANSYS-Fluent. The last one has been chosen for most of the calculations as it is considered more suitable for the objectives of this work. A description of the main benefits and drawbacks is presented in the following sections.

5.1.1 OpenFOAM libraries

OpenFOAM is an ensemble of C++ libraries. They are currently designed for solving a wide variety of physical and engineering problem but they have been originally developed for CFD applications.

One of the most distinctive properties of OpenFOAM is its strong customization capabilities. OpenFOAM is an open source software in which any user can program their own numerical solvers using pseudo-code. The original C++ libraries are toolboxes that can be load as modules when programming the solvers. This gives OpenFOAM a considerable flexibility in comparison with their competitors.

As mentioned, OpenFOAM has been used for MHD BB applications in Europe for many years. Indeed, MHD analyses of the HCLL (e.g. [118]),

WCLL (e.g. [119]) and DCLL (e.g. [120]) concept have been performed by the European teams using OpenFOAM solvers.

The previous works and most of the MHD work developed with OpenFOAM are based in a modification of the Pressure-Implicit with Splitting of Operators (PISO) algorithm (e.g. [121]). This solver joints the MHD equations in Φ-formulation to the regular Navier-Stokes equation. The algorithm is described step by step in [122].

The original algorithm was written for considering only one domain (the PbLi flow). Later, the algorithm has been extended for solving also Poisson equation for the electric potential (2.35) in the solid regions of the system. However, working with multi-domains systems with OpenFOAM is a more complex process than with any other CFD simulation platforms. Another important limitation of this algorithm is that it only admits transient calculations. Despite transient calculations are often unavoidable, steady-state computations can be useful in relatively simple but fusion relevant applications.

OpenFOAM offers the possibility of GPU acceleration which has been recently applied to MHD problems with success [123].

5.1.2 ANSYS-Fluent simulation platform

ANSYS-Fluent (or simply Fluent) is the other CFD simulation software that has been used during this research project. Unlike open source codes where the user is free to modified the code of the solvers, Fluent users are limited to the pre-defined solvers and modules. Despite this apparent limitation, Fluent solvers are relatively versatile and the user can choose between a considerable amount of options for adapting the calculations to the numerical and physical needs of each problem. For example, boundary conditions can be changed easily and relaxation parameters can be modified if needed to obtain convergence.

Being integrated in ANSYS, Fluent is compatible with geometry design interfaces and potent meshing tools (ICEM). This allows designing complex geometries and meshes without having to program source code.

Fluent integrates a MHD solver which works using both B-formulation and

Φ-formulation. Besides, both transient and steady-state computations can be carried out.

Fluent offers the user the possibility of using a graphic environment for setting up the calculations. This is useful but the real strength of Fluent relies in the possibility of performing multiphysics computations within the same platform. This way, MHD, thermal and tritium transport calculations can be launched simultaneously if needed. This is the main reason why Fluent has been chosen as the main simulation tool for this research. The possibility of using the results of the MHD computations as inputs for tritium transport computations within the simulation environment is extremely convenient.

Although ANSYS-Fluent is probably the most popular software for CFD computations, its MHD utility has not been used as extensively as OpenFOAM or HIGMAG. Some validation against experiments have been carried out with success [113] but further analyses are needed under different conditions. In particular, the computations conducted so far are based in the Φ-formulation (e.g. [124]). However, fully developed MHD calculations based in the B-formulation are very useful for the present research. Because of it, 2 validation tests of MHD fully developed computations conducted with Fluent in B-formulation are presented in sec: 5.1.2.1.

Probably the most important limitation of Fluent (and other ANSYS platforms) is that they cannot be easily parallelized in big clusters. It is not a technical issue but a commercial issue. Commercial licenses of ANSYS are normally limited to a few dozens of parallel threads. This means that Fluent would not be suitable for very big and long computations unless special licenses were acquired. Fluent incorporates acceleration capabilities based on GPU but their use in MHD simulations has not been studied yet.

5.1.2.1 Fluent Validation Test

For the purposes of this research (in particular, sec: 5.5) Fluent computations of fully developed flows using B-formulation need to be validated, especially for high Hartmann numbers. For this reason, two flows with known analytic solutions are computed with Fluent: the Shercliff flow [61] and the Hunt flow [59]. The analytic solutions of both flows are presented in sec: 2.1.5 together with graphical representations of the velocity

profile obtained with Fluent (fig: 2.3 and fig: 2.5).

As explained, the Shercliff flow consist of a rectangular section channel with perfect insulating walls under a transverse magnetic field. The Hunt flow system is almost equal to the Shercliff one but the Hartmann walls (perpendicular to the magnetic field) have a finite wall conductance ratio (C_w). The Side walls (parallel to the magnetic field) are still perfectly insulated. The Hartmann number used in this validation exercise is $7.63{\cdot}10^3$ which is relevant for the conditions of the DCLL OB equatorial module. The wall conductance ratio used for the Hunt flow has been selected arbitrarily ($C_w = 0.05$).

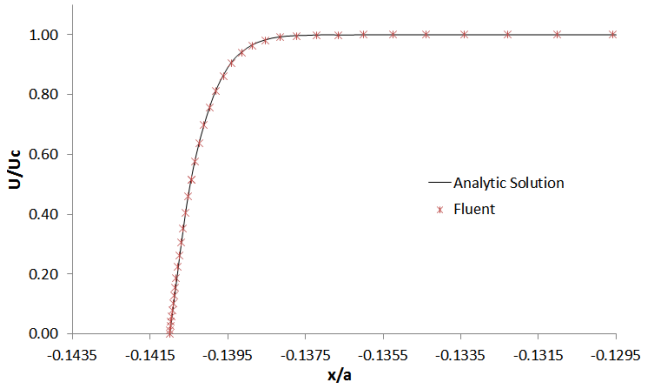

(a) Shercliff flow.

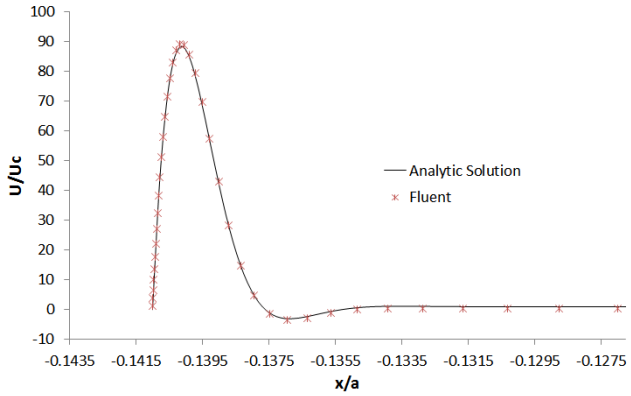

(b) Hunt flow.

Figure 5.1: Comparison between Fluent result and analytic solution [60].

Fig: 5.1 shows the velocity profile obtained with Fluent along a line perpendicular to the magnetic field that goes from the center of the channel to the wall. Results are depicted next to the Side BLs normalized with respect to the core velocity. The spatial coordinate is also normalized with respect to the

length parallel to the B field (l). The computational solutions are compared with the analytic solutions along the same curve. Results show a very good matching between computational results and analytic solutions.

5.2 MHD issues in the European DCLL

The estimation of the MHD pressure drop is a critical calculation in every PbLi-based blanket. An excessive pressure drop will force high pumping rates in the PbLi loops. Spending too much energy on moving the PbLi at the required rates can seriously compromise the efficiency of the plant. Besides, there are technological limits to the PbLi pumping systems that must be respected.

In this section, the European DCLL OB equatorial module design (version 3, sec: 1.4.1) is analyzed from the MHD pressure drop perspective. The critical regions have been identified and classified according to their expected importance. This exercise is of great interest since it allows identifying possible weaknesses of the design. Besides, it also helps understanding which are the MHD calculations that should be prioritized taking into account the limited resources available. In this chapter, solutions strategies are presented for the different issues identified.

Similar categorizations have been performed in the past for other blankets based on PbLi, such as the HCLL TBM or the US-DCLL [125]. However, this is the first time that such analyses are applied to the European DCLL.

The MHD pressure drop sources are classified into two main components. Firstly, the 2D MHD pressure drop sources. They come from the Lorentz forces created by the cross sectional currents (perpendicular to the flow). These are heavily dependent on the electrical coupling between the flow an the walls. Thus, they can be mitigated using FCIs or other electrical insulating mechanisms. Secondly, the 3D MHD pressure drop sources which appear in the 3D elements of the flow geometry (bends, flow expansions, obstacles...). They are created by the axial component of the induced currents inside the flow (parallel to the flow). Therefore, they are not dependent on the coupling between the flow and the wall and they cannot be mitigated by placing FCIs.

It is relatively common in literature expressing the 3D MHD pressure drop

in terms of the following empirical relation:

$$\Delta P_{3D} = \zeta \frac{\rho u_0^2}{2} \tag{5.1}$$

The parameter ζ depends on several factors like the external field, the velocity scale and the geometry. Despite experimental data suggest that there is a linear dependece with the interaction parameter ($\zeta \propto N$) [125], there is no clear correlation available.

5.2.1 MHD constants

The characteristic dimensionless numbers of the European DCLL channels are exposed in tab: 5.1 and tab: 5.2. In order to estimate the Grashof number in the different channels, the characteristic temperature difference ΔT has been estimated considering a simplified 1D conduction model. In other words, $\Delta T = \overline{q} \cdot b^2/\kappa$, where $\overline{q}$ is the average volumetric heating in the channel, b is the half of the channel length along the heat flux direction and κ is the thermal conductivity of PbLi. The Grashof number computed with this method is most likely an overestimation of the real value but it provides a preliminary value until more detailed calculations are performed (e.g. sec: 5.5.3 and 5.7).

	Outboard segment			
	Breeding zone		BSS channels	
	Front	Rear	Hot	Cold
Ha	$7.63 \cdot 10^3$	$8.46 \cdot 10^3$	$5.79 \cdot 10^4$	$4.18 \cdot 10^4$
N	$2.14 \cdot 10^3$	$1.98 \cdot 10^3$	$9.18 \cdot 10^3$	$1.26 \cdot 10^4$
Re	$2.72 \cdot 10^4$	$3.63 \cdot 10^4$	$3.65 \cdot 10^5$	$1.39 \cdot 10^5$
Rm	$1.56 \cdot 10^{-3}$	$1.51 \cdot 10^{-3}$	$8.35 \cdot 10^{-2}$	$7.86 \cdot 10^{-2}$
Gr	$5.98 \cdot 10^{11}$	$1.47 \cdot 10^{11}$	$5.19 \cdot 10^8$	$3.48 \cdot 10^7$

Table 5.1: Characteristic dimensionless constants of the DCLL outboard channels.

	Inboard segment			
	Breeding zone		BSS channels	
	Front	Rear	Hot	Cold
Ha	$1.75 \cdot 10^{4}$	$1.91 \cdot 10^{4}$	$9.19 \cdot 10^{4}$	$6.84 \cdot 10^{4}$
N	$1.04 \cdot 10^{4}$	$8.27 \cdot 10^{3}$	$3.29 \cdot 10^{4}$	$2.49 \cdot 10^{4}$
Re	$2.94 \cdot 10^{4}$	$4.40 \cdot 10^{4}$	$2.57 \cdot 10^{5}$	$1.88 \cdot 10^{5}$
Rm	$2.10 \cdot 10^{-3}$	$2.37 \cdot 10^{-3}$	$6.70 \cdot 10^{-2}$	$7.73 \cdot 10^{-2}$
Gr	$7.19 \cdot 10^{11}$	$3.16 \cdot 10^{10}$	$1.58 \cdot 10^{8}$	$1.56 \cdot 10^{8}$

Table 5.2: Characteristic dimensionless constants of the DCLL inboard channels.

5.2.2 Pressure drop in the breeding zone

The straight poloidal channels, which constitute the majority of the PbLi path, will be one of the main sources of MHD pressure drop in the breeding zone. As mentioned, the importance of this contribution is heavily affected by the quality of the response of the FCIs. If the FCI were able to electrically decouple the PbLi flow from the EUROFER structure effectively, the MHD pressure drop would be highly mitigated. Under steady-state conditions and far from the geometric 3D elements of the design (bends, flow expansions/contractions, etc) it is expected that the flow is fully developed [126]. As a consequence, a good estimation of the pressure drop and velocity profile can be obtained using 2D computations. This kind of analyses dedicated to the front channel of the OB equatorial module are presented in sec: 5.5 for three different FCI designs.

Concerning the 3D MHD pressure drop, the DCLL modules include 3 bends in the flow path per parallel circuit, two of them are 90° bends while the other is 180° (fig: 1.16c in sec: 1.4.1). According to previous studies [108, 127, 128], in the inertialess regime the pressure drop in a bend is comparable to that in a straight channel of the same length as long as the bend is contained in a plane perpendicular to the external magnetic field. This is the case for the 3 bends of the DCLL breeder zone. Thus, the contribution of these elements is not expected to be too large.

Besides the bends, there are flow contractions and expansions in the connection between the breeding zone and the BSS channels. A detailed view of this region is shown in fig: 5.2. These changes in the flow direction (contractions and expansions) are not exclusively contained in the plane

perpendicular to the external magnetic field. As a consequence, it is expected that their contribution to the pressure drop will be important. Similar conclusions were found in previous CFD studies for the HCLL concept [129]. Either complete 3D computations or experimental work are mandatory to deal with these regions and obtain correct estimations of their contribution to the total pressure drop.

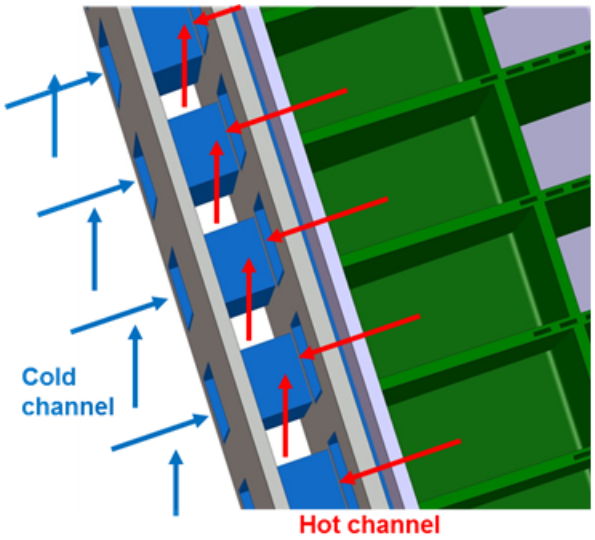

Figure 5.2: Detailed view of the connection between the module and the BSS channels showing in blue the inlet channels crossing the hot channel. The blue and reds arrows represents the expected flow path of the cold and hot PbLi, respectively [46].

5.2.3 Pressure drop in the BSS

The BSS is a much larger system that one module as it is formed by one single and continuous piece. Their two channels have a marked curvature (fig: 1.15, sec: 1.4.1) which is a source of 3D pressure drop. However, as in the case of the bends in the breeding zone the flow changes are contained in a plane perpendicular to the external field. Therefore, it is expected a pressure drop comparable to the pressure drop of a straight channel with similar length. The 2D pressure drop will be more important than the one induced by the BSS curvature. As a consequence, placing FCIs or other kind of electric insulation covering the BSS channels would mitigate the pressure drop effectively. The viability of placing FCIs on complex and big geometries like

the BSS channels is under study. It is not guaranteed that the BSS could be completed isolated which would be a serious issue for the design. An analysis of the MHD pressure drop in a purely insulated BSS is shown in 5.3.

More importantly, the BSS channels contain a considerable amount of obstacles in the PbLi flow. The module attachments crosses both channels in the radial direction dividing part of the flow into two symmetrical parts as shown in fig: 5.3. The influence of these obstacles in the pressure drop depends on the possible distribution of the electrical insulation components in the BSS channels. As the presence of this components in the BSS is unclear it is hard to anticipate the weight of the obstacles on the total MHD pressure drop.

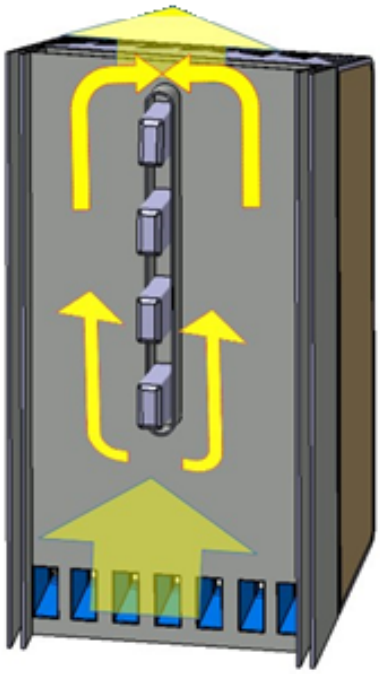

Figure 5.3: Back view of the BSS cold channel showing the attachments as an obstacle to the PbLi (yellow arrow) [46].

Regarding the obstacles, a substantially more complex situation is located in the vicinity of the inlet channels that connect the module with the cold BSS channel (fig: 5.2). These inlet channels not only constitute a grid of obstacles for the hot channel flow, which is an issue by itself, but they also contain a radial PbLi flow that can be electrically coupled with the hot channel flow depending on the configuration of the insulated components in this particular region. The

electrical coupling between 2 perpendicular flows is an unknown problem that has to be carefully evaluated. It is hard to anticipate their possible impact on pressure drop and flow partitioning. Specialized 3D analyses of this particular geometry are necessary to address this challenging problem.

Another important contribution to the pressure drop takes place in the connection between the BSS channels and the feeding and extraction PbLi pipes (fig: 1.15, sec: 1.4.1). Like in the inlet and outlet regions of the breeding zone, the contractions and expansions of the flow take place along every possible direction, including the direction parallel to the external magnetic field. As a consequence, these connecting regions are expected to have a very relevant contribution to the MHD pressure drop [110, 130].

5.2.4 Other sources of pressure drop

Besides the pressure drop caused by the purely geometrical aspects of the design, there are other processes that contribute to the total MHD pressure drop.

As already mentioned, the design of the European DCLL includes several parallel poloidal channels (both in the BSS and in the modules). Two adjacent parallel flows will be electrically coupled as the induced currents can flow from one duct to the other through the metallic wall. This effect can affect the flow partitioning between both channels as well as the total pressure drop [131]. The FCIs should mitigate this interaction which would be constrained to the gap flows making this contribution not as important as others. In a similar way that 2D fully developed computations are able to take into account the coupling between the gap flow and the bulk flow of a DCLL poloidal channel [126], this kind of fully developed calculations could provide a good first estimation of the importance of the electrical coupling between parallel channels.

Due to the FCI manufacturing and assembling procedures, the electrical insulation of the PbLi channels could present discontinuities in some points of the circuit. If that were the case, leak currents would reach the metallic structure through the discontinuitis producing an important increase of the pressure drop as predicted in [132].

Another issue is the pressure drop produced in the regions where the

magnetic field changes abruptly (fringing effect). This phenomenon has been observed experimentally [133] and analyzed theoretically [134]. The feeding pipes in the down side of each segment penetrate sharply into a region with a very intense magnetic field when approaching the vicinity of the reactor field coils (fig: 5.4). As a consequence, an additional pressure drop is expected in the feeding pipes. This effect appears in both sides; when the fluid enters the magnetic field region and when the fluid leaves it. As a consequence, similar pressure drop is also expected in the PbLi extraction pipes. 3D computations should be able to correctly estimate the pressure drop in these regions. A computation of the fringing magnetic field effect is presented in sec: 5.4.

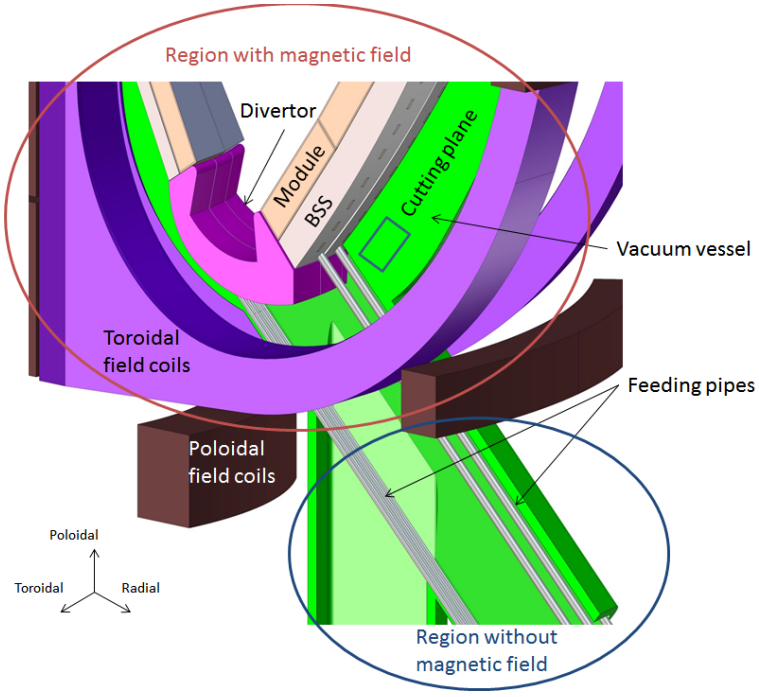

Figure 5.4: Schematic view of the bottom part of the BB. The toroidal field coils separates the region with magnetic field(surrounded in red) from the region without magnetic field (surrounded in blue).

Finally, the PbLi flow is be affected by magneto-convective effects. The blanket is heated up by the interacting neutrons and photons. They generates a directional power source that introduces high temperature gradients along the radial direction, especially in the front channels of the breeding zone. Previous analyses based on Q2D models [53] have shown that the velocity profile of these channels can be importantly affected by buoyancy effects [58]. The same kind of Q2D analyses are addressed for the European DCLL

channels to have a first estimation of the weight of the magneto-convective effects (sec: 5.7).

Tab: 5.3 exposes a summary of the pressure drop sources classified according to their expected importance for the design.

Note that, having analogous designs, every critical region or MHD issue of the OB module appears also in the IB module. The IB segments are immersed in a more intense external magnetic field which implies that the MHD pressure drop in the IB modules will be much higher for similar conditions. The MHD analyses carried out for this work are focused on the OB equatorial module as the design details of the IB modules are not as mature as the OB one. Analogous analyses of the IB modules should be performed in future.

MHD Pressure Source	Importance
Straight poloidal channels	Not very important[1]
Bends in the channels	Not very important
Connection between the BSS and the breeding zone	Very important
BSS curvature	Not very important
Obstacles in the BSS channels	Important
Connection between the feeding pipes and the BSS	Very important
Coupling between perpendicular channels	Unknown
Coupling between parallel channels	Not very important[1]
Discontinuities in the insulation	Important
Fringe magnetic field	Important
Buoyancy effects	Very important

Table 5.3: Summary of the MHD pressure drop sources in the European DCLL.

5.3 MHD analyses of the DCLL BSS

In this section, 3D MHD analyses of the BSS channels are presented. This computation is the only one performed with OpenFOAM of the present dissertation. As discussed in the previous section, the DCLL BSS is a complex system. The complete description of the BSS would be extremely expensive in

[1] Assuming good electrical insulation.

computational resources. In order to simplify the computations, the MHD analyses presented are based in the following assumptions:

1. Both channels are considered straight. Their curvature is neglected.
2. The obstacles present in the PbLi flow (connection pipes, stiffener plates, inlet holes...) are not considered.
3. The magnetic field is considered uniform in both channels (5.1 T pointing along the toroidal direction).
4. Each channel is considered at constant temperature (isothermal conditions).
5. The complex FCI configuration that would be needed for insulating the BSS channels is not considered in detail. Instead, it is assumed that the walls are perfectly insulating.

The previous approximations are assumed in order to minimize the computational cost of the calculations. The last one of them in particular allows two important simplifications. Firstly, the two channels are perfectly insulated from each other which means that the system can be treated as two individual subsystems. Secondly and more important, there is no need of solving the induction equation inside the walls. As mentioned, this is very convenient when working with OpenFOAM.

5.3.1 Input conditions

The present analyses are based on the version 2 of the European DCLL design (sec: 1.4.1). In particular, it is based in a subversion in which the BSS hot channel (or outlet channel) and the BSS cold channel (or inlet channel) flow anti-parallel. This idea was abandoned in the rest of the versions as the thermal behavior of this configuration is considered to be less efficient. Nevertheless, the assumptions of these calculations does not take into account the interaction between the parallel channels. Thus, the results can be directly applied to the DCLL version 1 as it is made in [135].

The inputs of the simulations are presented in tab: 5.4.

The relatively high Reynolds magnetic number, derived from the high velocity in both channels implies that the ϕ-formulation shall be avoided. Instead, B-formulation is used for these computations. Perfect insulating conditions written in this formulation adopt the form of Dirichlet boundary conditions for the induced magnetic field and the velocity field:

$$\vec{B_{ind}}|_{walls} = 0 \tag{5.2}$$

$$\vec{u}|_{walls} = 0 \tag{5.3}$$

	Inlet/Cold	Outlet/Hot
External field; B_0 (T)	5.1	5.1
Toroidal dimension; 2a (m)	1.16	1.16
Radial dimension (m); 2b	0.1	0.1
Length; L (m)	2.28	2.28
Average velocity; u_0 (cm/s)	15.77	16.26
Temperature; T (K)	573.2	823.2
Density; ρ (kg/m^3)	9839.7	9541.5
Viscosity; η (Pa s)	$2.15 \cdot 10^{-3}$	$1.02 \cdot 10^{-3}$
Electrical Conductivity; σ (S m^{-1})	$7.89 \cdot 10^5$	$7.2\ 8 \cdot 10^5$
Hartmann Number; Ha	$5.66 \cdot 10^4$	$7.89 \cdot 10^4$
Interaction Parameter; N	$7.67 \cdot 10^3$	$7.08 \cdot 10^3$
Reynolds Number; Re	$4.18 \cdot 10^5$	$8.78 \cdot 10^5$
Magnetic Reynolds Number; Rm	$9.07 \cdot 10^{-2}$	$8.63 \cdot 10^{-2}$

Table 5.4: Input parameters for the MHD calculations of the DCLL BSS.

It is important to recall that (5.2) is not strictly valid. The physical magnetic field does not go to zero abruptly in the walls even if they have null conductivity. Instead it can propagate among any media and rapidly falls to zero when move away from the walls. As a consequence, (5.2) is an approximation that can impact the results. This is an important limitation of the B-formulation which makes very convenient to solve the induction equation in the walls (even when σ_w=0) in order to ensure accurate results.

A hexaedral mesh with a linear grading in the directions perpendicular to the flow is used. The objective is having enough resolution close to the Hartmann and Side layers without expending too many resources in calculating the core flow. Nevertheless, the linear grading (the only one allowed by OpenFOAM)

is not the most adequate for MHD computations at high Hartmann numbers. The hyperbolic or exponential grading is much more convenient [109]. The mesh used is plotted in fig: 5.5.

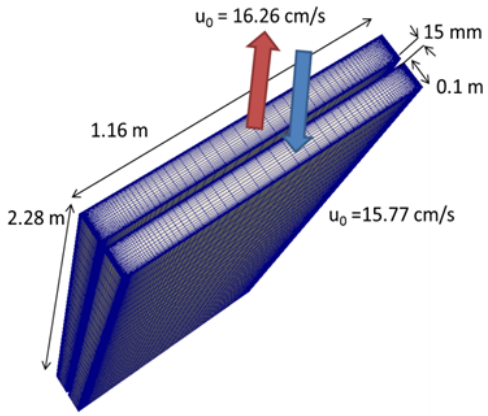

Figure 5.5: Scheme of the mesh used for solving the BSS flow.

5.3.2 Simulation results

As explained in sec: 5.1.1, a transient approach is used for computing the steady state. In this state, the velocity profiles of both channels are qualitatively similar (fig: 5.6). BLs appear close to the walls while the core flow remains approximately at the characteristic velocity.

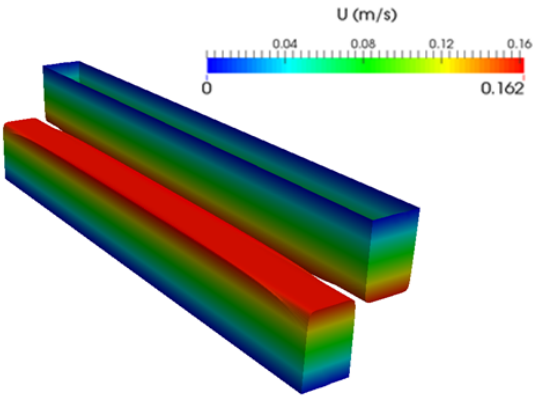

Figure 5.6: Velocity profile of the BSS.

Fig: 5.7 depicts the velocity along the central toroidal and central radial directions. The Hartmann and Side BLs can be observed.

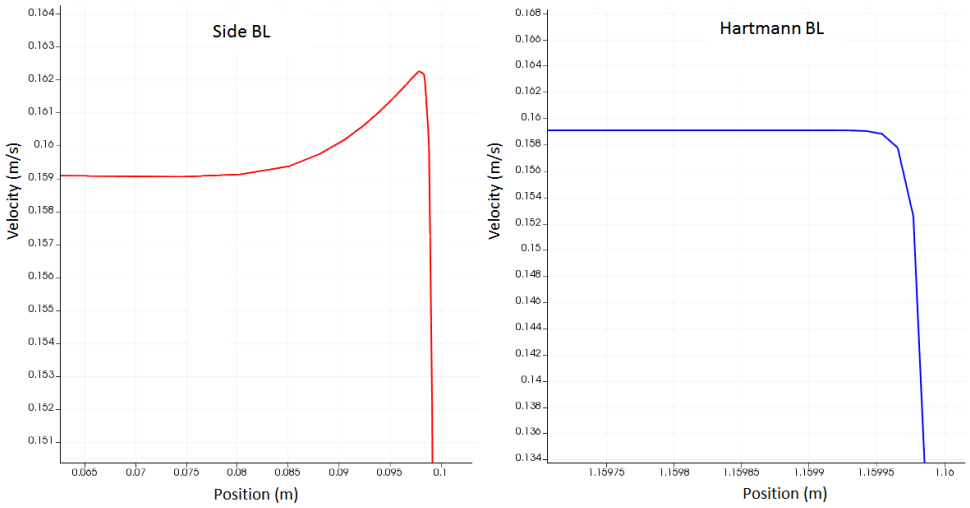

Figure 5.7: MHD BLs next in the BSS channels.

In the steady state all the induced currents are cross sectional (fig: 5.8) and the induced magnetic field points in the axial direction. This field exhibits a linear dependence with the toroidal coordinate (fig: 5.9) while it falls rapidly to zero next to the walls.

Concerning the pressure drop, once the system has reached the steady state, the pressure presents a linear profile whose slope is directly proportional to the core velocity of the flow and the conductivity of the PbLi at the operational temperature of the channel. The pressure drop along the axial direction is depicted in fig: 5.10.

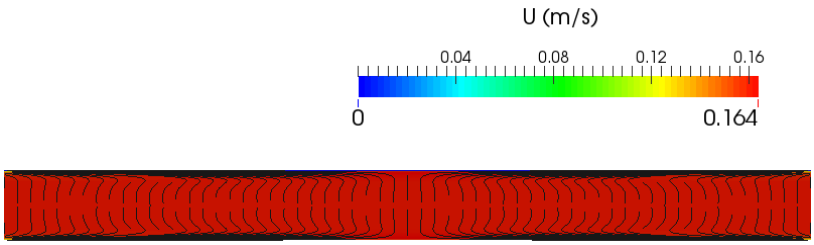

Figure 5.8: Induced currents in the BSS cross section.

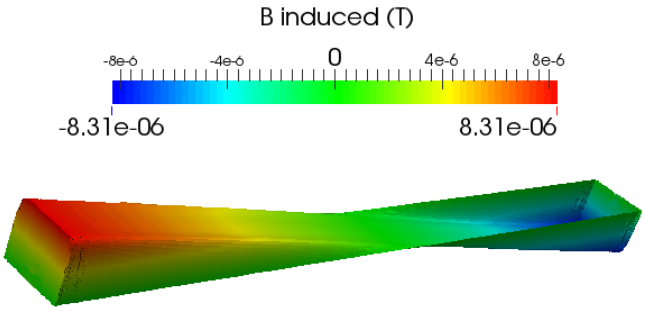

Figure 5.9: Induced magnetic field in the BSS cross section.

A pressure drop of 68.30 Pa/m has been obtained for the outlet channel while a pressure drop of 78.51 Pa/m has been found in the inlet channel. These relatively low values are consequence of the electrically insulated walls.

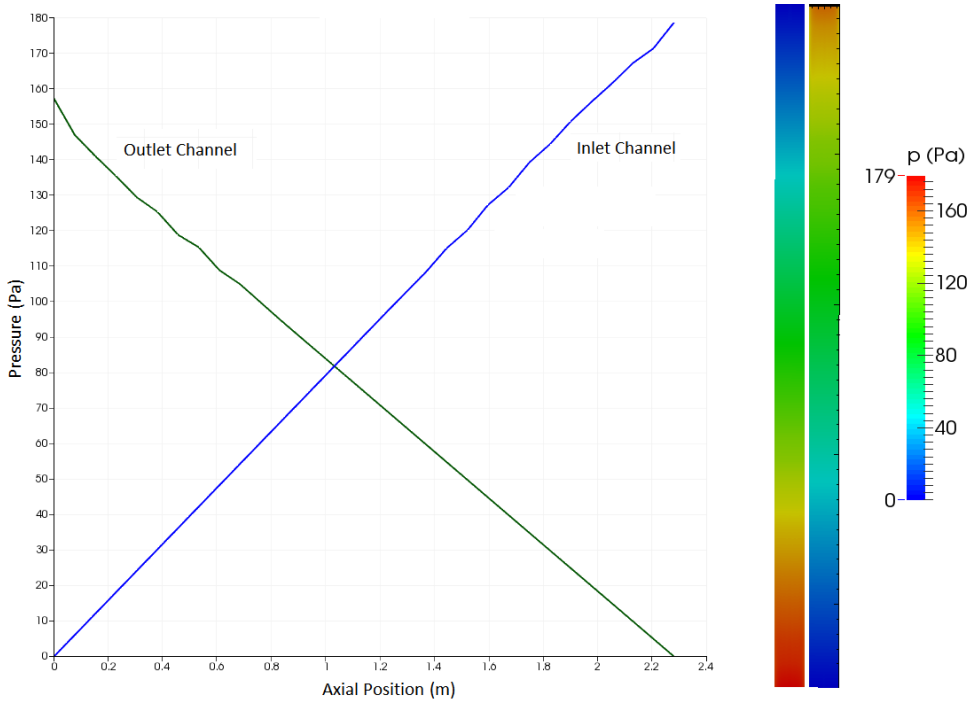

Figure 5.10: Pressure along the BSS channels.

5.3.3 Discussion

The results obtained with OpenFOAM for the BSS are limited by the approximations in which they are based. However, they are able to prove that

the MHD pressure drop of the BSS channels can be kept in tolerable values if good electrical insulation of the channel walls can be achieved. The 3D elements of the BSS (expansion at the inlet, obstacles,...) can still have very important contributions to the pressure drop as the FCI does not mitigate them. Dedicated analyses are mandatory for evaluating these issues.

Regarding the numerical matters, results are not satisfactory. The situation studied in this simplified analysis of the BSS should follow the Shercliff flow solution presented in sec: 2.1.5 [61]. However, the result obtained does not match with the analytic solution next to the side boundary layers. Indeed, the small jets that appear in fig: 5.7 should not appear. The M-shape obtained for the induced currents is also inconsistent as they should present a C-shape.

The previous effects indicate that the insulated walls are not correctly described with eq: (5.2). As mentioned before, the B-formulation is not well suited for imposing boundary conditions of perfect insulation. This is most likely the reason behind the numerical error. Taking into account that ϕ-formulation is not fully valid for high Reynolds magnetic numbers, it is mandatory to include the wall (even one with σ=0) as a physical domain in the computations if accurate results are wanted.

As mentioned in the sec: 5.1.1, for this dissertation it is preferred to use other CFD tools rather than OpenFOAM when dealing with multiple domains. The rest of the MHD and tritium transport computations presented in this document have been carried out with ANSYS-Fluent.

5.4 Pressure drop in fringing magnetic fields

In this section, 3D MHD pressure drop source associated to the MHD fringing effect is analyzed. It is the only MHD 3D problem that is treated directly in this work. The objective is showing the important impact that this kind of 3D geometries can have in the MHD pressure drop. The analysis has an academic approach rather than an engineering one as they do not reproduce the exact conditions of the DCLL feeding pipes when they crosses the DEMO field coils (fig: 5.4). These would be much more expensive from the computational point of view.

5.4.1 Input conditions

The analyzed system consist of a rectangular section channel in which a non-uniform transverse magnetic field is applied. The magnetic field is uniform in most of the channel volume but it exponentially falls to zero next to the inlet and outlet of the channel. The magnetic field distribution is exposed in fig: 5.11

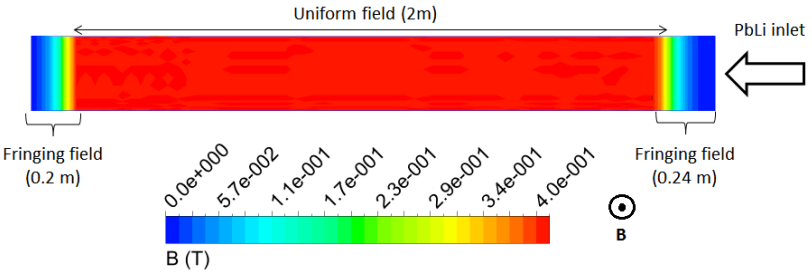

Figure 5.11: Non-uniform magnetic field distribution in a PbLi channel.

The inlet velocity in the channel is 1.7 cm/s. The magnetic field applied is 0.4147 T which is one order of magnitude smaller than the field in the blanket. This field reduction aims diminishing the computational time needed for reaching the steady state. Although this assumption makes the computations less relevant for the DCLL design, the Hartmann number is high enough for observing an important pressure drop in the fringing regions. All channel walls are considered perfectly insulated.

The dimensionless constants that define the regime of the system are exposed in tab: 5.5.

Hartmann Number; Ha	766.76
Interaction Parameter; N	64.30
Reynolds Number; Re	9072
Magnetic Reynolds Number; Rm	$1.32 \cdot 10^{-3}$

Table 5.5: Dimensionless parameters for the fringing magnetic field study.

In this study, the magnetic Reynolds number is of the order of 10^{-3}. This small value implies that the Φ-formulation of the MHD problems is valid. As explained in the previous section, this formulation allows using physical

boundary conditions in the insulating walls. That way the problem can be treated using only one domain.

5.4.2 Simulation results

The simulations have been launched using ANSYS-Fluent. Results have been obtained for the pressure field, the velocity field and the electric potential field. Fig: 5.12 shows the contours of the pressure field and the potential field in a central plane perpendicular to the external magnetic field.

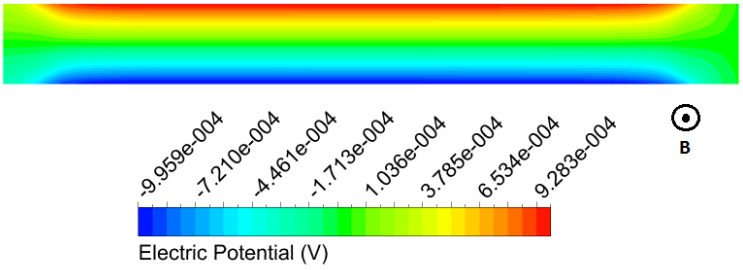

(a) Electric potential.

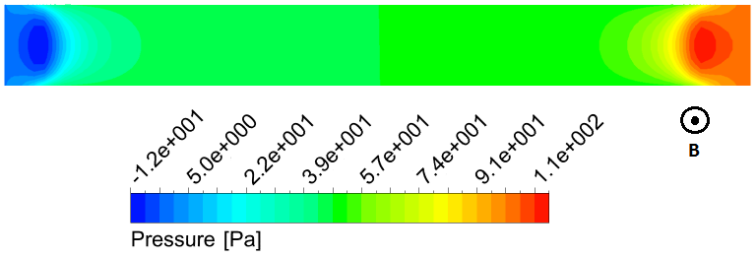

(b) Pressure field.

Figure 5.12: Contours of the electric potential and pressure field in a central plane perpendicular to the magnetic field.

In the center of the channel, where the fringing effects of the field are far enough, the flow evolves following the Shercliff analytic solution [61]. In such flows the electric potential depends linearly with the direction perpendicular to the magnetic field. Besides, the flow is fully developed in this region. Therefore, the pressure depends linearly with the axial coordinate and the velocity profile is almost flat (fig: 2.3, sec: 2.1.5). Neither the pressure, nor the electric potential depends on the coordinate parallel to the magnetic field.

Close to the inlet and outlet of the channel, where the magnetic field grows or falls exponentially (fringe regions), the flows behaves differently. In these regions there are currents with important axial components rather than the cross sectional currents characteristic of fully developed flows. As a consequence, a high current density region is developed in the fringe areas. The pressure drop increases heavily in those regions due to the increase of the Lorentz forces (fig: 5.12b).

Fig: 5.13 shows the induced currents next to the inlet of the channel in the central plane perpendicular to the magnetic field. A vector plot of the velocity is also depicted where it can be observed that the flow tends to accumulate close to the Side BLs where the Lorentz forces are weaker.

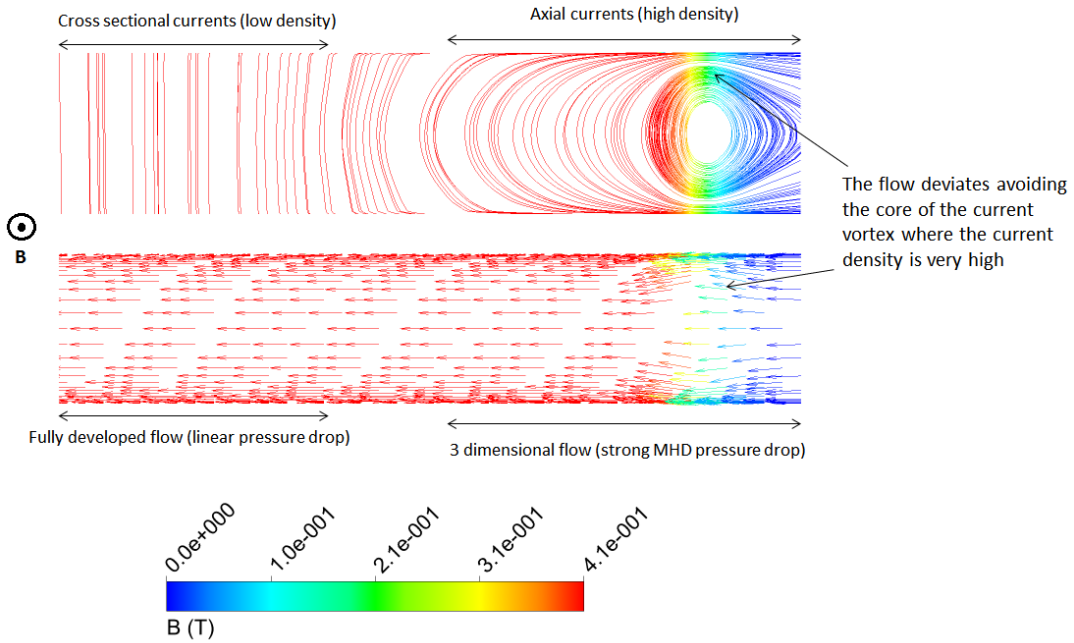

Figure 5.13: Induced currents and velocity vectors next to the fringing regions. The lines and vectors are colored following the external magnetic field contours.

The cross sectional velocity profile in the middle of the fringing region is shown in fig: 5.14. Two jets are developed next to the BLs as a result of the 3 dimensional (axial) currents.

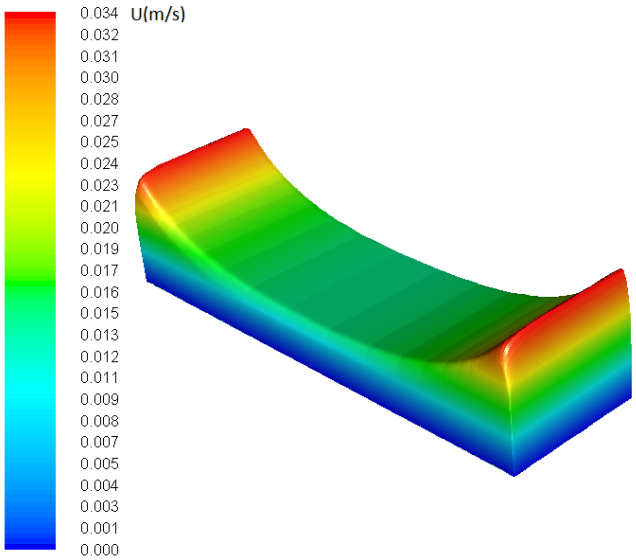

Figure 5.14: Velocity profile in the middle of the fringing region.

For computing the MHD pressure drop caused by the fringing effect, the pressure drop along the central axis of the channel is plotted together with the pressure drop along an axial line close to the Side BL in fig: 5.15.

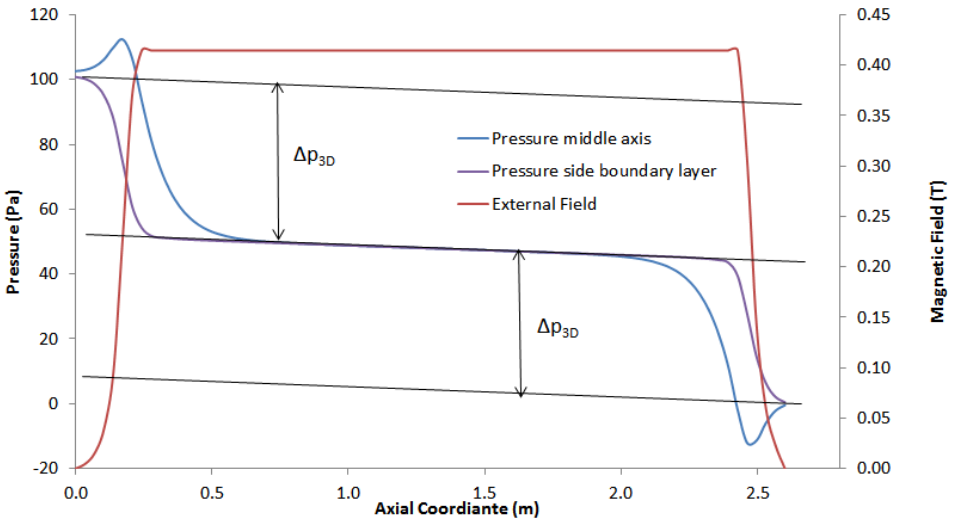

Figure 5.15: Pressure drop along different axis of the channel.

The pressure drop obtained in the central region is 2.995 Pa/m which deviates 0.58% from the Shercliff solution (2.999 Pa/m) eq: (2.55). The 3D pressure drop of the fringing region is defined as the difference between the

pressure at the inlet (or outlet) of the channel and the pressure at the inlet (or outlet) of a channel under a uniform field (e.g. [120]).

The fringing regions at the inlet and at the outlet are slightly different. As a consequence the 3D pressure drops obtained are 49 Pa at the inlet and 43.6 Pa at the outlet. This corresponds to $\zeta = 8.72$ and $\zeta = 7.77$ at the inlet and outlet, respectively.

5.4.3 Discussion

This analysis of the magnetic field fringing effect allows understanding the important role that the MHD 3D effects play on the total pressure drop in the blanket. Indeed, the 3D pressure drop of this example is more than one order of magnitude higher than the pressure drop caused by the straight regions of the channels.

The 3D pressure drop caused by the fringing field will grow with the Hartmann number. Therefore, a ζ parameter at least one order of magnitude bigger than the one obtained in this study is expected in the feeding and collecting pipes of the DCLL.

It is worth mentioning that this contribution is independent of the pressure drop reduction mechanisms. The geometry of the pipes may be optimized trying to reduce this contribution as much as possible but only small reductions shall be expected with these methods. The pressure drop caused by the fringing effect affects every PbLi-based concept unavoidably. Thus, finding accurate correlations for the ζ parameter are of great interest for blanket designing.

5.5 MHD evaluation of different FCI designs

Contrary to the previous analysis of the magnetic fringing effect, the present study is based on realistic EU-DCLL conditions. This way, without losing its academic purpose, the work gains the engineering relevance needed for the design activities.

The system of study is the central front poloidal channel of one DCLL OB equatorial module (version 3). The calculations are focused on the straight regions of the channel and, thus, they do not take into account any effect produced by the 3D elements of the geometry. The main objective is to analyze and compare the response of different alumina-based FCI designs. Fig: 5.16 depicts a sketch of the 3 different FCI designs that are under consideration for the DCLL. These options are: a thin sandwich design (0.5 mm steel-0.1 mm alumina-0.5 mm steel) [39] which is considered the baseline option, a thick sandwich design (1 mm steel-5 mm alumina-1 mm steel) and a naked alumina design (5 mm alumina) [136].

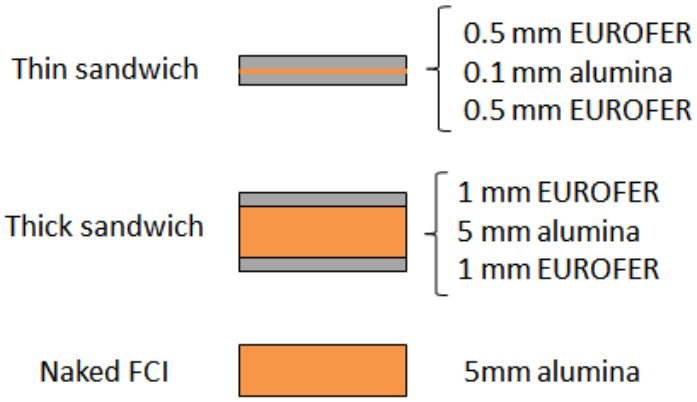

Figure 5.16: FCI design options under consideration for the European DCLL showing the alumina in orange and the EUROFER in grey.

5.5.1 Input conditions

As it can be observed in the module design (fig: 1.16, sec: 1.4.1), most of the PbLi flow path consists of straight parallel poloidal channels. The magnetic field points to the toroidal direction. Thus, it lays transversely to the PbLi flow. In order to mitigate the MHD pressure drop, FCI are placed embedded in the PbLi channels. The flow is consequently divided into two regions called bulk flow and gap flow following the terminology first employed in [126]. If the insulation is not perfect, both regions can interact electrically through the FCI. Inheriting the name of the BLs, the gap flow perpendicular to the magnetic field is usually called Hartmann gap while the gap flow parallel to the magnetic field is usually called Side gap. The corresponding walls next to the gaps are usually referred

as Hartmann walls and Side walls, respectively. Fig: 5.17 shows a sketch of one DCLL front central channel cross section.

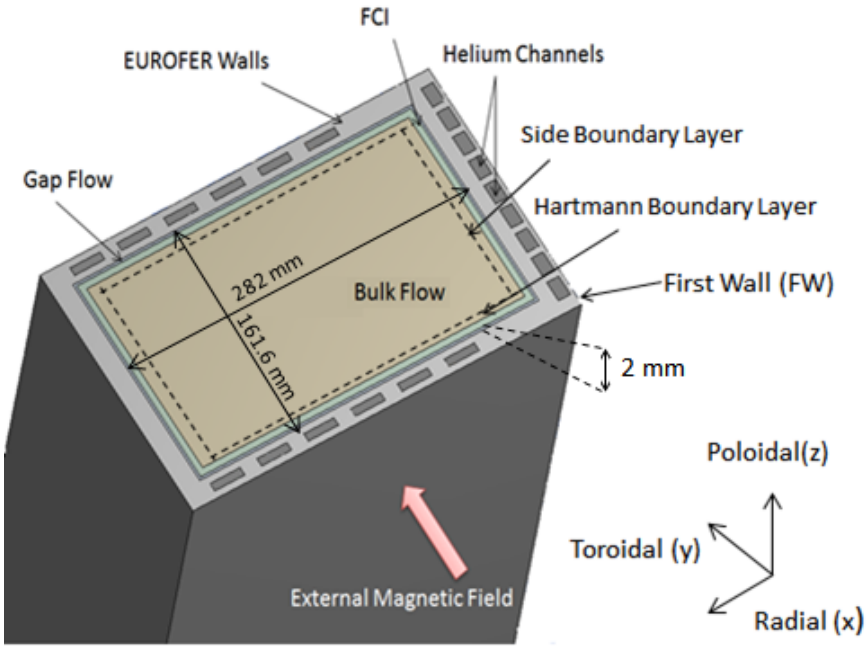

Figure 5.17: Sketch of the cross section of one DCLL central front channel showing the bulk flow, the gap flow, the FCI, the He channels and the MHD BLs.

The computations of this sections are based on the fully developed flow approximation described in detailed in sec: 2.1.3. The applicability of 2D MHD models in straight channels with FCI under transverse magnetic fields is discussed in [126]. Far from the 3D elements of the design (inlets, bends...) and when neither transient effects nor buoyancy effects are considered, the flow is expected to be fully developed.

In order to obtain convergence it is necessary to adapt the computational mesh to the heavy MHD requirements. So as to have enough resolution to resolve the Hartmann layers, it is necessary to provide a sufficient amount of mesh points in the layer, whose thickness scales with Ha^{-1}. Following the criteria described in [109], a hyperbolic mesh grading has been applied from the center of the flow to the layers. Fig: 5.18 shows a part of the computational mesh used for the thin sandwich FCI computation. The meshes used for the other two FCI designs have the same kind of grading.

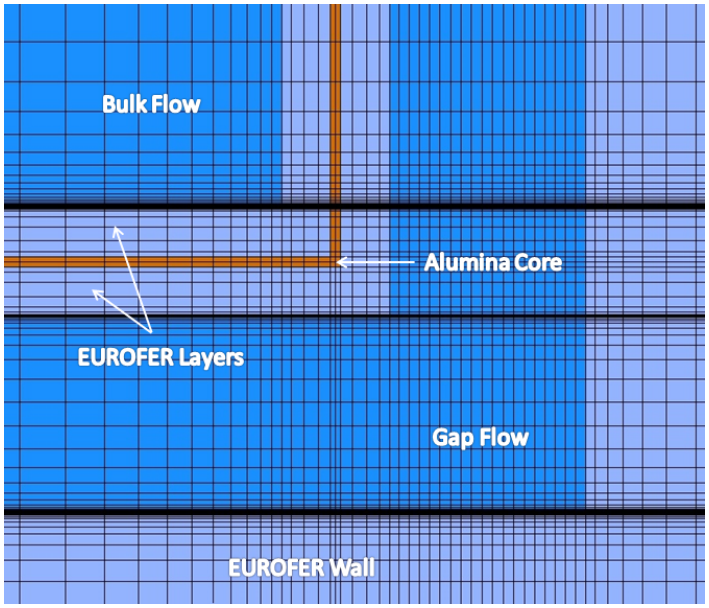

Figure 5.18: Detailed part of the computational mesh used for the thin sandwich FCI design.

The MHD velocity profiles computed with the 2D fully developed models have been used as an input for a steady-state 3D heat transfer analysis. The energy equation derived in sec: 2.2 is solved for the 3 FCI design options under consideration in order to study their influence on heat transfer between the He and PbLi.

A prototypical exponential shaped function along the radial direction (x) has been used for the volumetric thermal generation (5.4). The parameters of the function have been taken according to the result of the best fitting of the neutronic data concerning the European DCLL [137]. In the case of the OB equatorial module front channels the parameters are: $q = 7.41$ W/cm^3, $b = 6.3$ m^{-1} and $\omega = 0$ m (the point x = 0 is defined at the external side of the FW). Integrating the function in the channel volume a total heat generation of 0.2807 MW is obtained.

$$S_q = q \exp(b \cdot x + \omega) \tag{5.4}$$

Instead of computing the complete He flow inside the EUROFER, convective boundary conditions have been considered at the external side of the walls.

$$q = h_{He}(T_{wall} - T_{He}) \tag{5.5}$$

The convective boundary condition requires providing the helium temperature (T_{He}) and the heat transfer coefficient (h_{He}) in each wall of the channel. Instead of using an average He temperature, the results of a 1D heat transfer code developed for the DCLL design activities (PLATOON code [46]) have been employed. This code models the complete OB equatorial module. It discretizes the PbLi and He flows only along their respective flow directions (similarly to the tritium transport model described in chap: 4). Both flows are connected across solid materials with the appropriate surfaces, thicknesses and thermal properties. Heat generation inside the components of the model is also considered when needed. This 1D code does not take into account the specific shape of the PbLi and He velocity profile. Instead, it considers heat transfer between the fluids and the solid walls occurs by convection 5.4 and calculates h by means of empirical correlations of the Nusselt number. For the PbLi, the heat transfer coefficient is based on an experimental correlation obtained for flows under transverse fields and insulating walls [138]. At the interface between the steel and the He the code uses the Gnielinski correlation [139].

According to the results of the 1D model, the He temperature in the FW channel follows an almost linear profile. The He enters the bottom part of the channels at 317.7°C and leaves the top part at 433°C. This same linear profile has been imposed as boundary condition in the FW He channels for the present heat transfer calculations. An average heat transfer coefficient of 3084 W/m^{2}K has been established in the FW He channels based on the 1D model outputs.

Once the He exits the FW channels it descends through the radial walls. The 1D model predicts an increment of less than 4°C in the helium temperature between the top part and the bottom part of the radial walls (from 434.4°C to 437.6°C). Taking into account this almost uniform temperature, a constant He temperature of 436°C has been considered in both radial walls for the present heat transfer computations. Like in the FW He channels, an average heat transfer coefficient has been established in the radial walls He channels (3366.5 W/m^{2}K). Fig: 5.19 depicts an sketch of the He circulation showing the temperatures computed with PLATOON.

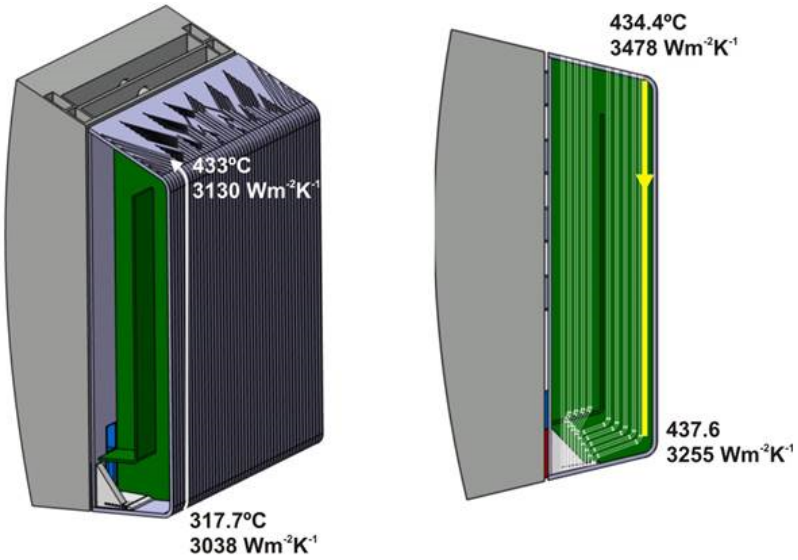

Figure 5.19: Helium flow path and temperatures in the DCLL (version 3).

The design of the DCLL module does not include He channels in the rear wall. A zero flux boundary condition has been imposed as a first approximation.

The dimensions and magnetic conditions used in the simulations are the ones of one DCLL outboard equatorial module central front channel (fig: 5.17). The FW and the radial walls are cooled with He flowing in rectangular channels inside the steel. The He channels introduce anisotropy in the wall electric conductivity that could alter the behavior of the PbLi flow (see sec: 5.6). However, according to previous studies these effects are expected to be small and located next to the MHD BLs [117]. As a first approach, the thicknesses of the steel walls have been readjusted to effective values extrapolated through the volume fraction steel/helium of the walls. The main input data used in the simulations are summarized in tab: 5.6.

The mechanical, electrical and thermal properties of PbLi [140, 141] and EUROFER [142, 143] used in the computations are exposed in tab: 5.7. The expected PbLi inlet and outlet temperatures in the front channel are approximately 300°C and 500°C, respectively. As a consequence, an average temperature of 400°C has been used for the PbLi properties. In this channel, EUROFER temperatures are expected to be in the range of 400-550°C, reaching the maximum temperature in the FCI layers. Taking into account the small variation of the EUROFER properties in this range, these at 500°C has been used for the computations.

Input Parameter	Value
Toroidal Size; 2a (mm)	161.6
Radial Size; 2b (mm)	282
Length; L (m)	2
Gap Thickness; t_{gap} (mm)	2
First Wall thickness; t_{fw} (mm)	18.64
Radial Walls thickness; t_{sw} (mm)	13.48
Rear Wall thickness; t_{rw} (mm)	16.5
Flow rate; F_0 (L/s)	0.775
PbLi inlet temperature; T_{in} (°C)	308
First wall He inlet temperature; $T_{He\ FWin}$ (°C)	318
First wall He outlet temperature; $T_{He\ FWout}$ (°C)	433
Radial walls He average temperature; $T_{He\ SW}$ (°C)	436
External Magnetic Field; B_0 (T)	4.147

Table 5.6: Input parameters for the FCI comparison study.

The electric properties of the alumina considered for the present FCIs have been measured in recent experimental campaigns [136] whose results show a very good electrical insulating capability in a large temperature range (200-600°C). Alumina thermal properties are taken from the commercial specifications of the KA997 aluminum oxide.

	PbLi	EUROFER	Alumina
ρ (kg/m^3)	9720	7608	3950
σ (S/m)	$7.63 \cdot 10^5$	$8.33 \cdot 10^5$	10^{-8}
η (Pa s)	$1.497 \cdot 10^{-3}$	–	–
Cp (J/kg K)	189	730	880
κ (W/m K)	15.14	30.35	28

Table 5.7: Materials properties used in the FCI comparison study.

5.5.2 Pressure drop and flow distribution results

Results for 3 different FCI designs have been obtained. For comparison purposes the velocity profile of the central front channel without FCI has been calculated as well. The obtained velocity profiles are exposed in fig:5.20.

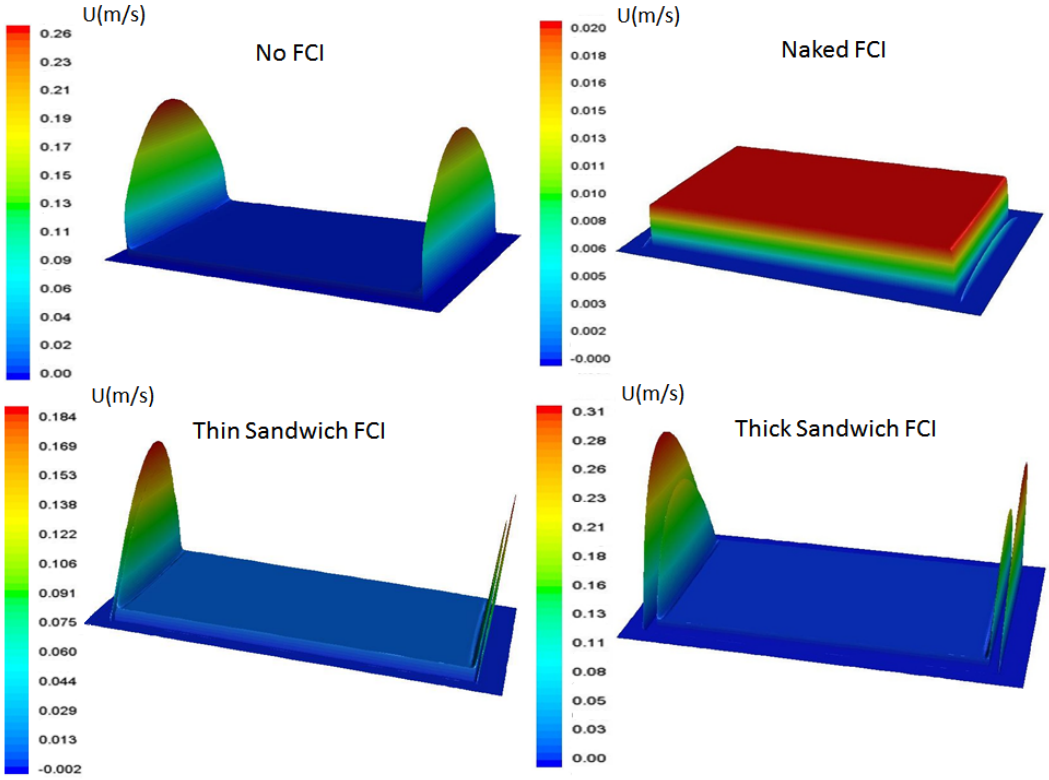

Figure 5.20: Velocity profiles for the central front channel with 3 different FCI designs and without FCI.

Analyzing the velocity profiles it can be deduced that the alumina is able to effectively decouple the bulk flow from the gap flow. Indeed, the naked alumina FCI case exhibits in the bulk flow the characteristic flat profile of a rectangular channel with perfectly insulating walls (Shercliff flow [61]). This implies that there is no interaction between the bulk flow and the gap flow. For the two sandwich-like FCI designs there is also an effective decoupling between the bulk flow and the gap flow, but in these cases EUROFER layers are in contact with the PbLi. Those layers act as thin conducting walls which produce the characteristic MHD flow of a channel with conducting walls: a flat core and two jets in the Side layers [144].

Qualitatively, the gap flow behaves similarly for the three FCI designs. Fig: 5.21 shows the current distribution of the thin sandwich FCI case. It can be observed that the currents in the gaps next to the Side walls (Side gaps) flow mainly in the toroidal direction, parallel to the external magnetic field. As

a consequence, the Lorentz forces in these gaps are small and viscous effects are dominant. It causes an almost parabolic profile along the radial direction (fig: 5.22). The opposite situation takes place in the gaps next to the Hartmann walls (Hartmann gaps). In these regions the currents are mainly perpendicular to the external field and the Lorentz forces are very intense. Therefore, the flow is almost static and the vast majority of the gap flow goes through the Side gap.

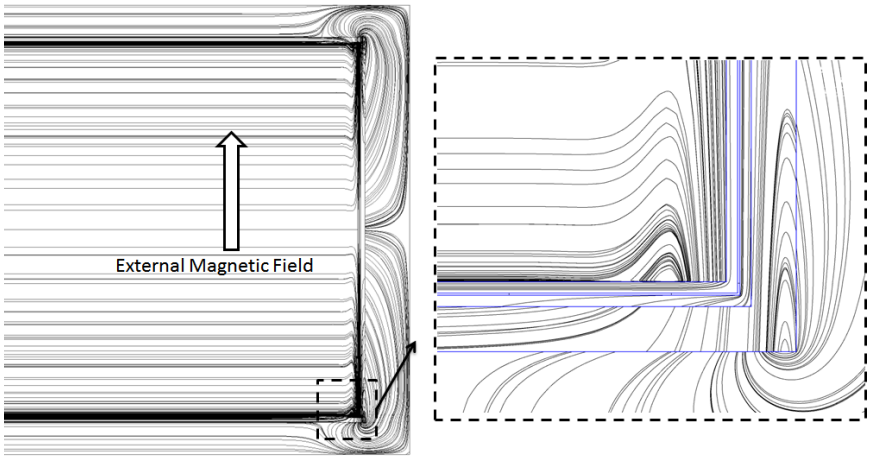

Figure 5.21: Current distribution for the DCLL central poloidal channel with a thin sandwich FCI.

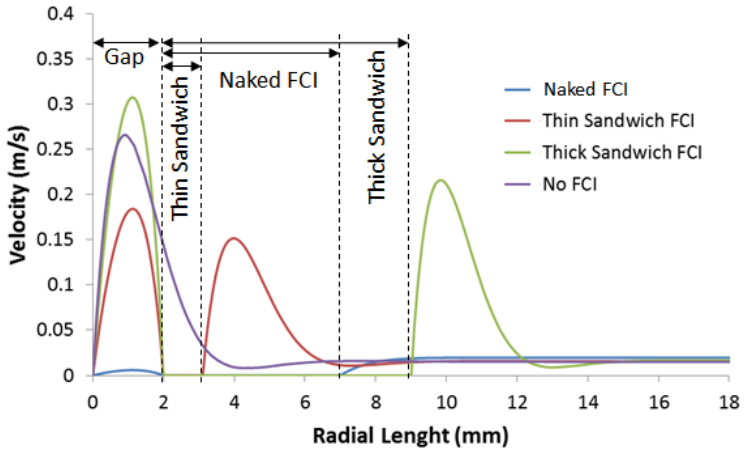

Figure 5.22: Axial velocity next to the Side wall along a radial line that crosses the center of the channel (y = 0).

The total flow rate in the four cases is the same (0.775 L/s) but the MHD phenomena affects the flow partitioning between the bulk and the gap regions. For the sandwich-like FCI designs, the high resistance that the MHD forces impose on the bulk flow makes that a significant flow rate goes through the Side gaps where the resistance is much lower. This causes high velocity jets in the gap flow. Besides the MHD effects, the geometry of the channels has an impact on the velocity scale as the cross sectional area depends on the FCI thickness. As a consequence, mean velocities are different even the flow rate is not. In order to compare the profiles, a 2D plot along a straight radial line that crosses the center of the channel is presented in fig: 5.22.

From these 2D fully developed analyses useful information can be obtained. The pressure drop per unit length associated to the different FCI designs is exposed in tab: 5.8. The pressure drop reduction factor associated to each FCI design is shown as well. This magnitude is defined as the ratio between the pressure drop of a channel without FCI $(\Delta p/\Delta z)_0$ and the pressure drop of the same channel with FCI.

	$\frac{\Delta \mathrm{p}}{\Delta \mathrm{z}}\left(\frac{\mathrm{Pa}}{\mathrm{m}}\right)$	$\frac{\left(\frac{\Delta \mathrm{p}}{\Delta \mathrm{z}}\right)_0}{\left(\frac{\Delta \mathrm{p}}{\Delta \mathrm{z}}\right)}$
No FCI	34224.6	–
Naked FCI	36.1	948.05
Thin Sandwich FCI	1739.5	19.67
Thick Sandwich FCI	3861.1	8.86

Table 5.8: Pressure drop associated to 3 different FCI designs.

The naked FCI provides the best pressure drop mitigation as it has no EUROFER in contact with the bulk flow which reduces significantly the density of induced currents (and the Lorentz forces). In the sandwich like FCI designs the thickness of the EUROFER layer is the parameter that determines the pressure drop mitigation. No matter how perfect the electrical insulation properties of the alumina core are, the steel layer always reduces significantly the FCI effectiveness.

In tab: 5.9, the velocity of the flat core in the bulk flow is shown together with the average velocity. The peak velocity of the jets at both sides of the FCI next to the Side wall is shown as well. Moreover, the percentage of flow that

goes through the bulk and the gap is exposed in tab: 5.10. The total flow rate is the same in every case ($F_0 = 0.775$ L/s).

	U_{core} (cm/s)	U_{avg}(cm/s)	U_{jets} (cm/s)	
			Bulk	Gap
No FCI	1.48	1.17	26.60	–
Naked FCI	1.97	1.88	–	0.59
Thin Sandwich FCI	1.59	1.74	15.41	18.72
Thick Sandwich FCI	1.64	1.95	21.51	30.69

Table 5.9: Characteristic velocities of the fully developed flow computations.

	$\frac{F_{Bulk}}{F_0}$(%)	$\frac{F_{Gap}}{F_0}$(%)	
		Side	Hartmann
No FCI	100	–	–
Naked FCI	99.77	0.2297	0.0003
Thin Sandwich FCI	92.87	7.113	0.017
Thick Sandwich FCI	88.15	11.809	0.041

Table 5.10: Flow distribution for 3 different FCI designs.

From the computational results it can be observed that for all FCI design there is a very small percentage of flow rate through the Hartmann gap. This situation is especially pronounced for the naked FCI design. In both sandwich-like designs, a high flow rate goes through the Side gaps which is translated into high velocities jets in these regions. This effect is more prominent for the thick FCI design.

5.5.3 Heat transfer results

Results of temperature contours for the central radial-poloidal plane and for the mid sectional plane are exposed in fig: 5.23 and 5.24, respectively.

Analyzing the previous figures, it can be observed the effect of the MHD velocity profile over heat transfer. On the one hand, the exponential generation profile produces important temperature differences along the radial direction.

On the other hand, the small velocities in the Hartmann gaps turn them into hot regions. The result of both phenomena is the oval shape of the temperature contours that can be observed in fig: 5.24.

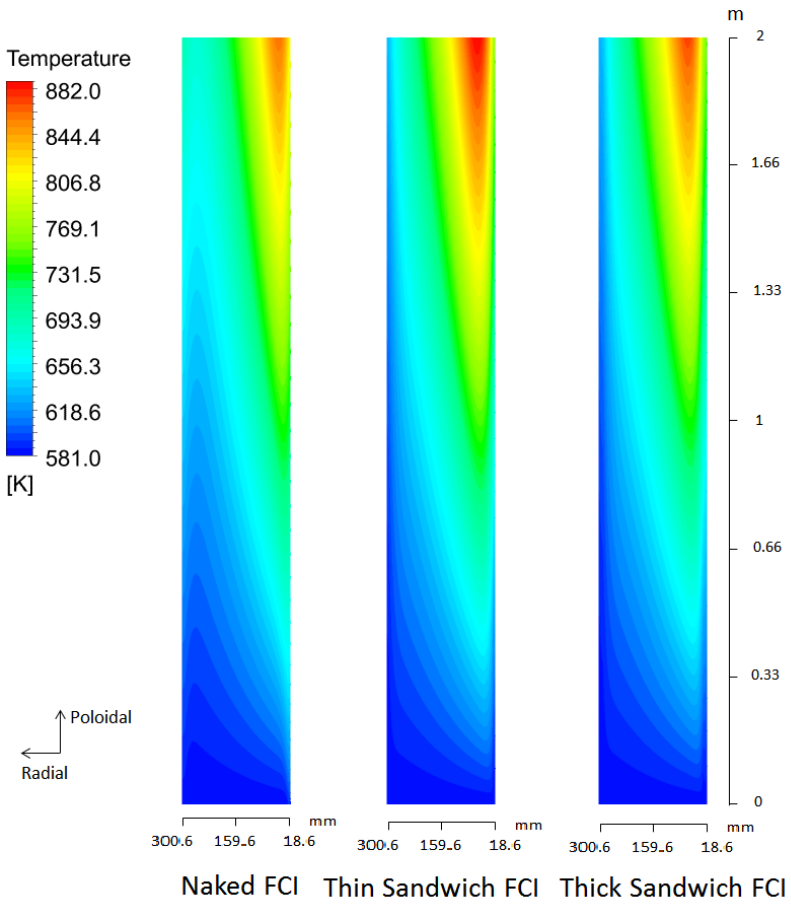

Figure 5.23: Temperature contours in the central radial-poloidal plane.

From this analysis the heat losses from the PbLi to the He circuit can be derived. It is worth mentioning that the heat flows through the channel walls in both directions. Locally, there are regions where the PbLi is colder than the He. In this regions, the heat flows from the He to the PbLi. This is true mainly next to the inlet. However, in the majority of the system the PbLi is hotter than the He which is translated into a heat flux from the PbLi to the He. By integrating the heat flux along the contact surface the total heat that goes from the PbLi to the He can be obtained (tab: 5.11).

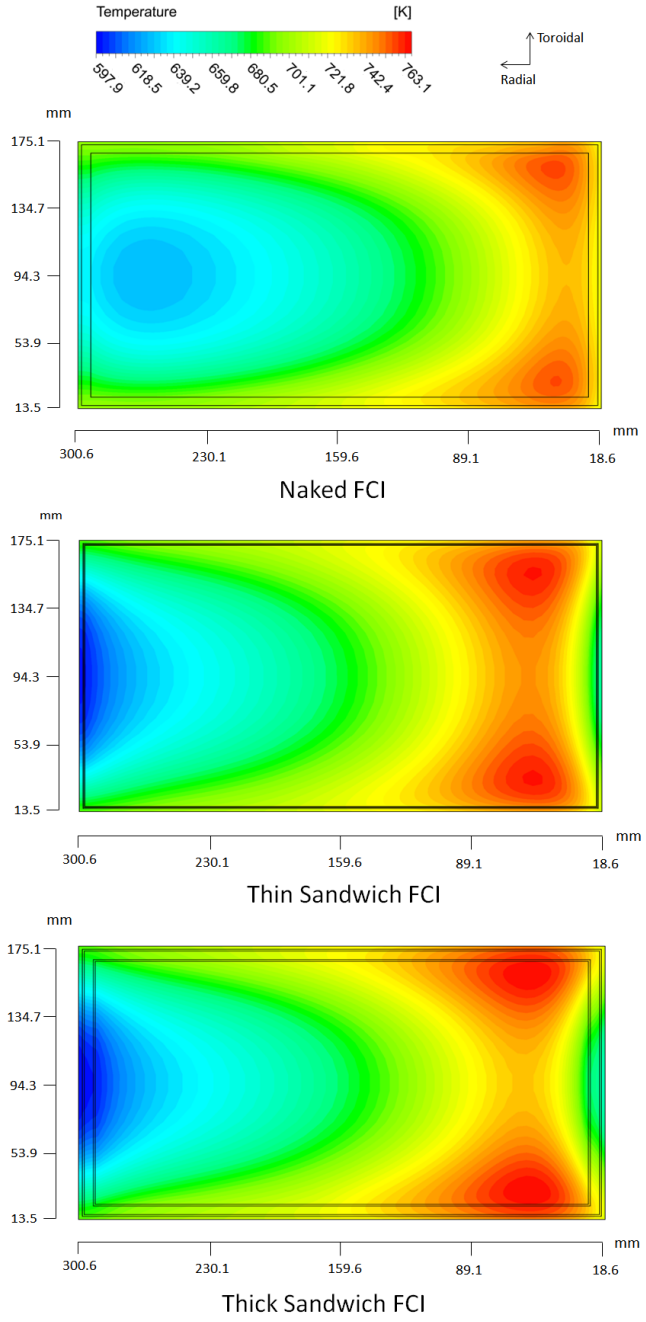

Figure 5.24: Temperature contours in the middle section (z=L/2).

The naked FCI design develops small velocities in the gap next to the FW compared with the other two designs. For this reason the heat flux from the PbLi to the He circuit in the FW is much higher. In fig: 5.23 and 5.24 it can

be observed that the temperature next to the FW is lower for the sandwich-like designs as the Side jets cool the FW more efficiently.

The almost stagnant flow in the Hartmann gap made that, in these regions, the heat flows almost exclusively by conduction along the sectional planes. This causes that the heat flux through the radial walls is significantly affected by the thickness of the FCI. Indeed, the heat generated in the bulk zone is mostly removed by the PbLi flow while the heat generated in the Hartmann gap and in the FCI is removed either by the cooling effect of the bulk flow or the He flow, depending on the zone. In the case of the thin FCI there is more heat generated in the bulk zone because of its smaller volume while in the other 2 designs there is more heat produced inside the FCI. For this reason, in the thick designs the magnitude of the heat transferred to the Hartmann gap and extracted by the helium flow is higher than in the case of the thin FCI (tab: 5.11).

	q_{FW} (W)	q_{Radial} (W)	$\frac{q_{He}}{q_0}$(%)
Naked FCI	21926.83	10890.78	11.69
Thin Sandwich FCI	10890.26	810.88	4.17
Thick Sandwich FCI	10675.39	9185.24	7.07

Table 5.11: Net heat fluxes through the channel walls (from PbLi to He) for 3 different FCI designs.

According to the present calculations, the Grashof number in the OB front channels is $Gr = 2.93 \cdot 10^{10}$ which is one order of magnitude less than the preliminary estimations given in tab: 5.1. This value is more accurate but still not completely representative as the buoyancy forces have not been taken into account in the pressent calculations. Regardless, considering the high Grashof number obtained, it is expected that the temperature variations in the channel cross section (fig: 5.24) will generate buoyancy effects that can affect the velocity profile [58] and consequently the heat transfer. In order to analyze the buoyancy phenomenon, magneto-convective computations including the coupling between temperature field, the magnetic field and the velocity field are presented in sec: 5.7.

5.5.4 Discussion

Sandwich-like FCI and naked FCI present different benefits and drawbacks. Velocity profiles of the sandwich-like designs are significantly different compared with the naked design. The EUROFER layers of the sandwich FCI allow tangent currents to penetrate in it. This entails to the jet formation next to the Side BLs. Besides, the pressure drop reduction factor of the sandwich-like concepts is severely affected by the thickness of the EUROFER layers. From this point of view, the thick sandwich design is the less effective option of the ones studied.

Not having any steel layers, the naked FCI provides the best pressure drop mitigation. However, the flow partitioning between the bulk flow and the gap flow is very unalike for this design. The small flow rate through the gap causes hotter regions next to the FW in comparison with the sandwich-like designs. For the naked FCI more than 11% of the energy generated in the channel goes to the He circuit. From this point of view, the thin sandwich FCI design provides the best thermal behavior as only 4.17% of the energy generated in the channel goes to the He circuit.

The viability of any FCI design depends on more factors than the ones analyzed. For example, the jets of the sandwich-like concepts provide a better cooling of the FW but the high velocities that exhibit (0.1 m/s) could be unacceptable from the corrosion point of view [41, 43]. Besides, the temperature gradients between the faces of the FCI might lead to important thermal stresses. This could be critical for the sandwich like designs where different thermal expansion coefficients of the alumina and the EUROFER would produce unacceptable stresses in the FCI [136]. These deformations could potentially affect the flow partitioning and the gap flow velocity profile as well. The pressure difference between the gap flow and the bulk flow can also produce stresses in the FCI. Pressure equalization holes or slots (e.g. [32]) have been proposed for solving this problem. However, they present important manufacturing difficulties. Experimental analyses are planned for testing the FCI performance in PbLi loops under relevant magnetic field. They could help determining whether this pressure difference will present mechanical problems for the FCI or not.

5.6 Effect of the helium cooling channels on the PbLi gap flow

According to the results of the previous sections, the gap flow and bulk flow are electrically decoupled in any DCLL PbLi channel at least far from the 3D elements of the design. Besides, according with the tritium transport model described in sec: 4.3.3.1, the gap flow and the bulk flow are also completely decoupled from the tritium transport point of view, as the alumina is a very efficient permeation barrier.

Unfortunately, alumina is not a good thermal insulator (its conductivity is very similar to the EUROFER's). As a consequence, the bulk flow and the gap flow are thermally coupled with the implications that this may have on the flow.

Nevertheless, as a first approach, the gap flow can be treated independently from the bulk flow, at least for performing MHD and tritium transport analyses. With this purpose, dedicated MHD analyses of the gap flow geometry are presented in this section.

The objective is not repeating the fully developed analyses of sec: 5.5.2. In this case, the attention is moved to the anisotropy introduced by the He channels in the wall electrical conductivity. Studying the effect of the He channels is important for following tritium transport analyses (sec: 6.5) as these He channels act as the tritium sinks.

5.6.1 Input conditions

The present analysis considers only the gap flow of the DCLL OB front channel (version 3). As in sec: 5.5.2, MHD fully developed models are used for computing the velocity profile. It is worth mentioning that the flow rate that goes through the gap used as input for this computation (0.17825 L/s) comes from results of the previous section. The flow partitioning between the bulk flow and the gap flow is presented in tab: 5.10.

For this analysis, only the base-line FCI; the thin sandwich FCI [39], is considered. As a consequence, only the external EUROFER layer of the FCI is modeled as it effectively acts as the internal wall of the annular geometry (gap

flow).

Concerning the external walls of the flow, the geometry of the central front channel of the DCLL OB equatorial module is used. The complete set of He channels present in this channel is considered at their exact design location. The electrical coupling between parallel PbLi channels is not considered. For this reason, only half of the radial walls and half of the back wall are modeled as the other half belong to the adjacent channel. Fig: 5.25 shows the geometry modeled in this calculation.

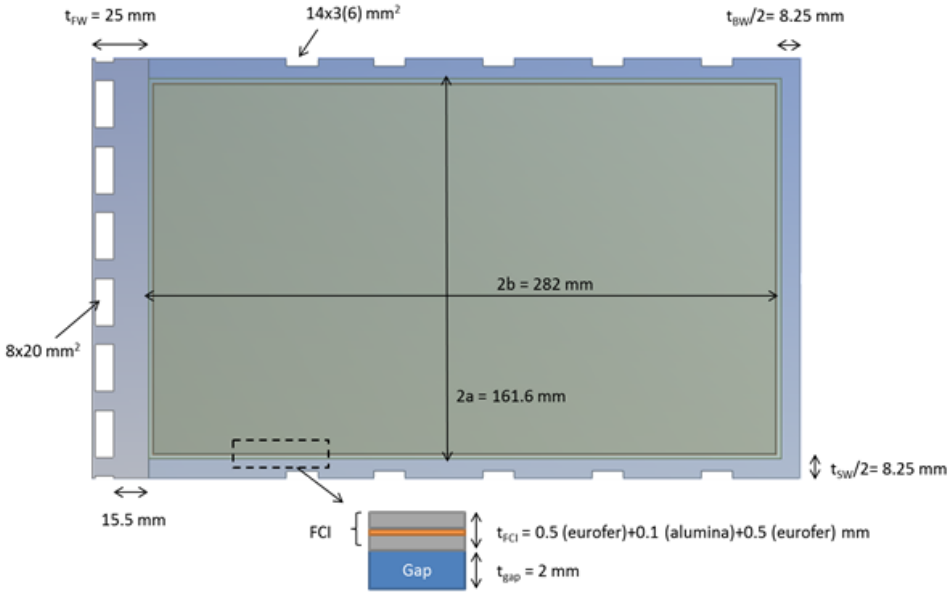

Figure 5.25: Geometry of the OB equatorial front channel showing the distribution of He channels among the walls.

Including the He channels in the model implies a more complex and larger mesh, especially if multi-block hexahedral meshes are wanted. Fortunately, this potential increase in the computational resources needed is strongly mitigated by the fact that the core flow is not included in the model. As explained, for MHD and tritium transport computations it is not necessary to consider the volume surrounded by the alumina core (neglecting thermal effects). Fig: 5.26 shows a detailed zone of the computational mesh designed for this calculation. As usual in MHD computations at high Hartmann numbers, a hyperbolic grading towards the interfaces is imposed to increase stability and obtain convergence.

The rest of the inputs needed for the MHD calculations can be found in tab: 5.6 and 5.7. The He flow is not included in the simulation, the He channels are treated using an insulating boundary condition ($\sigma = 0$).

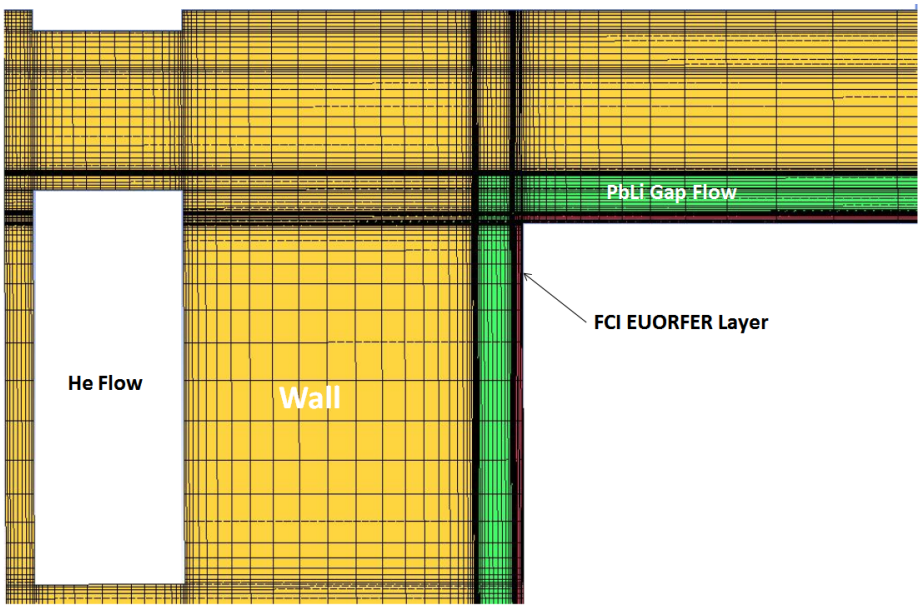

Figure 5.26: Detailed view of the computational mesh used for the He channels study.

5.6.2 Simulation results

Results show that the He channel anisotropy produces little effect over the PbLi flow. In fact, the velocity profile obtained (fig: 5.27) is globally very similar than the one obtained in sec: 5.5 (fig: 5.20). The most relevant part of the velocity profile (the Side gap) is barely affected by this effect.

When analyzing closely certain regions of the system, the effect of the He channels arises. Indeed, induced currents are logically affected by the presence of He channels as they have to avoid them (fig: 5.28).

The effect of the He channels in the current distribution have necessarily an impact over the induced magnetic field (and the electric potential as well). The reason why this influence affects poorly the PbLi flow is just a matter of distance. Indeed, the FW He channels are too far from the gap to influence it significantly. Nevertheless, the situation is drastically different in the radial

walls. They are significantly thinner than the FW and, moreover, the currents in them are perpendicular to the magnetic field. This makes that any local variation of the currents affects more strongly the Hartmann gap flow than the Side gap flow.

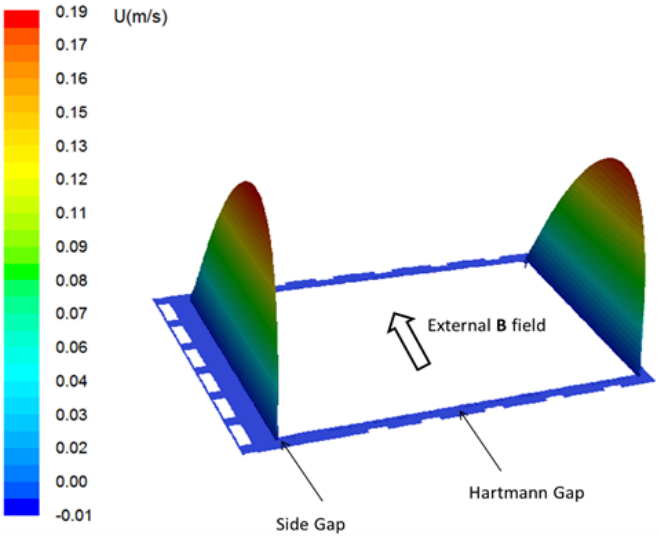

Figure 5.27: Gap flow velocity profile.

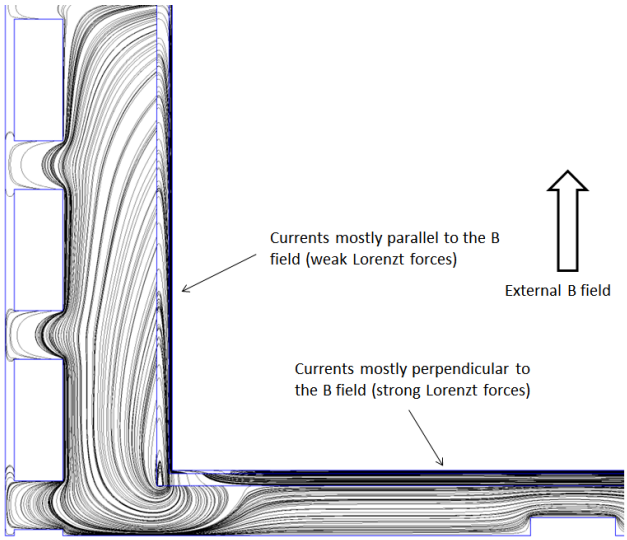

Figure 5.28: Induced currents next to the corner of the DCLL front channel.

Fig 5.29 depicts the induced magnetic field along radial and toroidal lines placed at different distances from the gap. The lines are depicted surrounding the graph.

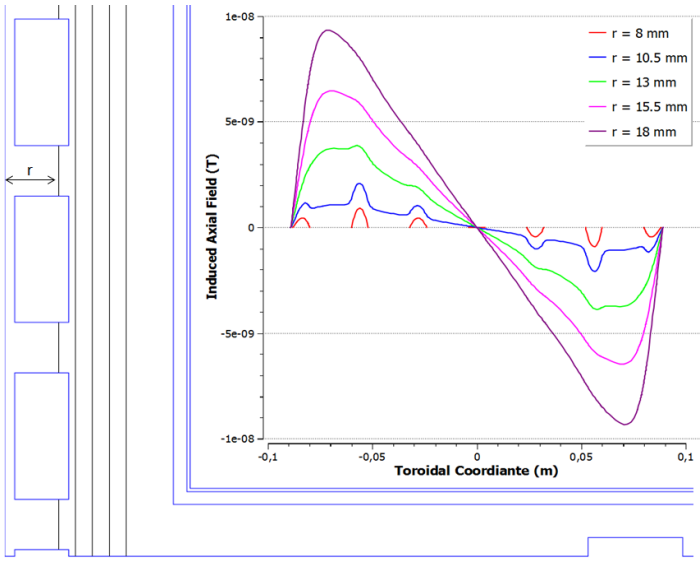

(a) First Wall.

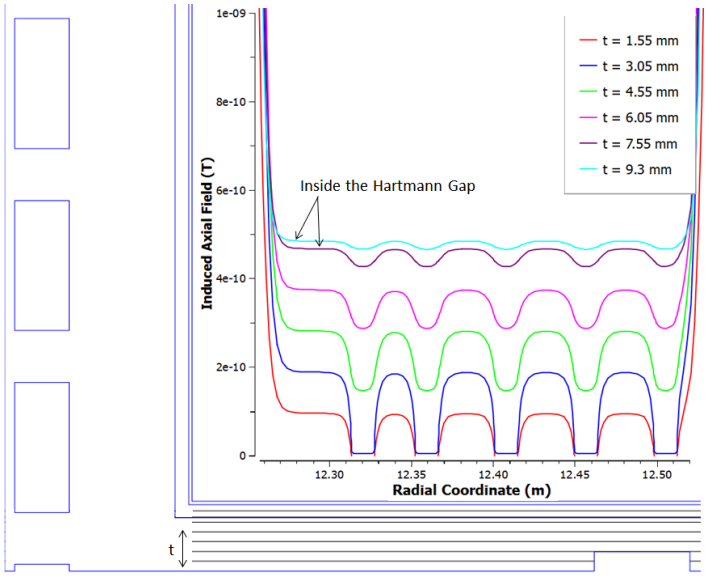

(b) Radial Wall.

Figure 5.29: Induced magnetic field along radial and toroidal lines placed at different distances. The lines are indicated next to the graph.

In the FW the distortion introduced by the He channels in the induced field vanished fairly quickly with distance. This influence is almost negligible in the

PbLi flow. Fig: 5.29b proves that the situation is very different in the radial wall. The distortion of the induced field is perfectly noticeable inside the PbLi Hartmann flow. The reason why this influence cannot be detected in fig: 5.27 is that the velocity in the Hartmann gap is several orders of magnitude lower than in the Side gap. However, when plotting the velocity profile along a radial line that crosses through the center of the Hartmann gap, the effect of the He channels on the flow becomes perfectly noticeable (fig: 5.30).

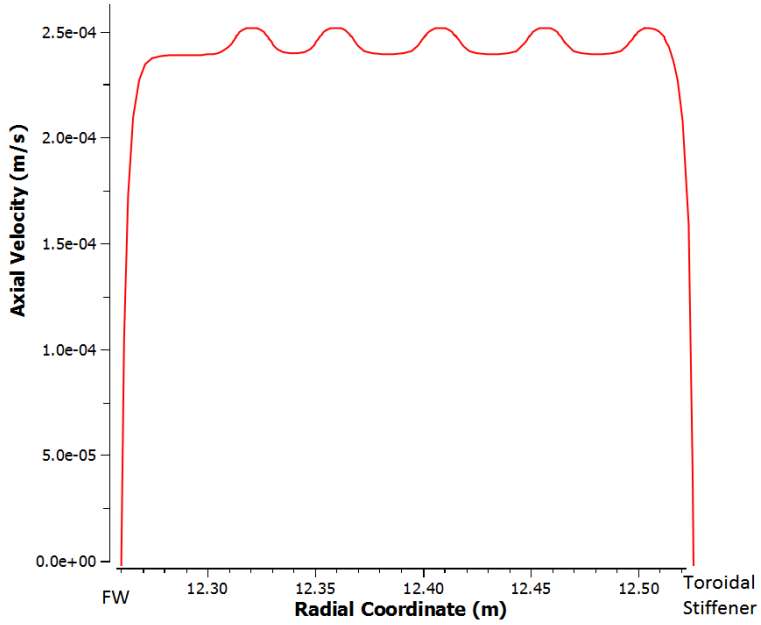

Figure 5.30: Velocity profile in the center of the Hartmann gap.

5.6.3 Discussion

Results obtained in this analysis are in very good agreement with previous analyses related the influence of He channels in the HCLL blanket [117]. In that study, the He channels are placed in the Side walls and the authors found a small effect, mainly located in the BLs.

Complementary, in the present study, similar effects are observed in the Hartmann walls and Hartmann gap flow. In any case, the effect of the He channels can be probably considered negligible at leading order. Nevertheless, having access to a realistic MHD velocity profile in the gap flow that includes

the presence of the He channels is necessary for the tritium transport deep level models presented in sec: 6.5.

5.7 Magneto-convective analyses of the DCLL OB equatorial module

The objective of this section is analyzing the combination of buoyancy and MHD interactions (magneto-convection) in relevant conditions for the DCLL. The differential formulation employed is described in sec: 2.2.

The system of study is one of the 7 toroidal circuits of the OB equatorial module (version 3, sec: 1.4.1). This system is of great complexity. Even neglecting the influence of the other toroidal circuits, the 2 poloidal channels (rear and front) of each circuit are coupled, both electrically and thermally. Besides, the complete set of 3D MHD effects identified in subsec: 5.2.2 are present in the system. Moreover, the channels (and the intermediate regions) are covered with thin sandwich FCI. This implies that every channel is formed by two flows (gap flow and bulk flow) that also interact thermally. Finally, the FCI could present discontinuities in some points of the flow path which allows the electric interaction between the bulk flow, gap flow and the metallic structure.

In order to make the calculations less demanding, the Q2D formulation of the MHD effects is employed. The Q2D formulation has been employed in the past for magneto-convection computations of straight channels with insulated walls (e.g. [58]). The details about the Q2D formulation and the conditions in which is valid are presented in sec: 2.1.4. Summarizing, the Q2D formulation is only valid when there is toroidal symmetry. Geometrically, the toroidal circuits have an almost perfect toroidal symmetry. The same happens with the heat(and tritium) generation which only have radial dependence.

Unfortunately, the FCI and breaks the toroidal symmetry of the circuits according to the results presented in sec:5.5. Nevertheless, a simplified situation in which the Q2D formulation is valid can help understanding the interaction between MHD and buoyancy forces in the DCLL module. With this purpose, the following simplifications are assumed:

1. The channels have perfect electrical insulated walls. The FCI and the gap are not directly considered, the situation is similar to having a ceramic coating.
2. The effect of helium cooling in the radial walls is neglected. The temperature profile present toroidal symmetry.
3. The velocity profile keeps the toroidal symmetry in the 3 bends of the breeder zone. Taking into account that the 3 bends are located in a plane perpendicular to the B-field, the influence of the bends is not expected to be important [108, 127, 128].

The previous assumptions are too restrictive to be fully representative of the DCLL conditions. However, they describe a simplified system similar in many aspects to the real DCLL design. As a consequence, the magneto-convection effects computed for this simplified system can be qualitatively extrapolated to the DCLL module.

5.7.1 Inputs conditions

The inputs conditions used for this section are representative to the DCLL OB module. Consequently, the modeled geometry is a radial-poloidal section of the breeder zone. The dimensions of this geometry are exposed in fig: 5.31a. They follow the design dimensions everywhere but near the PbLi outlet. In this location an extra volume is added in order to mitigate the counter-flow that appears as a consequence of the boundary conditions at the outlet. Adding this extra volume, the non-physical buoyancy effects are expected to be confined in it while representative results can be obtained at the real outlet of the breeding zone.

Concerning the thermal input conditions, a similar approach than in sec 5.5.1 is applied. Helium flows are not directly modeled. Instead, convective boundary conditions (5.5) are applied in the FW, the top wall and bottom wall. The helium temperatures are exposed in fig: 5.31b together with the heat transfer coefficients. Like in sec: 5.5.1, these values are taken from the PLATOON code calculations [46]. A zero flux is considered in the back wall as first approximation. The internal stiffening wall is coupled thermally with the PbLi (continuous T and q).

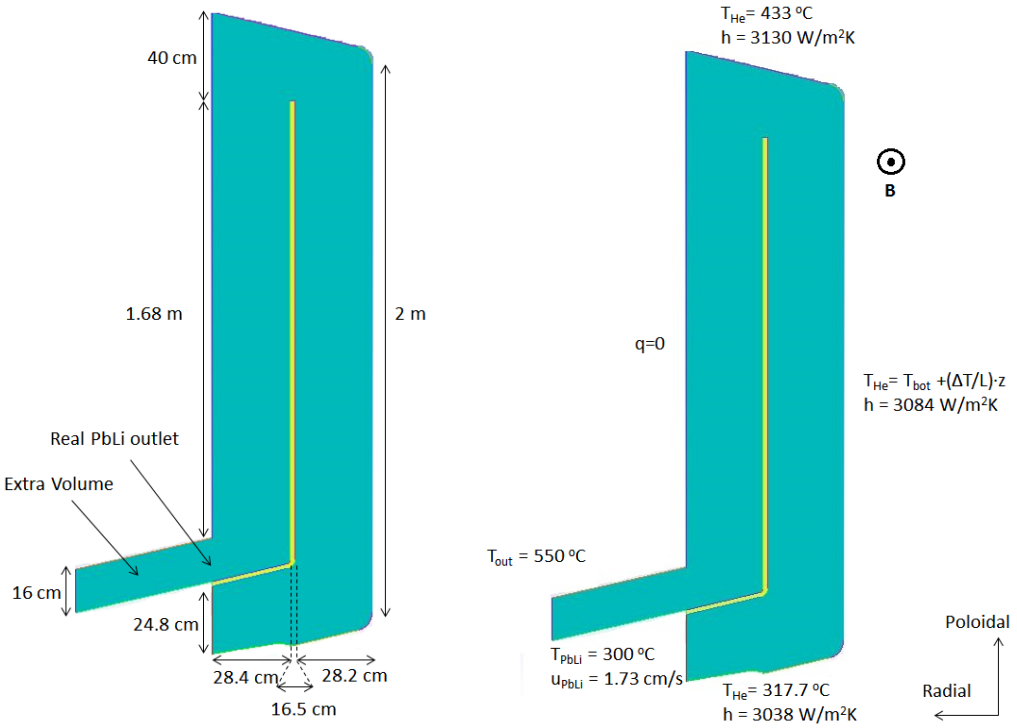

(a) Geometrical inputs.

(b) Thermal inputs.

Figure 5.31: Radial-poloidal section of the DCLL OB equatorial module.

An exponential heat volumetric generation is imposed along the channel (fig: 5.32). As with tritium transport calculations, the parameters of the generation function came from the neutronic calculations devoted to the DCLL [65, 137]. Besides, a correction factor has been included in the generation to take into account the heat losses through the radial walls. The value of these losses is taken from heat transfer system level computations (PLATOON code [46]):

$$S_q = q\exp(br) - l = 0.2715[\frac{W}{cm^3}]\exp(5.236[m^{-1}]r) - 0.1195[\frac{W}{cm^3}] \qquad (5.6)$$

As in most MHD problems, a multi-block hexahedral mesh is used for this computation (fig: 5.33).

The Hartmann braking time imposed in the PbLi flow is 0.6314 ms. This time is a crucial parameter for the Q2D formulation as it completely determine

the intensity of the MHD effects (see sec: 2.1.4). It has been obtained using and average magnetic field of 4.096 T and an average temperature of 450°C.

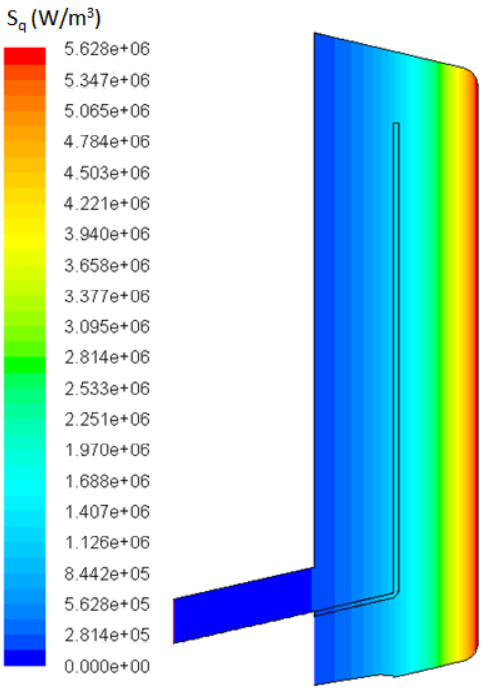

Figure 5.32: Volumetric heat generation in the DCLL OB equatorial breeder zone.

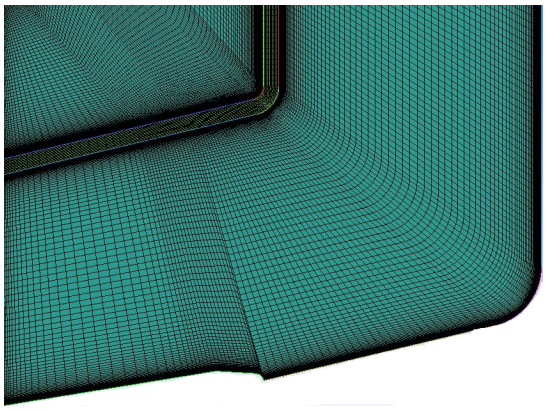

Figure 5.33: Detailed view of the mesh used for the magneto-convective computation.

As with regular convection computations, a transient approach gives more stability to the calculations. Integration steps of 1 ms were used for the first few

hundreds of seconds. Once the solution is stabilized, the integration step was gradually increased up to 100 ms. The integration is considered finished once the energy balance is below the 0.2% of the power generated. At that point, there is almost no accumulation of energy in the system, the power gains and power losses are balanced. It is worth noticed that the velocity profile does not reach a complete steady state. Vortexes are constantly moving, being created and destroyed in the rear channel. However, the temperature variations are small and local.

5.7.2 Simulation results

Results obtained are exposed compared with the same system in which there is no magnetic field applied. This way it can be clearly observed how the purely forced convection flow is affected by the magnetic field turning it into a magneto-convective flow. Results for temperatures and velocities are exposed in fig: 5.34 and 5.35, respectively.

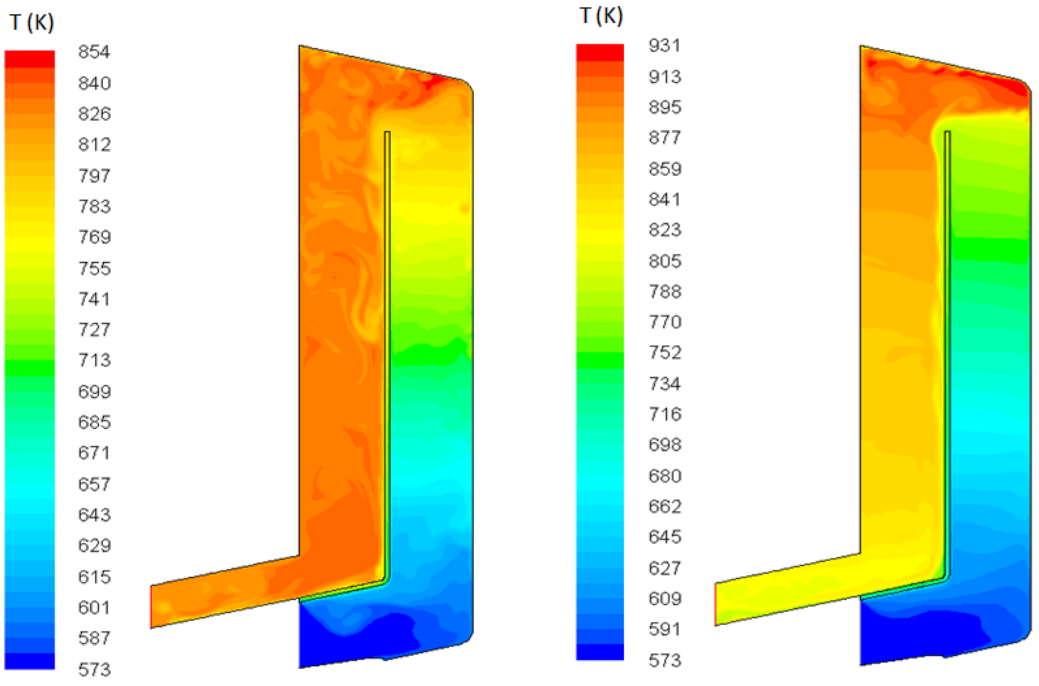

(a) Without magnetic field.

(b) With magnetic field.

Figure 5.34: Temperature contours in the radial-poloidal section of the DCLL.

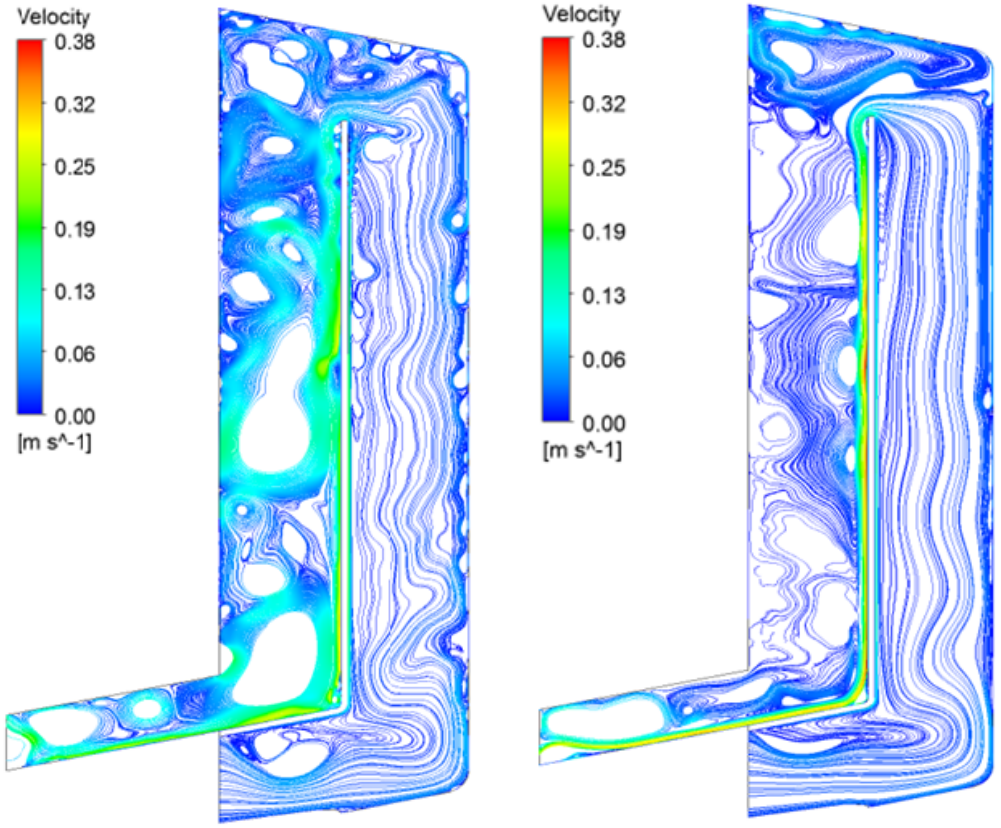

(a) Without magnetic field. (b) With magnetic field.

Figure 5.35: Velocity streamlines in the radial-poloidal section of the DCLL.

Analyzing the results obtained, it can be observed that there are some effects that arises due only to thermal interaction. In both scenarios, the temperature increases along the front channel due to the volumetric generation. The temperature reaches the maximum value next to the top-left corner of the image.

Due to the buoyancy effect, PbLi tends to go along the hottest part of the cross section when the flow goes upwards while it tends to go along the coldest part of the cross section when the flow goes downwards. The front channel flow (upwards) finds the hottest region next to the middle stiffener due to the influence of the hot rear channel at the other side. The opposite is also true for the rear channel flow (downwards) which finds the coldest part next to the middle stiffener as well. This means that the flow developed high velocity jets at both sides of this stiffener.

When there is not magnetic field, buoyancy forces are dominant. Numerous eddies are developed close to the FW due to the cooling effect of the He. Large convective vortexes are formed in the rear channel. These mix the colder PbLi close to the mid wall with the hot PbLi coming from the top region. This homogenizes the temperature which varies relatively little in the rear channel. On the contrary, when the magnetic field is present, it stabilizes the flow quite efficiently. The big convective vortexes are highly mitigated and they are reduced to smaller structures close to the mid wall (fig: 5.36). In the front channel the vortexes close to the FW are almost fully disappeared.

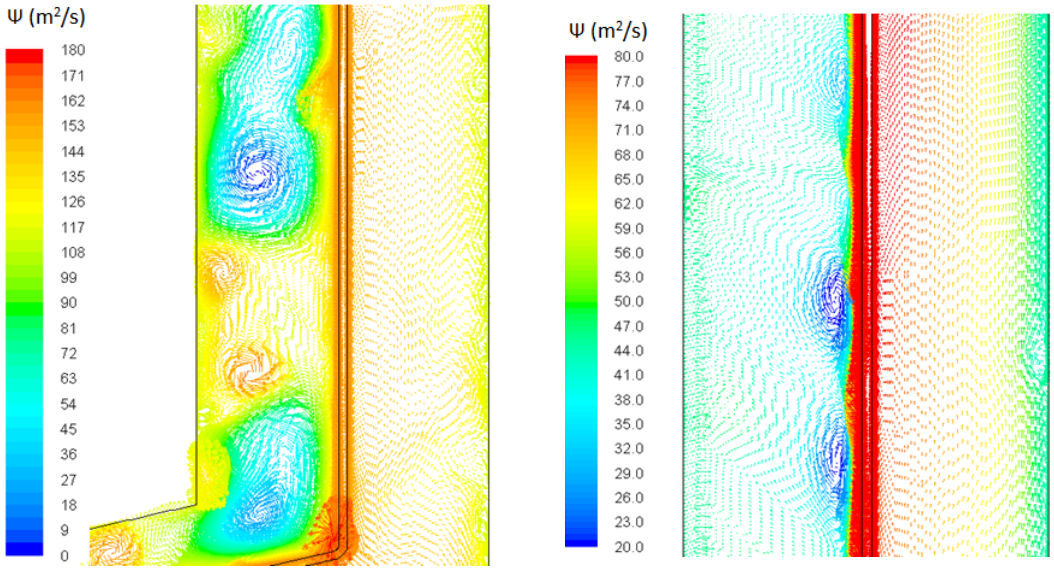

(a) Without magnetic field.

(b) With magnetic field.

Figure 5.36: Vector field in the middle part of the DCLL OB equatorial module.

The top part of the module reaches significantly higher temperatures when there is magnetic field. The stabilization of the flow makes that the top part of the module is almost isolated from the rest of the PbLi flow reducing the self-cooling of the PbLi (fig: 5.37). Moreover, the cooling effect of He is not effective as rather small vortexes are developed close to the top wall.

The vector fields depicted in fig: 5.36 and fig: 5.37 are colored using the contours of the so called stream function (ψ) (e.g. [50]). In a two dimensional incompressible flow this function is defined as follows:

$$u_x = \partial_x \psi \qquad u_y = -\partial_y \psi \tag{5.7}$$

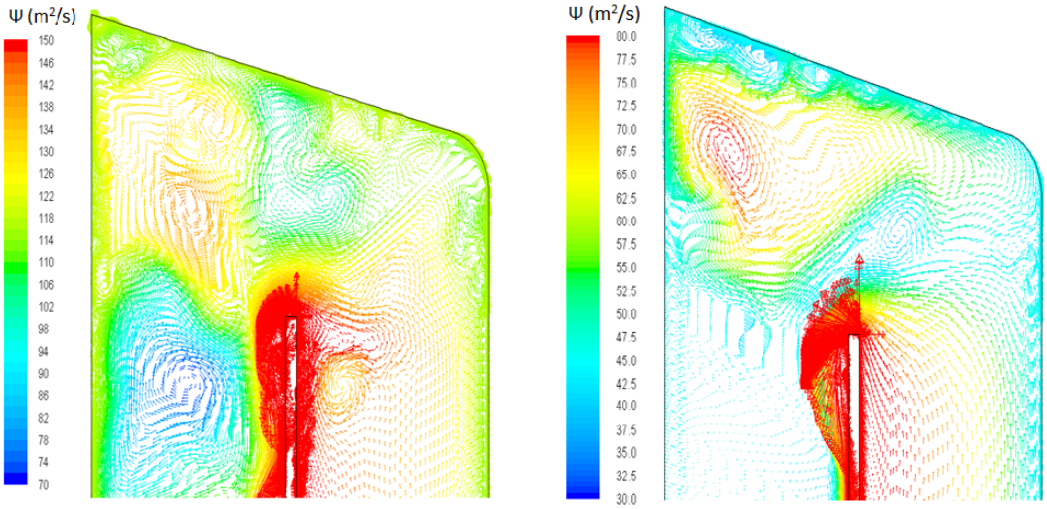

(a) Without magnetic field.

(b) With magnetic field.

Figure 5.37: Vector field in the top part of the DCLL OB equatorial module.

It can be proven using the Stokes' theorem that the isolines of the stream function are the streamlines of the velocity profile. This makes the stream function a good representation of the flow path.

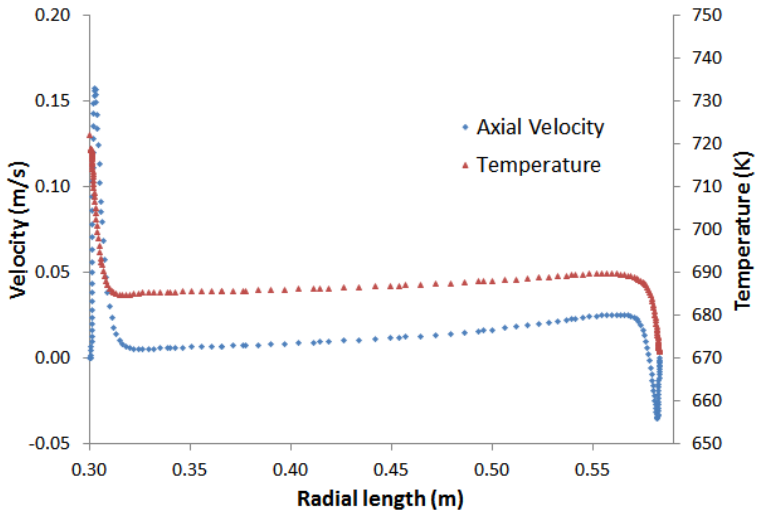

Figure 5.38: Velocity and temperature profile in the front channel of the DCLL module.

It is important noting that results depicted in this section are plotted in a particular instant of the transient simulation. The velocity profile does not

reach a full steady state in neither of the two cases. However, in the case with magnetic field, the front channel does reach a steady-state. Only in the rear channel the magneto-convetive vortexes moves constantly and irregularly. The stationary velocity and temperature profiles in the mid axial position of the front channel are exposed in fig: 5.38. In this 2D plot the tendency of the PbLi of flowing along the hottest part of the cross section can be perfectly distinguish.

The most important outcomes of this magneto-convective calculation are exposed in tab: 5.12. The PbLi breeder zone outlet temperatures are close to 550°C which is in good agreement with the system level heat transfer analyses performed for the blanket [46].

	Without field	With field
Maximum temperature in PbLi (°C)	580.5	657.4
Average temperature in PbLi (°C)	482.7	498.5
Breeder zone outlet PbLi temperature (°C)	557.4	545.6
Maximum temperature in EUROFER (°C)	520.4	517.1
Average temperature in EUROFER (°C)	478.2	474.8
Heat generated (MW)	0.343	0.343
Heat transferred to the He (MW)	0.038	0.046
Peak velocity (cm/s)	31	38

Table 5.12: Outcomes of the magneto-convective and forced convective computations.

5.7.3 Discussion

Despite the computations developed in this section are dedicated to a simplified system compared with the real DCLL OB module, important and relevant for the DCLL conclusions can be derived from it. Indeed, two important issues appear in this system which would certainly affect the real DCLL. Firstly, the peak temperature in PbLi (657.4°C) is too high for being compatible with EUROFER whose mechanical properties are not good over 550°C. Secondly, the high velocity jets that are present at both sides of the

middle stiffener are too high from the corrosion point of view. The middle stiffener will not resist the blanket operational lifetime in these conditions.

Possible solutions to both issues should be analyzed in future. For example, the helium cooling path may be inverted in order to have colder helium next to the hottest part of the module reducing the peak temperatures but increasing probably the heat transfer to the helium circuit. Other possibility would be modified the geometry of the middle stiffener forcing the PbLi to go closer to the top wall favoring the self-cooling.

Regarding the PbLi high velocities, cooling the middle stiffener would reduce the jet in the front channel but not in the rear channel. Possibly, cooling the back plate would attract part of the flow towards this wall reducing the jet velocity close to the mid wall.

Chapter 6

Deep level tritium transport model for DCLL blanket

In this chapter, several tritium transport computations at deep level are presented. The numerical formulation developed for the simulations as well as the computational tools employed are explained first. The initial calculations are focused on analyzing the influence of two particular phenomena on tritium transport: the volumetric generation and the MHD effects. Results considering different Hartmann numbers are exposed and compared. Upgrades of component level models are developed in order to reproduce the deep level results. Finally, a deep level tritium transport model of the DCLL gap flow is presented. This model includes the MHD profiles, the volumetric generation and the anisotropy introduced by the He channels. Results are compared with the ones of a system level model with the same geometry and conditions. Improvements of this model are achieved for increasing the accuracy of the outcomes.

6.1 Numerical formulation

The tritium transport deep level models developed for this section are based on the conservation laws described in detail in sec: 3.1. The evolution equation of the tritium concentration field (c) in the steady state is written as follows:

$$\partial^j \left(u_j c - D \partial_j c \right) = S_c \tag{6.1}$$

Where u_j is the velocity field of the fluid ($u_j = 0$ for solid materials), D is the diffusivity constant and S_c is the volumetric source term. Being a conservation law, the evolution of the concentration field in each domain can be well modeled dividing the space into small volumes and imposing mass conservation in each one (finite volume method [145]). This is not a challenge for most commercial CFD software. However, for BB applications it is necessary to take into account the surface processes that takes place in the interfaces between materials. In particular, the simplest but probably most relevant system for tritium permeation contains an interface liquid/solid in which the following interface conditions are satisfied:

$$\frac{c_1}{K_{s1}} = \frac{c_2}{K_{s2}} \tag{6.2}$$

$$-D_1(\partial_n c_1)_i = -D_2(\partial_n c_2)_i \tag{6.3}$$

As explained in sec: 3.1.2 this means that the concentration field is a discontinuous function and the diffusion flux is a continuous function. Computationally, the problem could be solved imposing internal boundary conditions in the interfaces between domains. In one side of the interface, Dirichlet boundary conditions could be imposed while in the other side Neumann boundary conditions could be compelled. This would imply defining one different concentration field in each domain of the system. This solution has been employed for nuclear applications using Fluent User Defined Functions (UDF) and Fluent User Defined Scalars (UDS) [95].

It is worth noticing that if the concentration scalar field were continuous, there would not be necessary imposing any kind of internal boundary conditions. Equation (6.1) could be solved in a single domain in which the discontinuities in the materials properties (diffusivity) fringe between materials introducing a discontinuity in the field gradient. This is what is usually done when performing heat transfer calculations as the temperature is a continuous function. This approach is simpler and also more stable than the first one as the mass conservation at both sides of the interface is treated like in any other computational volume of the system.

The deep level tritium transport analyses developed for this dissertation does not uses internal boundary conditions. Instead, they are based on a new formulation based in some changes of variables. This formulation aims at

obtaining a continuous function that carries the same information than the tritium concentration scalar field but that helps the computational processes. Indeed, a continuous scalar field named $\hat{c}$ can be defined with the following change of variables:

$$\hat{c}(x_i) := \begin{cases} \frac{c(x_i)}{K_{s1}} & x_i \in M_1 \\ \frac{c(x_i)}{K_{s2}} & x_i \in M_2 \end{cases} \tag{6.4}$$

Where K_{s1} and K_{s2} are the tritium solubilities in the interface between the domains M_1 and M_2 at both sides. As described in sec: 3.1.2, the field $c(x_i)$ is defined in every material (or domain) of the system in which tritium is present in its atomic form (PbLi, EUROFER, Alumina, etc...). The field $\hat{c}$ is consequently well defined in every domain in which c is defined. It has units of $Pa^{0.5}$.

The change of variables (6.4) is useful when $\partial_\tau(K_s c) \sim K_s(\partial_\tau c)$ in the interface (∂_τ refers to the derivative with respect to the two interface tangent coordinates). This is strictly true when the interface is at constant temperature. This condition can be considered valid also when temperature changes are sufficiently soft in comparison with concentration changes in the interface. In the calculations presented in this chapter, this condition is always satisfied.

Applying (6.4) to (6.1) the following differential evolution equation of $\hat{c}$ is obtained:

$$\partial^j \left[K_s \left(u_j \hat{c} - D\partial_j \hat{c}\right)\right] = S_c \tag{6.5}$$

The scalar field $\hat{c}$ also obeys a convection-like differential equation. The diffusion flux is proportional to the permeation instead to the diffusivity and the advection term is given by a fictitious vector field defined as $K_s \cdot u_i$ instead by the physical velocity field:

$$\hat{J}_i = -D \cdot K_s \partial_i \hat{c} = -\Phi \partial_i \hat{c} \tag{6.6}$$

$$\hat{u}_i = K_s u_i \tag{6.7}$$

It is worth mentioning that the source term does not suffer any modification when changing from (6.1) to (6.5) as long as it does not depends

on the concentration.

The scalar field $\hat{c}$ is defined to be a continuous function with continuous diffusion flow across the interfaces. This can be checked by applying (6.4) in (6.2) and (6.3).

$$\frac{c_1}{K_{s1}} = \frac{c_2}{K_{s2}} \quad \Rightarrow \quad \hat{c_1} = \hat{c_2} \tag{6.8}$$

$$-D_1(\partial_n c_1)_i = -D_2(\partial_n c_2)_i \quad \Rightarrow \quad -\Phi_1(\partial_n \hat{c}_1)_i = -\Phi_2(\partial_n c_2)_i \tag{6.9}$$

Using this new formulation written in terms of an auxiliary scalar field $\hat{c}$, it is possible solve the mass conservation equation (6.1) (or equivalently (6.5)) without imposing internal boundary conditions.

The computational procedure employed consist of solving (6.5) first and obtaining the solution for the auxiliary field $\hat{c}$. Thereafter, the change of variables can be easily reverted to obtain the distribution of the tritium concentration field in the whole domain. The tritium concentration field computed this way will respect the conditions (6.2) and (6.3) in every interface.

Interfaces liquid/solid and solid/solid in which tritium travel across in atomic form are well described with the previous formulation. However, as explained in sec: 3.1.2, there is a second kind of interface that plays an important role in BB applications. When recombination processes of tritium and hydrogen take place in the interface, the molecular flow follows (3.8). In an interface where only T_2 are dissociating and recombining, such as the DCLL interfaces, the auxiliary scalar field $\hat{c}$ obey the following equation:

$$\hat{J}_T = 2\sigma K_d p_{T_2} - 2\sigma K_r K_s^2 \hat{c}^2 = 2\sigma K_d (p_{T_2} - \hat{c}^2) \tag{6.10}$$

Therefore, by adapting the recombination constant ($\hat{K_r} \equiv K_r K_s^2 = K_d$), recombination and dissociation interfaces can be included as well using the $\hat{c}$ formulation. The pressure of T_2 molecules in the gaseous part of the interface can be described by another scalar field (p_{T_2}) or just by a boundary condition in which $p_{T_2} = f(x_i)$.

6.1.1 Customization capabilities of ANSYS-Fluent

ANSYS-Fluent allows the user defining up to 50 UDS fields (ψ) which are ruled by the following general convection equation [146]:

$$\partial_t \psi + \partial^i (F_i \psi - \Gamma \partial_i \psi) = S_\psi \tag{6.11}$$

The transient term ($\partial_t \psi$), the advection flow (F_i) and the diffusion constant (Γ) can be defined by the user employing UDF [147]. Making use of these Fluent customization capabilities, equation (6.5) can be defined and solved with Fluent. The vector F_i and the constant Γ are defined following (6.6) and (6.7), respectively:

$$\Gamma = \Phi \tag{6.12}$$

$$F_i = K_s u_i \tag{6.13}$$

The real concentration scalar field is computed by Fluent using also a simple UDF that reverts the change of variables at the end of the computation. For this dissertation, only steady-state computations have been carried out when developing deep level models. If the transient term is wanted to be included, it should be redefined as well ($K_s \partial_t \hat{c}$).

6.1.2 Fluent tritium transport validation test

Validation tests are presented in this section based on the analytic solutions presented in sec: 3.2. The same two simple cases analyzed analytically in that section are solved also numerically using Fluent and the $\hat{c}$ formulation.

The first case allows verifying that Fluent solvers written in terms of the $\hat{c}$ auxiliary field are able to correctly described an interface in which no dissociation and recombination processes takes place. Numerical results are compared with the analytic solutions in fig: 6.1. There is a very good agreement between them.

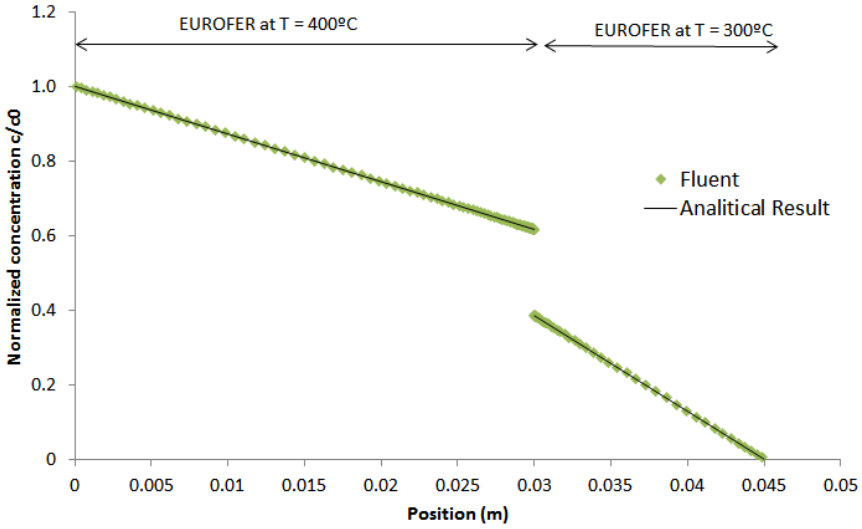

Figure 6.1: Comparison between analytic solutions and numerical results close to an interface.

The second case allows verifying that recombination boundary conditions (6.10) can be correctly included in Fluent computations when using a formulation based on the UDS field $\hat{c}$. Validation results are depicted in fig: 6.2. Once again the matching between numerical results and the analytic solution is almost perfect for every permeation regime tested (diffusion limited, surface limited and intermediate regime).

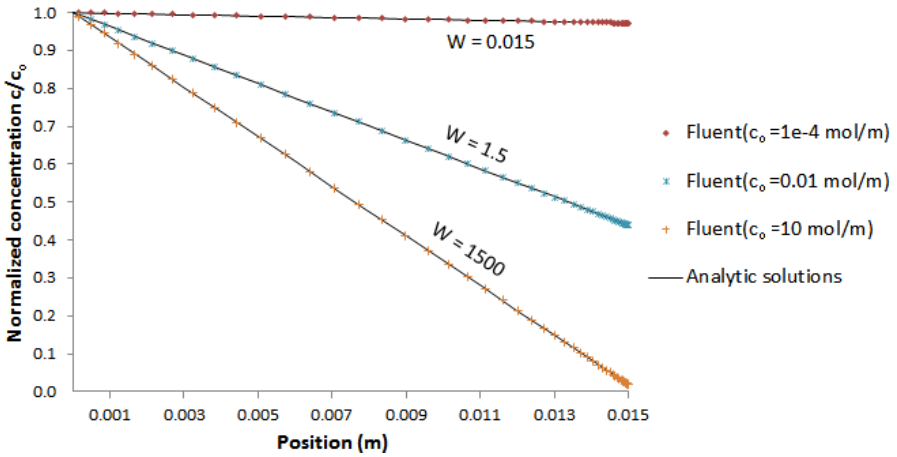

Figure 6.2: Comparison between analytic solutions and numerical results when considering recombination boundary conditions.

This two simple validation test cannot be considered sufficient for a complete validation of the computational tool and procedure (this would require of experimental validation). However, they are necessary conditions that have been satisfied.

6.2 Tritium transport in laminar flows

The first tritium transport deep level model presented aims at analyzing the effect of a hydrodynamic laminar flow on tritium permeation. This problem has been studied in detail both theoretically and experimentally (using hydrogen) in the second half of the XX century [148–151]. These studies are focused on the effect of the geometry (cylindrical tubes and rectangular channels) and the fluid properties on mass transport. They also study the effect of the hydrodynamic regime (laminar, turbulent and intermediate) on hydrogen permeation.

The experimental work does not consider mass volumetric generation. Therefore, the BL approximation presented in sec: 3.1.4 is generally applied for the data analyses. Indeed, the Sherwood number is usually given as the main outcome of the experiments. Correlations of the following shape are deduced:

$$Sh = \alpha Re^{\beta} Sc^{\gamma} \tag{6.14}$$

The parameters α, β and γ are obtained as the best fit of experimental data. They strongly depend on the experimental conditions: flow regime, permeation regime, geometry, etc.

It is also possible to extrapolate data from heat transfer experimental work (e.g. [152, 153]). Indeed, correlations that relate the Nusselt number with the Reynolds number and the Prandtl number are equivalent to (6.14).

6.2.1 Deep level model results

Taking into account the extensive and high quality work performed in the past concerning mass transfer under laminar and turbulent regimes, the present analysis does not aim at obtaining a new correlation based on numerical results.

The main objective is providing a reference scenario for the optimization of component level models.

The system of study is based on a PbLi channel of the OB equatorial module of the European DCLL (Version 3, sec: 1.4.1). The channel is simplified in order to isolate effects and facilitate the analysis of the results. Because of that, the thicknesses of the walls are considered uniform (15 mm) and isothermal conditions are imposed. The geometrical inputs of the channel are presented in fig: 6.3.

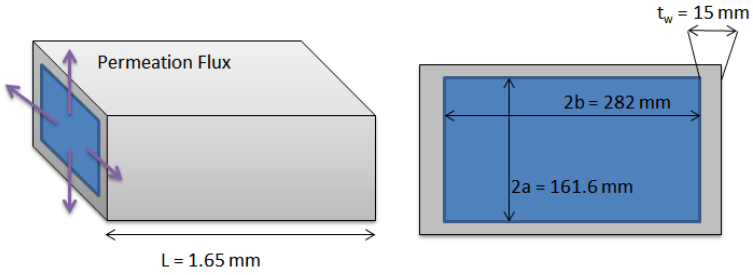

Figure 6.3: Geometrical inputs for the tritium transport analysis in laminar regime.

The rest of the inputs are exposed in tab: 6.1. It is worth mentioning that the inlet concentration value is taken in accordance with the results of the initial system level model for the DCLL blanket (chap: 4). This way, the methodology loop that relates deep level models and component level models described in sec: 1.3.2 (fig: 1.11) is followed.

Recombination processes are imposed as a boundary condition in the external side of the wall. The surrounded volume is supposed to be sufficiently large for having zero partial pressure. In other words, $p_{T_2} = 0$ is set in (6.10). The permeation number under this conditions is $W \sim 0.2$ which means that the channel is in an intermediate regime in which the surface processes are comparable with the diffusion dynamics inside the wall. In practice, this means that a non-zero concentration at the external wall is expected.

As mentioned, laminar regime is assumed in the PbLi channel. Turbulence effects have not been studied in this dissertation as MHD interactions strongly mitigate them inside PbLi blanket channels. MHD velocity profiles are considered instead in sec: 6.4 as a follow-up of this analysis.

Inlet velocity; u_0 (cm/s)	1.8
Average temperature; T_{avg} (°C)	400
Density of PbLi; ρ (kg/m^3) [141]	9720
Viscosity of PbLi; η (Pas) [141]	$1.497 \cdot 10^{-3}$
Diffusivity of tritium in PbLi; D_{PbLi} (m^2/s) [77]	$1.24 \cdot 10^{-9}$
Diffusivity of tritium in EUROFER; $D_{EUROFER}$ (m^2/s) [74]	$4.91 \cdot 10^{-9}$
Solubility of tritium in PbLi; Ks_{PbLi} (mol/Pa$^{0.5}$m^3) [77]	$1.01 \cdot 10^{-3}$
Solubility of tritium in EUROFER; $Ks_{EUROFER}$ (mol/Pa$^{0.5}$m^3) [74]	$1.51 \cdot 10^{-3}$
EUROFER recombination coefficient; Kr (m/mol s) [75]	$4.77 \cdot 10^{-5}$
EUROFER dissociation coefficient; Kd (mol Pa/m^{2}s) [75]	$1.09 \cdot 10^{-10}$
Inlet concentration; c_0 (mol/m^3) (chap: 4)	10^{-3}

Table 6.1: Input data for the tritium transport simulation in laminar regime.

Contours of the velocity profile and concentration profile in the mid sectional plane of the channel are presented in fig: 6.4.

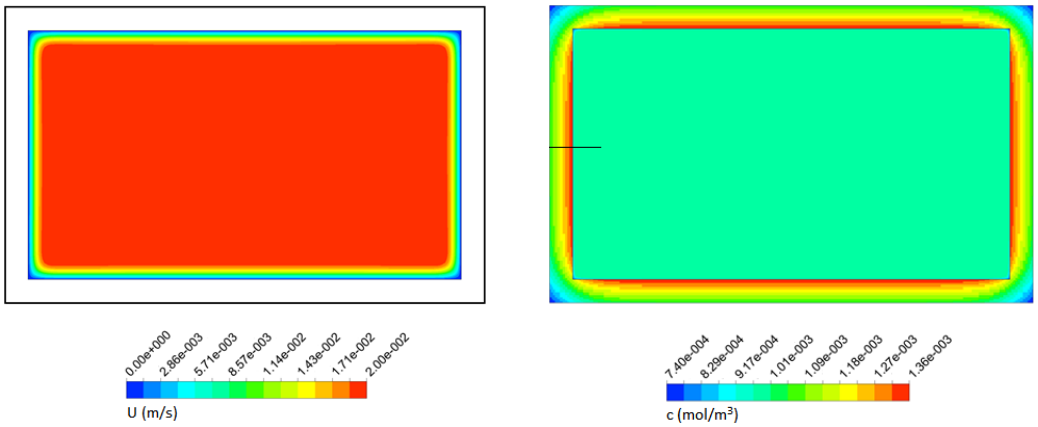

(a) Velocity. (b) Concentration.

Figure 6.4: Velocity profile and concentration profile in the mid sectional plane.

A relatively thin velocity BL can be observed in fig: 6.4a as the channel length is shorter than the entry length and the flow is not fully developed [67]. The concentration discontinuity is also noticeable in the interface between the PbLi and the channels walls in fig: 6.4b. However, the concentration BL is too thin to be easily observed. In order to distinguish this BL, 2D plots like the ones presented in the next subsection are needed.

The permeation rate obtained with Fluent is approximately $5 \cdot 10^{-10}$ g/s. The mass transfer coefficient has been obtained from the average of the flux and the concentration in the internal walls of the channel. The value obtained is $1.25 \cdot 10^{-6}$ m/s which is in the same order than experimental correlations (e.g. $1.97 \cdot 10^{-6}$ m/s [150] or $1.50 \cdot 10^{-6}$ m/s [153]).

6.2.2 Upgrade of component level models

The same PbLi channel has been modeled using component level models developed with EcosimPro. 3 different EcosimPro models are compared in this section. The simplest model consists of a flow connected with a solid material imposing Sievert boundary conditions at the interface (fig: 6.5). This simple approach is the one employed for the initial tritium transport models at system level for the EUROfusion blankets [37, 81].

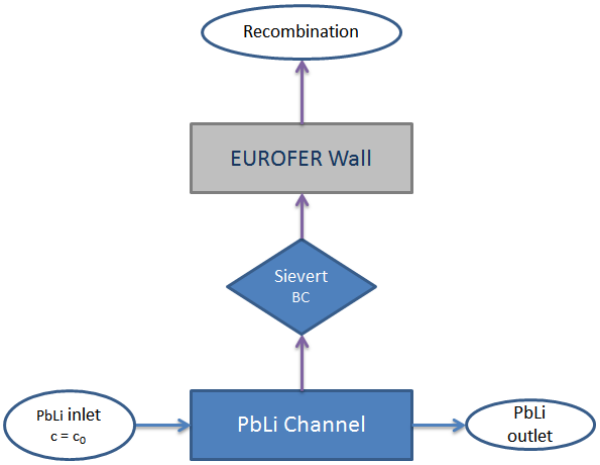

Figure 6.5: PFD of a PbLi channel.

This simple model does not consider any kind of BL in the PbLi flow. The concentration is uniform in the PbLi along the cross sectional dimensions. It is equivalent of having an infinitely large mass transfer coefficient with and infinitely thin BL. This approach is conservative in terms of permeation as it provides the upper bound for this magnitude. This is the main reason why this important simplification is extensively used for tritium transport models in BB. However, the error introduced with this simplification is significant.

For evaluating the accuracy of a system level model or a component level model in comparison with the deep level result, the relative deviation (ϵ) is used (6.15). The deviation of a result (x) with respect to the reference value (x_0) can be expressed using a percentage. In this chapter the reference values are given by the deep level model results developed with Fluent.

$$\epsilon = 100\frac{|x - x_0|}{x_0} \tag{6.15}$$

In this first component level model, the deviation between the component level results and the deep level result is a bit higher than 13.5% (tab: 6.2).

Two alternative approaches are tested in order to increase the accuracy of the EcosimPro models. Both are based on the BL approximation described in sec: 3.1.4. Their objective is reproducing the concentration drop found in the BL by imposing (3.23). In the first approach, equation (3.23) is implemented as an interface condition before imposing the discontinuity in the concentration field (Sievert boundary condition). This approach has been called ideal BL. The ideal BL has no physical thickness, only one extra node in the interface is needed, only one extra algebraic equation is added (per axial node).

Alternatively, the BL can be treated as a solid material ($u_i = 0$) with a finite thickness δ, the same solubility than the PbLi and an effective diffusivity equal to $K_t \cdot \delta$. This approach has been called physical BL. With it, the tritium concentration in the PbLi is no longer uniform along the cross sectional dimensions. This solution has been implemented recently for the tritium transport models of the US-DCLL using experimental correlations for estimating K_t [91]. The flowcharts used with both approaches are shown in fig: 6.6.

The mass transfer coefficient used for the EcosimPro computations is taken from the Fluent deep level model ($K_t = 1.25 \cdot 10^{-6}$ m/s). This way, the value of the mass transfer coefficient should be close to optimal when using the ideal BL approach. If deep level model results are not available, mass transfer coefficient can be taken from experimental correlations as the differences should not be dramatic.

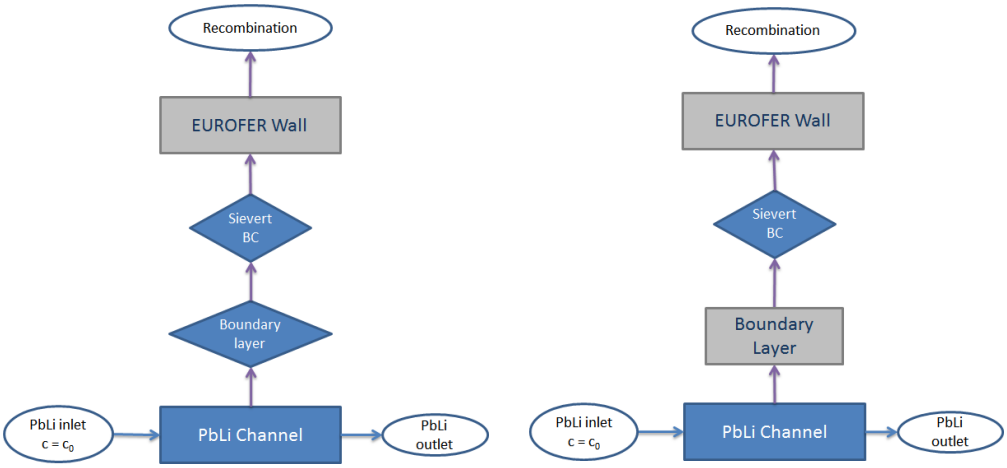

(a) Ideal BL. (b) Physical BL.

Figure 6.6: Upgraded PFDs of a PbLi channel.

In the case of the physical BL approach, the thickness of the BL should be estimated as well before launching the computations. This introduces some uncertainty in the results as this thickness is not constant in the channel (it grows approximately with the square root of the axial distance). For this case, an average BL thickness is taken from the Fluent results. However, it is not longer true that the previous mass transfer coefficient is optimal in combination with this thickness.

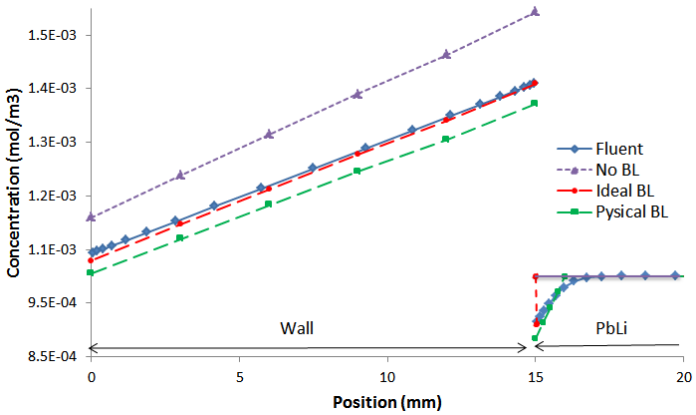

Figure 6.7: Comparison between component level and deep level models in the mid axial position (z=L/2) of the channel.

Results of the 3 component level models designed with EcosimPro are presented compared with the deep level model designed with Fluent (fig: 6.7). Results are plotted along the black line depicted in fig: 6.4b.

The 3 main outcomes of the model are the permeation rate through the external walls, the tritium inventory in the PbLi and the tritium inventory in the wall. Both inventories are obtained integrating the concentration field in the corresponding volume. The tritium permeation rate is obtained integrating the tritium flux in the external wall surface. Results are exposed in tab: 6.2.

		Permeation Rate (10^{-10} g/s)		Inventory PbLi (10^{-4} g)		Inventory Wall (10^{-5} g)	
		Value	Deviation (%)	Value	Deviation (%)	Value	Deviation (%)
Fluent		4.99	–	2.266	–	8.307	–
EcosimPro	No BL	5.66	13.51	2.268	0.087	8.658	4.23
	Ideal BL	4.88	2.13	2.268	0.089	8.200	1.29
	Physical BL	4.66	6.58	2.266	0.002	7.807	6.02

Table 6.2: Results comparison between one deep level model and 3 component level model.

The ideal BL approach is able to reproduce the deep level model results with better accuracy than the physical BL approach. The exception is the inventory in the PbLi which is reproduced better with the physical BL. This is expected as the former approach is the only one that discretizes the BL. However, at least for relatively high velocities, when the BL is thin, the deviation of the inventory in PbLi is below 0.1% in any case. Therefore, the ideal boundary approach is preferred as it is easier to select the parameters (K_t) that produces smaller deviations.

It is worth noting that K_t and δ could be optimized for obtaining permeation rates with the physical BL as accurate as the ideal BL approach. However, this optimization process can be avoided by using the ideal BL approach if the error on the PbLi inventory is considered acceptably small.

6.3 Tritium transport in laminar flows with volumetric generation

The computations presented in this section are focused on analyzing the influence of the volumetric tritium generation over tritium permeation through the walls. The volumetric generation logically influences the system level tritium transport results, such as the one presented in chap: 4.3. Indeed, the generation inside the PbLi produces a global increase of the concentration that enhances permeation. Certainly, this effect will be present in deep level results as well. Besides this global effect, the generation profile will be coupled with the velocity profile producing a non-uniform concentration profile that can affect tritium permeation importantly. Deep level models are the only ones capable of computing this coupling. In fact, inside the BL the concentration is no longer expected to have a linear profile as:

$$\partial_i J^i \simeq S_c \neq 0 \tag{6.16}$$

As a consequence, the mass transfer coefficient is no longer well defined. The flow is not proportional to the concentration difference between the core and the wall. Moreover, for no constant generation rates like the ones relevant in fusion there is not even a well defined concentration core.

In order to reproduce relevant DCLL conditions, the generation profile imposed has the prototypical exponential shape (3.3) along the radial coordinate of the blanket. The exponential parameter is given by the neutronics computations [137] while the pre-exponential parameter has been adjusted to have a generation rate of 10^{-6} mol/s.

$$S_c = 3.125 \cdot 10^{-5} [\frac{mol}{m^3 s}] \exp(-6.3013[m^{-1}]x) \tag{6.17}$$

The volumetric source term can be defined and hooked to the same Fluent model developed for the previous section using an UDF. The rest of the inputs used for this computation (including the inlet concentration) are the same than the ones which are exposed in tab: 6.1 and fig: 6.3. Note that the CFD computation is the same than in the previous section. As a consequence, the velocity profile in the channel is the one shown in fig: 6.4a.

6.3.1 Deep level model results

Results of the tritium concentration in the steady state obtained with a deep level model developed with Fluent are presented in fig: 6.8. Concentration contours are depicted in the mid sectional plane (radial-toroidal) and in the middle radial-poloidal plane. The color legend follows a logarithmic scale in order to differentiate better the concentration variations in the bulk of the PbLi.

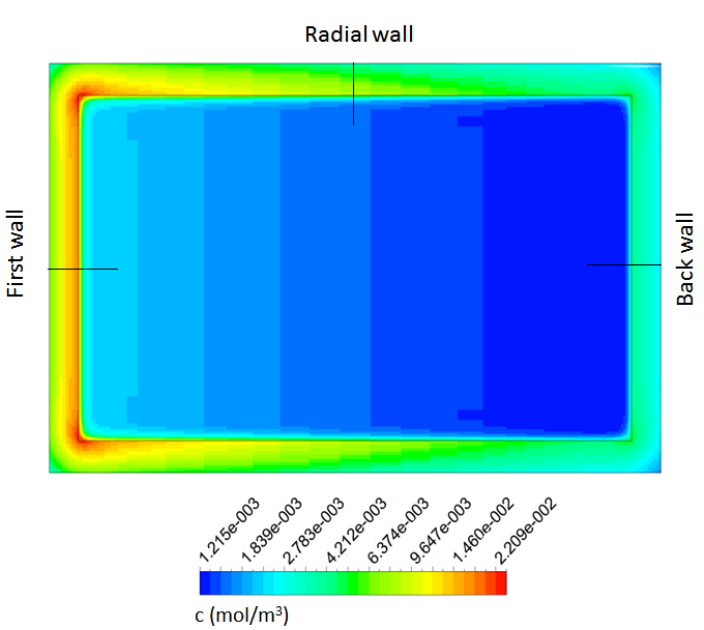

(a) Mid radial-toroidal plane.

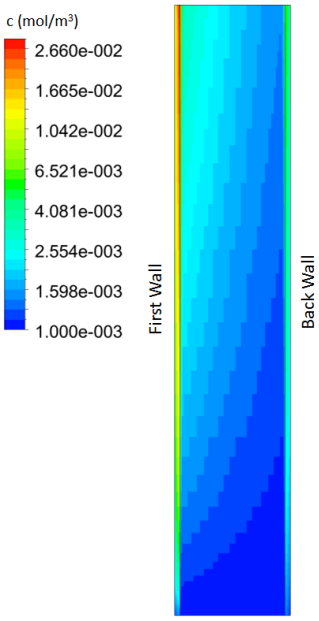

(b) Mid radial-poloidal plane.

Figure 6.8: Concentration profile in a channel with volumetric generation.

Thanks to the logarithmic scale, the concentration increase in the bulk of the PbLi can be noticed. Indeed, the concentration grows from the Back Wall (BW) to the FW due to the effect of the non-uniform generation rate. This cannot be reproduced easily by 1D component level models.

In order to analyze the concentration BL, a 2D plot along the black lines shown in fig: 6.8a is exposed in fig: 6.9. The results of a simple component level model developed with EcosimPro (no BL considered) is depicted as well for comparison purposes.

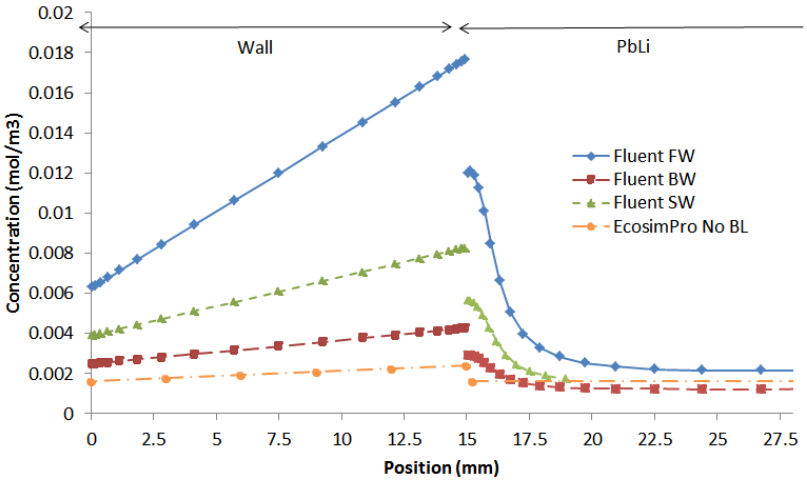

Figure 6.9: Concentration BL next to the channel walls.

According to the results, the volumetric generation produces a different kind of BLs close to the walls of the channel. Contrary to the case without generation, these BLs are peaks of tritium concentrations instead of drops. This tritium accumulation is caused by the coupling between the volumetric generation and the velocity BLs. Indeed, close to the BLs the velocity is much smaller than in the core flow. This makes that tritium produced inside them is dragged by the flow less efficiently compared with the core flow producing the observed accumulation. The peak of tritium concentration is logically higher in the FW BL where the generation rate is also higher.

Contrary to the results obtained without generation, the EcosimPro model without BL underestimates the permeation rate and the inventory in the wall. The deviations from the deep level results are very significant (tab: 6.4).

It is important to recall that very close to the walls the tritium concentration diminish a bit before penetrates in the steel. This is caused by the absorption effect created by the wall which is always present besides any advection or generation phenomenon. Indeed, the diffusion flux is a continuous function across the interfaces which means that, sufficiently close to the interface, the sign of the flow has to be negative also in the PbLi side.

6.3.2 Upgrade of component level models

The optimization of component level models is once more focused on upgrading the description of the mass transfer BLs. These are the regions that affect more the tritium permeation and tritium inventories as they determine the concentration at the interface.

According to the results presented in fig: 6.9, the tritium concentration could still be approximated by a linear profile in the central part of the BL. The sign of the profile slope is logically different than in the previous case. Using the results of the deep level model, an average of this slope can be derived. This has been approximated by the difference between the average concentration in the corresponding surface and the average concentration in the PbLi. This way, a modified mass transfer coefficient ($\hat{K}_t[m/s]$) can be defined as the ratio between the average permeation flux and the concentration difference.

$$\hat{K}_t = \frac{|J_{avg}|}{c_{avg} - c_{wall}} \tag{6.18}$$

In the channel analyzed in this computation is obtained that: $\hat{K}_t \sim 3.5 \cdot 10^{-7}$ m/s. The modified mass transfer coefficient is a new parameter defined for describing BLs with generation using component level models. It is important noting that the physical meaning of the mass transfer coefficient (K_t) cannot be extended to $\hat{K}_t$.

At the light of the deep level results, it is deduced that it not correct implementing a component level model of a PbLi channel following the flowchart shown in fig: 6.6b when there is volumetric generation (as it is done in past: e.g. [91]). If this were done, similar profiles than the ones exposed in fig: 6.7 would be obtained. Indeed, only concentration drops can be obtained with that method. The slope of the concentration would have unavoidable different sign that the one desired. This is a good example of how deep level models can refute assumptions of system level models that are considered correct.

As a consequence, For optimizing the system level channel model, the approach followed consist of imposing a generation rate also inside the BL component. In other words, the BL is no longer treated as a solid material of

thickness δ and diffusivity $K_t \cdot \delta$ but as a solid material with thickness δ, difussivity $\hat{K}_t \cdot \delta$ and volumetric generation rate G_{BL}. Consequently, a truly important parameter is the percentage of tritium generated in each BL with respect to the total generation amount in the channel.

Integrating (6.17) in the volumes of the BLs and the core flow, the total generation in each region is obtained. The total generation rates are exposed in tab 6.3. The average BL thickness is set $\delta = 2.5$ mm. This number is deduced from Fluent deep level results.

	Generation rate (g/s)	Relative generation rate (%)
Core Flow; G_c	$2.857 \cdot 10^{-6}$	94.76
First Wall BL; G_{FW}	$5.671 \cdot 10^{-8}$	1.88
Back Wall BL; G_{BW}	$9.745 \cdot 10^{-9}$	0.32
Radial Wall BL (x2); G_{SW}	$4.561 \cdot 10^{-8}$	1.51

Table 6.3: Integrated generation rate in the different regions of the PbLi channel.

The first attempt for upgrading the channel system level model uses the generation rates depicted in tab: 6.3 as input parameters. The results of this attempt in the FW BL are depicted in fig: 6.10 and tab: 6.4.

Far from improving the results, this first attempt overestimate the permeation rate and the inventories unacceptably (deviations over 700% with respect to the Fluent results). From this failure, 2 important conclusion are deduced. Firstly, in order to avoid the obtained parabolic shape of the concentration profile, the generation rate must be displaced towards the channel wall. This way, the linear profile towards the core flow can be reproduced while having also permeation through the wall. Secondly, the computed generation rate in the BL (tab: 6.3) produces too high concentrations peaks. The reason is that when considering the BL as a solid material ($u_i = 0$), the advection is neglected completely. In the 3D system, the BL has less velocity than the core but not zero. Therefore, there are some advection losses in each BL that has to be taken into account.

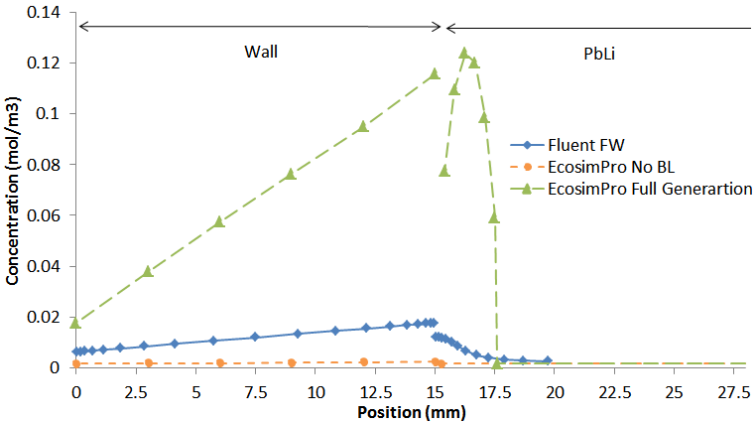

Figure 6.10: Concentration profile in next to the FW with a generating BL.

Following these conclusions, 2 important adjustments are introduced in the second attempt:

1. The tritium is generated only in the closest node to the wall.
2. The amount of tritium generated in the BLs is diminished in order to take into account the advection losses in the layers.

Unfortunately, there is not direct way to obtain the best generation rate distribution between the core and the BLs from the Fluent deep level results. As a consequence, an optimization process around the generation rate in the FW BL (G_{FW}) is performed using the EcosimPro component level models. The relative proportions between the generation rates in the different BLs are kept in their original values (tab: 6.3). This way, the optimization process respects the following constrains:

$$\frac{G_{BW}}{G_{FW}} = 0.172 \tag{6.19}$$

$$\frac{G_{SW}}{G_{FW}} = 0.804 \tag{6.20}$$

$$G_c = G_{tot} - G_{FW} - G_{BW} - 2G_{SW} \tag{6.21}$$

The constrain 6.21 ensures that the total amount of tritium generated in the channel is always the same. The optimization processes consist of a parametric

sweep of G_{FW}. The results of the optimization process are shown in fig: 6.11. The color boxes in fig: 6.11a represent the Fluent result with a deviation of $\pm 5\%$. With this picture it is possible to identify a region in which the three quantities have deviation below 5%. The value that minimizes the total deviation ($G_{min} = 0.021\%$) is contained in this region.

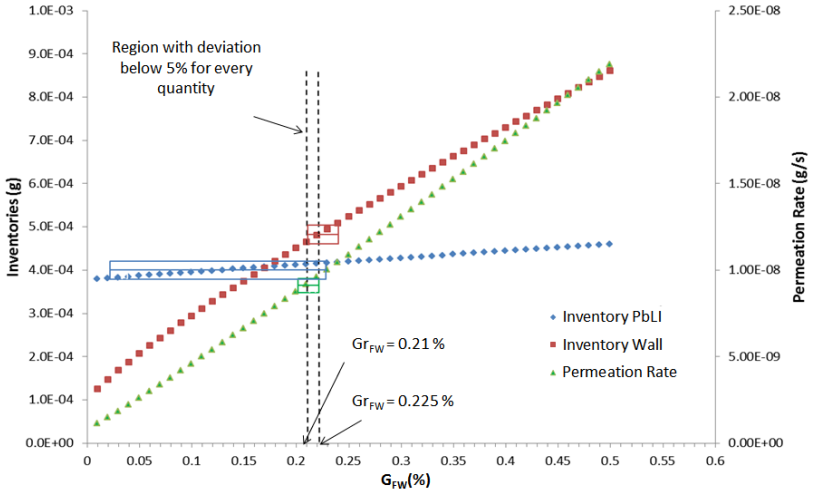

(a) Absolute values.

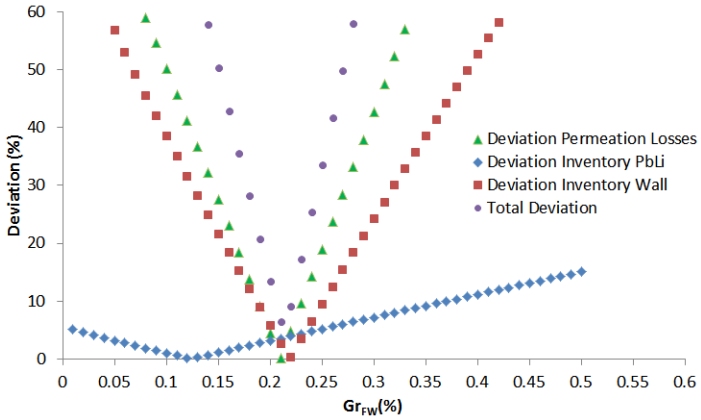

(b) Deviations.

Figure 6.11: Optimization study around the generation in the FW BL.

Once the optimized generation rate in the FW BL has been identified, the component level model is able to reproduce the deep level model results with a very significant improvement of accuracy (fig: 6.12 and tab: 6.4).

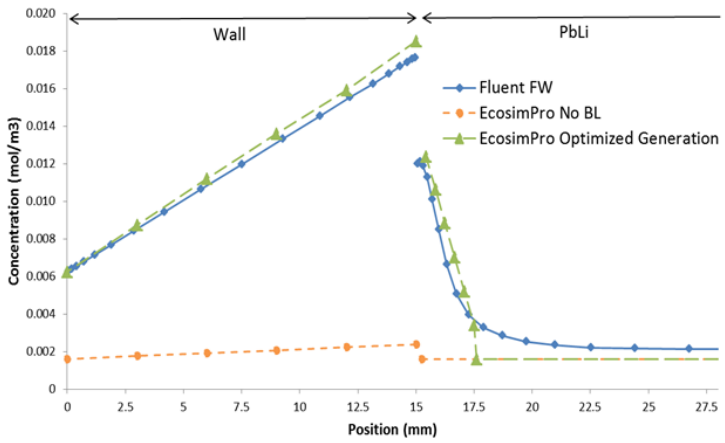

(a) First Wall.

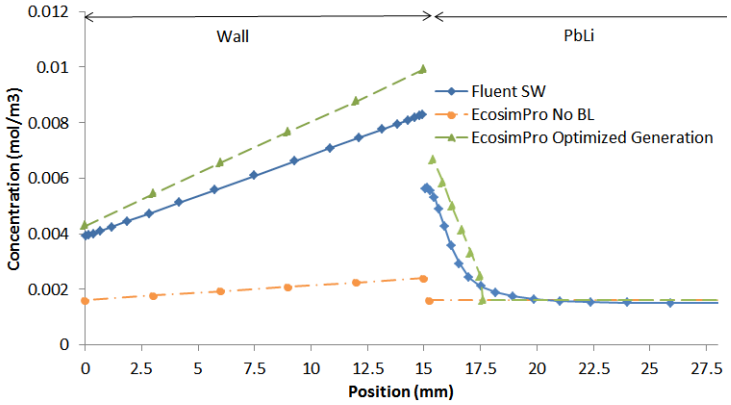

(b) Radial walls.

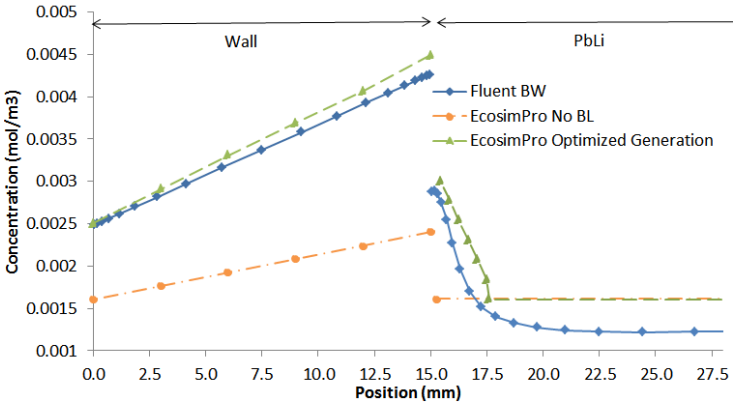

(c) Back wall.

Figure 6.12: Concentration profile in the BL after the optimization process.

		Permeation Rate (10^{-9} g/s)		Inventory PbLi (10^{-4} g)		Inventory Wall (10^{-4} g)	
		Value	Deviation (%)	Value	Deviation (%)	Value	Deviation (%)
Fluent		9.13	–	3.98	–	4.78	–
EcosimPro	No BL	1.27	86.13	3.79	4.83	1.36	71.57
	BL with generation	76.4	737.07	10.01	155.05	22.5	371.14
	BL with optimized generation	9.14	0.17	4.21	3.56	4.65	2.69

Table 6.4: Permeation rate and inventories in a PbLi channel with generation.

6.4 Tritium transport models in MHD fully developed flows

The objective of this section is analyzing the effect of the magnetic field on tritium evolution. For this purpose, fully developed MHD flows with different Hartmann numbers are employed. The system of study is the same PbLi channel used in sec: 6.2. In this case, the channel is immersed in a transversal magnetic field. Tritium transport deep level models with MHD velocity profiles are obtained considering first a constant inlet concentration and then imposing a volumetric generation.

6.4.1 MHD profiles in the the PbLi channel

In order to study the effect of the external magnetic field on tritium permeation, the MHD velocity profiles needs to be computed first. The fully developed approximation is employed for this purpose. The assumptions in which MHD fully developed flows are based and the mathematical description of the MHD interactions under this approximation are presented in detail in sec: 2.1.3. Besides, examples of fully developed computations in DCLL conditions are exposed in sec: 5.5 and sec: 2.1.5. The MHD flow in a rectangular section channel with conducting walls was first studied by Walker in 1981 [144].

The magnetic field imposed in the channel is perpendicular to the longer wall of the channel. This wall is called Radial Wall (RW) for analogy with the DCLL poloidal channels in the tokamak torus. Hartmann numbers of different orders of magnitude are considered. The maximum Hartmann number (Ha = 7500) is relevant for DEMO applications in the outboard segments. The rest of

the inputs needed for the computations are exposed in tab: 6.5.

Average velocity; u_0 (cm/s) [46]	1.8
Average temperature; T_{avg} (°C) [46]	400
Density of PbLi; ρ (kg/m^3) [141]	9720
Viscosity of PbLi; η (Pas) [141]	$1.497 \cdot 10^{-3}$
Conductivity of PbLi; σ (Sm) [140]	763535
Conductivity of EUROFER; σ_w [142]	763535

Table 6.5: Inputs for the MHD fully developed computations.

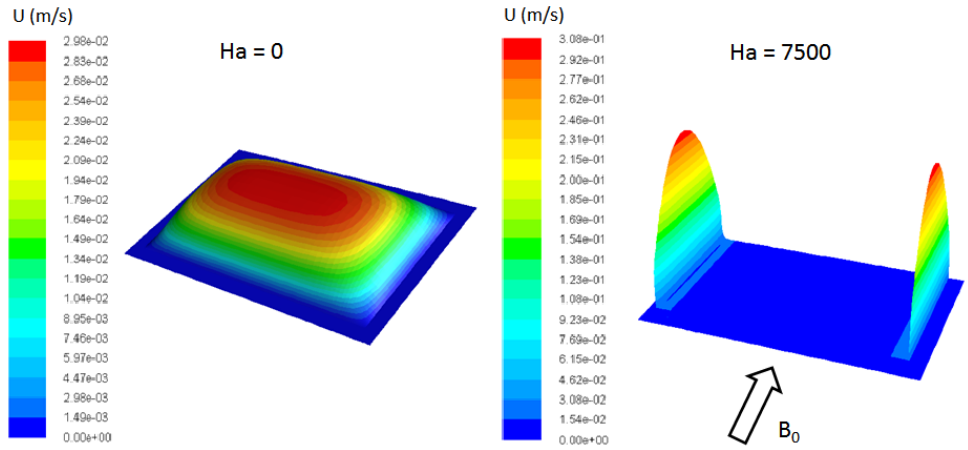

Figure 6.13: Fully developed velocity profiles with and without magnetic field.

Results of the 2D fully developed velocity profiles for the extreme cases (Ha = 0 and Ha = 7500) are exposed in fig: 6.13. The results of the computations for 5 different Hartmann numbers are plotted along the central line perpendicular to the magnetic field and the central line parallel to the magnetic field (fig: 6.14).

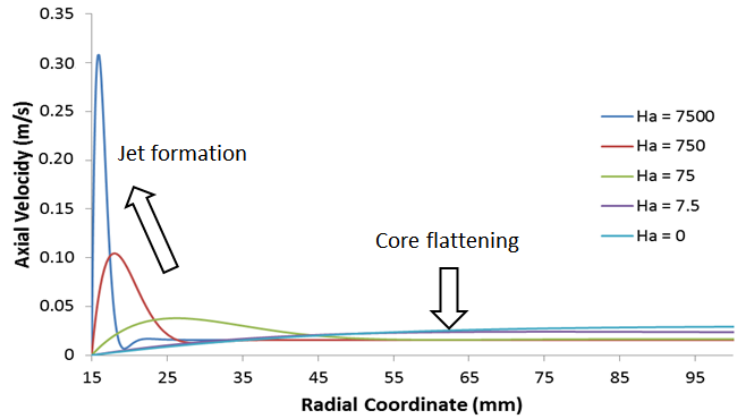

(a) Side BL.

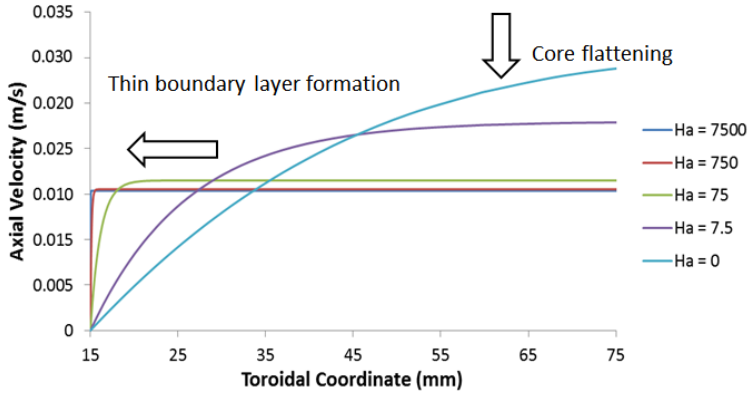

(b) Hartmann BL.

Figure 6.14: Fully developed flows for different Hartmann numbers next to the Hartmann and Side BLs.

6.4.2 Tritium transport in MHD flows without volumetric generation

Using the velocity profiles computed with the fully developed approach, 3D tritium transport computations are launched in the channel. The procedure is similar than the heat transfer analysis presented in sec: 5.5.3. The MHD velocity profile is kept fixed along the complete length of the channel and only tritium transport equations in the formulation described in sec: 6.1 are solved with Fluent.

Inlet concentration and material properties are exposed in tab: 6.1. Results are plotted along the central axis of the mid sectional plane (same as in fig: 6.14).

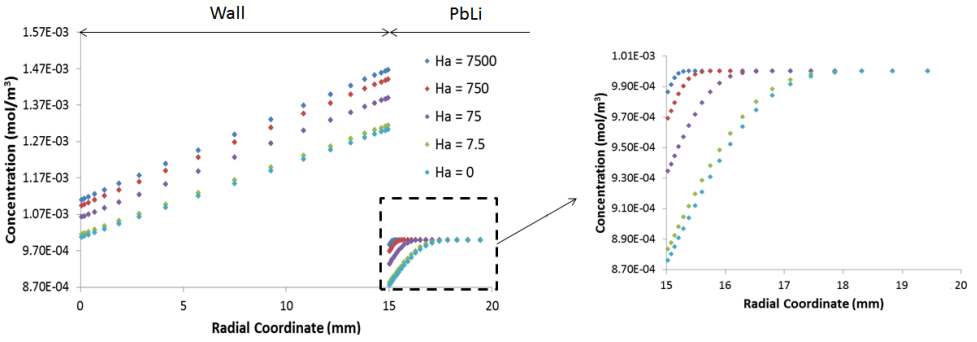

(a) Side BL.

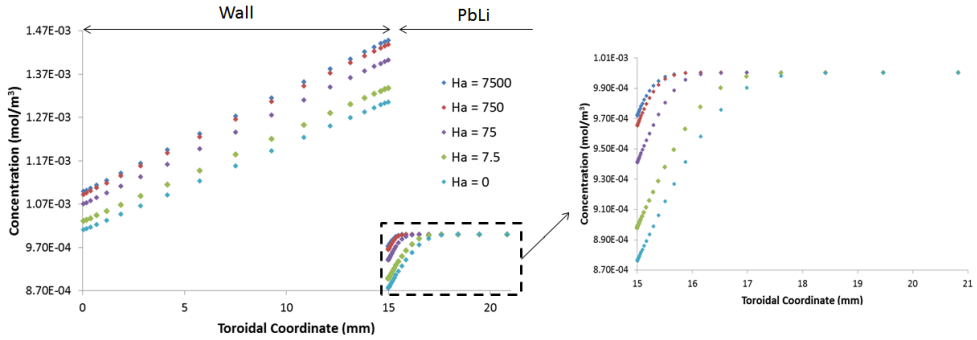

(b) Hartmann BL.

Figure 6.15: Concentration BL in MHD flows with different Hartmann numbers.

The concentration BL seems to depend only of the thickness of the velocity BL. Indeed, the shape of the concentration BL is always the same, the one shown schematically in fig: 3.2. This is independent of the jet formation in the Side BL at high Hartmann numbers. In other words, there is not a qualitatively difference between Hartmann BL and Side BL.

The reason for which the jets seem to have little impact on tritium concentration is that these simulations compute only the steady state of the system. Indeed, it can be proven that the concentration profile is independent of the velocity profile in most of the flow when the inlet concentration is uniformly distributed and the flow is fully developed:

$$u_i \partial^i c - D \partial_i \partial^i c = 0 \quad \Rightarrow \quad \partial_z c = \frac{D}{u} \partial_i \partial^i c \tag{6.22}$$

The diffusivity is of the order of 10^{-9} which means that only when $u \to 0$ (i.e. very close to the wall), the profile is different from the boundary condition at the inlet. As a consequence, having a jet with a velocity one order of magnitude higher than the core does not affect the tritium permeation, only regions with very low velocities does. It is worth noting that this is only true in the steady state when $\partial_t c = 0$. The high velocity jets will definitely impact the transient state

As explained in sec: 2.1.5, the thickness of MHD velocity BL scales with Ha^{-1} in the case of the Hartmann BL and with $Ha^{-0.5}$ in the case of the Side BL. This causes a concentration reduction higher in the Side BL than in the Hartmann BL. In other words, the mass transfer coefficient K_t and the permeation rate are higher through the Hartmann BL (direction parallel to the magnetic field) than through the Side BL (direction perpendicular to the magnetic field).

Results of the total permeation rate through the EUROFER, tritium inventory in Pbli and tritium inventory in the wall are presented in tab: 6.6.

Ha	Permeation Rate (10^{-10} g/s)	Inventory PbLi (10^{-4} g)	Inventory Wall (10^{-4} g)	K_t (10^{-6} m/s)	Sh
0	3.828	2.261	0.790	0.618	102.79
7.5	4.150	2.263	0.809	0.795	132.22
75	4.782	2.267	0.855	1.645	273.59
750	5.079	2.267	0.879	3.097	515.11
7500	5.193	2.268	0.889	4.489	746.71

Table 6.6: Deep level tritium transport results for different Hartmann numbers in an PbLi channel immersed in a magnetic field.

Based on the results presented in this section, it is possible to deduce a correlation between the Sherwood number and the Hartmann number. The relation between both dimensionless numbers is plotted in fig: 6.16. The best fitting of 2 different curves is depicted as well.

The usual power law inspired in the experimental correlations between the Sherwood number and the Reynolds and Schmidt number (sec: 3.1.4) is depicted in blue. The fitting is not very satisfactory as $R^2 = 0.969$. On the contrary, a rational expression is found to provide a much better fitting with $R^2 = 0.99986$. The best fitted parameters are the following:

$$Sh = 109.78 \cdot Ha^{0.218} \qquad R^2 = 0.969 \qquad (6.23)$$

$$Sh = \frac{104.75 + 4.30 \cdot Ha}{1 + 7.48 \cdot 10^{-3} Ha - 2.44 \cdot 10^{-7} Ha^2} \qquad R^2 = 0.99986 \qquad (6.24)$$

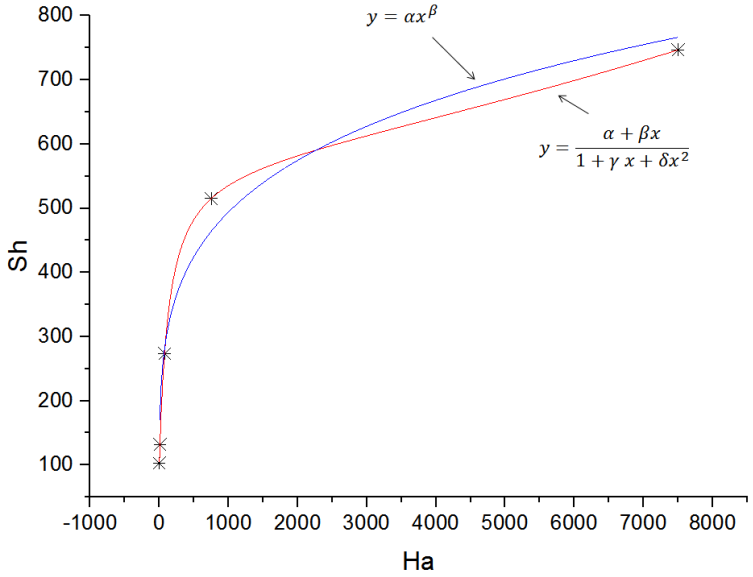

Figure 6.16: Correlation between the Hartmann number and the Sherwood number in a rectangular section PbLi channel.

It is worth noting that the quadratic term in the denominator of (6.24) is only relevant for high Hartmann numbers ($Ha > 1000$). For small Hartmann numbers ($Ha < 1000$), a fitting formula of the shape of (6.23) is much more accurate.

The correlations exposed should be seen as preliminary. More simulations considering different Reynolds and Schmidt numbers should be studied as well. Besides, experimental validation of the results is definitely needed to give more credibility to the results.

6.4.3 Tritium transport in MHD flows with volumetric generation

As a follow-up of the previous calculations, tritium volumetric generation is considered in the PbLi. As in sec: 6.3, a generation exponential profile which

varies in the direction perpendicular to the magnetic field is imposed. The exponential factor is b = -6.3013 m^{-1} [137] while the pre-exponential factor has been adjusted for having a total generation in the channel of 8 10^{-8} mol/s:

$$S_c = 2.51 \cdot 10^{-6} \exp(-6.3013x) \tag{6.25}$$

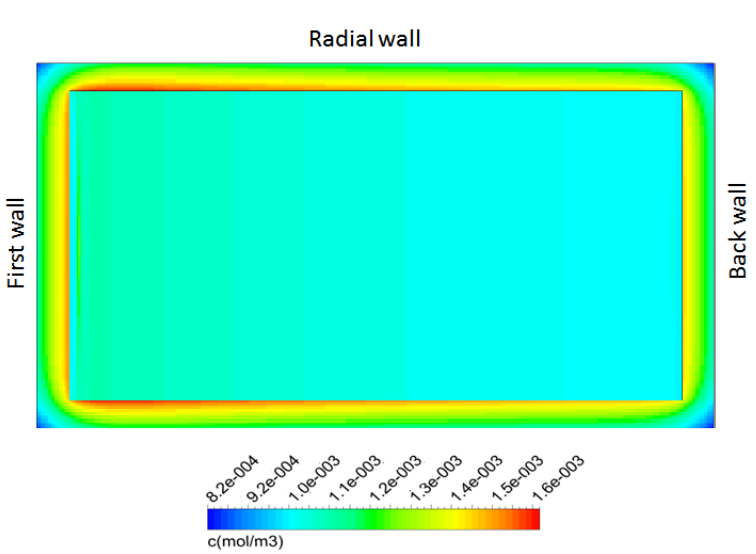

(a) Mid radial-toroidal plane.

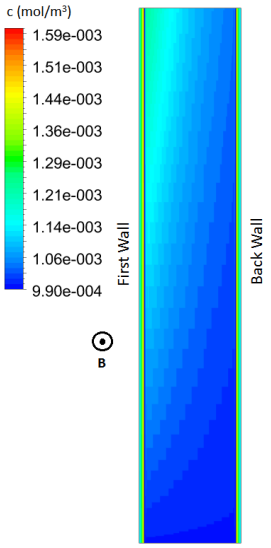

(b) Mid radial-poloidal plane.

Figure 6.17: Concentration contours in a PbLi channel with Ha = 7500 and exponential-shaped volumetric generation.

The rest of the inputs are kept the same than in the previous study in which no generation is considered. The source term breaks the simplicity of the steady-state equations (6.22). Therefore, the velocity profile influences the concentration solution in the whole PbLi domain and not only int he regions where $u \to 0$. In particular, the high velocity jets developed for high Hartmann numbers impact strongly the concentration distribution along the cross section of the channel. Fig: 6.17a shows the concentration contours in the mid-sectional plane of the channel for the case with Ha = 7500. Fig: 6.17b exposes the concentration contours in the central plane perpendicular to the magnetic field. In both figures, the effect of the velocity jet can be clearly observed next to the FW of the channel where the generation rate is higher. The existence of volumetric generation (no matter the kind of profile)

produces an increase of the tritium concentration along the axial direction. The shape of the profile S_c creates a concentration growth towards the FW.

In order to appreciate better the combining effect of the magnetic field and the volumetric generation, the concentration profile along a central line contained in the mid sectional plane perpendicular to the magnetic field is plotted in fig: 6.18.

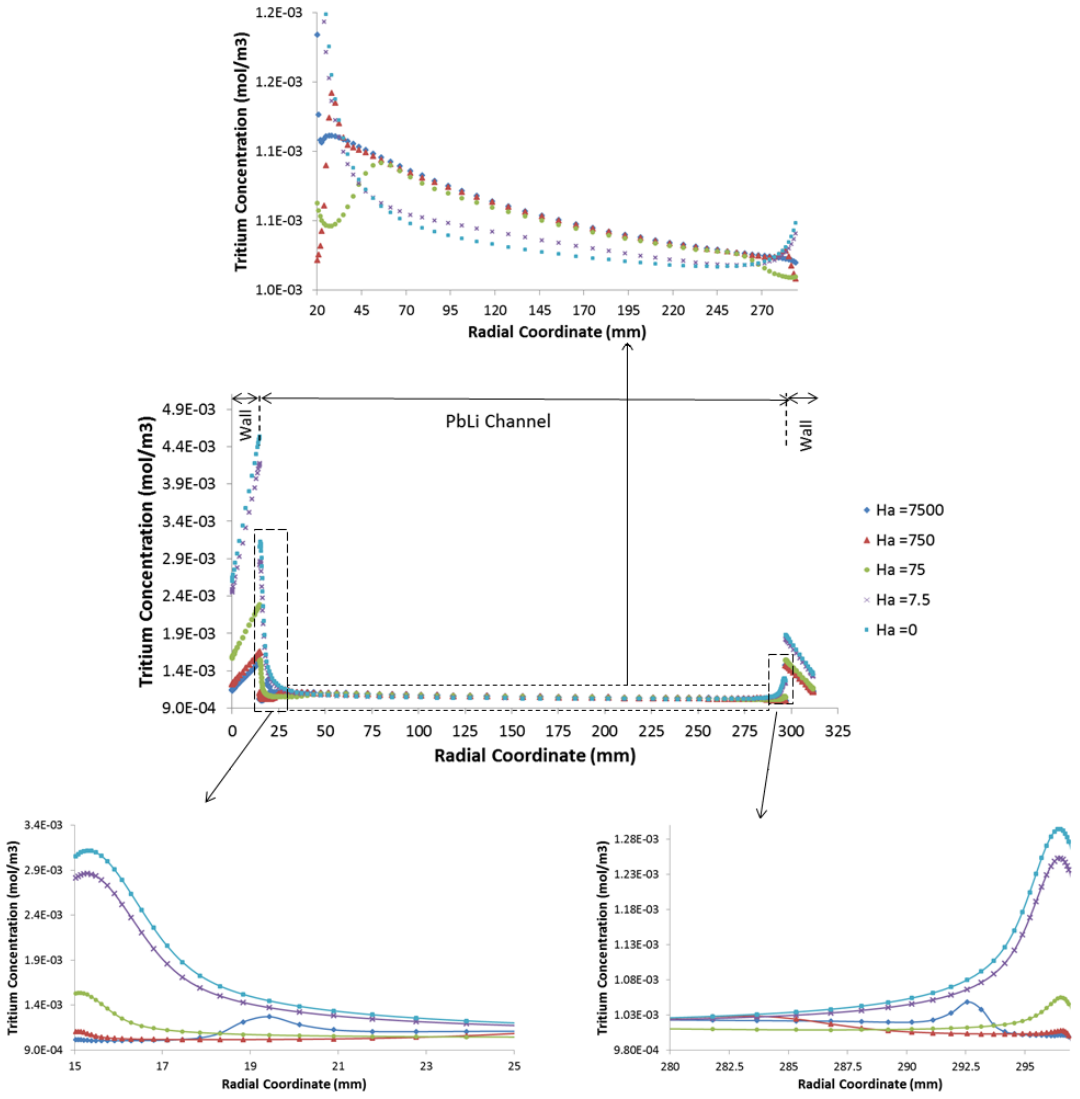

Figure 6.18: Concentration profile along a line perpendicular to the magnetic field in a PbLi channel with volumetric generation.

From the concentration profile obtained, several conclusions can be deduced:

- In contrast to the case without generation, the magnetic field reduces the permeation losses through the walls. The thin BL does not favor the tritium accumulation next to the walls. Besides, the high velocity jets in the Side BL increase the efficiency of tritium dragging next to the walls. This causes a concentration reduction in the BL which is translated into a smaller permeation rate.

- In the core flow, the concentration profile adopts the exponential profile of the generation profile.

- When the Hartmann number is of the order of 10^2 or higher, the concentration profile in the core is almost independent of the Hartmann number along the generation direction. This is a consequence of the characteristic flat velocity of this kind of flows (fig: 6.14).

- For Hartmann numbers of the order of 10^2 or higher, the concentration presents peaks in the fringing region between the BL and the core flow. Indeed, in these regions the velocity field develops small zones with velocities smaller than in the core flow. As a result of the advection, a minimum in the velocity implies a maximum in the concentration.

The last item of the list can be clearly observed in fig: 6.19, where the concentration is plotted together with the velocity for high Hartmann numbers.

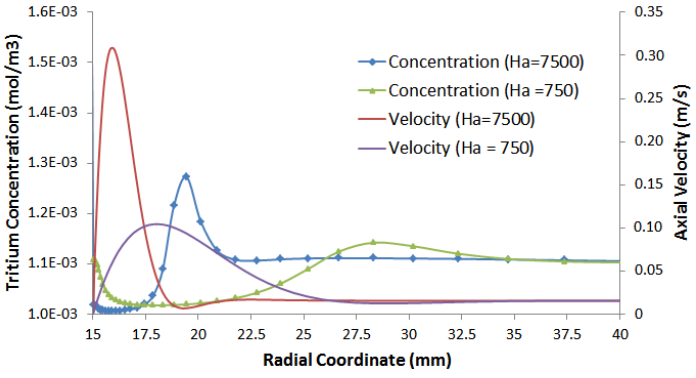

Figure 6.19: Concentration and velocity profiles next to a BL for high Hartmann number in a PbLi channel with volumetric generation.

For completeness, the concentration profile along a central line of the mid-sectional plane parallel to the magnetic field is plotted in fig: 6.20.

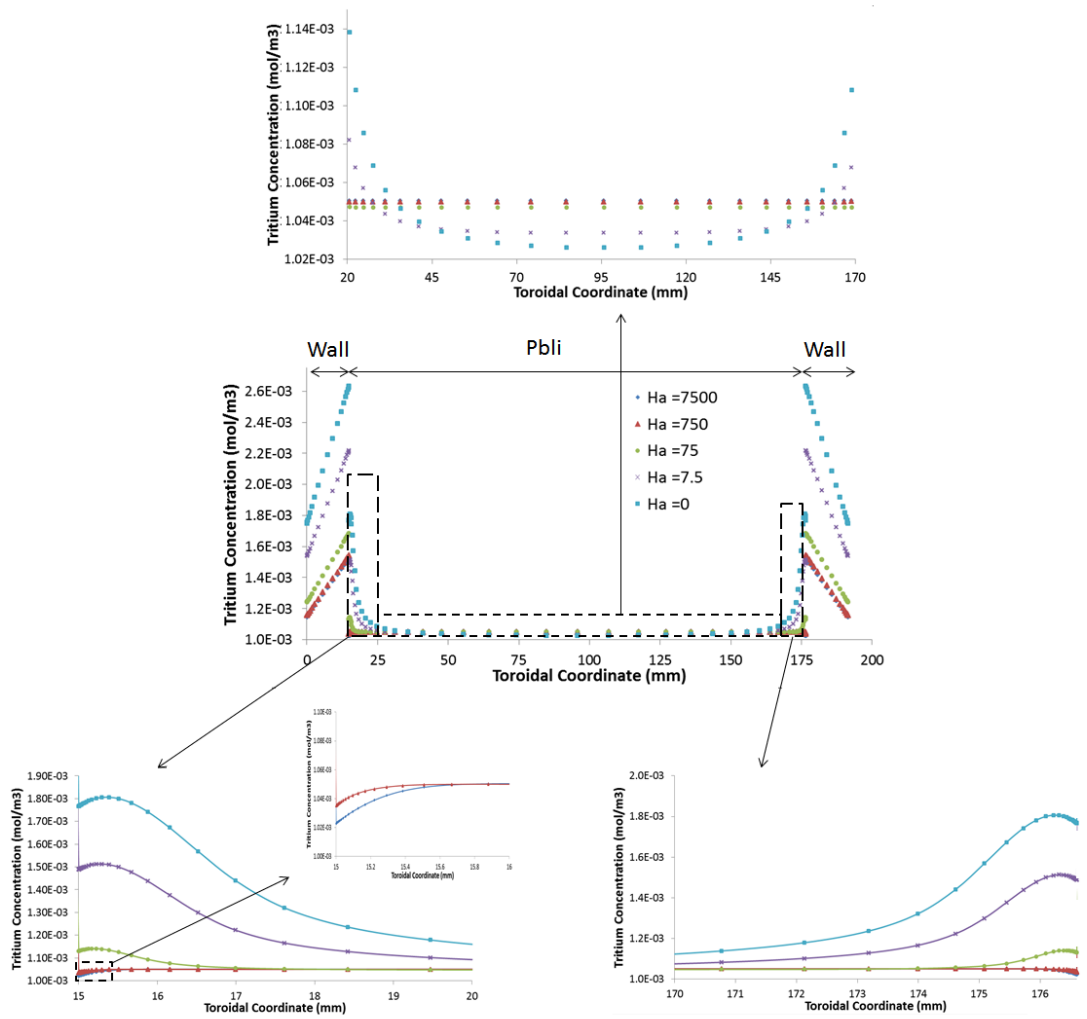

Figure 6.20: Concentration profile along a line parallel to the magnetic field.

The volumetric generation is constant along the direction parallel to the magnetic field. Therefore, the concentration is only affected by the velocity profile. This means that the core flow profile is almost flat for Hartmann numbers of the order 10 or higher. It is worth noting that for Hartmann numbers of the order of 10^2 or higher the BL is so thin that the diffusion processes are enough for removing the tritium generated inside it. This way, the concentration peak that appears in the BL in any other case that involves volumetric generation do not manifest when there is a sufficiently high magnetic field.

Global results of the tritium inventory in PbLi, tritium inventory in EUROFER and permeation losses through the wall are exposed in tab: 6.7.

Ha	Permeation Rate (10^{-9} g/s)	Inventory PbLi (10^{-4} g)	Inventory Wall (10^{-4} g)
0	1.918	2.542	1.757
7.5	1.454	2.461	1.497
75	0.703	2.386	1.061
750	0.578	2.390	0.943
7500	0.561	2.395	0.924

Table 6.7: Deep level tritium transport results for different Hartmann numbers in a PbLi channel with volumetric generation.

6.5 Tritium transport model of the DCLL gap flow

Tritium deep level analyses presented so far in this section have mainly a theoretical approach. Their objective is studying the influence of certain phenomena (volumetric generation and MHD velocity profile) on tritium permeation. For this reason, the system chosen for computing tritium evolution is relatively simple; a rectangular-section PbLi straight channel with conducting walls in isothermal conditions. The simplicity of the system allows isolating each phenomenon of study and understanding better its effect.

The conditions chosen for the previous system are as representative as possible of DCLL conditions. Parameters such as, temperature, magnetic field, wall thickness, characteristic velocity, characteristic lenght, inlet concentration, etc., are taken in order to be representative of the DCLL OB equatorial module (version 3). Despite the useful information that is derived from the analysis presented so far, it is undeniable that the geometrical simplicity of the studied channel is far from being relevant for the DCLL design.

Taking into account that one of the main objectives of the present dissertation is the improvement of DCLL system level models, it is necessary to perform a deep level analysis of a more realistic DCLL geometry. The

chosen geometry is the PbLi gap flow of the front channel in the OB equatorial module. This choice is motivated by the results obtained in sec: 4.3.3.1. In that section, it is found that the whole permeation losses from the PbLi to the He loop and the tritium inventory retained in the structural materials have their origin in the tritium generated in the gap flow. Consequently, the gap flow is considered as the most relevant geometry for computing tritium behavior.

In sec: 5.5.2, it is exposed that the gap flow is electrically decoupled from the bulk flow when considering a FCI made of alumina. Based on these results, independent MHD analysis of the gap flow geometry are presented in sec: 5.6. Thus, both tritium transport and MHD effects in the gap flow are completely independent of the bulk flow dynamics. As a consequence, under isothermal conditions, a deep level tritium transport model of the gap flow including the MHD fully developed profile, the volumetric generation and the exact geometrical distribution of the He channels can be carried out without considering the bulk flow influence. In this section, such a model is presented and its results are analyzed.

6.5.1 Deep level model results

The geometry of the studied system is exactly the same than the one presented in sec: 5.6. Therefore, the velocity profile imposed in the gap flow as an input for the tritium transport analyses is the one shown in fig: 5.27 and fig: 5.30.

Tritium transport inputs are very similar than the ones used in sec: 6.4. The inlet concentration is 10^{-3} mol/m^3. Concerning the generation rate, $8 \cdot 10^{-8}$ mol/s are generated in the whole channel following an exponential profile with an exponential factor b = -6.3013 m^{-1}. This means that $3.39 \cdot 10^{-9}$ mol/s are generated in the gap flow. The transport properties in Pbli and EUROFER are shown in tab: 6.1.

In the He channels, recombination boundary conditions with $p_{T_2} = 0$ are imposed. It is considered that the He removes the molecular tritium that permeates to the He circuits fast enough to consider a zero partial pressure. The same condition is imposed in the external side of the FW while zero-flux boundary conditions are imposed in the RW and BW as first approximation to

represent the presence of the neighbor channel.

Concentration contours in the steady state are presented in fig: 6.21. Concentration contours are projected towards the axial direction, which allows observing clearer the concentration gradients.

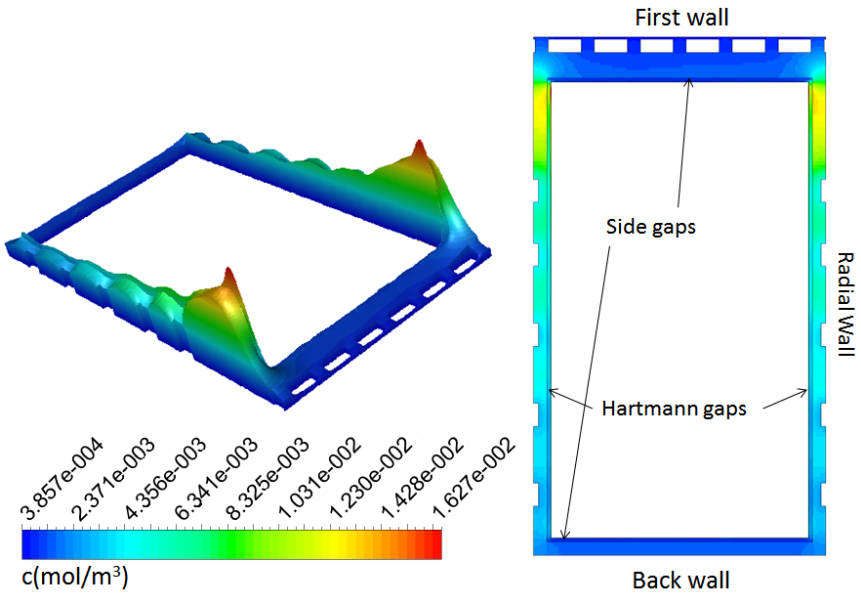

Figure 6.21: Concentration contours in the mid sectional plane of the PbLi gap flow.

The He channels act as sinks of tritium. They are responsible of the wavy concentration profile along the radial direction, especially in the RW. It is important noting that the vast majority of the permeation flux from the PbLi to the He channels goes through the RW. This flux has its origin in the tritium generated in the Hartmann gap. The high velocity jet in the Side gap drags the tritium generated in it rather efficiently. Therefore, tritium concentration is much lower in the Side gap even in the closest region to the FW where the generation is maximal.

The 2 peaks of highest concentration are located in the FCI EUROFER external layer. In the steady state, this layer is in equilibrium with the gap flow in every point of the space as the alumina is supposed to be a perfect permeation barrier. As a consequence, the highest concentration zones in the PbLi (corners of the Hartmann gaps) are in contact with an even higher concentration peak in the EUROFER layer of the FCI.

Fig: 6.22 exposes the vector plot in of the diffusion flux in the wall ($J[mol/m^2s]$). It allows identifying the regions of highest permeation rate. Besides, it is found that part of the tritium that permeates from the Hartmann gap into the RW re-enters the PbLi through the Side gap. This is due to the small concentration in the Side gap which acts like a good tritium sink as well. It is important noting that the vector sizes are not normalized with respect to their magnitude. All vectors have the same size, the color represent its intensity.

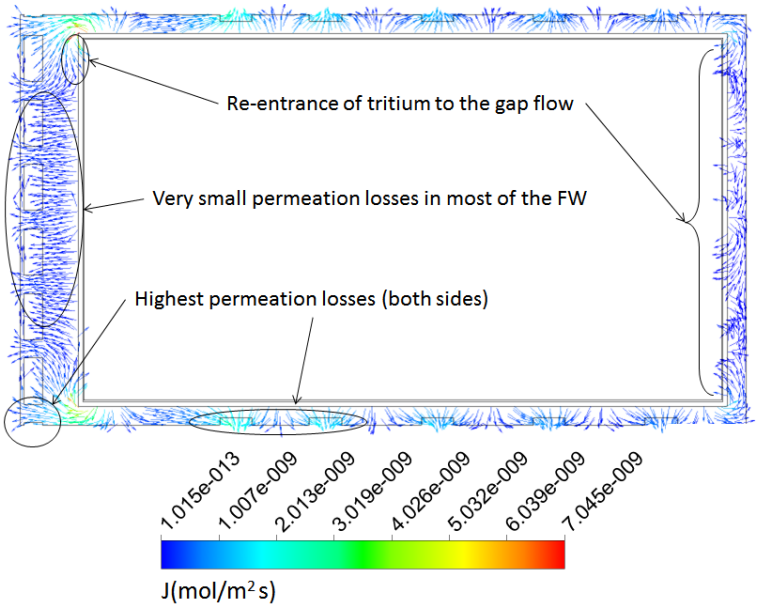

Figure 6.22: Tritium diffusion flux inside the wall of one DCLL channel.

Like in the previous cases that consider volumetric generation, there is an axial dependence of the concentration. This dependence is shown in fig: 6.23 where the concentration of tritium in the interface between the PbLi and the wall is shown (PbLi side). The concentration grows with the axial coordinate due to the accumulation caused by the generation. The sink effect of the helium channels can be clearly distinguished as well in this figure.

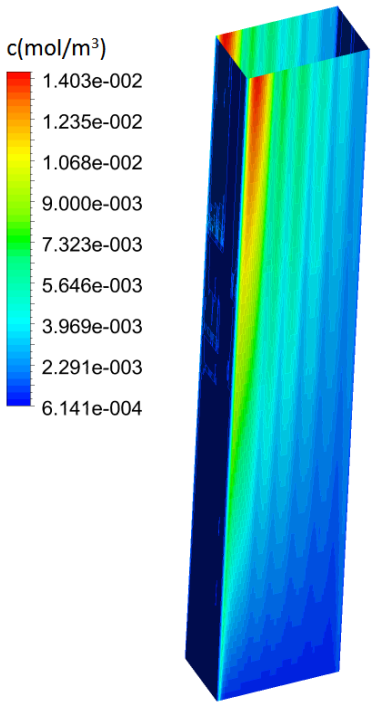

Figure 6.23: Concentration at the interface PbLi gap/wall (PbLi side).

The global results of the model i.e., the tritium inventories and the permeation rate are exposed in tab 6.8.

Inventory PbLi gap flow (10^{-4} g)	0.273
Inventory wall (10^{-4} g)	1.618
Inventory FCI EUROFER layer (10^{-5} g)	0.105
Total permeation rate (10^{-9} g/s)	1.556

Table 6.8: Results of the deep level tritium transport study of the DCLL gap flow.

6.5.2 Upgrading of system level models

In order to take benefit from the results of the deep level model, it is necessary to develop a system level model of the system formed by the gap PbLi flow, the EUROFER walls and the external EUROFER layer of the FCI. A model of this

kind is presented in chap 4 when exposing the PFDs of the initial system level model of the DCLL (fig: 4.8). That model must be upgraded if the deep level results are wanted to be reproduced.

At the light of the results exposed in fig: 5.27, fig: 6.21 and fig: 6.22 the following modifications are applied to the model:

1. The PbLi flow rate distribution between the bulk flow and the gap flow is no longer given by the cross sections. Instead, the flow partitioning obtained in sec: 5.5.2 is used. Besides, the gap flow rate is no longer equally distributed between the Side gaps and the Hartmann gaps. The partitioning is given in terms of a parameter α. This value is obtained with the MHD analyses of sec: 5.6.

2. The great concentration differences between the Hartmann gaps and the Side gaps implies that there is an important tritium flux accross the corners of the gap flow. The four PbLi channels that formed the gap flow are now connected using the following relation:

$$J = K_t(c_1 - c_2) \tag{6.26}$$

   Where J is the tritium flow between the channels. c_1 and c_2 are the concentration of the two channels in contact through the corner. The mass transfer coefficient K_t must be optimized in accordance with the Fluent results.

3. According to fig: 6.22 there is also an important tritium diffusion flux around the corners of the the channel walls. This causes important permeation fluzes towards some particular helium channels of the FW. EcosimPro components does not allow diffusion fluxes in the direction parallel to the interface. If this were added to the component model code, it would lost its 1D nature with their corresponding loss of computational speed. Instead, permeation surfaces in the He channels have been artificially adapted for correcting this corner flux. The FW external surface has been increased by a factor ψ_{FW} while the RW external surface has been reduced by a factor ψ_{RW}. This way, permeation through the FW is enhanced and permeation through the RW is mitigated. The exact values of ψ_{FW} and ψ_{RW} must be determined with an optimization procedure. Note that the coefficient ψ_{FW} and ψ_{RW}

does not represent the same than in chap: 4 where they are based on the results of [100].

It is worth noting that surface correction parameters (ψ_{FW} and ψ_{RW}) are considered better suited for reproducing deep level results than mass transfer coefficients defined in the interface PbLi/EUROFER. The reason is that mass transfer coefficients can only mitigate the permeation rate but they cannot enhance it. Increasing the permeation rate using a BL approach would require generate tritium inside the BL. This entails to a much more complex optimization procedure with too many unknown parameters.

The new flowchart designed for the gap flow system level model is exposed in fig: 6.24.

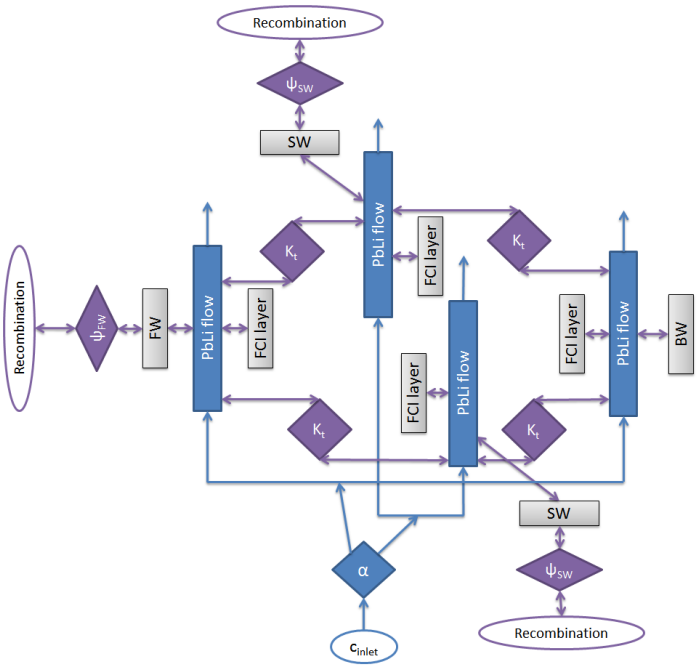

Figure 6.24: PFD used for upgrading the gap flow system level model. The optimization parameters are inside purple diamonds.

Taking into account that the parameter α is directly given by the MHD computation(tab: 5.10, sec: 5.5.2), the gap flow model at system level has 3 parameters that can be used for its upgrading: K_t, ψ_{FW} and ψ_{RW}. The objective of the optimization procedure is obtaining deviations from the deep level results inferior to 5% for the 3 main global outcomes: the inventory in the PbLi, the

inventory in the wall and the permeation rate to the He. It has been found impossible obtaining small deviations just by modifying K_t and setting $\psi_{FW} = \psi_{RW} = 1$. Either the permeation rate, the inventory in the wall or the inventory in PbLi deviates significantly from the deep level results.

As a consequence, sweeps of the 3 parameters have been carried out systematically. After some testing, it was found that the tritium inventory in the wall varies relatively little with ψ_{FW} (fig: 6.25).

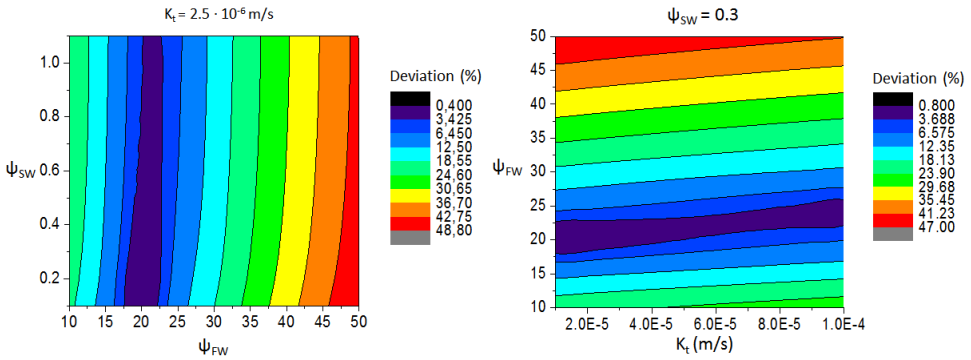

Figure 6.25: Tritium inventory in the wall. Deviation of system level model results with respect to deep level model results.

At the light of the results shown in fig: 6.25, $\psi_{FW} = 20$ seems to be a good starting value for the optimization of the two other parameters. Following this criteria, sweeps of ψ_{RW} and K_t are performed fixing ψ_{FW} to 20. The results of this optimization procedure are exposed in fig: 6.26.

According to the results, the following set of parameters reduces significantly the deviation of the 3 outcomes: $K_t = 2 \cdot 10^{-5}$ m/s, $\psi_{FW} = 20$ and $\psi_{RW} = 0.4$. Unfortunately, the deviation of the wall inventory is still over the goal of 5%. A sweep of ψ_{FW} fixing the other two parameters to the previous values is therefore needed. Results of this new sweep show that smaller deviations are obtained with $\psi_{FW} = 25$ (fig: 6.27).

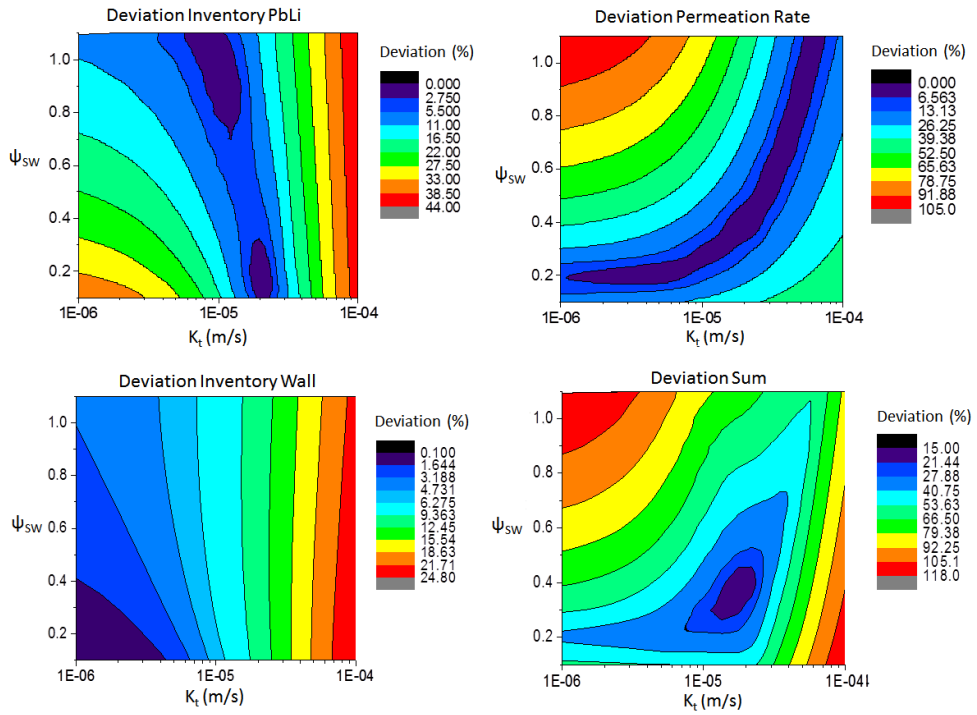

Figure 6.26: Parametric sweep of K_t and ψ_{RW} with $\psi_{FW} = 20$ for the DCLL gap flow.

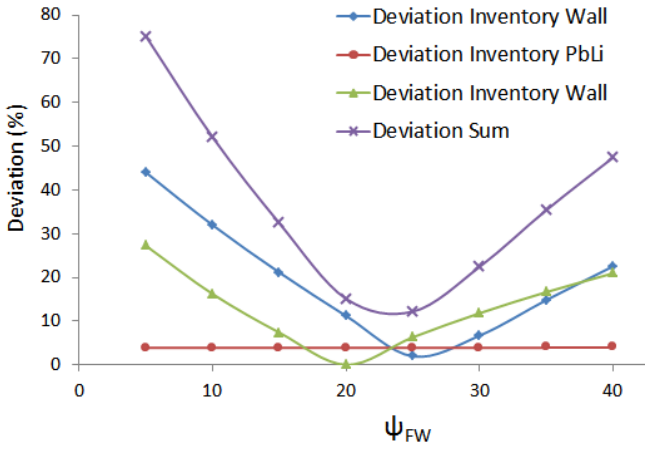

Figure 6.27: Parametric sweep of ψ_{FW} for the DCLL gap flow ($K_t = 2 \cdot 10^{-5}$ and $\psi_{RW} = 0.4$).

Considering the results shown in fig: 6.27, a second iteration of the parametric sweep exposed in fig: 6.26 is repeated with $\psi_{FW} = 25$. In this case,

the goal of having deviations below 5% is fulfilled for the set of parameters: $K_t = 2 \cdot 10^{-5}$ m/s, $\psi_{FW} = 25$ and $\psi_{RW} = 0.3$. Indeed, the minimum of deviations sum is smaller for $\psi_{FW} = 25$ than for $\psi_{FW} = 20$ (fig: 6.28).

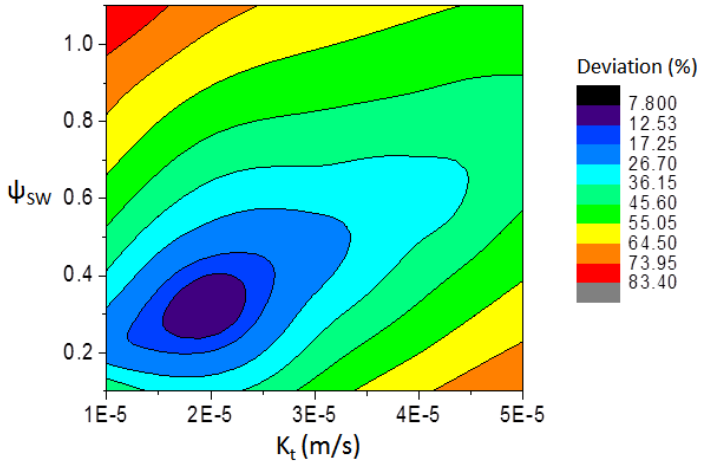

Figure 6.28: Parametric sweep of K_t and ψ_{RW} with $\psi_{FW} = 25$ for the DCLL gap flow.

Tab: 6.9 shows the final results of the optimization process. The original system level model (no modifications) underestimate the permeation rate and the tritium inventories in one order of magnitude. This is mainly due to the unalike distribution of flow in the gap caused by the MHD effects. Therefore, in this specific annular geometry, the magnetic field is enhancing the permeation in contrast to what is obtained for cross sectional channel with generation (sec: 6.4.3). When correcting the flow distribution between the bulk and the gap flow using the MHD results exposed in sec: 5.5.2, there is a good improvement in every quantity. Besides, the permeation rate is in this case overestimated, which is conservative for the safety requirements. Consequently, only with the flow rate modification the improvement in the results is notorious. Naturally, the optimized system level model provides the minimum deviations of the 3. The deviation of the magnitudes respect the Fluent results is below 4% for every quantity when using the optimized set of parameters.

		Permeation Rate (10^{-9} g/s)		Inventory PbLi (10^{-5} g)		Inventory Wall (10^{-4} g)	
		Value	Deviation (%)	Value	Deviation (%)	Value	Deviation (%)
Fluent		1.556	–	2.725	–	1.618	–
EcosimPro	No upgrading	0.239	84.67	0.930	65.88	0.398	75.42
	Flow distribution corrected	2.542	63.36	3.072	12.74	0.868	46.38
	Optimized model	1.495	3.89	2.663	2.25	1.589	1.84

Table 6.9: Results comparison between deep level model and system level models for the gap flow of the DCLL.

6.6 Discussion

In this chapter, the influence of the magnetic field and the volumetric generation on the tritium transport in the steady state is studied extensively. Both effects are analyzed independently first in a simple PbLi channel, for theoretical purposes. From these analyses, the following important conclusions can be derived concerning the influence of the magnetic field in tritium permeation:

- When there is no volumetric generation in the channel, tritium concentration develops BLs next to the walls. The concentration in the BL is lower than in the core flow. The magnetic field reduces the thickness of the BLs which mitigates the falling of tritium concentration next to the interfaces enhancing tritium permeation through the wall. The higher the field is the higher the tritium permeation.
- When there is volumetric generation in the channel, tritium concentration also develops BLs next to the walls but with opposite shape. In other words, the concentration is higher in the BL than in the core flow. In this case, the magnetic field mitigate the accumulation of concentration next to the interface which reduces the permeation rate. The higher the field is the lower the tritium permeation.

When no volumetric generation is considered, component level models are able to reproduce the deep level models results with relatively ease. It is found enough to impose an appropriate mass transfer coefficient in the BL. Mass

transfer coefficient can be derived from deep level analyses. In this regard, a preliminary correlation for computing the mass transfer coefficient for any field is given.

Reproducing 3D results with component level models when there is volumetric generation is more complex. Simple BL with mass transfer coefficients are no longer valid (at least for low magnetic fields). BL components that includes generation inside them are found to be valid for these cases. An optimization of the parameters of the generating BL is unfortunately necessary for obtaining accurate results.

From a more practical perspective, a particular analysis of the DCLL gap flow is presented as well. This simulation studies the effect of the MHD and the volumetric generation in an annular geometry. Besides, the He channels are not uniformly distributes in the channel walls creating tritium sinks in the middle of geometry. The quasi-stagnant PbLi regions created by the magnetic field in the annular geometry increases the permeation rate importantly in comparison with the case with no field.

A system level model based on the correction of the permeation surfaces is presented. After an optimization process of these surfaces, the deep level results are replicated with small deviations. This optimized model will serve for the advanced tritium transport model at system level of the DCLL presented in chap: 7.

Chapter 7

Advanced system level model of the DCLL blanket

In this chapter, an advanced version of the system level tritium transport model of the DCLL blanket is developed. The model characteristics are introduced first, enumerating the upgrades and modifications introduced with respect to the initial version shown in chap: 4.3. Results are exposed for 3 different scenarios. The first does not take into account any 3D nor MHD effect. The second uses the MHD information derived from the simulations of sec: 5.5. The last scenario makes use of the optimization process developed with deep level model in sec: 6.5. Finally, sensitivity analyses of some key parameters are presented.

7.1 Model description

The system level model of the complete DCLL blanket and its associated subsystems presented in this chapter is designed as an advanced version of the initial model explained in chap: 4. Following the work methodology exposed in fig: 1.11 (sec: 1.3.2), this advanced model constitutes the last step for closing the feedback cycle. Indeed, this version make use of the information given by the deep level tritium transport analysis of chap 6, in particular in sec: 6.5, for increasing its accuracy.

The advanced system level model includes considerable improvements with

respect to the initial version. The modifications are listed as follows:

- In order to adapt the model to the needs of the DCLL design project, the advanced model is based in version 3 of the DCLL design (sec: 1.4.1). Besides, this model is based on the DEMO 2015 which is formed by 18 sectors.
- The PbLi piping outside the blanket is now considered in detail, including the computations of the permeation losses from the pipes to the room.
- The He loop is now fully included in the model. This involves the He piping, the CPS and the secondary HX.
- The BSS which acts as PbLi and He manifold is now included in the model. The BSS constitutes a considerable amount of PbLi which is still close enough to the plasma to have tritium generation inside it. Besides, PbLi and He manifolds are placed next to each other which implies an extra permeation surface that is not considered in the initial version.
- Instead of using average temperatures in the different channels and walls of the blanket, linear temperature profiles are imposed in this model. The PbLi and He channels includes linear temperature profiles along the flow direction while the solid materials includes temperature profiles along the diffusion direction. Temperature impact tritium transport properties as they follow an Arrhenius formula. The code does not compute heat transfer. The temperature map in the blanket is treated like an input.
- The PbLi gap flow in the module channels accepts a flow distribution based on the results of sec: 6.5. The initial partitioning (no MHD effects considered in the gap) is simulated also for comparative purposes.

It is important noticing that this system level model is designed using the basic component level models presented in sec: 4.2. Indeed, the transport equations in the bulk of fluid and solid materials as well as the surface processes at the interfaces are the same. The component level upgrades are focused on the description of the concentration BL and in the adjustments of the gap flow surfaces. However, the main increase of complexity comes from the design of more realistic PFDs.

7.1.1 Process flow diagrams

As explained in sec: 4.3, system level models of BB are developed based on the repetition of what is called minimal geometrical unit. For the advanced version, the minimal geometrical unit does not conceptually change with respect to the initial system level model. The toroidal segmentation of the module in parallel circuits is still present in the design. Therefore, the minimal unit is once more one the toroidal circuits. Nevertheless, the PbLi and He flow paths and number of circuits per module are different from version 1 to version 3 (fig: 1.16, sec: 1.4.1). The minimal unit of the advanced model is adapted to the version 3.

The minimal geometrical unit of this system level model is shown in fig: 7.1 together with the PFD used for modeling it.

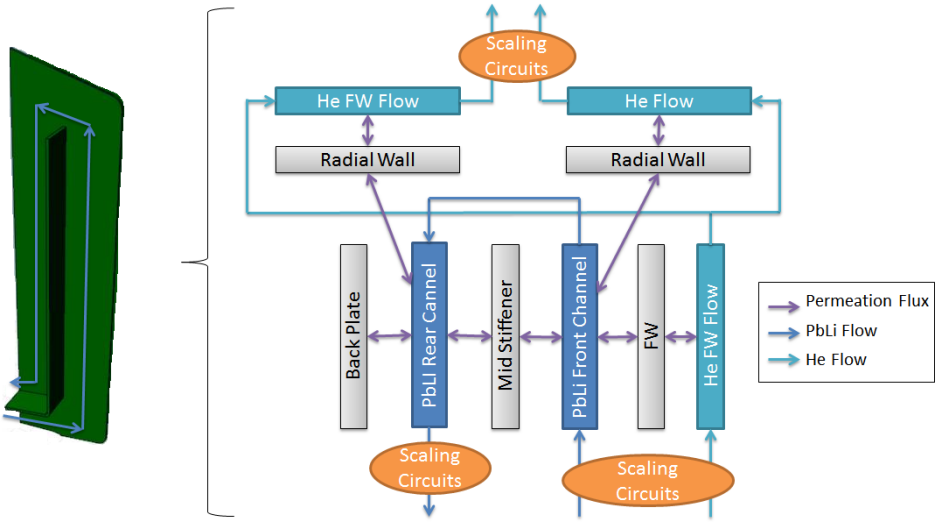

Figure 7.1: Minimal geometrical unit and its corresponding flowchart of the advanced DCLL tritium transport model at system level.

The orange ovals in the flowcharts scale the flow in accordance with the number of equal elements. For example, there are 7 parallel circuits per module, thus, the flow that enters in one module is divided by 7. Complementary, when the flow is leaving the module it is multiplied by the same number. When computing the inventory, the total number of equivalent units must be taken into account.

As mentioned, the BSS is included in this model. Therefore, before the PbLi and He flows reaches the external loops they pass through their respective manifolds contained in the BSS. Fig 7.2 shows the PFD employed for modeling this geometry together with a schematic view of the BSS.

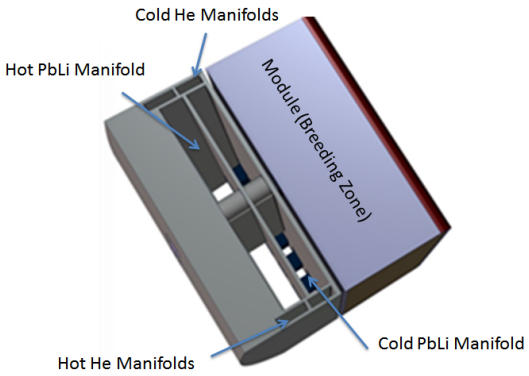

(a) Top view of an OB module.

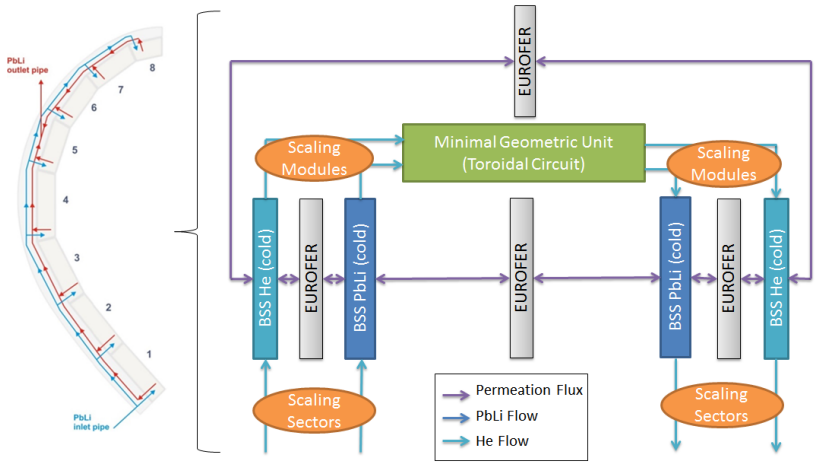

(b) PFD.

Figure 7.2: PFD used for modelling the BSS manifolds of the DCLL blanket.

It is worth noting that the PFD exposed in fig: 7.1 (minimal geometric unit) is used as a component in the one shown in fig: 7.2. This way the system level model is build layer by layer from the component level models to the global model of the blanket.

The PFD of fig: 7.2 represents one segment of the DCLL. The differences between OB segments and IB segments are not considered. As a consequence, the tritium transport model of the complete DCLL is formed simply by the

repetition of the 18 sectors with 5 segments per sector (90 segments). Besides the channels needed for modeling the blanket, the model includes the PbLi and He loops. Note that the total number of He loops and PbLi loops is different. Consequently, the PbLi and He flows are scaled differently as well. The most external PFD of the DCLL system is exposed inf fig: 7.3.

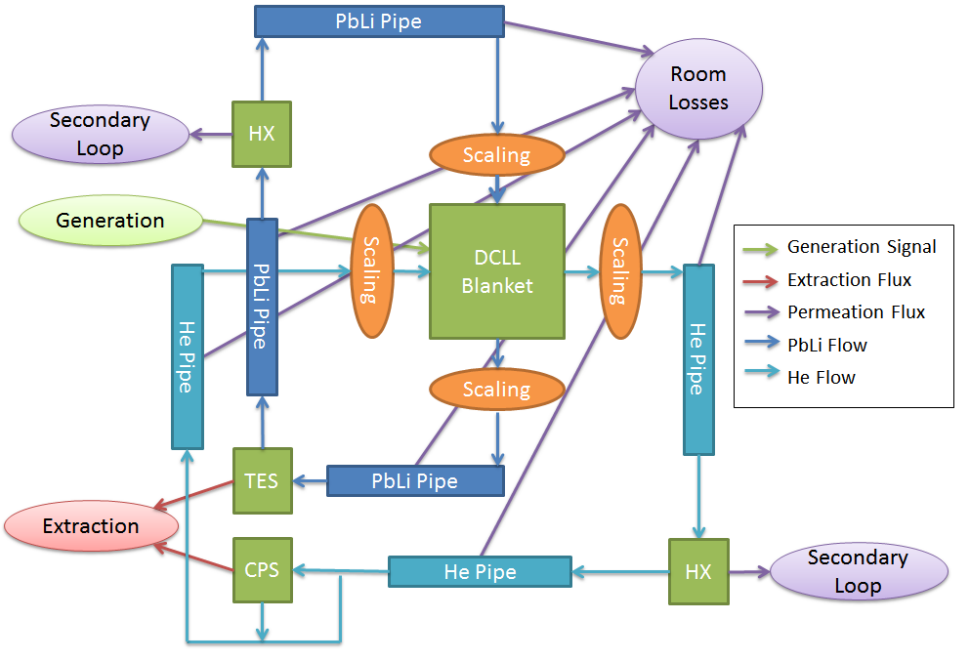

Figure 7.3: PFD for the advanced tritium transport model of the DCLL blanket and its main auxiliary systems.

The CPS is modeled exactly as the TES, i.e using a black-box approach of certain efficiency (sec: 4.2.4). The main difference between CPS and TES models is that CPS does not process the full flow rate of the loop. There is a bypass upstream the CPS that allows selecting which percentage of flow is processed. Specific values of the TES and CPS parameters are obtained from the designers of these auxiliary systems [105, 154].

The HX model is already exposed in sec: 4.3.1. It essentially consists of some volume of fluid in contact with a material. In this version, a linear temperature gradient is imposed aiming at reproducing the heat exchange. The HXs of the He and PbLi loop have different material composition, permeation surfaces and temperatures but they are modeled in the same way. The main difference is that the HX of the PbLi loop uses water in the secondary loop (steam generator)

while the HX of the He loop uses a molten salt ($NaNO_3$-$NaNO_2$-KNO_3) in the secondary loop. This salt is carried afterwards to an steam generator serving as an intermediate power storage system.

7.1.2 Input parameters

There are many input parameters in this model. Most of them are related with the geometrical configuration of the blanket OB module. These dimensions are taken directly from the DCLL design specifications [46]. Fig: 7.4 depicts the mid radial-poloidal (left) and mid radial-toroidal (right) cuts of one OB segment. The dimensions of the channels are shown as well.

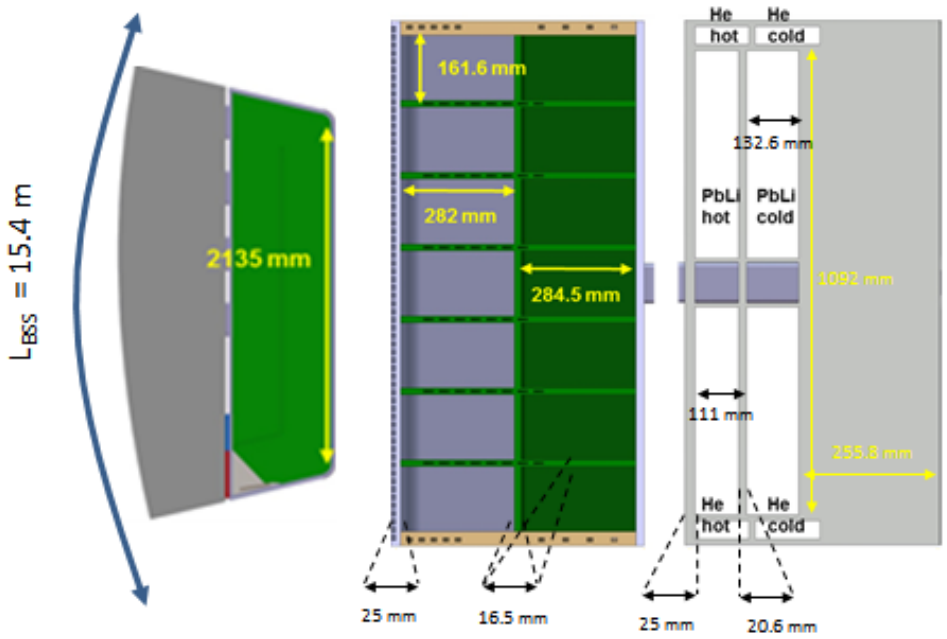

Figure 7.4: Dimensions of one OB DCLL segment.

Concerning the temperatures, it is assumed that the BSS manifold channels work in isothermal conditions. The PbLi and He hot channels have a temperature of 550°C and 455°C, respectively. Both cold channels work at 300°C. The PbLi temperature map inside the breeder zone is shown in fig: 7.5 while the He temperature map in the module walls is depicted is fig: 5.19 (sec: 5.5).

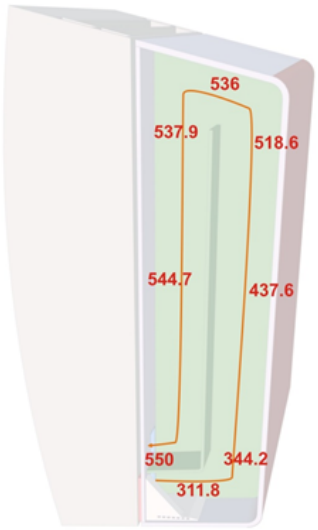

Figure 7.5: PbLi temperature map in the DCLL breeder zone.

The input data concerning the PbLi loop are given by the European research group in charge of the design of these loops [155]. There is some lack of information as the PbLi loops are still in a preliminary design phase. In particular, only the total length of the loops is avaliable (55 m). Therefore, in this model the lengths of each PbLi stretch are estimated based on functional considerations. For example, it is logical to assume that the pipes from the blanket to the TES and from it to the HX are shorter than the pipe from the HX to the blanket. The dimensions of the PbLi loop are depicted in tab: 7.1. The mass transfer coefficients in the pipes are calculated using the Berguer-Hau experimental correlation [150] which is valid for turbulent flows in pipes. The values of K_t is considerably high. Therefore it is not expected a significant permeation reduction in the external pipes caused by the diffusion in the BL.

Concerning the He loops, there are not specific available data yet within the EUROfusion project. Unfortunately, the coolant loops for HCPB and WCLL blankets [156] have been prioritized over the other concepts. As a consequence, with the objective of getting input data as relevant as possible, the HCPB coolant loops has been re-scaled to the temperatures and flow rates of the DCLL helium loops. The inputs considered are exposed in tab: 7.2.

PbLi external loops	
Total number of loops; N (-)	12
Mass flow rate per loop; $\dot{m}$ (kg/s)	2101.4
Internal diameter; D_{in} (mm)	354
Wall thickness; t (mm)	26
Pipe length before HX; L_1 (m) and L_2 (m)	5
Pipe length after HX; L_3 (m)	45
PbLi temperature before HX; T_1 (°C) and T_2 (°C)	550
PbLi temperature after HX; T_3 (°C)	300
Mass transfer coefficient before HX; K_{t1} (m/s) and K_{t2} (m/s)	$2.15 \cdot 10^{-4}$
Mass transfer coefficient after HX; K_{t3} (m/s)	$6.23 \cdot 10^{-5}$
TES extraction efficiency; η_{TES} (%)	80

Table 7.1: PbLi loops input parameters.

He external loops	
Total number of loops; N (-)	9
Mass flow rate per loop; $\dot{m}$ (kg/s)	249.34
Internal diameter; D_{in} (mm)	292
Wall thickness; t (mm)	16
Pipe length before the HX; L_1 (m)	12.43
Pipe length between the HX and the CPS; L_2 (m)	4.2
Pipe length after the CPS; L_3 (m)	91.17
He temperature before HX; T_1 (°C) and T_2 (°C)	455
He temperature after HX; T_3 (°C)	300
CPS extraction efficiency; η_{CPS} (%)	90
Relative flow rate processed by the CPS; α (%)	0.1

Table 7.2: He loops input parameters.

Regarding the HX of both loops, design information is supplied by the European design team in charge of these subsystems [157]. The baseline design is based on what is called bayonet tube type design. In contrast to a helical coil design, the bayonet tube type consist on a certain number of straight tubes immersed in the PbLi flow. Inside each tube, pressurized water is injected through a slave conduit, converted into steam and extracted through an annular tube. The schematic design of one tube is presented in fig: 7.6.

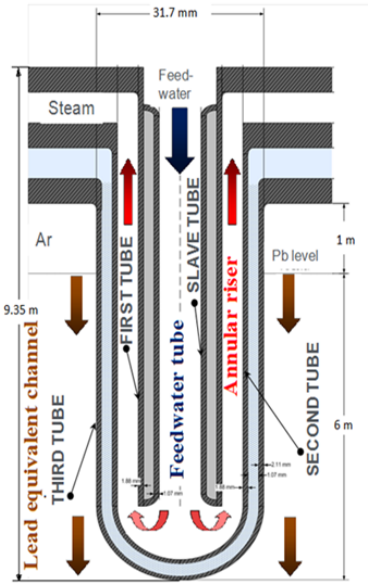

Figure 7.6: Schematic view of one tube of the PbLi HX.

Unfortunately, the design of the He HX is not as mature as the PbLi one. The base line option is still a straight tube design but it is unclear yet how the molten salt flow path will be. There is also lack of information regarding the rest of operational conditions of the molten salt loop. Besides, the transport properties of this salt are not available in literature. As a consequence, it has been decided to considered this intermediate loop as the final step of tritium transport permeation. In other words, the tritium that reaches the molten salt is considered a loss to the environment as it would be with the secondary water loop of a steam generator. This approach is the most conservative one from the safety point of view. The numerical inputs needed for the tritium transport models of the PbLi and He HX are exposed in tab: 7.3.

Finaly, most of the transport properties of the materials involved in the blanket can be found in tab: 4.1 (sec: 4.3.2). For this model, the tritium solubility in PbLi is taken from Chan's and Veleckis' work [158]. In this work the authors found an intermediate value between the extreme cases considered in sec: 4.3.4 (fig: 4.11). The pipe walls for both loops and the tubes of the HX are made of 316L steel. The transport properties of this steel are exposed in tab: 7.4 which are taken from experimental data [76].

	PbLi HX	He HX
Number of HX; N_{HX}	6	4
Number of tubes per HX; N_{tubes}	1669	11975
Contact tube length; L (m)	6	18
Tube outer diameter; D (mm)	31.73	15.08
Tube wall thickness; t (mm)	5.06	1.5
Primary loop inlet temperature: T_{in}	550	455
Primary loop outlet temperature: T_{out}	300	300
Secondary loop inlet temperature; T_{sec}	270	280

Table 7.3: Input data for the HX tritium transport model.

		316L Steel
D	$D_0(m^2/s)$	$5.9 \cdot 10^{-7}$
	Ea (kJ/mol)	-51.9
K_s	K_{s0} (mol/Pa$^{0.5}$m^3)	0.349
	Ea (kJ/mol)	-11.7
σK_r	σK_{r0}(m^4/mol s)	$6.64 \cdot 10^{-6}$
	Ea (kJ/mol)	-44.7
σK_d	σK_{d0}(mol/Pa s m^2)	$8.1 \cdot 10^{-7}$
	Ea (kJ/mol)	-68.1

Table 7.4: Hydrogen transport properties of 316L steel.

7.2 Reference case results

In this advanced tritium transport system level model of the DCLL blanket, 3 different scenarios are compared as candidates for reference case scenario. They are named as follows:

1. Original model: This model does not consider any MHD nor deep level tritium transport model information presented in chap: 5 and chap: 6. This means that the flow distribution between the gap flow and the bulk flow in every PbLi channel is given just by the differences between cross sections. Besides, the gap flow is evenly distributed between the Side gaps and the Hartmann gaps. This is the approach used in the initial model (chap: 4.3).

2. MHD corrected model: This model takes into account the MHD analyses

presented in sec: 5.5. This implies that the distribution between the bulk flow, the Side gap flow and the Hartmann gap flow is imposed taken into account the fully developed MHD velocity profiles (fig: 5.27).

3. Optimized model: This model takes into account both, the MHD flow distribution and the optimization process presented in sec: 6.5. Therefore, the permeation surfaces close to the gap flow and mass transfer coefficients have been corrected to reproduce the steady-state deep level tritium transport analyses carried out for this system.

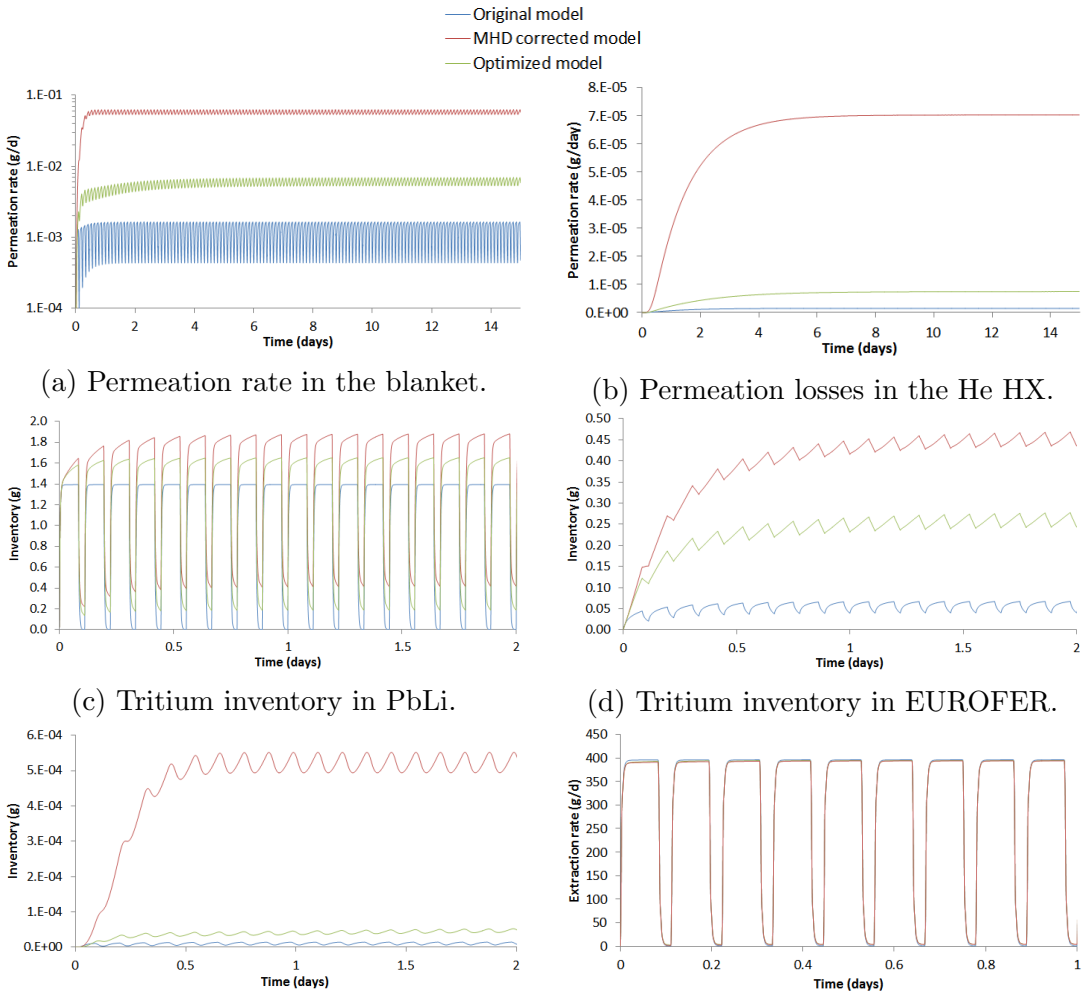

(a) Permeation rate in the blanket.

(b) Permeation losses in the He HX.

(c) Tritium inventory in PbLi.

(d) Tritium inventory in EUROFER.

(e) Tritium inventory in He.

(f) Extraction rate in the TES.

Figure 7.7: Global outcomes of the DCLL advanced tritium transport model at system level.

By comparing the 3 kinds of models, the impact of the 3D elements in global results can be observed. Results of the system level model for the 3 scenarios are exposed in fig: 7.7.

The original model provides the lowest permeation rate and consequently the lowest tritium inventory in EUROFER and He. On the contrary, the MHD corrected model computes the highest permeation rate. This is a direct consequence of the influence of the quasi-stagnant Hartmann gap. When the MHD flow distribution is considered, the majority of the tritium produced in the Hartmann gap permeates through the He as the PbLi velocity is very small in this region. The optimized model produces an intermediate value of the permeation rate. Despite te velocity distribution is the same, the permeation surfaces of the RW (Hartmann walls) have been corrected to reproduced the diffusion along the radial direction.

As in the initial system level model presented in chap: 4.3, the vast majority of the tritium generated ends up extracted by the TES. There is a small difference between the extraction rate in the 3 scenarios. Indeed, the tritium concentrations in PbLi at the exit of the blanket (fig: 7.8a) are similar but not equal. The original model has a slightly higher concentration in PbLi at the exit of the blanket which implies slightly higher extraction rate (fig: 7.8b).

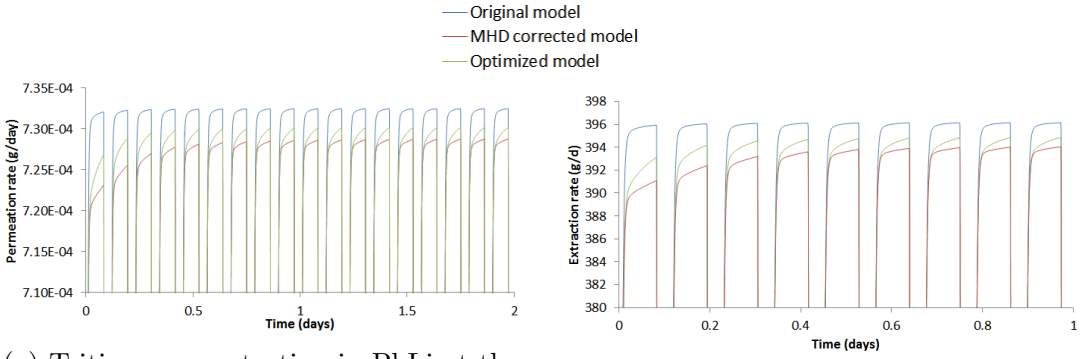

(a) Tritium concentration in PbLi at the exit of the blanket.

(b) Extraction rate in the TES.

Figure 7.8: Concentration in PbLi and extraction rate zoomed in on the peak values.

The numerical outcomes of the models are depicted in tab: 7.5.

	Original model		MHD corrected model		Optimized model	
	Maximum	Minimum	Maximum	Minimum	Maximum	Minimum
Generation rate (g/day)	396.27	0	396.27	0	396.27	0
Extraction rate TES (g/day)	396.15	0.77	394.16	4.36	394.91	4.26
Extraction rate CPS (mg/day)	1.638	0.716	61.21	54.74	6.75	3.99
Blanket permeation rate (mg/day)	1.639	0.432	62.62	53.56	6.93	5.24
He HX permeation rate (μg/day)	1.500	1.495	70.26	70.09	7.46	7.32
T concentration in PbLi (exit) (mol/m^3)	$7.32 \cdot 10^{-4}$	$1.43 \cdot 10^{-6}$	$7.29 \cdot 10^{-4}$	$8.20 \cdot 10^{-6}$	$7.30 \cdot 10^{-4}$	$7.92 \cdot 10^{-6}$
T_2 concentration in He (exit) (mol/m^3)	$8.25 \cdot 10^{-9}$	$3.61 \cdot 10^{-9}$	$3.08 \cdot 10^{-7}$	$2.76 \cdot 10^{-7}$	$3.40 \cdot 10^{-8}$	$2.06 \cdot 10^{-8}$
Inventory in PbLi (g)	1.39	$2.56 \cdot 10^{-3}$	1.88	0.42	1.65	0.19
Inventory in EUROFER (g)	$6.97 \cdot 10^{-2}$	$4.16 \cdot 10^{-2}$	0.47	0.44	0.29	0.25
Inventory in He (g)	$1.48 \cdot 10^{-5}$	$6.58 \cdot 10^{-6}$	$5.53 \cdot 10^{-4}$	$4.95 \cdot 10^{-4}$	$6.09 \cdot 10^{-5}$	$5.00 \cdot 10^{-5}$

Table 7.5: Main global outcomes of the DCLL system level advanced model.

The permeation losses in the PbLi HX needs more than 2 months for reaching the steady state. Once this period is passed, the 3 models provides similar permeation rate losses ($6.3 \cdot 10^{-7}$ g/day). The permeation losses through the pipes to the rooms are found to be negligible (below 10^{-20} g/day). Therefore, in any of the scenarios considered, the permeation losses to the environment are significantly small, below the commonly accepted safety limit of 1 mg/day.

It is worth mentioning that the peak tritium concentration inside PbLi is around 0.7 mg/m^3 which is close but not equal to the result obtained in the initial version ($\sim$1 mg/m^3).

For the parametric studies presented in the next section, the optimized model is selected as the reference case. This does not mean that the optimized case fully represent the real tritium behavior in the DCLL. It is important to recall that the optimization of parameters were carried out with respect to a 3D computation based on certain approximations (steady state, isothermal conditions...). Therefore, results obtained in the optimized case are not complete accurate. However, it is a more sophisticated model and it is reasonable to think that the accuracy of this scenario is higher than the other 2. Besides, the results lays in between of the other 2 cases which makes this case more suitable for parametric studies.

7.3 Parametric studies

As it is shown in sec: 4.3.4, one of the most important strengths of system level models is the possibility of performing fast parametric studies that could help the blanket design activities. For this purpose, three of these studies are presented in this section.

7.3.1 T solubility in PbLi

Besides the design interest, there are certain parameters whose small variations can have a very relevant impact on tritium permeation. Sensitivity analyses allow studying its importance. This is the case of the tritium solubility in PbLi which is known that heavily affects tritium permeation. Indeed, experimental measurements available in literature differs in orders of magnitude (see fig: 4.11). In this first parametric study 3 different solubilities are compared: Reiter's solubility [77] which is the lowest value, Chan's solubility [158] which is an intermediate value (reference) and Aiello's solubility [107] which is the highest value.

$$K_s\left[\frac{mol}{m^3 Pa^{0.5}}\right] = 1.29\cdot 10^{-3}\exp\left(\frac{-1350}{RT}\right) \qquad \text{Reiter} \qquad (7.1)$$

$$K_s\left[\frac{mol}{m^3 Pa^{0.5}}\right] = 2.66\cdot 10^{-2}\exp\left(\frac{-9283.05}{RT}\right) \qquad \text{Chan} \qquad (7.2)$$

$$K_s\left[\frac{mol}{m^3 Pa^{0.5}}\right] = 0.237\exp\left(\frac{-12844}{RT}\right) \qquad \text{Aiello} \qquad (7.3)$$

Results of the parametric study are shown in fig: 7.9.

The impact of the solubility is notorious. Indeed, using Reiter's solubility implies a permeation rate in the blanket (from PbLi to He) two orders of magnitude smaller than when using Aiello's. The reference case (Chan's solubility) provides an intermediate value. Similar effect is observed in the initial model as well (fig: 4.20).

It is important noticing that T solubility in PbLi also influences the permeation rate in the He HX. The reason is that the tritium inventory in He (and consequently the concentration of T_2) grows with the permeation rate.

Nevertheless, permeation losses are still below the safety limit of 1 mg/day but they are much closer when considering Reiter's solubility (∼0.1 mg/day) than in the reference scenario (∼7 μg/day).

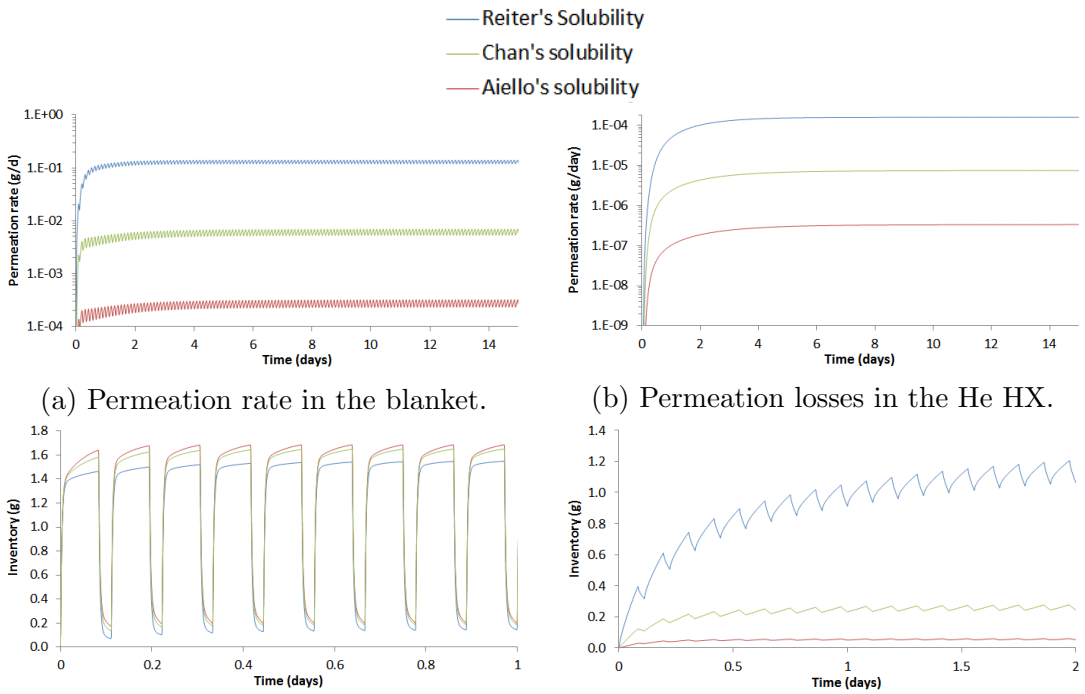

(a) Permeation rate in the blanket.

(b) Permeation losses in the He HX.

(c) Tritium inventory in PbLi.

(d) Tritium inventory in EUROFER.

Figure 7.9: Sensitivity analysis of tritium solubility in Pbli.

7.3.2 PbLi mass flow rate

An important parameter from the conceptual perspective is the mass flow rate of PbLi. A high mass flow rate is what characterizes the DCLL concept in comparison with low velocity concepts (sec: 1.4). The mass flow rate needs to be high enough for self-cooling the PbLi but too high velocities can be unacceptable due to the corrosion of the structural materials [41]. Therefore, mass flow rate is a parameter which needs to be adjusted in every design version. Consequently, it is of interest knowing its influence on tritium evolution. Results of this study are presented in fig: 7.10, the outcomes are plotted after 15 days of simulation.

Results shows that the mass flow rate of PbLi affects the tritium permeation in the blanket. Indeed, high mass flow rates boost the extraction

in the TES keeping the concentation and the permeation rate low. This way, low velocity concepts ($\dot{m}_{loop} \sim 100$ kg/s) presents permeation rates which are orders magnitude higher. This puts a lot of pressure on the developing of efficient coolant purification techniques.

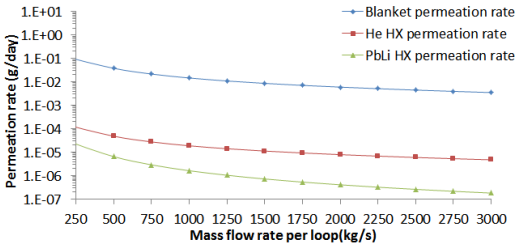

(a) Permeation rates.

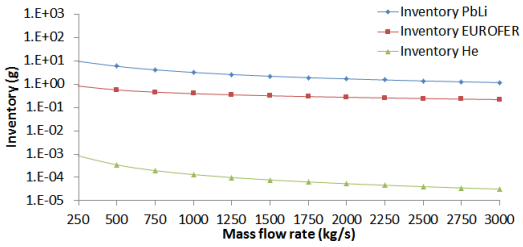

(b) Inventories.

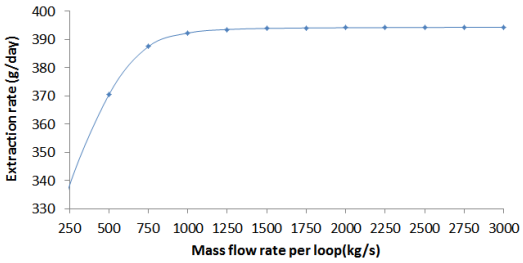

(c) TES extraction rate.

Figure 7.10: Sensitivity analysis of the PbLi mass flow rate.

As expected, the inventory follows a similar dependence than the permeation rate. The extraction rate also growth with the mass flow rate but it almost saturates when reaching a similar value than the generation ratet ($\dot{m}_{loop} > 1000$ kg/s). It is important to recall that the strong impact of the mass flow rate is given by the way the TES is described in the model. When defining the TES as a black box with certain efficiency, the higher masss flow rate, the higher the number of recirculations through the TES and the higher the extraction rate. However, tritium extraction techniques from PbLi, like permeation against vacuum are less efficient for high mass flow rates [105]. Therefore, the exponential decrease of permeation rate and tritium inventories with the mass flow rate is not expected to be so steep when more realistic models of TES are included.

7.3.3 TES extraction efficiency

The last sensitivity analysis studies the influence of the TES extraction efficiency. This study is complementary to the mass flow rate one as the effect on tritium permeation rate and tritium inventory are qualitatively similar. Results of the study are shown in fig: 7.11.

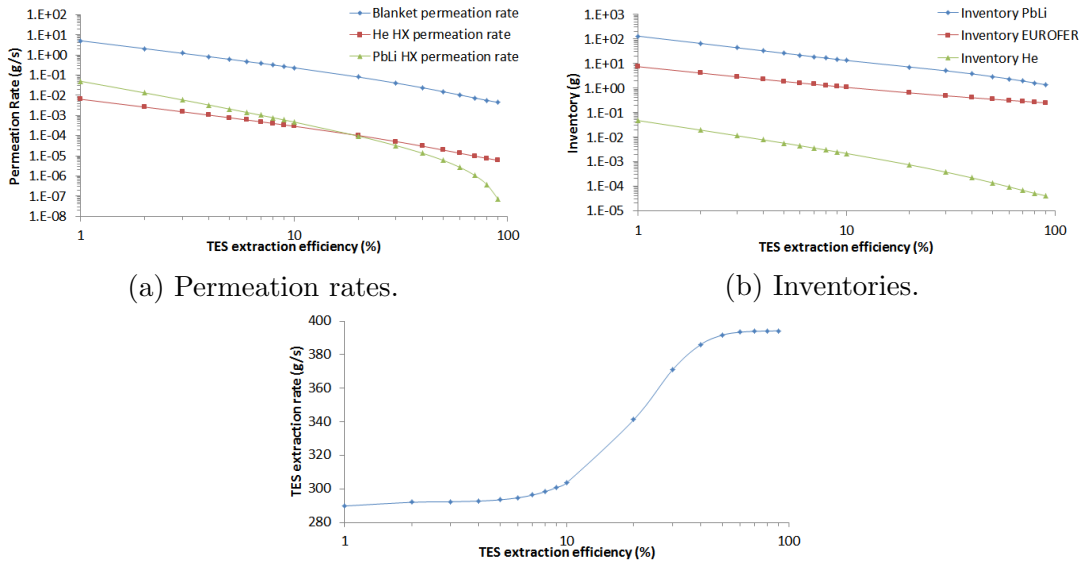

(a) Permeation rates.

(b) Inventories.

(c) TES extraction rate.

Figure 7.11: Sensitivity analysis of the PbLi mass flow rate.

Similar to what is obtained in the initial model, a high TES extraction efficiency is not required for having very good extraction rates. Indeed, as long as the TES can process the 100% of the flow, a high extraction rate will be guarantied by the enormous mass flow rate that characterized the DCLL blanket. Extraction efficiencies over 30% are enough to extract over 99% of the tritium generated. Nevertheless, it is important noting that when small extraction efficiencies are considered ($\eta < 10\%$), permeation losses to the environment in both HXs exceed the safety limit of 1 mg/day.

7.4 Discussion

The advanced model developed in this chapter constitutes an important upgrade of the initial model presented in chap: 4.3 from different perspectives.

Firstly, it is adapted to a newer and more relevant version of the DCLL and DEMO machine, which improves the relevance of the work. Secondly, it considers more subsystems than the previous version, in particular: the PbLi and He pipes, the HX and the CPS. Thirdly, the PFDs that describes the blanket are more sophisticated since they include physical models of the PbLi and He manifolds. Finally, the model integrates the information obtained by the MHD computations and the deep level tritium transport models dedicated to the DCLL (chap: 5 and 6).

Results exposed in sec: 7.2 prove the important impact that 3-dimensional effects have over tritium evolution. These complex effects are not only constrained to local disruptions and curios concentration profiles. They have a crucial impact on the global outcomes of the system. Indeed, fig: 7.7 shows differences of orders of magnitude on the total blanket permeation rate and on the tritium releases to the environment (mainly in the He HX) when using different approaches for reproducing 3D effects and MHD effects. This impact shall be taken into account in future as none of the tritium models developed so far for the American FNSF (e.g. [91]), the ITER TBM project (e.g. [159]) or the EUROfusion blankets (e.g. [81]) consider it in detail.

With the implementation of this model, the first iteration of the optimization feedback loop shown in fig: 1.11 is completed. The outcomes (tritium concentration in PbLi) could be used as boundary conditions for a re-run of the deep level model presented in sec: 6.5. The new deep level could be used for determining new optimization parameters and for launching a second version of the advanced model. With this second iteration of the optimization loop, the accuracy of the advanced model would be refined. The process can be repeated recursively as explained in sec: 1.3.2.

Concerning the sensitivities analysis, important conclusions can be derived. On the one hand, the experimental uncertainty of the tritium solubility in PbLi (see fig: 4.11) introduces the highest uncertainty in the model, specially in the blanket permeation rate and the permeation losses in the He HX. On the other hand, the PbLi mass flow rate and the TES extraction efficiency determine together the extraction rate in the system. As long as the flow rate is as high as in the DCLL concept, there is no need of having extraction efficiencies higher than 30% for obtaining very high extraction rate. Complementary, when the extraction efficiency is high (η >80%), loop mass

flow rates over 1000 kg/s barely increase extraction rate. It is important to recall that for TES extraction efficiencies lower than 10% the permeation losses in the PbLi HX takes values over the safety limit of 1mg/day. In this scenario, tritium concentration in PbLi is unacceptably high. Similar situation is observed in low velocity concepts ($\dot{m}_{loop} \sim 100$ kg/s) in which the extraction rate is not as high and permeation rates to the coolant are of the order 10 g/day (e.g. [37]).

Conclusions

This work has been focused on the development of tritium transport models for the BB concept DCLL. For this purpose, a new methodology based on the recursive use of system level and deep level tritium transport models has been employed. The main goal was reducing as much as possible the error introduced by the geometrical approximations in system level models. This keeping the relatively short computational times that characterizes system level models.

All the activities developed for this dissertation have the European DCLL as the object of study. This blanket concept is based on liquid metal flowing at high velocities. As a consequence, MHD effects plays a fundamental role in the evolution of any magnitude, including tritium concentration. The MHD issues associated to the DCLL have been studied in detail, paying special attention to the effect of the MHD forces on tritium evolution. This work is the first detailed study of the MHD-tritium transport interaction in relevant conditions for the EU-DCLL concept.

The most important activities carried out in this work and the main conclusions derived from it are listed as follows:

1. The first system level tritium transport model of the European DCLL has been developed.

    - This model has confirmed the good properties of the DCLL concept regarding tritium permeation.
    - The model has been programmed using the simulation environment EcosimPro which has proven its versatility and its capabilities for developing multi-component models.
    - The model has allowed identifying the PbLi gap flow as the most

relevant geometry of the whole blanket for the tritium permeation to the He circuit.

2. Important progress on the MHD phenomena in the DCLL have been achieved.

   - The regions of the European DCLL design which contributes to the MHD pressure drop have been identified and classified according with its importance.
   - Different MHD computations have been performed with the platform ANSYS-Fluent. Its MHD module has been validated against analytic solutions for the first time at high Hartmann numbers.
   - Following the conclusions extracted from the initial tritium transport model at system level, MHD computations focused on the gap flow annular geometry have been performed.
   - Other important systems for the DCLL have been studied from the MHD point of view. This is the case of the fringing effect in the feeding pipes or the magnetoconvective flow in an OB equatorial module.

3. Deep level tritium transport models have been implemented. This models are based in finite volume methods developed with the customization capabilities of Fluent.

   - Two validation cases against analytic solutions have been successfully accomplished. Experimental validation shall be carried out in future.
   - The effect of the external magnetic field and the volumetric generation on tritium transport has been studied in a rectangular section PbLi channel.
   - Results from previous analyses have been used for upgrading the component level models. In particular, BL in solid/liquid interfaces have been introduced for upgrading permeation estimations.
   - Tritium evolution in the annular gap flow geometry has been computed including the MHD forces, the volumetric generation and the anisotropic distribution of the He channels.

4. An advanced version of the DCLL system level tritium transport model at system level has been developed.

- This model includes an important part of the information derived from the MHD and deep level tritium transport computations. This way, corrections to the surface permeation and mass transfer coefficients have been included for decreasing the model uncertainty.
- Results from these models manifest the importance of 3D effects which can alter the order of magnitude of the global results.
- The parametric studies show the uncertainty associated to the transport constants and to the design parameters.
- The model closes the methodological loop proposed for this research work.

It is worth noting that some of the techniques employed in this work can be applied to other technologies and facilities that employs liquid metal. In particular, the deep level tritium transport models coupled with MHD profiles are of great interest to other PbLi-based blanket concepts, to the PbLi TBMs of ITER or to the loop of an experimental facility.

Despite the work carried out, it is clear that the research must continue if fully representative tritium transport models of the DCLL are to be developed. There is still a lot of work pending in a critical field for the development of viable BB and, thus, of the civil fusion energy. The following research lines are still open:

1. Studying the effect of the 3D temperature maps on tritium transport. Despite the European DCLL is a low temperature concept, the PbLi temperature gradient inside one module is considerable ($\sim 250°C$). This temperature difference will affect the materials transport properties and consequently, the tritium behavior.

2. Analysis of the magneto-convective flows in the DCLL. The interaction between the MHD phenomena and buoyancy effects is very complex from the computational perspective. Nevertheless, this problem shall not be ignored as it can importantly alter the PbLi velocity profiles and, by extension, tritium transport.

3. Simulation of the complex geometries involved in the DCLL. Certain regions of the design can affect the MHD interactions and tritium

transport. Some examples of geometries that should be studied are: The connection between the BSS channels and the modules, the discontinuities of the FCI or the bends in the Pbli flow path.

4. Refining the component level models. Component level models shall be upgraded for including as much relevant physical effects as possible. This is the case of the Soret effect, the copermeation, the trapping or the tritium decay.

5. Improving the connection between the deep level model and the system level (or component level) models. Obtaining correlations that allows adjusting the parameters of component level models is of great interest. With this development, a lot of computational time could be saved.

6. Experimental validation of the computational results. As in every theoretical work, it is necessary to verify the obtained results against experiments. This validation shall be performed in specialized facilities that work with liquid metal and hydrogen isotopes.

In conclusion, this work has accomplished their initial objectives but the research on this field still needs of further improvements. Indeed, more efforts shall be invested from different perspectives if new objectives are to be achieved.

Conclusiones

Este trabajo se ha centrado en el desarrollo de modelos de transporte de tritio para la el concepto de envoltura regeneradora DCLL. Para ello se ha empleado una nueva metodología basada en el uso recursivo de modelos de transporte de tritio a nivel de sistema y de modelos de volúmenes finitos de más alto nivel. El objetivo principal era reducir lo máximo posible el error introducido por las aproximaciones geométricas en los modelos a nivel de sistema manteniendo los tiempos de computacin cortos que caracterizan a este tipo de modelos.

Todas las actividades desarrolladas para este trabajo tienen como objeto de estudio el diseño del DCLL europeo. Siendo una envoltura basada en metal líquido de alta velocidad, los efectos MHD tienen un papel fundamental en la dinámica de cualquier magnitud, incluyendo la concentración de tritio. La problemática MHD asociada al DCLL ha sido estudiada en detalle prestándose especial atención al efecto de las fuerzas MHD sobre el transporte de tritio. En este trabajo se realiza el primer estudio detallado de la interacción MHD-transporte de tritio en condiciones relevantes para el DCLL.

Se resumen las actividades más importantes llevadas a cabo en el este trabajo y las conclusiones principales obtenidas en la siguiente lista:

1. Se ha desarrollado el primer modelo de transporte de tritio nivel de sistema del DCLL europeo.

    - Este modelo ha confirmado el buen comportamiento del concepto DCLL en lo referente a las permeación de tritio.
    - El modelo ha sido desarrollado con la herramienta computacional EcosimPro que ha demostrado su versatilidad y capacidad para desarrollar modelos de muchos componentes.

- El modelo permite analizar las incertidumbres asociadas. Estas tienen su origen tanto en la incertidumbre experimental de las constantes de transporte como en las aproximaciones computacionales introducidas.
- El modelo ha permitido identificar el flujo de la ranura (*gap flow*) como la geometría con mayor relevancia para la permeación de tritio al circuito de helio en toda la envoltura.

2. Se han desarrollado importantes avances relativos al estudio de la fenomenología MHD en el DCLL.

   - Se han identificado y clasificado acorde a su importancia las regiones del diseño que contribuyen a la cada de presión MHD.
   - Se han realizado distintos cálculos MHD con la plataforma ANSYS-Fluent cuyo módulo MHD ha sido validado con éxito por primera vez frente a soluciones analíticas con altos números de Hartmann.
   - Siguiendo a las conclusiones extraídas del modelo de transporte de tritio inicial, se han realizado cálculos MHD centrados en el estudio del flujo en la ranura.
   - Se han analizado otros fenómenos MHD importantes para el DCLL como el efecto de borde del campo magnético externo o el estudio magneto-convectivo del flujo de PbLi en el circuito de un mdulo ecuatorial.

3. Se han implementado modelos de transporte de tritio tridimensionales basados en métodos de volúmenes finitos utilizando las capacidades de personalización de Fluent.

   - Se han realizado dos casos de validación respecto a soluciones analíticas. Sin embargo, estos modelos deben ser validados frente a experimentos en el futuro.
   - Se ha estudiado el efecto del campo magnético en el transporte de tritio así como el efecto de la generación volumétrica en el perfil de concentración en un canal rectangular de PbLi.
   - Los resultados previos han servido para la mejora de los modelos a nivel de componente. En concreto se han introducido capas límite en las interfaces sólido/líquido para mejorar las estimaciones de permeación.

- Se ha calculado la evolución del tritio en la geometría anular del flujo en la ranura teniendo en cuenta las fuerzas MHD, la generación volumétrica y la distribucin anisótropa de canales de helio.

4. Se ha desarrollado un modelo de transporte de tritio a nivel de sistema avanzado para la envoltura DCLL.

    - Este modelo incluye gran parte de la información obtenida mediante los cálculos MHD y de transporte de tritio 3D. De esta manera se incluyen correcciones en la superficie de permeación y en los coeficientes de transferencia de masa para disminuir la incertidumbre asociada al modelo.
    - Los resultados de este modelo dejan de manifiesto la importancia de los efectos tridimensionales que pueden llegar a variar el orden de magnitud de los resultados globales.
    - Los estudios paramétricos realizados muestran la incertidumbre asociada a las constantes de transporte y a los parámetros de diseño.
    - Con este modelo se completa el ciclo metodológico de trabajo propuesto para esta tesis.

Parte de las técnicas empleadas en este proyecto pueden ser utilizadas en otras tecnologías e instalaciones basadas en metal líquido. En particular, los modelos 3D de transporte de tritio acoplados a perfiles de velocidad MHD son de gran interés para otros conceptos de envoltura basados en PbLi, para los TBMs de ITER o para lazos experimentales.

Pese al trabajo realizado, es indudable que esta investigación debe continuar si se quieren obtener modelos de transporte de tritio completamente representativos. Aún hay mucho por hacer en un campo de gran importancia para el desarrollo viable de envolturas regeneradoras y, por tanto, de la energía civil de fusión. En el caso particular del transporte de tritio dentro del DCLL, se pueden nombrar las siguientes líneas abiertas de investigación:

1. Estudiar el efecto de los mapas de temperatura tridimensionales. En efecto, pese a que el DCLL europeo es un concepto de baja temperatura, el gradiente de temperaturas del PbLi dentro de los módulos es

importante ($\sim$ 250°C). Estas diferencias de temperaturas afectan a las propiedades de transporte de los materiales y por tanto a la evolución de la concentracin de tritio.

2. Análisis de los flujos magnetoconvectivos en el DCLL. La interacción entre los fenómenos MHD y de flotación es sin duda un problema de gran complejidad computacional. Sin embargo, este problema no debe ser ignorado dado que puede modificar enormemente los perfiles de velocidad y con ello afectar de forma importante al transporte de tritio.

3. Simulación de las geometrías complejas implicadas en el DCLL. Ciertas regiones del diseño pueden afectar de forma no trivial tanto a las fuerzas MHD como al transporte de tritio. Algunas ejemplos de regiones cuyo comportamiento debe ser estudiado son: la conexión entre los canales de la BSS y el módulo, las discontinuidades de los FCI o los giros en el camino del flujo de PbLi.

4. Refinar los modelos a nivel de componente. Éstos deben ser mejorados para incluir la mayor cantidad de efectos fsicos relevantes posibles. Tal es el caso del efecto Soret, la co-permeación, el atrapamiento de tritio en la red cristalina de los sólidos o la desintegración del tritio.

5. Mejorar la conexión existente entre los modelos tridimensionales y los modelos a nivel de sistema (o componente). La obtención de correlaciones que permitan ajustar los parámetros de los modelos a nivel de componente en los distintos casos es de gran interés. Con ello, se podría ahorrar una gran cantidad de tiempo computacional.

6. Validación experimental de los resultados de las simulaciones. Como cualquier trabajo teórico, es fundamental verificar experimentalmente los resultados obtenidos. Estos ejercicios de validación deben llevarse acabo en instalaciones especializadas de metal líquido e isótopos de hidrógeno.

En conclusión, este trabajo ha cumplido los objetivos de investigación que se habían marcado inicialmente pero el trabajo en este campo necesita de más desarrollo. En efecto, se ha iniciado una investigación en la que se deberá continuar trabajando desde varias perspectivas si se quieren alcanzar nuevos objetivos.

Bibliography

[1] DNVL-GL. Energy transition outlook 2017. Technical report, Det Norske Veritas, 2017.

[2] BP. Statistical review of world energy. Technical report, British Petroleum, 2016.

[3] Enerdata. Global energy statistical year book 2017. Technical report, Enerdata, 2017.

[4] P. M. Cox, R. A. Betts, C.D. Jones, S. A. Spall, and I. J. Totterdell. Acceleration of global warming due to carbon-cycle feedbacks in a coupled climate model. *Nature*, 408:184–187, 2000.

[5] M. L. Bell, D. L. Davis, and T. Fletcher. A retrospective assessment of mortality from the london smog episode of 1952: the role of influenza and pollution. *Environ. Health Perspect.*, 112(1):6–8, January 2004.

[6] A. McCrone, U. Moslener, F. D'Estais, and C. Grunig. Global trends in renewable energy investment 2017. Technical report, Frankfurt School UNEP Collaborating Centre for Climate and Sustainable Energy Finance, 2017.

[7] IAEA. The fukushima daiichi accident report. Technical report, International Atomic Energy Agancy, 2015.

[8] P. Rocco and M. Zucchetti. Advanced management concepts for fusion waste. *J. Nucl. Mater.*, 258-263:1773 – 1777, 1998.

[9] W. Greiner, S. Schramm, and E. Stein. *Quantum Chromodynamics. Third Edition.* Springer, 2007.

[10] J. Suhonen. *From Nucleons to Nucleus. Concepts of Microscopic Nuclear Theory*. Springer, 2007.

[11] K. L. G. Heyde. *The Nuclear Shell Model*. Springer, 1994.

[12] A. Kamal. *Nuclear Physics*. Springer, 2014.

[13] A. Einstein. Zur elektrodynamik bewegter krper. *Ann. Phys.*, 1905.

[14] S. Esposito and O. Pisanti. Enrico Fermi and the physics and engineering of a nuclear pile: the retrieval of novel documents. Technical report, Cornell University Library, 2008.

[15] S. Glasstone and R. H. Lovberg. *Controlled Thermonuclear Reactions*. Robert E. Krieger Publishing CO, 1960.

[16] I. Palermo. *Diseño nuclear de un reactor de fusión por confinamiento magnético con envoltura regeneradora líquida de doble refrigerante He/LiPb (DCLL)*. PhD thesis, Departamento de Ingenieria Energetica. Universidad Nacional de Educacion a Distancia, 2014.

[17] I. E. Tamm and A. D. Skharov. *Theory of magnetic thermonuclear reactor*. Pergamon, Oxford, 1961.

[18] L. Spitzer. The stellarator concept. *The Physics of Fluids*, 1(4):253–264, 1958.

[19] G. Federici, R. Kemp, D. Ward, C. Bachmann, T. Franke, S. Gonzalez, C. Lowry, M. Gadomska, J. Harman, B. Meszaros, C. Morlock, F. Romanelli, and R. Wenninger. Overview of EU DEMO design and R&D activities. *Fusion Eng. Des.*, 89(7):882 – 889, 2014.

[20] European research roadmap to the realisation of fusion energy. Technical report, EUROfusion, 2018.

[21] M. Kovari, M. Coleman, I. Cristescu, and R. Smith. Tritium resources available for fusion reactors. *Nucl. Fusion*, 58(2):026010, 2018.

[22] S. Dingwall, C. E. Mills, N. Phan, K. Taylor, and D. R. Boreham. Human health and the biological effects of tritium in drinking water: Prudent policy through science - addressing the odwac new recommendation. *Dose-Response*, 9(1):6–31, 2011.

[23] D. McMorrow. Tritium. Technical report, JASON. The MITRE Corporation, 2011.

[24] L.M. Giancarli, M. Abdou, D.J. Campbell, V.A. Chuyanov, M.Y. Ahn, M. Enoeda, C. Pan, Y. Poitevin, E. Rajendra Kumar, I. Ricapito, Y. Strebkov, S. Suzuki, P.C. Wong, and M. Zmitko. Overview of the ITER TBM program. *Fusion Eng. Des.*, 87(5):395 – 402, 2012.

[25] L. V. Boccaccini, G. Aiello, J. Aubert, C. Bachmann, T. Barrett, A. Del Nevo, D. Demange, L. Forest, F. Hernandez, P. Norajitra, G. Porempovic, D. Rapisarda, P. Sardain, M. Utili, and L. Vala. Objectives and status of EUROfusion DEMO blanket studies. *Fusion Eng. Des.*, 109-111, Part B:1199–1206, 2016.

[26] H. S-C. Deville and L. Troost. Sur la permeabilite du fer a haute temperature. *C. R. Phys.*, 57(965), 1863.

[27] B. Bornschein, C. Day, D. Demange, and T. Pinna. Tritium management and safety issues in ITER and DEMO breeding blankets. *Fusion Eng. Des.*, 88:466–471, 2013.

[28] J. Knaster, P. Garin, H. Matsumoto, Y. Okumura, M. Sugimoto, F. Arbeiter, P. Cara, S. Chel, A. Facco, P. Favuzza, T. Furukawa, R. Heidinger, A. Ibarra, T. Kanemura, A. Kasugai, H. Kondo, V. Massaut, J. Molla, G. Micciche, S. Ohira, K. Sakamoto, T. Yokomine, E. Wakai, and the IFMIF/EVEDA Integrated Project Team. Overview of the ifmif/eveda project. *Nucl. Fusion*, 57(10):102016, 2017.

[29] A.F. Rowcliffe, L.M. Garrison, Y. Yamamoto, L. Tan, and Y. Katoh. Materials challenges for the fusion nuclear science facility. *Fusion Eng. Des.*, 2017.

[30] J. Hoffmann, M. Rieth, L. Commin, P. Fernndez, and M. Roldn. Improvement of reduced activation 9%Cr steels by ausforming. *Nuclear Materials and Energy*, 6:12 – 17, 2016.

[31] H. John, S. Malang, and H. Sebening. DEMO-relevant test blankets for NET/ITER. Technical Report KfK 4908, Kernforschungszentrum Karlsruhe, 1991.

[32] S. Malang and M. S. Tillack. Development of self-cooled liquid metal breeder blankets. Technical Report FZKA 5581, Forschungszentrum Karlsruhe, 1995.

[33] I.R Kirillov, I.V Danilov, S.I Sidorenkov, Yu.S Strebkov, R.F Mattas, Y Gohar, T.Q Hua, and D.L Smith. Liquid lithium self-cooled breeding blanket design for ITER. *Fusion Eng. Des.*, 39-40:669 – 674, 1998.

[34] S. Malang and K. Schleisiek. Dual coolant blanket concept. Technical Report KfK 524, Kernforschungszentrum Karlsruhe, 1994.

[35] P. Norajitra, L. Buhler, A. Buenaventura, E. Diegele, U. Fischer, S. Gordeey, E. Hutter, R. Kruessmann, S. Malang, A. Orden, G. Reimann, J. Reimann, G. Vieider, D. Ward, and F. Wasastjerna. Conceptual design of the dual-coolant blanket within the framework of the EU power plant conceptual study (TW2-TRP-PPCS12). Technical Report FZKA 6768, Forschungszentrum Karlsruhe, 2003.

[36] S.Zheng and T. N. Todd. Study of impacts on tritium breeding ratio of a fusion demo reactor. *Fusion Engineering and Design*, 98-99:1915 – 1918, 2015.

[37] F. R. Urgorri, C. Moreno, E. Carella, J. Castellanos, A. Del Nevo, and A. Ibarra. Preliminary system modeling for the eurofusion water cooled lithium lead blanket. *Fusion Sci. Technol.*, 71(3):444–449, 2017.

[38] D. Demange, L.V. Boccaccini, F. Franza, A. Santucci, S. Tosti, and R. Wagner. Tritium management and anti-permeation strategies for three different breeding blanket options foreseen for the european power plant physics and technology demonstration reactor study. *Fusion Eng. Des.*, 89(7):1219 – 1222, 2014.

[39] P. Norajitra, W. W. Basuki, M. Gonzalez, D. Rapisarda, M. Rohde, and L. Spatafora. Development of sandwich flow channel inserts for an EU DEMO dual coolant blanket concept. *Fusion Sci. Technol.*, 68(3):501–506, 2015.

[40] L. Bühler. Magnetohydrodynamics of liquid metals lecture. In *Karlsruhe International School on Fusion Technologies*, 2015.

[41] J. Sannier, M. Broc, T. Flament, and A. Terlain. Corrosion of austenitic and martensitic stainless steels in flowing Pb17Li alloy. *Fusion Eng. Des.*, 14(3):299 – 307, 1991.

[42] J. Konys, W. Krauss, H. Steiner, J. Novotny, and A. Skrypnik. Flow rate dependent corrosion behavior of eurofer steel in Pb15.7Li. *J. Nucl. Mater.*, 417(1):1191 – 1194, 2011.

[43] J. Sannier, T. Flament, and A. Terlain. Corrosion of martensitic steels in flowing Pb17Li. In *Fusion Technology*, 1990.

[44] H. Hurzlmeier, B. Meszaros, and C. Bachmann. Demo tokamak complex. Technical Report EFDA-D-2M9JM7 v2.0, EUROfusion, 2014.

[45] I. Fernández-Berceruelo, D. Rapisarda, I. Palermo, F. R. Urgorri, L. Maqueda, and D. Alonso. DCLL design report 2015. Technical Report EFDA-D-2MYHGZ, EUROfusion, 2016.

[46] I. Fernández-Berceruelo, I. Palermo, F. R. Urgorri, L. Maqueda, D. Alonso, and J. Olalde. DCLL design report 2016. Technical Report EFDA-D-2MMM6Q, EUROfusion, 2017.

[47] D. Rapisarda, I. Fernández-Berceruelo, I. Palermo, F. Martin-Fuertes, E. Mas de les Valls, T. Melichar, O. Frybort, L. Vala, Z. Simankova, P. Norajitra, W. W. Basuki, and M. Reungoat. DCLL blanket 2014 design description document. Technical Report EFDA-D-2MKUUT, EUROfusion, 2015.

[48] D. Rapisarda, I. Fernández-Berceruelo, I. Palermo, F. R. Urgorri, M. Gonzalez, T. Melichar, O. Frybort, L. Vala, L. Maqueda, D. Alonso, H. Neuberger, P. Norajitra, M. Reungoat, and M. Utili. Design description document 2015 for DCLL (update of DDD 2014). Technical Report EFDA-D-2MT44J, EUROfusion, 2016.

[49] S. Smolentsev, C. Wong, S. Malang, M. Dagher, and M. Abdou. MHD considerations for the DCLL inboard blanket and access ducts. *Fusion Eng. Des.*, 85(7):1007 – 1011, 2010.

[50] F. M. White. *Fluid Mechanics*. McGraw Hill, 1999.

[51] J. Vanderlinde. *Classical Electromagnetic Theory*. Kluwer Academic Publishers, 2004.

[52] J. Hartmann. *Hg-Dynamics I. Theory of the laminar flow of an electrically conductive liquid in a homogeneous magnetic fiedl.* Levin & Munksgaard Copenhagen, 1937.

[53] J. Sommeria and R. Moreau. Why, how, and when, MHD turbulence becomes two-dimensional. *J. Fluid Mech.*, 118:507518, 1982.

[54] S. Smolentsev and R. Moreau. Moeling quasi-two-dimensional turbulence in MHD duct flows. In *Proceedings of the Summer Program 2006*, 2006.

[55] S. Cuevas and B. F. Picologlou. Liquid-metal MHD flow in rectangular ducts with thin conducting or insulating walls: laminar and turbulent solutions. *Int. J. Engng Sci.*, 35(5):485–503, 1997.

[56] L. Bühler. Instabilities in quasi-two-dimensional magnetohydrodynamic flows. *J. Fluid Mech.*, 323:125–150, 1990.

[57] S. Smolentsev, N. Vetcha, and M. Abdou. Effect of a magnetic field on stability and transitions in liquid breeder flows in a blanket. *Fusion Eng. Des.*, 88(6):607 – 610, 2013.

[58] S. Smolentsev, R. Moreau, and M. Abdou. Characterization of key magnetohydrodynamic phenomena in PbLi flows for the US DCLL. *Fusion Eng. Des.*, 83:771–783, 2008.

[59] J. C. R. Hunt. Magnetohydrodynamic flow in rectangular ducts. *J. Fluid Mech.*, 21(4):577–590, 1965.

[60] M. Ni, R. Munipalli, P. Huang, N. B. Morley, and M. Abdou. A current density conservative scheme for incompressible MHD flows at low magnetic Reynolds number. part ii. *J. Comput. Phys.*, 2007.

[61] J. A. Shercliff. Steady motion of conducting fluids in pipes under transverse magnetic fields. *Math. Proc. Cambridge Philos. Soc.*, 49(1):136144, 1953.

[62] K. Miyazaki, S. Inoue, N. Yamaoka, T. Horiba, and K. Yokomizo. Magneto-hydro-dynamic pressure drop of lithium in rectangular ducts. *Fusion Sci. Technol.*, 10:830–836, 1986.

[63] J. P. Holman. *Heat Transfer.* McGraw Hill, 2005.

[64] J. B. Fourier. *Theorie analytique de la chaleur*. Libraires pour les mathematiques, la arquitecture hydraulique et la marine, 1822.

[65] I. Palermo, D. Rapisarda, I. Fernández-Berceruelo, and A. Ibarra. Tritium production assessment for the DCLL EUROfusion DEMO. *Nucl. Fusion*, 56(10):104001, 2016.

[66] I. Palermo, I. Fernández, D. Rapisarda, and A. Ibarra. Neutronic analyses of the preliminary design of a DCLL bblanket for the EUROfusion DEMO power plant. *Fusion Eng. Des.*, 109-11:13–19, 2016.

[67] F. P. Incropera, D. P. Dewitt, T. L. Bergman, and A. S. Lavine. *Fundamentals of Heat and Mass Transfer*. John Wiley and Sons, 2007.

[68] A. Fick. Ueber diffusion. *Ann. Phys.*, 170(59), 1855.

[69] J. Crank. *The mathematics of diffusion*. Oxford Science Publications, 1956.

[70] E.S. Hotston and G.M. McCracken. Trapping of energetic hydrogen ions in reactive metals. *J. Nucl. Mater.*, 68(3):277 – 285, 1977.

[71] M.A. Rahman and M.Z. Saghir. Thermodiffusion or Soret effect: Historical review. *Int. J. Heat Mass Transfer*, 73:693 – 705, 2014.

[72] W. Henry. Experiments on the quantity of gases absorved by water, at different ttemperature, and under different pressures. *Philos. Trans. Roy. Soc. London*, 93:29–42, 1803.

[73] M. I. Baskes. A calculation of the surface recombination rate constant for hydrogen isotopes ion metals. *J. Nucl. Mater.*, 92:318–324, 1980.

[74] G. A. Esteban, A. Pe na, I. Urra, F. Legarda, and B. Riccardi. Hydrogen transport and trapping in EUROFER'97. *J. Nucl. Mater.*, 367-370:473–477, 2007.

[75] G. A. Esteban, A. Perujo, L. A. Sedano, and B. Mancinelli. The surface rate constants of deuterium in the reduced activating martensitic steel OPTIFER-IVb. *J. Nucl. Mater.*, 282:89–96, 2000.

[76] F. Reiter, K. S. Forcey, and G. Gervasini. A compilation of tritium-material interaction parameters in fusion reactor materials. Technical Report EUR 15217 EN, Joint Research Center, 1993.

[77] F. Reiter. Solubility and diffusivity of hydrogen isotopes in liquid Pb-17Li. *Fusion Eng. Des.*, 14:207–211, 1997.

[78] K. Kizu, A. Pisarev, and T. Tanabe. Co-permeation of deuterium and hydrogen through Pd. *J. Nucl. Mater.*, 289:293–302, 2001.

[79] K. Kizu and T. Tanabe. Counter-diffusion and counter-permeation of deuterium and hydrogen through palladium. *J. Nucl. Mater.*, 258-263:1133–1137, 1998.

[80] C. San Marchi, B. P. Somerday, R. S. Larson, and S. F. Rice. Solubility of hydrogen and its isotopes in metals from mixed gases. *J. Nucl. Mater.*, 372:421–425, 2008.

[81] E. Carella, C. Moreno, F. R. Urgorri, D. Rapisarda, and A. Ibarra. Tritium modelling in HCPB breeder blanket at a system level. *Fusion Eng. Des.*, 124:687 – 691, 2017.

[82] F. R. Urgorri and C. Moreno. Consolidated tritium transport modeling for the WCLL blanket. Technical Report EFDA-D-123456, EUROfusion, 2017.

[83] E.T. Denisov, O.M. Sarkisov, and G.I. Likhtenshtein. *Chemical Kinetics*. Elsevier Science, 2003.

[84] P. W. Humrickhouse and B. J. Merril. Vacuum permeator analysis for extraction of tritium from DCLL blankets. *Fusion Sci. Technol.*, 68:295–302, 2015.

[85] S. Fukada, T. Muneoka, M. Kinjyo, R. Yoshimura, and K. Katayama. Hydrogen transfer in Pb-Li forced convection flow with permeabe wall. *Fusion Eng. Des.*, 96-97:95–100, 2015.

[86] E. Gabowitsch and G. Spannagel. Computer simulation of tritium system for fusion technology. *Fusion Technol.*, 16:143–148, 1989.

[87] F. Franza, L.V. Boccaccini, A. Ciampichetti, and M. Zucchetti. Tritium transport analysis in HCPB DEMO blanket with the FUS-TPC code. *Fusion Eng. Des.*, 88(9):2444 – 2447, 2013.

[88] A. Santucci, A. Ciampichetti, D. Demange, F. Franza, and S. Tosti. Tritium migration in HCLL and WCLL blankets: Impact of tritium

solubility in liquid pb-17li. *IEEE Trans. Plasma Sci.*, 42(4):1053–1057, 2014.

[89] G. R. Longhurst. *TMAP7 User Manual*. Idaho National Laboratory, Idaho Falls, Idaho 83415-3860.

[90] G. R. Longhurst and J. Ambrosek. Verification and validation of the tritium transport code TMAP7. Technical Report INEEL/CON-04-01593, Idaho National Engineering and enviromental laboratory., 2004.

[91] P. W. Humrickhouse and B. J. Merrill. Tritium aspects of the fusion nuclear science facility. *Fusion Eng. Des.*, In Press, 2017.

[92] P. W. Humrickhouse and B. J. Merril. Tritium permeation and extraction in the fusion nuclear science facility. In *Tritium 2016*, 2016.

[93] M. Zucchetti, M. Utili, L. Nicolotti, A. Ying, F. Franza, and M. Abdou. Tritium control in fusion reactor materials: A model for tritium extracting system. *Fusion Eng. Des.*, 98-99:1885 – 1888, 2015.

[94] A. Ying, H. Zhang, M.Y. Anh, and Y. Lee. Tritium transport evolutions in HCCR TBM under ITER inductive operations. *Fusion Sci. Technol.*, 68(2):346–352, 2015.

[95] P. W. Humrickhouse, P. Calderoni, and B. J. Merril. Implementation of tritium permeation model in the CFD code fluent. *Fusion Sci. Technol.*, 60:1564–1567, 2011.

[96] L. R. Petzold. A description of DASSL: A differential/algebraic system solver. Technical Report SAND82-8637, Sandia National Laboratories, 1982.

[97] P. Martínez-Alcalde, C. Moreno, and A. Ibarra. Parametric analysis of LIBRETTO-4 and 5 in-pile tritium transport model on EcosimPro. *Fusion Eng. Des.*, 89(7):1510 – 1515, 2014.

[98] C. Bachmann, G. Aiello, R. Albanese, R. Ambrosino, F. Arbeiter, J. Aubert, L. Boccaccini, D. Carloni, G. Federici, U. Fischer, M. Kovari, A. Li Puma, A. Loving, I. Maione, M. Mattei, G. Mazzone, B. Meszaros, I. Palermo, P. Pereslavtsev, V. Riccardo, P. Sardain, N. Taylor, S. Villari, Z. Vizvary, A. Vaccaro, E. Visca, and R. Wenninger. Initial DEMO

tokamak design configuration studies. *Fusion Eng. Des.*, 9899:1423 – 1426, 2015.

[99] E. Carella, C. Moreno, F. R. Urgorri, D. Demange, J. Castellanos, and D. Rapisarda. Tritium behavior in HCPB breeder blanket unit: modeling and experiments. *Fusion Sci. Technol.*, 71:357–362, 2017.

[100] W. Farabolini, A. Ciampichetti, F. Dabbene, M. A. Ftterer, L. Giancarli, G. Laffont, A. Li Puma, S. Raboin, Y. Poitevin, I. Ricapito, and P. Sardain. Tritium control modelling for a helium cooled lithium-lead blanket of a fusion power reactor. *Fusion Eng. Des.*, 81:753–762, 2016.

[101] R. M. Roberts, T. S. Elleman, H. Palmour III, and K. Verghese. Hydrogen permeability of sintered aluminum oxide. *J. Am. Ceram. Soc.*, 62(9-10), 1979.

[102] J. D. Fowler, D. Chandra, T. S. Elleman, A. W. Payne, and K. Verghese. Tritium diffusion in Al_2O_3 and BeO. *J. Am. Ceram. Soc.*, 60(3-4), 1977.

[103] F. Legarda, G. Alberro, I. Pealva, A. Sarrionandia-Ibarra, and G. A. Esteban. Experimental determination of reference Sieverts' constant and diffusivity values for tritium in LiPb. Technical Report TW6-TTBC-005, EFDA, 2010.

[104] J. I. Linares, A. Cantizano, Y. Maratilla, and L. Batet. Alternative range of viable secondary coolants and options for thermodynamic cycles. Technical Report EFDA-D-2KYPZB, EUROfusion, 2014.

[105] B. Garcinuño, D. Rapisarda, I. Fernández, C. Moreno, I. Palermo, and A. Ibarra. Design of a permeator against vacuum for tritium extraction from eutectic lithium-lead in a DCLL DEMO. *Fusion Eng. Des.*, 117:226–231, 2017.

[106] Al. Santucci, S. Tosti, and F. Franza. Model improvements for tritium transport in DEMO fuel cycle. *Fusion Eng. Des.*, 9899:1880 – 1884, 2015.

[107] A. Aiello, A. Ciampichetti, and G. Benamati. Determination of hydrogen solubility in lead lithium using sole device. *Fusion Eng. Des.*, 81:639–644, 2006.

[108] L. Bühler. Magnetohydrodynamic flows in arbitrary geometries in strong, nonuniform magnetic fields a numerical code for the design of fusion reactor blankets. *Fusion Technol.*, 27(1):3–24, 1995.

[109] S. Smolentsev, N. Morley, and M. Abdou. Code development for analysis of MHD pressure drop reduction in a liquid metal blanket using insulation technique based on a fully developed flow model. *Fusion Eng. Des.*, 73:83–93, 2005.

[110] T. Rhodes, S. Smolentsev, and M. Abdou. Magnetohydrodynamic pressure drop and flow balancing of liquid metal flow in a prototypic fusion blanket manifold. *Phys. Fluids*, 30:057101, 2018.

[111] A. Khodak. Numerical analysis of 2-d and 3-d MHD flows relevant for fusion applications. *IEEE Trans. Plasma Sci.*, 45(9):2561–2565, 2017.

[112] A. Khodak. Adaptation of general purpose CFD code for fusion MHD applications. In *Proceedigns- Symposium on Fusion Engineering*, 2016.

[113] P. Satyamurthy, P.K. Swain, V. Tiwari, I.R. Kirillov, D.M. Obukhov, and D.A. Pertsev. Experiments and numerical MHD analysis of LLCB TBM test-section with NaK at 1T magnetic field. *Fusion Eng. Des.*, 91(Supplement C):44 – 51, 2015.

[114] P.K. Swain, A. Shishko, P. Mukherjee, V. Tiwari, S. Ghorui, R. Bhattacharyay, A. Patel, P. Satyamurthy, S. Ivanov, E. Platacis, and A. Ziks. Numerical and experimental mhd studies of lead-lithium liquid metal flows in multichannel test-section at high magnetic fields. *Fusion Engineering and Design*, 132:73 – 85, 2018.

[115] S. Sahu and R. Bhattacharyay. Validation of comsol code for analyzing liquid metal magnetohydrodynamic flow. *Fusion Engineering and Design*, 127:151 – 159, 2018.

[116] Y. Yan, S. Smolentsev, and M. Abdou. Validation of COMSOL multiphysics for magnetohydrodynamic (MHD) flows in fusion applications. In *COMSOL Conference Boston*, 2017.

[117] C. Mistrangelo and L. Bühler. Influence of helium cooling channels on magnetohydrodynamic flows in the HCLL blanket. *Fusion Eng. Des.*, 84:1323–1328, 2009.

[118] L. Bühler, C. Mistrangelo, H.-J. Brinkmann, and C. Koehly. Pressure distribution in MHD flows in an experimental test-section for a HCLL blanket. *Fusion Eng. Des.*, 127:168 – 172, 2018.

[119] L. Bühler and C. Mistrangelo. MHD flow and heat transfer in model geometries for WCLL blankets. *Fusion Eng. Des.*, 124:919 – 923, 2017. Proceedings of the 29th Symposium on Fusion Technology (SOFT-29) Prague, Czech Republic, September 5-9, 2016.

[120] L. Bühler and C. Mistrangelo. Pressure drop and velocity changes in MHD pipe flows due to a local interrumption of the insulation. *Fusion Eng. Des.*, 2017.

[121] H. K. Versteeg and W. Malalasekera. *An introduction to computational fluid dynamics. The fine volume method*. Longman Sicentific andTechnical, 1995.

[122] E. Mas de les Valls. *Development of a simulation tool for MHD flows under nuclear fusion conditions*. PhD thesis, Dept. of Physics and Nuclear Engineering. Universitat Politcnica de Catalunya, 2011.

[123] Q. He, H. Chen, and J. Feng. Acceleration of the OpenFOAM-based MHD solver using graphics processing units. *Fusion Eng. Des.*, 101:88 – 93, 2015.

[124] S. Selimli, Z. Recebli, and E. Arcaklioglu. MHD numerical analyses of hydrodynamically developing laminar liquid lithium duct flow. *Int. J. Hydrogen Energy*, 40:15358–15364, 2015.

[125] S. Smolentsev, R. Moreau, L. Buhler, and C. Mistrangelo. MHD thermofluid issues of liquid-metal blankets: Phenomena and advances. *Fusion Eng. Des.*, 85(7):1196 – 1205, 2010.

[126] S. Smolentsev, N. B. Morley, and M. Abdou. Magnetohydrodynamic and thermal issues of the SiCf/SiC flow channel insert. *Fusion Sci. Technol.*, 50(1):107–119, 2006.

[127] R. Stieglitz, L. Barleon, L. Bühler, and S. Molokov. Magnetohydrodynamic flow in a right-angle bend in a strong magnetic field. *J. Fluid Mech.*, 326:91123, 1996.

[128] J. S. Walker. Liquid metal flow trough a thin walled elbow in a plane perpendicular to a uniform magnetic field. *Int. J. Eng. Sci.*, 24:1741, 1986.

[129] L. Bühler and L. Giancarli. Magnetohydrodynamic flow in the European HCLL blanket concept. Technical Report FZKA 7069, Institut fr Kern- und Energietechnik, 2005.

[130] S. Smolentsev, T. Rhodes, G. Pulugundla, C. Courtessole, M. Abdou, S. Malang, M. Tillack, and C. Kessel. MHD thermohydraulics analysis and supporting R&D for DCLL blanket in the FNSF. *Fusion Eng. Des.*, 2017.

[131] C. Mistrangelo and L. Bühler. Electro-magnetic flow coupling for liquid metal blanket applications. *Fusion Eng. Des.*, 109-111(Part B):1452 – 1457, 2016.

[132] L. Bühler and C. Mistrangelo. Liquid metal MHD flows near noninsulated gaps between flow channel inserts in DCLL blankets. *IEEE Trans. Plasma Sci.*, 42(3):510–515, March 2014.

[133] K. Miyazaki, K. Konishionishi, and S. Inoue. MHD pressure drop of liquid metal flow in circular duct under variable transverse magnetic field. *J. Nucl. Sci. Technol.*, 28(2):159–161, 1991.

[134] G. Pulugundla, S. Smolentsev, T. Rhodes, C. Kawczynski, and M. Abdou. Transition to a quasi-fully developed MHD fflow in an electrically conducting pipe under a transverse non-uniform magnetic field. *Fusion Sci. Technol.*, 88:684–689, 2015.

[135] D. Rapisarda, I. Fernández, I. Palermo, F.R. Urgorri, L. Maqueda, D. Alonso, T. Melichar, O. Frbort, L. Vla, M. Gonzalez, P. Norajitra, H. Neuberger, and A. Ibarra. Status of the engineering activities carried out on the european DCLL. *Fusion Eng. Des.*, 124:876 – 881, 2017.

[136] I. Fernández-Berceruelo, M. Gonzalez, I. Palermo, F.R. Urgorri, and D. Rapisarda. Large-scale behavior of sandwich-like FCI components within the EU-DCLL operational conditions. *Fusion Eng. Des.*, 2018.

[137] I. Palermo, D. Rapisarda, I. Fernández-Berceruelo, and A. Ibarra. Optimization process for the design of the DCLL blanket for the european DEMOnstration fusion reactor according to its nuclear performances. *Nucl. Fusion*, 57(7):076011, 2017.

[138] H. C. Ji and R. A. Gardner. Numerical analysis of turbulent pipe flow in a transverse magnetic field. *Int. J. Heat Mass Transfer*, 40(8):1839–1851, 1997.

[139] V. Gnielinski. New equations for heat and mass transfer in turbulent pipe and channel flow. *Int. Chem. Eng*, 16(2):359–368, 1976.

[140] B. Schulz. Thermophysical properties of the Li(17)Pb(83) alloy. *Fusion Eng. Des.*, 14(3):199 – 205, 1991.

[141] E. Mas de les Valls, L.A. Sedano, L. Batet, I. Ricapito, A. Aiello, O. Gastaldi, and F. Gabriel. Leadlithium eutectic material database for nuclear fusion technology. *J. Nucl. Mater.*, 376(3):353 – 357, 2008.

[142] F. Tavassoli. Fusion DEMO interim structural design criteria appendix a material design limit data A3.S18E Eurofer steel. Technical report, DMN, 2004.

[143] F. Gillemot, E. Gaganidze, and I. Szenthe. Material property handbook pilot project on EUROFER97(MTA EK, KIT). Technical Report EFDA-D-2MRP77, EUROfusion, 2016.

[144] J. S. Walker. Magnetohydrodynamic flows in rectangular ducts with thin conducting walls. *Journal de Mcanique*, 20(1), 1981.

[145] M. Schäfer. *Computational-Engineering-Introduction to Numerical Methods*. Springer, 2006.

[146] ANSYS. Inc. *ANSYS-FLUENT 18.0 User's Guide*, 2016.

[147] ANSYS. Inc. *ANSYS FLUENT UDF manual*, 2011.

[148] J. M. Kooljman. Laminar heat or mass transfer in rectangular channels and cylindrical tubes for fully developed flow: comparison of solutions obtained for various boundary conditions. *Chem. Eng. Sci.*, 28:1149–1160, 1973.

[149] P. Harriott and R. M. Hamilton. Solid-liquid mass transfer in turbulent pipe flow. *Chem. Eng. Sci.*, 20:1073–1078, 1965.

[150] F. P. Berger and K. F. F.-L. Hau. Mass transfer in turbulent pipe flow measured by the electrochemical method. *Int. J. Heat Mass Transfer*, 20:1185–1194, 1977.

[151] W. H. Linton and T. K. Sherwood. Mass transfer from solid shapes to water in streamline and turbulent flow. *Chem. Eng. Prog.*, 46:258, 1950.

[152] E. N. Sieder and G. E. Tate. Heat transfer and pressure drop of lliquid in tubes. *Ind. Eng. Chem. Fundam.*, 28(12):1429–1435, 1936.

[153] T. H. Chilton and A. P. Colburn. Mass transfer (absorption) coeficients: Prediction from data on heat transer and fluid friction. *Industrial and Engineering Chemistry*, 1934.

[154] A. Santucci, A. Frattolillo, M. Incelli, and S. Tosti. The coolant purification system in DEMO: Interfaces and requirements. *Fusion Eng. Des.*, 124:744 – 747, 2017.

[155] M. Utili. Preliminary design of LiPb loops. Technical Report EFDA-D-2ML9BZ, EUROfusion, 2016.

[156] L. Barucca, M. Caramello, M. Marconi, and A. Barbensi. Support to the finalization of the HCPB/WCLL BB PHTS design and systems design review and PHTSs cost preliminary evaluation (industry task). Technical Report STU-DEMO-0008, ANSALDO NUCLEARE, 2018.

[157] A. Del Nevo, E. Martelli, M. Tarantino, F. Giannetti, V. Narcisi, and G. Caruso. Pbli heat exchanger and fluid technology. In *PPPT WPBOP Task Review Meeting*, January 2018.

[158] Y. C. Chan and E. Veleckis. A thermodynamic investigation of dilute solutions of hydrogen in liquid Li-Pb alloy. *J. Nucl. Mater.*, 122 & 123:935–940, 1984.

[159] I. Ricapito, P. Calderoni, A. Ibarra, C. Moreno, Y. Poitevin, A. Rueda, and J. Serna. Tritium transport modelling: first achievements on ITER test blanket ssystem simulation and perspectives for DEMO breeding blanket. In *25th IAEA Fusion Energy Conference*, number FIP/P4-9, 2014.

Publications and conference contributions

Publications in peer-reviewed international scientific journals:

1. F. R. Urgorri, S. Smolentsev, I. Fernández-Berceruelo, D. Rapisarda, I. Palermo and A. Ibarra.

   Magnetohydrodynamic and thermal analysis of PbLi flows in poloidal channels with flow channel insert for the EU-DCLL blanket. Nuclear Fusion, (2018) 58(10):106001

   `https://doi.org/10.1088/1741-4326/aad299`

2. I. Fernández-Berceruelo, M. Gonzalez, I. Palermo, F. R. Urgorri, D. Rapisarda.

   Large-scale behavior of sandwich-like FCI components within the EU-DCLL operational conditions. Fusion Engineering and Design, (2018) In Press.

   `https://doi.org/10.1016/j.fusengdes.2018.03.044`

3. I. Fernández-Berceruelo, D. Rapisarda, I. Palermo, F. R. Urgorri, P. Agostinetti, F. Cismondi, H. P. L. De-Esch and A. Ibarra.

   Integration of the Neutral Beam Injector System into the DCLL Breeding Blanket for the EU DEMO. IEEE Transactions on Plasma Science, (2018) 46(7):2708-2716

   `https://ieeexplore.ieee.org/document/8353728`

4. F. R. Urgorri, C. Moreno, E. Carella, D. Rapisarda, I. Fernández-Berceruelo, I. Palermo and A. Ibarra.

Tritium transport modeling at system level for the EUROfusion Dual Coolant Lithium-Lead breeding blanket. Nuclear Fusion, (2017) 57(11):116045

https://doi.org/10.1088/1741-4326/aa7f9d

5. D. Rapisarda, I. Fernández, I. Palermo,F. R. Urgorri, L. Maqueda, D. Alonso, T. Melichar, O. Frbort, L. Vla, M. Gonzlez, P. Norajitra, H. Neuberger, A. Ibarra.

   Status of the engineering activities carried out on the European DCLL. Fusion Engineering and Design, (2017) 124:876-881

   https://doi.org/10.1016/j.fusengdes.2017.02.022

6. E. Carella, C. Moreno, F. R. Urgorri, D. Rapisarda.

   Tritium modelling in HCPB breeder blanket at system level. Fusion Engineering and Design, (2017) 124:687-691

   https://doi.org/10.1016/j.fusengdes.2017.01.051

7. F. R. Urgorri, C. Moreno, E. Carella, j. Castellanos, A. Del Nevo and A. Ibarra.

   Preliminary system modeling for the EUROfusion water cooled lithium lead blanket. Fusion Science and Technology, (2017) 71:444-449

   http://www.tandfonline.com/doi/abs/10.1080/15361055.2016.1273712

8. E. Carella, C. Moreno, F. R.Urgorri, D. Demange, J. Casterllanos, and D. Rapisarda.

   Tritium behavior in HCPB breeder blanket unit: modelling and experiments. Fusion Science and Technology, (2017) 71:444-449

   http://www.tandfonline.com/doi/abs/10.1080/15361055.2017.1289584

Contributions to international conferences:

1. 9th International Conference on Computational Methods (ICCM2018). August 2018. Rome, Italy.

   Oral contribution: Magneto-convective analyses of the EU-DCLL outboard equatorial module using Q2D methods.

2. 13th International Symposium on Fusion Nuclear Technology. Kyoto, Japan.

   Poster contribution: Large-scale behavior of sandwich-like FCI components within the EU-DCLL operational conditions.

3. 11th International Conference on Tritium Science and Technology (Tritium2016). April 2016. Charleston, USA.

   Oral contribution: Preliminary system moldelling for the Water Coolant Lithium Lead Blanket.

List of technical reports for EUROfusion:

1. I. Fernández, I. Palermo, F. R. Urgorri. DCLL Design Report 2017 (2018) EDFA-D-2NP3RD.

2. F. R. Urgorri and C. Moreno. Consolidated Tritium Transport Modelling for WCLL at System Level (2017) EFDA-D-123456.

3. I. Fernández, D. Rapisarda, I. Palermo, F. R. Urgorri, L. Maqueda, D. Alonso, J. Olalde. DCLL Design Report 2016 (2017) EFDA-D-2MMM6Q.

4. F. R. Urgorri and C. Moreno. Preliminary System Modeling for DCLL. (2016) EFDA-D-2MX463.

5. I. Fernndez, D. Rapisarda, I. Palermo, F. Roca, L. Maqueda and D. Alonso. DCLL Design Report 2015 (2016) EFDA-D-2MYHGZ.

6. D. Rapisarda, I. Fernández, I. Palermo, F. Roca, M. Gonzalez, T. Melichar, O Frybort, L. Vala, L. Maqueda, D. Alonso, H. Neuberger, P. Norajitra, M. Reungoat, M. Utili, Design Description Document 2015 for DCLL (2016) EFDA-D-2MT44J.

7. F. R. Urgorri and C. Moreno. Preliminary System Modeling for WCLL (2015) EFDA-D-2MKYST.

Participation on research projects:

1. December 2017-November 2018: Modelling of tritium transport in HCLL and HCPB-TBS: further development on the EcosimPro based codes (F4E-GRT-0897).

   Fusion for Energy.

   Project leader: David Rapisarda Socorro.

2. January 2015-December 2018: T transport Analyses at System level for BB (WP BB-6.2.1).

   EUROfusion Consortium.

   Project leader: David Demange (2016), Ion Cristescu.

3. January 2015-December 2018: Hydrogen isotopes studies in liquid metal systems for fusion applications (ENE2013-43650-R HISMEFUS).

   Spanish Ministry of Economy.

   Main researcher: David Rapisarda Socorro and Joaquin Mollá.

4. September 2016-Febreuary 2017: Development of the simulation tool, based on the EcosimPro platform, for tritium migration through HCLL and HCPB-TBS: verification and preliminary validation Grant 771 (F4E-GRT-771).

   Fusion for Energy.

   Project leader: David Rapisarda Socorro.